The Dissertation Committee for Mackenzie Denali Day certifies that this is the approved version of the following dissertation:

Pattern formation and preservation in aeolian systems

Committee:

Gary Kocurek, Supervisor

William Anderson

John Holt

Wonsuck Kim

David Mohrig

Pattern formation and preservation in aeolian systems

by

Mackenzie Denali Day, B.S. Geo.

Dissertation

Presented to the Faculty of the Graduate School of

The University of Texas at Austin

in Partial Fulfillment

of the Requirements

for the Degree of

Doctor of Philosophy

The University of Texas at Austin

May 2017

Acknowledgements

The contents of this dissertation would not have been possible with the generous support and assistance of many people and groups. Funding support was provided by Shell Exploration and Production Company, Conoco Phillips, the NASA Mars Science Laboratory Participating Scientists Program, the National Science Foundation Graduate Research Fellowship Program, and the Jackson School of Geosciences. Field work associated with these chapters was conducted with the help of David Mohrig, Sarah Brothers, Travis Swanson, Anine Pedersen, Jasmine Mason, Cecelia Lopez-Gamundi, and John Day. Jim Buttles and Greg Klein helped design the wind tunnel experimental setup, and Ashwin Vasavada graciously served as host at the Jet Propulsion Laboratory during the Bagnold Dune Field sampling campaign of *Curiosity*. I thank the thesis committee, including in memoriam Nathan Bridges, for the support of and intellectual contributions to this dissertation, and especially thank Gary Kocurek for the patience and wisdom that are responsible for my fascination with dunes.

Pattern formation and preservation in aeolian systems

Mackenzie Denali Day, PhD

The University of Texas at Austin, 2017

Supervisor: Gary Kocurek

Aeolian sediment transport forms natural patterns common on Earth and other planetary bodies. The self-organization of sand in transport results in dune fields with dune morphologies determined by wind regime. Patterning in dune fields is known to arise from the autogenic process of dune interactions, but the evolution of dune patterns over time remains poorly constrained. In this work dune fields were parameterized in terms of dune interactions to quantify dune-field pattern stability. Interactions are fundamental to dune-field development, but studies of interactions have focused on their surface expression, and how interactions are expressed in the ancient record has yet to be documented. This problem is addressed with five examples of interaction-generated stratigraphy identified in well-known Jurassic aeolian sandstones using criteria based on recent near-surface interpretations of interaction stratigraphy form White Sands Dune Field, New Mexico. Interactions control the autogenic development of dune fields, but allogenic factors including basin subsidence, water table rise, and sediment supply largely control the accumulation and preservation of aeolian strata. In a case study of a section of the Jurassic Entrada Sandstone, this work addresses the interplay between allogenic and autogenic controls on what is actually preserved in the rock record, and demonstrates how long stretches of time can be collapsed into surfaces between geologic units that represent relatively short-lived events. The competition between allogenic and

autogenic influences on aeolian pattern formation is not unique to Earth, and Mars also hosts patterned landscapes thought to be generated by aeolian sediment transport. Such landscapes include intra-crater layered mounds such as Aeolis Mons in Gale crater, the landing site of the Mars Science Laboratory rover. Competing hypotheses about whether these mounds formed by aeolian erosion of crater-filling deposits, or by aeolian deposition were addressed with wind tunnel and large eddy simulation experiments. The results are compatible with an erosional origin of the mounds. Additional analyses of wind-formed landscapes within and around Gale crater further supported the wind-erosion hypothesis of the central mound.

Table of Contents

List of Tables

List of Figures

Chapter 1: Introduction

The transport of sand creates a diverse range of natural patterns on Earth and other planets (Bagnold, 1941; Sagan et al., 1972; Greeley and Arvidson, 1990). Whether depositional, such as ripple and dune fields, or erosional, such as yardangs and ventifacts, the geomorphic features resulting from sediment transport record information about the history of local winds as integrated over both modern and geologic time (Blackwelder, 1934; Cooper, 1958; Allen, 1970; Hunter, 1977a; Greeley and Iversen, 1987). In active surface systems, the transport of sand forms bedforms that can grow to become dune fields. These dune fields form patterns through the autogenic process of dune interactions, in which dunes collide, merge, and split (Kocurek et al., 2010). Captured in experimental (Endo et al., 2004; Hersen and Douady, 2005; Ping et al., 2014), modeling (Werner, 1995; Katsuki et al., 2005; Eastwood et al., 2011), and field studies (Gay, 1999, Elbelrhiti et al., 2005, Brothers et al., 2017), interactions commonly occur in association with bedform terminations or defects (Werner and Kocurek, 1997), and represent imperfections in well-developed dune-field patterns. In Chapter 2 this work addresses the long-standing hypothesis that dunes evolve toward a stable pattern equilibrium by using the natural scale-invariance of dune pattern morphologies as measured by interaction density to test for changes in dune patterns with time.

The history of dune fields can also become incorporated into the rock record in the form of sets of cross-strata deposited by migrating lee faces (Sorby, 1869; Allen, 1963). Set architectures in aeolian deposits preserve the history of dune shape, behavior, and migration. Methods for interpreting aeolian stratigraphic architectures largely predate the initial documentation of dune interactions (e.g., Brookfield, 1977; Hunter and Rubin, 1983; Rubin and Hunter 1983; Rubin 1987; Kocurek 1996), and although much recent

progress has been made in modeling (Gao et al., 2015; Swanson, 2015) and documenting (Brothers et al., 2017) interaction stratigraphy, incorporating interactions into interpretations of stratigraphy is still in its infancy, and no examples of ancient interaction architecture have been documented. In Chapter 3 of this work, criteria for identifying interaction-generated stratigraphy developed from near-surface strata at White Sands Dune Field, New Mexico, are applied to a survey of Jurassic aeolian sandstones. Five examples of dune interactions preserved in the ancient rock record are presented as evidence that interactions, ubiquitous in modern systems, also shaped dune fields in the ancient past.

Connecting the behaviors of modern aeolian dune fields with their expression in the rock record is at the core of interpreting preserved aeolian stratigraphy. However, the boundary conditions and allogenic forcings that promote the accumulation and subsequent preservation of an aeolian deposit are not necessarily the same as those that promote the initial establishment of the dune field (Kocurek and Havholm, 1993). In many cases, dunes form and migrate across an area without ever leaving a record of their passage, simply bypassing along a surface. The conditions necessary for a) dune fields to form, b) dune fields to deposit strata, and c) that strata to be preserved, are complex and subject to both allogenic and autogenic forcings. Some autogenic processes such as cannibalization of underlying strata by deeply scouring troughs (Paola and Borgman, 1991), or removal of dunes by interactions (Kocurek et al., 2010), precludes for preservation of aeolian deposits. The accumulation and preservation of aeolian strata mostly rely on allogenic forcings, such as regional wind patterns, water table rise, regional sand supply, and basin subsidence. In Chapter 4, a case study of a section of the Jurassic Entrada Sandstone explores what stages of dune field development are actually represented in a 60 m aeolian vertical section. The study uses the gross set architecture to

define distinct periods of dune-field accumulation, erosion, and preservation, to assess how much time is actually represented in the rock record, and compare how much time is collapsed into outcrop-scale bounding surfaces.

Patterns formed by aeolian sediment transport are not unique to Earth. On Mars, aeolian processes have been the dominant force for geomorphic change for the past few billion years (Edgett and Malin, 2000; Greeley et al., 1976; Greeley et al., 1993). Early in the history of Mars (Noachian: 4.5-3.7 Ga), flowing surface water created canyon systems (Costard and Kargel, 1995), gullies (Malin et al., 2006), lakes (Cabrol and Grin, 2010), and potentially a northern hemispheric ocean (Head et al., 1999). Impact cratering during the late heavy bombardment spotted the landscape with craters that served as sedimentary basins across the planet (Grotzinger and Milliken, 2012). Whether early Mars hosted a “warm and wet” climate with persistent surface water, or a “cold and dry” climate with ephemeral surface water remains a topic of much debate (Kerr, 2003; Squyres and Kasting, 1994; Wordsworth, 2016), but during the Noachian, the martian landscape exhibited an enigmatic range of sedimentary processes comparable to that of modern Earth. At the end of this period, Mars transitioned into a new mineralogical and climatological period known as the Hesperian (3.7-3.1 Ga) (Bibring et al., 2006).

The Noachian-Hesperian transition has been hypothesized to represent a change in the sedimentological regime of Mars from one where lacustrine and fluvial deposition occurred to one where a cessation of fluvial processes was followed by a dominance of aeolian processes that included wind erosion of sedimentary strata and widespread occurrences of dune fields (Grotzinger and Milliken, 2012; Malin and Edgett, 2000). A continuation of the dominance of aeolian processes during the Amazonian period (3.1 Ga to present) has created the martian landscape evident today. The Hesperian and Amazonian total more than three billion years during which winds could shape the

martian landscape without the confounding influence of overprinted marine, fluvial or tectonic signatures. Mars is thus an excellent natural laboratory for studying end-member landscape evolution governed by aeolian erosion over long time scales.

One genre of martian landscape thought to be carved by aeolian erosion are intra-crater layered mounds. First identified by Malin and Edgett (2000), intra-crater layered mounds form in crater interiors and exhibit a spectrum of morphologies from crater-filling, to central mounds, to isolated buttes. Competing hypotheses debated whether these mounds formed from initially crater-filling deposits that had been slowly carved to their present forms by aeolian erosion (Grotzinger and Milliken, 2012; Malin and Edgett, 2000), or whether the mounds formed in place depositionally by dust-fall from the atmosphere (Kite et al., 2013; Kite et al., 2016). In Chapter 5, wind-tunnel experiments and large eddy simulations were applied to test the hypothesis that aeolian erosion could carve crater-interior deposits and autogenically form the eroding morphological spectrum proposed by Malin and Edgett (2000).

Gale crater hosts an intra-crater layered mound known as Aeolis Mons or colloquially as “Mount Sharp,” and is immediately adjacent to the landing site of the Mars Science Laboratory rover *Curiosity* (Anderson and Bell, 2010; Cabrol et al., 1999; Hobbs et al., 2010). Consequently, the data available for this particular intra-crater layered mound represent the highest spatio-temporal resolutions anywhere on Mars, and include both orbital- and ground-based imaging. Gale crater also hosts a wide variety of geomorphic features generated by aeolian sediment transport including dune fields, yardangs, wind streaks, and transverse aeolian ridges. When formed, each of these features records a wind direction integrated over different time scales depending on the formation time scale of the feature. To further address the hypothesis discussed above and tested in Chapter 5, geomorphic features in Gale crater were analyzed to determine

whether aeolian features on the central mound were consistent with sculpting by crater-scale winds. Analyses in Chapter 6 integrated observations from scales as large as the crater itself and as small as centimeter-scale nodules observed on rock surfaces by *Curiosity* to reconstruct the history of winds forming this landscape.

Chapter 2: How perfect is perfect in a dune-field pattern?

2.1 INTRODUCTION

Aeolian dune fields self-organize into patterns within a set of boundary conditions. Where dune fields originate upon a planar surface of loose granular material, many small proto-dunes emerge on the surface, and these evolve into patterns with progressively fewer, larger and more widely spaced dunes (Bagnold, 1941; Werner, 1995, 1999). Evolving dune-field patterns show collisions between dunes and dune segments with disparate migration rates, and many dunes end in free terminations or "defects." Collisions between dunes are termed "interactions" and consist of several geomorphic processes such as dune combination, merging, cannibalization, and ejection of dune segments (Kocurek et al., 2010), all of which represent a redistribution of sand within the dunes. Dune defects are a major driver in dune interactions because these migrate faster than the main body of the dunes and frequently collide with downwind dunes (Werner and Kocurek, 1997). Dune interactions have been observed in nature (Elbelrhiti et al., 2008; Ewing and Kocurek, 2010a), and simulated in experiments (Endo et al., 2004; Hersen and Douady, 2005), and in numerical models (Génois et al., 2013; Swanson et al., 2016a). It is now recognized that dune interactions are the dynamics by which the dune-field pattern evolves. Because these dynamics are autogenic processes inherent to the dunes within the system, the pattern that emerges self-organizes. Boundary conditions, which are external environmental parameters such as the wind regime, nature of the sand supply, and size and shape of the topographic container that houses the dune field, define the attractor basin of the system and thus the limits within which the dune-field pattern may evolve (Werner, 2003).

The hypothetical end product of dune-field self-organization is a "perfect pattern," in which dune crestlines are continuous across the field, large dunes are widely

spaced, and all dunes maintain the same size and migration rate such that dune interactions no longer occur (Werner and Kocurek, 1999). On Earth the perfect dune-field pattern is thought to be rarely, if ever, achieved because of the time required for large, slow-migrating dunes to arrive at this configuration versus the frequency in which boundary conditions change and the pattern is reformed (Kocurek and Ewing, 2005). Rather, a natural dune field is thought to approach this state when free defects have been consumed by interactions, and interactions of any type are rare between large, widely spaced dunes.

Implicit in this understanding of evolving dune fields is that free defects, as measured by the "defect-density" parameter (Werner and Kocurek, 1997), and dune interactions become progressively fewer through time where a dune field originates over an underlying sand source, or in space where a dune field originates from an upwind point or line source of sand (Ewing et al., 2006; Ewing and Kocurek, 2010b). Measurements from dune fields do indeed concur that defect density decreases over a wide range of dune types and sizes on Earth and other planets as dune spacing increases (Ewing et al., 2015), and the number of dune interactions has been shown to decrease downwind from a line sand source (Ewing and Kocurek, 2010a). Dune spacing is taken as a proxy for time because dunes grow more widely spaced as the dune-field pattern evolves.

This work is motivated by the observation that dune-field patterns, as with many other natural phenomena such as mud cracks, snowflakes or branching rivers, exhibit similar patterns over a range of scales (Mandelbrot, 1967; Turcotte and Huang, 1995). Without a scale, meter-scale beach dunes are largely indistinguishable from kilometer-scale dunes in the Sahara. By measuring the spatial density of dune interactions over a wide range of dune spacing, and non-dimensionalizing this measurement to compare

dunes across arbitrary scales, we show that while interactions do become spatially farther apart as the dune pattern evolves, the non-dimensional interaction density remains constant. Restated, as dune-field patterns coarsen or expand overall with time and space, the pattern, as defined by dune morphology and a relative spatial density of interactions, does not change. This result implies that dune-field patterns achieve a dynamic steady-state over relatively short periods of time that is then maintained over the life of the dune field. Moreover, the spatial density of interactions measured in globally distributed fields of crescentic and linear dunes, the two most common dune types, resulted in parallel but statistically distinct trends with spacing for each morphology. This result implies that dune-field pattern evolution is independent of boundary conditions except those that control the dune morphology.

2.2 METHODS

A global survey of modern dune fields measured dune spacing and identified interactions in 16 dune fields with crescentic dunes and 11 dune fields with linear dunes (Fig. 2.1). Fields were selected based on dune morphology and with an aim to cover a wide range of scales (see Appendix A material for complete list of fields and references). In each field a study area was chosen near the center of the field where the dune morphology was homogenous and apparently unaltered by local topography or edge-effects associated with dune-field margins. For crescentic dune fields, the selected areas covered 7-10 dune spacings in both the transport and cross-transport directions, an area sufficient to fully represent the pattern (Swanson et al., 2016b). For linear fields the selected areas were extended further parallel to the dune crestlines to ensure a statistically significant number of interactions were captured. Mean dune spacing was calculated from

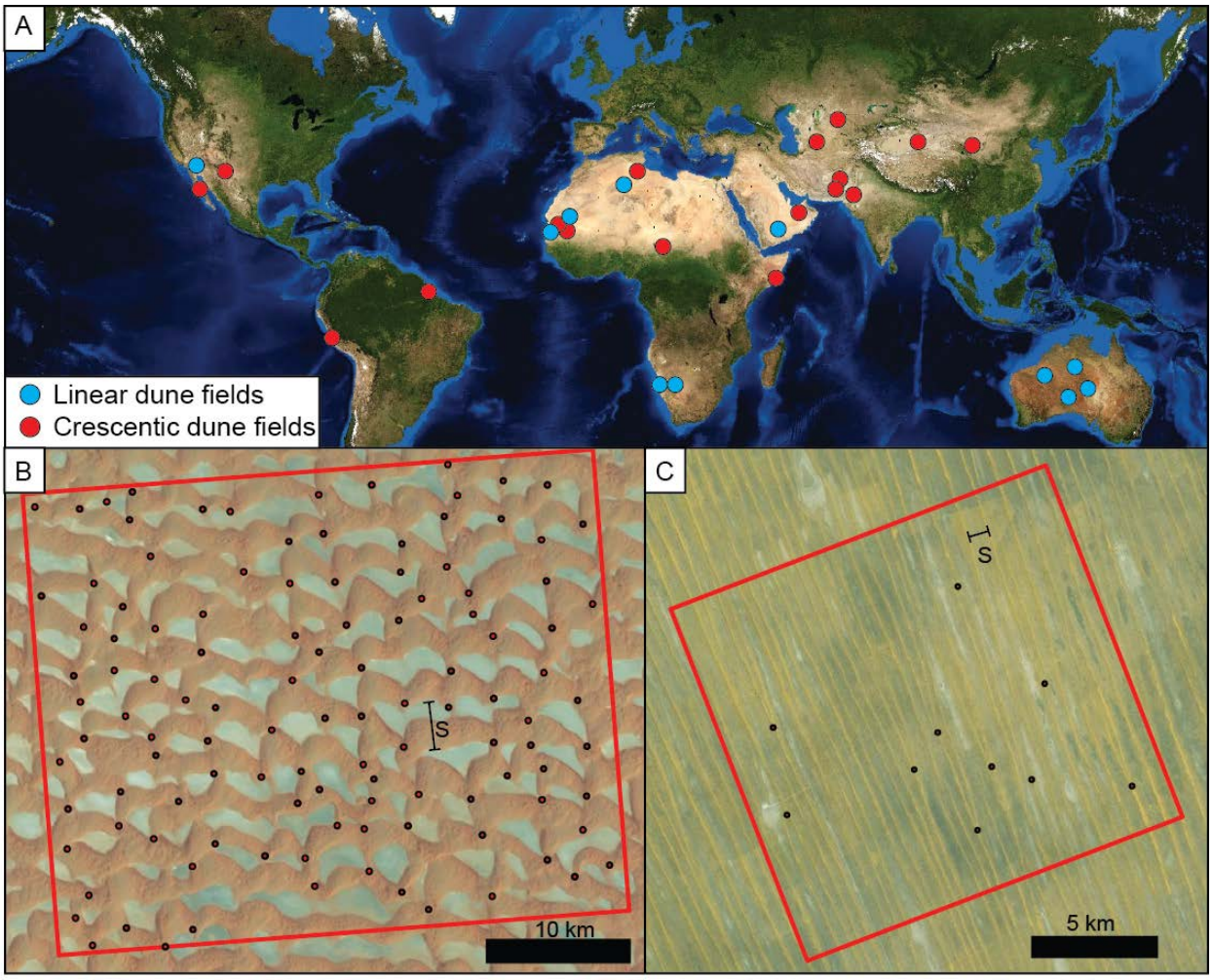

Figure 2.1: Examples of dune-field patterns analyzed in this study. (A) Global map of the locations of measured dune fields (see Appendix A for more information). (B) Crescentic dunes in the Rub ‘al Khali Desert. (C) Linear dunes in the Kalahari Desert. In (B) and (C) the area measured is boxed in red and all interpreted interactions are marked with dots. Dune spacing was measured along transects in the image, but for simplicity one representative spacing is shown (black bracket). North is up in all images.

spacing measured along 3-5 transects within the measured area. Lastly, all interactions were identified and counted within the area. For the purposes of this paper, interactions were considered any bedform collision occurring in the image or interpreted imminent collision where two or more bedforms (including defects) were separated by < 0.1 times the mean spacing. The interpretation of interactions is necessarily subjective as the images studied represent only a snapshot in time. To limit potential error in this

measurement, all measurements were made by the same observer and visual inspection by another observer revealed the conservative identifications were subject to at most a 20% variation in the total number of interactions present (Fig. 2.2). In many cases the studied dunes exhibited superimposed patterns of smaller bedforms on stoss or lee slopes. These patterns were ignored and only the largest-scale pattern in the image was measured. Because dunes occur on other planetary bodies, a smaller set of three martian crescentic dune fields using images from the High Resolution Imaging Science Experiment, and two Titan linear dune fields using Cassini Radar data were also measured in this analysis (Appendix A).

2.3 RESULTS

The spatial density of interactions (I) was calculated as a ratio of the number of interactions counted (n) to the area in which these were observed (A) (Fig. 2.1):

$$I = n/A. \tag{2.1}$$

Figure 2.2 shows the interaction density for each of the measured fields plotted against mean dune spacing in that field. The interaction density monotonically decreases as mean dune spacing increases, but crescentic and linear dunes follow statistically distinct trends (Student's two-sample t-test, $p = 0.90$). Both trends, however, can be modeled using the power law relation:

$$I = \alpha S^{\beta} \tag{2.2}$$

where S is the mean spacing for the dune field, and α and β are constants. The power-law fit to each dune type yields $(\alpha, \beta) = (0.58, -2.0)$ for crescentic dune fields, and $(\alpha, \beta) = (0.04, -2.0)$ for linear dune fields with 95% confidence intervals on β of [-2.3, -1.8] and [-2.6, -1.5] for crescentic and linear dune fields, respectively. The sample correlation

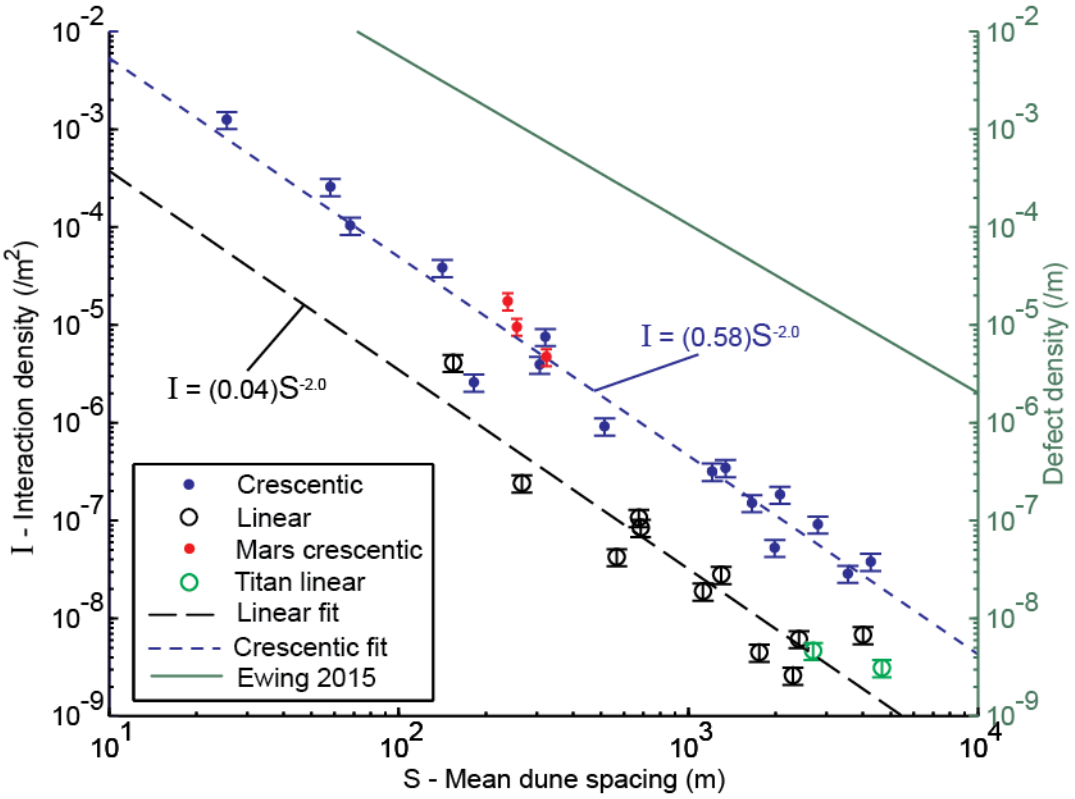

Figure 2.2: Interaction density measured in aeolian dune fields. Interaction density (I; Eq. 2.1) is plotted against the mean dune spacing (S) for the 32 dune fields measured in this study. Dune fields with crescentic and linear dune morphologies sampled statistically distinct populations, and each population was modeled by the power-law fit shown. Crescentic martian (red) and linear Titan (green) dunes were not included in this fit, but plot along the respective trends nevertheless. Error bars show 20% deviation from counted number of interactions in each direction. Plotted against the right-hand axis is the power-law fit to defect density measured by Ewing et al. (2015). The defect and interaction densities result in similar fits but are measured in different units and therefore difficult to directly compare.

coefficients were $r^2 = 0.96$ and $r^2 = 0.87$ again for crescentic and linear dune fields, respectively.

To compare the spatial interaction density in morphologically similar fields of different scales, the measured interaction density was parameterized into a dimensionless interaction density or simply "interaction index" (I^*) by the characteristic length scale (S):

$$I^* = (n/A)S^2 = IS^2. \quad (2.3)$$

The mean spacing can be considered to have units of meters per spacing. Thus, the interaction index, although dimensionless, describes the number of interactions expected in an area of one square spacing. Using the definition in Equation (2.3) and the modeled fit in Equation (2.2), the dimensionless parameterization can be rewritten as:

$$I^* = IS^2 = \alpha S^{\beta+2}. \quad (2.4)$$

The form of Equation (2.4) suggests that the interaction index is a function of spacing (and therefore time), however, the modeled fit to both crescentic and linear dune fields results in $\beta = -2.0$, in which case the exponent in Equation (2.4) becomes zero and I^* becomes a constant (α). Although values of α differ for crescentic and linear dunes, the modeled β values do not, indicating that the two morphologies are defined by distinct but constant interaction indices. Plotting calculated values of interaction index against dune spacing confirms this result (Fig. 2.3), and various regressions to the plotted data all yielded correlation coefficients of <0.1, indicating that no trend describes the data better than the predicted flat line. Physically this means that the density of interactions as measured in terms relative to the field itself is not a function of the dune spacing within the field. If the modeled fit to the data had yielded a value of $\beta < -2.0$, the interaction index would depend on dune spacing and interactions would become less frequent in the pattern as spacing increased. Conversely if $\beta > -2.0$ the interaction index would also be dependent on spacing, but larger spacings would yield more interactions within the pattern.

Although the exact relationship between dune spacing and time is incompletely characterized, the lack of dependence on spacing in the interaction index necessarily requires a lack of dependence on time. Similarly, the dune fields measured in this study

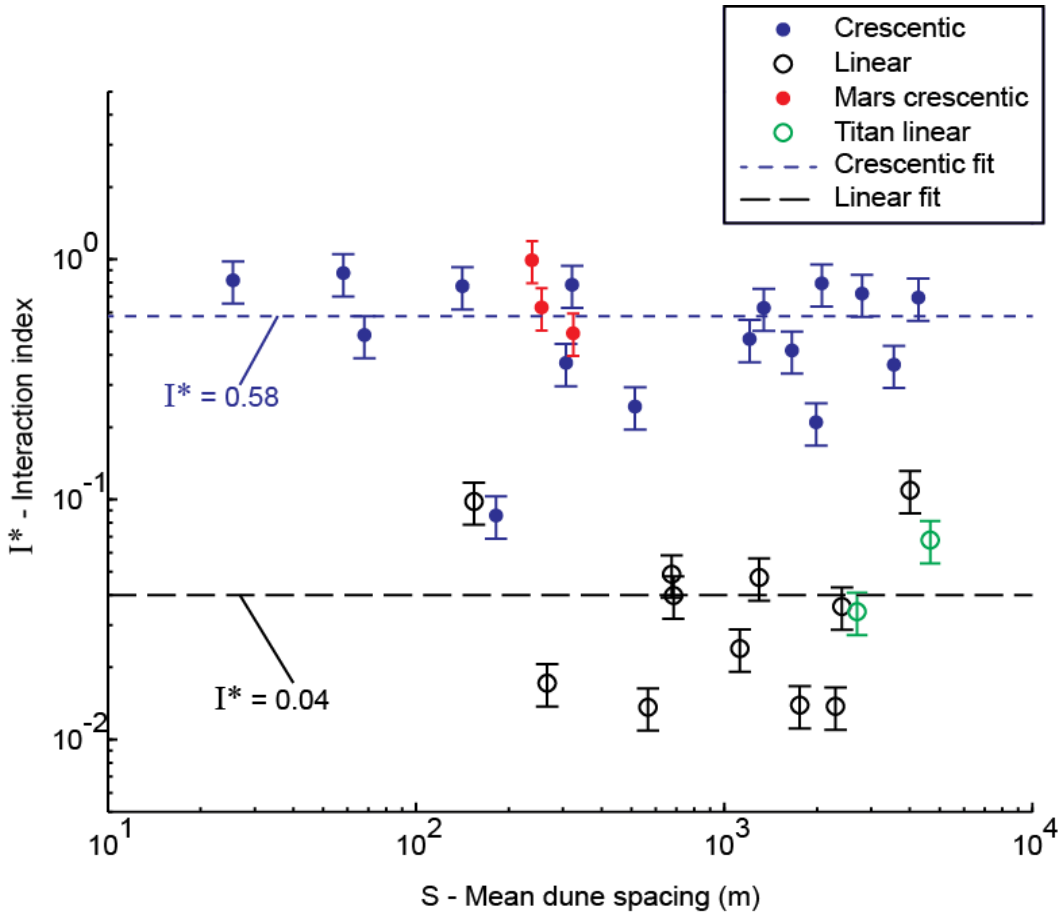

Figure 2.3: Interaction index. The interaction index (I*; Eq. 2.3), a non-dimensional parameterization of the data in Figure 2.2, is plotted against spacing (S) to demonstrate that there is no dependence on spacing in the interaction index. The dashed lines correspond to the power-law fits to the data for crescentic and linear dune fields. No trend is apparent or statistically significant in this plot, and any trend that might potentially exist is both within the noise of the data and too slight to manifest over geologic time. Error bars show 20% deviation from counted number of interactions in each direction.

cover a wide range of boundary conditions. The fields include both coastal and continental fields, fields bounded by mountain ranges and those without topographic confinement, and fields with a wide variety of types of sediment sources. Despite the highly variable boundary conditions, all the measured fields plot along the trends described in Equation (2.2), suggesting that the distribution of interactions is only

dependent on those boundary conditions that determine dune morphology, and independent of other boundary conditions thereafter.

Martian crescentic dune fields were measured as per their terrestrial counterparts, but were not included in the power-law fit to the terrestrial data. Nevertheless, Figures 2.2 and 2.3 show that the martian crescentic dunes fall along the trend modeled for terrestrial crescentic dunes. The morphologies typical of linear dunes on Earth are largely absent on Mars, but Titan is dominated by morphologically similar linear dunes. Titan dunes have only been imaged with Cassini Radar and therefore can only be resolved at wavelengths of >2 km (Lorenz, 2006). Two regions of the Fensal Sand Sea on Titan (Radebaugh et al., 2008; Radebaugh et al., 2010) with mean spacings of 2.7 and 4.6 km were measured and compared with terrestrial data. As with the martian crescentic dune fields, the measured interaction density for Titan linear dunes agrees with the expected value based on the terrestrial linear dune model.

2.4 DISCUSSION

The patterns in terrestrial dune fields as described by interaction density show scale-invariance than can be modeled by a power-law relationship. This result in itself is unsurprising given the abundance of self-similar patterning seen in nature (Mandelbrot, 1967; Turcotte and Huang, 1995). However, in this case because the characteristic length scale (spacing) is a proxy for time, the particular magnitude of the power-law exponent determines whether dune-field patterns evolve toward more, fewer, or a constant number of interactions through time as spacing increases. The central result of this work can be distilled to the data-fit resulting in the power-law exponent $\beta = -2.0$, which removes all dependence on spacing in the normalized interaction density (interaction index), and implies pattern similarity at all scales. The value of the power-law exponent $\beta = -2.0$

appears to be robust. Although some error in β is inherent to a fit to measured data, the modeled value of β is (1) the same for both crescentic and linear dunes to three significant figures, despite differences in the constant of proportionality α of more than an order of magnitude, and (2) the calculated values of interaction index show no trend with spacing (Fig. 2.3). Indeed, even if the calculated β value is an overestimate and the actual value is $\beta < -2.0$, the hypothetical decrease in interaction index with spacing is so small as to be within the error of the measurements, and would not make an appreciable difference even over geologic time. Instead, the simpler explanation is that the calculated β value reflects a quadratic relationship between interaction density and spacing, and when parameterized to be in terms relative to the dune field alone, the dimensionless interaction index becomes independent of spacing and therefore time.

This conclusion runs counter to the prevailing hypothesis that dune fields are evolving toward a "perfect pattern" in which dune interactions leave the system or stop migrating and the pattern has therefore achieved stability (Werner and Kocurek, 1999). The results of this study do confirm previous works by showing that dune interactions decrease spatially as the dune field constructively evolves, and concur that this trend is both highly predictable and directly related to spacing. This trend is in tandem to the decrease in defect density with time as dune spacing increases (Werner and Kocurek, 1999; Ewing et al., 2015). However, parameterizing the data so that interaction density is presented in terms of the spacing within the dune field (i.e., the interaction index) shows no trend in the frequency of interactions as dune fields evolve. Fundamentally, dune-field pattern evolution is limited by the topographic containers in which these reside (Ewing and Kocurek, 2010b), and pattern coarsening cannot continue indefinitely. Moreover, interactions among barchan dunes contribute to a size selection within the field (Elbelrhiti et al., 2008), but not the development of continuous crestlines because these dunes exist

in a sand-limited boundary condition. However, as measured over orders of magnitude (Fig. 2.2), interactions persist in both crescentic and linear dune fields of all sizes at a constant relative density.

Although $\beta = -2.0$ for both crescentic and linear dunes, the constant of proportionality α in the power law fit (Eq. 2.2) is 0.58 for crescentic dune fields but for linear dune fields it reduces to 0.04. Given $\beta = -2.0$ in Equation 4, the expected value for interaction index $I^* = 0.58$ for crescentic dune fields and $I^* = 0.04$ for linear dune fields, regardless of the dune spacing. This result implies that interaction index is dependent on dune morphology, but the range of dune fields sampled in this study implies that interaction index is independent of all other boundary conditions that do not contribute to dune morphology. Dunes with similar morphologies necessarily have boundary conditions in common, such as wind regime and sand supply (Rubin and Hunter, 1987; Courrech du Pont et al., 2014), but also occur within a set of boundary conditions that are otherwise different. Especially considering the inclusion of dunes on Titan and Mars, the agreement between the wide range of dune fields argues that interaction density is a function only of dune morphology and the dynamics that those morphologies imply.

Although the dynamics of crescentic and linear morphologies that give rise to their disparate interaction indices are not completely understood, some differences in behaviors are apparent. With crescentic dunes, free defects at both dune terminations are available to impinge on downstream dunes and instigate interactions, whereas for linear dunes only the downstream free defect is available and the upstream defect is erosional. However, for dune fields of comparable spacing and length, this morphological difference would yield only a factor of two in the difference in the number of available defects to cause interactions, and therefore would yield similar interaction indices and not the order of magnitude difference observed. Additionally, crescentic dunes are more

sinuous than linear dunes, and this sinuosity enhances the range in local spacing between dunes. Small local spacing increases the likelihood of an interaction between the nearby dunes. Secondary flow on crescentic dunes, arising from the local incidence angle between the brinkline segment and the primary wind, results in a constant deformation of the dunes with migration (Eastwood et al., 2012; Swanson et al., 2016b). These variations around the long-term crestline orientation (Rubin and Hunter, 1987; Swanson et al., 2016b) also enhance the possibilities for interactions. In contrast, except for winds that are transverse to the brinkline, all other winds striking the straight brinkline of linear dunes are deflected to cause along-slope transport on the lee face, thereby suppressing sinuosity and enhancing the linear morphology (Werner and Kocurek, 1997; Rubin, 2012). Moreover, interactions in linear dunes are dominated by the collision of a free defect with another dune, forming the characteristic Y-junction that opens opposite of the net transport direction, whereas a much broader range of interaction types occur with crescentic dunes (Kocurek et al., 2010).

Having established that dune-field patterns are maintained over the lifetime of an evolving dune field, the question then becomes why does this occur? How can dune-field patterns expand and evolve via dune interactions, while also maintaining a constant spatial density of interactions as measured relative to dune spacing? The results of this work suggest that dune-field patterns reach a dynamic steady state over geologically short time scales, and that the formed patterns are then maintained as the dune field evolves and expands. The reason for this may lie with the dune interactions themselves.

Field observations (Ewing and Kocurek, 2010a) and simulations (Eastwood et al., 2011; Gao et al., 2015; Swanson et al., 2016a) show that after the initial development stage of the dune field, dune interactions propagated through the system and the number of interactions is conserved. For crescentic dune fields, interactions such as merging,

cannibalization, and lateral linking of defects that all reduce the number of dunes or defects in an absolute sense occur in the early stages of pattern development, and subsequent interactions more commonly involve dune collisions where dunes combine, but also eject a dune segment. The ejected dune segment and its defects then migrate downwind to instigate additional interactions (Landry and Werner, 1994). Although never documented in nature, in a simplified model, this type of interaction increases dune spacing, but the number of defects and interactions is conserved (Werner and Kocurek, 1999). This process would end when all defects and interactions work their way through the dune field, but the required time given large, slow-migrating dunes in large dune fields is typically greater than the time on Earth over which boundary conditions change and the pattern begins to reform (Ewing et al., 2006). The inherent sinuosity and deformation of crescentic dunes with migration also enhances the possibility of continued interactions. In addition, in many natural systems new, faster migrating dunes are introduced at the upwind dune-field margin, and thereby introduce fresh waves of interactions into the system.

The long-term behavior of the Y-junction type of interactions that dominate in linear dunes has not been documented in nature, but observations suggest that it is either conserved in the pattern or leads to ejected segments as with crescentic dunes. In a simplified model of linear dunes originating at the upwind dune-field margin, Y-junctions form with the collision of free defects with adjacent dunes, causing a downwind progression in which dune spacing increases (Werner and Kocurek, 1999). Natural dune fields in the Simpson (Folk, 1971) and Kalahari (Bullard et al., 1995) deserts approximate this pattern, where the Y-junctions appear to be conserved in the pattern. Conversely, some simulations (Swanson et al., 2016a) show examples where the dune collision that yields the Y-junction is followed by an ejection, which creates a free defect that may

instigate yet another interaction. This behavior would account for the occurrence of free defects well into a well-formed linear dune-field pattern, and the lateral merging of the upwind defect of the ejected segment with an adjacent dune would yield the uncommon occurrence of Y-junctions opening downwind (Breed et al., 1979). Finally, with either crescentic or linear dune fields, any spatial or temporary change in boundary conditions that disrupts the pattern acts to introduce new defects and interactions (Bullard et al., 1995).

2.5 CONCLUSIONS

In crescentic and linear dune fields, the dune-field pattern can be represented by a dimensionless interaction index that is independent of spacing, time, and boundary conditions not already captured in the dune morphology. This independence extends to the planetary-scale boundary conditions of gravity and fluid density, as exampled by dunes on Mars and Titan. Dune-field patterns reach a dynamic steady state rapidly with a constant relative density of interactions (interaction index) dependent on dune morphology, and this pattern is maintained even as the dune field pattern coarsens to larger and larger scales. The spatial density of interactions decreases quadratically with spacing following a constant of proportionality that differs in crescentic and linear dune fields. Because the dependence on spacing is quadratic, normalizing by spacing to create the non-dimensional interaction index yields a constant interaction index of 0.58 for fields of crescentic dunes, and 0.04 for fields of linear dunes. Differences between the interaction behaviors in crescentic and linear dune fields are attributed to morphological differences, and the positive and negative morphological feedbacks set up by secondary flows in crescentic and linear fields, respectively. The constant relative density of dune

interactions across a wide range of scales may arise from the conservation and propagation of the interactions within the pattern.

2.6 Acknowledgments

The authors thank N. Lancaster for his helpful suggestions of study areas used in this work, and D. Mohrig for his thoughts and guidance on the interpretation.

Chapter 3: Aeolian dune interactions preserved in the ancient rock record

3.1 INTRODUCTION

Aeolian dune fields self-organize into patterns dependent upon local boundary conditions that include parameters related to sediment supply, wind regime, and antecedent topography (e.g., Werner, 1999, 2003; Baas, 2007; Ewing and Kocurek, 2010a, b; Kocurek et al., 2010). It is now understood that dune-field pattern evolution occurs through autogenic dune interactions, which include dynamics such as collisions, dune segment combination, ejection of dune segments, cannibalization, and merging (Werner and Kocurek, 1997; Hersen et al., 2004; Elbefiglrhiti et al., 2005; Diniega et al., 2010; Gao et al., 2015). Dune interactions have been documented in experiments (Endo et al., 2004; Hersen and Douady, 2005; Ping et al., 2014), models (Werner, 1995; Eastwood et al., 2011; Génois et al., 2013; Swanson et al., 2016a), and field studies (Elbelrhiti et al., 2008; Hugenholtz and Barchyn, 2012; Brothers et al., 2017), and it is now recognized that dune interactions are ubiquitous in modern aeolian dune fields.

In contrast to the progress in understanding dune interactions in modern dune fields, incorporating dune interactions into the interpretation of the aeolian stratigraphic record has received far less attention. Aeolian deposits record the shape and behavior of ancient dunes as sets of cross-strata and bounding surfaces that result from dune migration. When dunes interact, an additional dynamic is imposed upon ordinary dune migration and this dynamic should be represented in the stratigraphy. However, existing methodologies for the interpretation of set and bounding surface architectures (e.g., Brookfield, 1977; Hunter and Rubin, 1983; Rubin and Hunter, 1983; Kocurek, 1996; Mountney, 2006a) predate the recognition of dune interactions. As a result, current models for generating aeolian cross-strata (Rubin, 1987; Rubin and Carter, 2006) rely

upon the translation of bedforms that never undergo interactions. Although dune interactions are realistically captured in more recent dune-surface models (e.g., Pelletier, 2009; Duran et al., 2010; Parteli et al., 2014; Worman et al., 2013), some of which (Gao et al., 2015; Swanson et al., 2016a) imply stratigraphic expressions of dune interactions, field evidence of interaction architectures in the ancient record has thus far not been documented.

In a modern dune field, compelling documentation of the stratigraphic architecture arising from a dune interaction requires both a record of the interacting dunes and identification of the resultant stratigraphic architecture. In the one such example of which we are aware, Brothers et al. (2017) correlated dune interactions observed in a half-century of remote images of the White Sands Dune Field, New Mexico, with cross-strata created by the interactions as revealed in interdune exposures and ground-penetrating radar (GPR) images. The types of dune interaction studied at White Sands are very common in this and other dune fields (Elbelrhiti et al., 2008; Ewing and Kocurek, 2010a; Hugenholtz and Barchyn, 2012), and belong to the class of interactions where two dunes collide, combine, and eject a dune segment. Documentation of interaction architectures at White Sands established a set of criteria by which a record of this type of interaction could be identified, and distinguished from already known architectures in the ancient record created by ordinary dune migration.

In this study, we use the criteria established by Brothers et al. (2017) to identify five examples of interaction architectures in well-known Jurassic aeolian sandstones. The interpretation of these outcrops as examples of interaction architecture illustrates the inevitable point that dune interactions, ubiquitous in modern dune fields, must also leave a stratigraphic record. This recognition implies that interaction architectures may have

been misidentified in the past, and emphasizes the need for revision of current methods for the interpretation of aeolian strata.

3.2 IDENTIFICATION OF AN ANCIENT INTERACTION

3.2.1 Interaction type and dynamics

The dune interaction types addressed at White Sands by Brothers et al. (2017) are termed defect repulsion and bedform repulsion by Kocurek et al. (2010), and both are driven by the dune terminations or defects (c.f., Werner and Kocurek, 1997). In these types of dune interactions, an upwind, faster-migrating defect ("impactor" of Brothers et al., 2017) collides with the stoss slope of a slower-migrating downstream dune (the "target"), migrates up its stoss slope, and attaches at the target brinkline, forming a triple or Y-junction (Fig. 3.1A). Time-series images of these types of interactions at White Sands (Ewing and Kocurek, 2010a; Brothers et al., 2017) show that as the impactor nears the target dune, the segment of the target downwind of the impactor bows out in the transport direction and assumes a parabolic shape (Fig. 3.1A). As the interaction progresses, the impactor and the lateral target segment combine into a continuous brinkline, and the now-parabolic arm of the redundant target dune segment thins (Fig. 3.1A). The interaction culminates with the combination of the target and impactor dune segments (originally entirely separate dunes), and ejection of the parabolic-shaped redundant target segment (the "ejecta dune," Fig. 3.1A). Not shown in Figure 3.1A, the trailing defect of the ejecta dune swings to point downstream as the ejected segment migrates away from the interaction, creating a new fast-migrating defect available to instigate a new interaction (Ewing and Kocurek, 2010a; Brothers et al., 2017). Defect repulsion and bedform repulsion interactions, both of which are documented in Brothers et al. (2017), form via the same mechanism described above, but with a defect repulsion

only one defect of the impactor dune collides with the target, whereas with a bedform repulsion both defects of the impactor dune collide with the target.

3.2.2 Distinguishing criteria

Distinguishing criteria of the interaction architecture, discussed in detail by Brothers et al. (2017) and only summarized here, arise from: (1) the dynamics of the interaction, (2) the orientation of the impactor defect relative to that of the target dune,

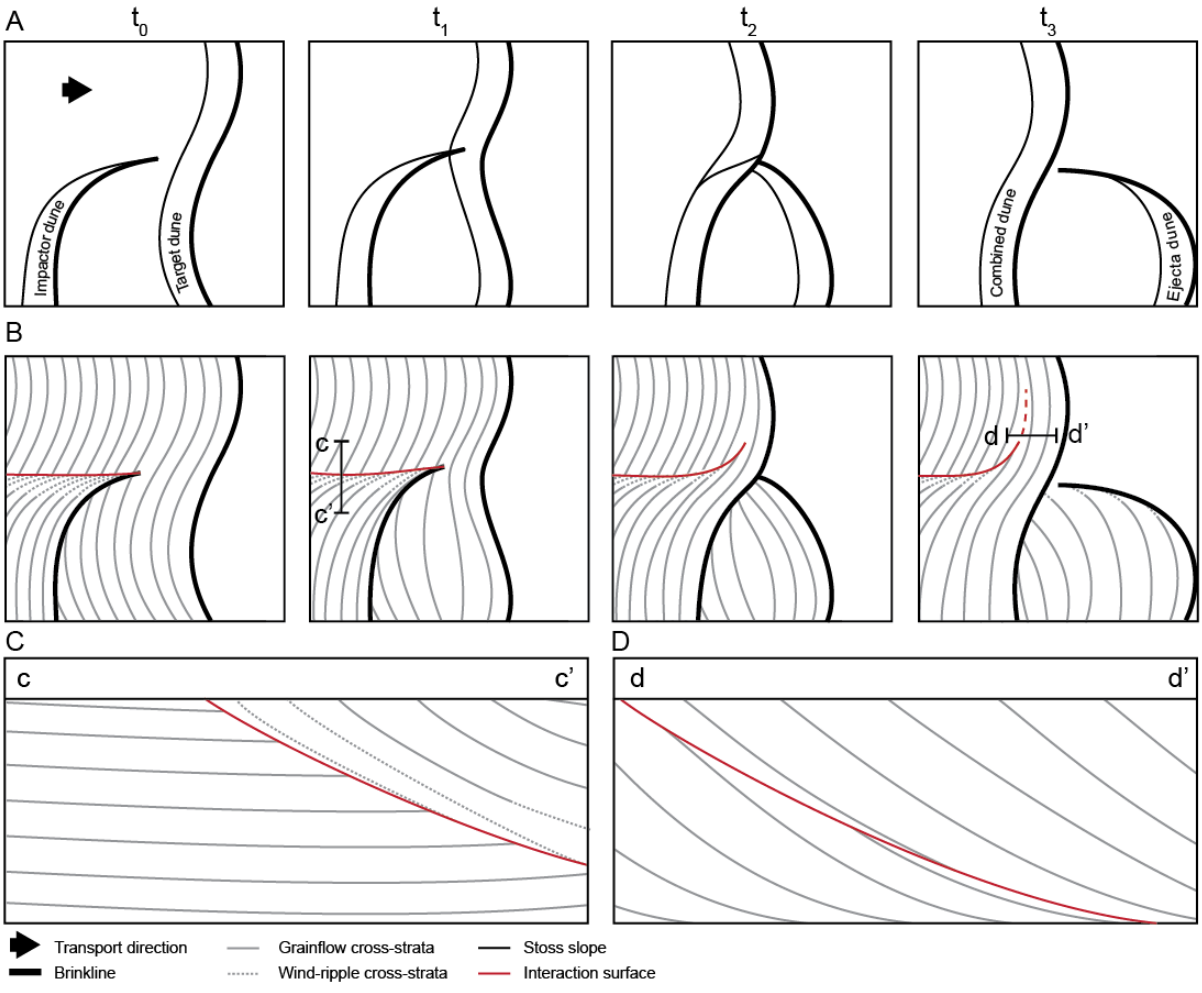

Figure 3.1: Defect-driven interaction morphology and stratigraphy

Figure 3.1: Defect-driven interaction morphology and stratigraphy. (A) Plan-view progression of an interaction. Time progresses from left to right as the dune morphology develops during the interaction. At t_0 the impactor dune approaches the target dune from upstream with an elongated defect arm. At time t_1 the impactor defect migrates up the stoss slope of the target and the downwind segment of the target begins to become parabolic. At time t_2 the defect of the impactor has attached to the brinkline of the target dune, and a continuous brinkline has formed. The lee face of the combined dune extends downslope over the thinning arm of the redundant target segment. At t_3 the combined lee face continues to migrate as the parabolic ejecta dune migrates away. (B) Generation of sets of cross-strata and interaction bounding surface corresponding in time with (A) above. At t_0-t_1 the interaction surface forms with scour of the underlying target set as the overlying impactor defect set overrides the target dune. The target set is laterally truncated by the interaction surface at a high angle, and cross-strata of the impactor defect approach the surface at an acute angle to tangentially onlap the surface (Criterion 1). Across the bounding surface, target and impactor cross-strata diverge by ~90° (Criterion 2), and target grainflow cross-strata contrast with wind-ripple cross-strata of the impactor defect laminae (Criterion 3). At time t_2 the interaction surface, which has been trending in the transport direction, curves to become parallel to the target lee face (Criterion 4). (C) Strike-section across the interaction surface as shown in t_1. Impactor cross-strata (right) downlap onto the interaction surface, which truncates the target strata. (D) Dip-section across the interaction surface as shown in t_3. The interaction surface is nearly parallel with the target (left) and combined-dune cross-strata (right). Adapted from Brothers et al. (2017).

grainfall and wind-ripple cross-strata of Hunter, 1977b) and the incidence angle between the wind and the brinkline orientation (Eastwood et al., 2012). Figure 3.1B shows the progressive generation of sets of cross-strata corresponding to the morphological stages shown above in Figure 3.1A. At the beginning of the interaction (t_0) as the defect of the impactor dune approaches the target dune, a key distinction between impactor and target is their orientation. The target dune is oriented in the general trend of dunes in the field, whereas the defect trend is typically 45°-55° to this trend (Swanson et al., 2016b). Because the general dune trend is as transverse as possible to all constructive winds (i.e., the gross bedform-normal orientation of Rubin and Hunter, 1987a), cross-strata of the target dune will consist of grainflow deposited during any transverse wind events (Eastwood et al., 2012). The defect, however, is oblique to these winds and is typically

characterized by wind-ripple cross-strata deposited by ripples migrating along the slope of the lee slope (Eastwood et al., 2012).

As the impactor continues to migrate (t_1), it scours into the underlying target set, producing a bounding surface that laterally truncates the target set and that dips toward the impactor set (Fig. 3.1C). Wind-ripple laminae of the defect downlap onto the surface in a strike cross-section (Fig. 3.1C) and tangentially approach the surface in plan-view (t_1 in Fig. 3.1B). The interaction bounding surface tracks the trajectory of the faster-migrating defect and trends in the transport direction. As the impactor attaches to the target brinkline (t_2 in Fig. 3.1A), the surface curves to trend parallel to the target lee face as the impactor and target begin to combine (t_2 in Fig. 3.1A-B). As the trailing arm of the redundant target segment diminishes and pulls away as the ejecta dune, the combined dune lee face extends progressively downward until it reaches the floor of the interdune area (t_3 in Fig.1A-B). In dip sections across the bounding surface, the surface truncates the target cross-strata at a low angle and cross-strata of the impactor downlap onto the surface (Fig. 3.1D). Away from the Y-junction in plan-view, the surface loses definition laterally into target cross-strata (t_3 in Fig. 3.1A).

The dune interaction dynamics described above yield four distinguishing criteria for this type of interaction, as summarized below from Brothers et al. (2017).

1. Cross-strata of the target dune are laterally truncated by the interaction bounding surface at a high angle, and cross-strata of the impactor defect approach the surface from the other side at an acute angle to then tangentially onlap the surface in plan-view.
2. Across the interaction bounding surface, target and impactor cross-strata diverge at a high angle, approaching 90° immediately across the surface.

3. Across the interaction bounding surface, target strata are typically dominated by or contain grainflow cross-strata, whereas impactor cross-strata consist of wind-ripple laminae.
4. The interaction bounding surface separating the impactor and target set trends in the transport direction and dips toward the impactor set, but then curves and trends parallel to the target cross-strata and laterally is lost as the two sets combine into one.

3.2.3 Comparison between interaction and other known architectures

The interaction architecture with its distinguishing criteria listed above are distinct from architectures created with ordinary dune migration. The plan-view section is most diagnostic because it shows two sets separated by a bounding surface combining into one set in the migration direction as the interaction surface curves and subsequently loses definition laterally (Fig. 3.1B). Cross-strata of the combined set are then continuous from the former impactor set into the former target set. Prior to the formation of the combined set, the juxtaposition across the interaction surface of the abruptly truncated cross-strata of the target set with that of the impactor set with their divergent cross-strata dip orientations and different stratification types is distinct.

Cross-sectional views of the interaction architecture are considerably more ambiguous, as discussed in detail in Brothers et al. (2017). In a dip section across the interaction surface, target cross-strata, interaction surface, and impactor cross-strata all dip in the general transport direction (Fig. 3.1D). This architecture is very similar to that of reactivation surfaces (Kocurek, 1996; 3rd order surfaces of Brookfield, 1977). Reactivation surfaces arise with any redefinition of the lee face that results in scour of already deposited cross-strata, such as with a change in wind directions. These surfaces

are characterized by the same general dip direction as the subjacent and superjacent cross-strata (Hunter and Rubin, 1983; Rubin, 1987; Rubin and Carter, 2006). However, especially where these surfaces form because of a cyclic wind regime, reactivation surfaces typically occur as multiple irregularly to regularly spaced surfaces within a set, whereas an interaction surface would be a singular feature. Superposition surfaces (Kocurek, 1996; 2nd order surfaces of Brookfield, 1977) created by the migration of dunes superimposed upon the lee face of a larger bedform can resemble reactivation surfaces in dip sections, except that the cross-strata and the surfaces have different orientations (Rubin and Hunter, 1983; Rubin, 1987; Rubin and Carter, 2006). In addition, as with reactivation surfaces, superposition surfaces typically occur as multiple features created by trains of migrating superimposed dunes.

In a strike section across the interaction surface, the architecture is essentially that of trough sets (e.g., Rubin, 1987, his fig. 34). With migrating crescentic dunes, however, the concave-downwind dune segment is typically preserved, whereas the defects are not preserved (e.g., Rubin, 1987, his fig. 34). With defect or bedform repulsion, the surface scour and its fill result from the migration of the defect. Hence, an indication that the structure shown in Figure 3.1C does not represent simple trough cross-strata is the abrupt, perhaps mid-trough, truncation of the target set, in contrast to the adjacent defect set characterized by wind ripple cross-strata oriented at a high angle to the cross-strata of the target set.

3.3 STUDY AREAS AND METHODS

Outcrops of aeolian sandstones were surveyed in the vicinity of Page, Arizona, and Arches National Park, Utah (Fig. 3.2; Table 3.1). The survey targeted well-known aeolian units including the Jurassic Navajo Sandstone, the Jurassic Page Sandstone, and

the Jurassic Entrada Sandstone (e.g., Kocurek, 1983; Blakey et al., 1988; Havholm et al., 1993). Because of the ambiguity in identifying interaction architecture in cross-sections, as discussed above, focus was upon outcrops with extensive plan-view exposures. In addition, because the spatial density of interactions decreases as the dune-field pattern evolves, this study focused upon outcrops showing smaller sets (<100 m wide) of cross-strata in order to maximize the probability of encountering interaction architecture. Interaction architectures identified near Page, AZ (i.e., in Page and Entrada Sandstones; Fig. 3.2A) were photo-documented, and the orientations of cross-strata and bounding surfaces were measured with a Brunton compass. Divergence angles between impactor and target cross-strata were measured from surface trends and these are reported to the nearest 5°. For interaction architectures identified in Arches National Park (i.e., in Navajo Sandstone; Fig. 3.2B), a total station theodolite was additionally used to measure and georeference cross-strata and bounding surfaces.

Table 3.1: Names and locations of outcrops interpreted as records of ancient interactions

Site	**Location (UTM Zone 12)**
Example A	0623476 E, 4276534 N
Example B	0623967 E, 4276650 N
Example C	0622498 E, 4279287 N
Example D	0449695 E, 4086874 N
Example E	0446048 E, 4094290 N

3.4 EXAMPLES OF PRESERVED INTERACTION STRATIGRAPHY

3.4.1 Example A: Navajo Sandstone

Example A shows a prominent bounding surface separating two distinct sets of cross-strata, and occurs over a 10 x10 m plan-view exposure of Navajo Sandstone ~700 m east of the La Sal Mountains Viewpoint (Fig. 3.2B; Table 3.1). The bounding surface

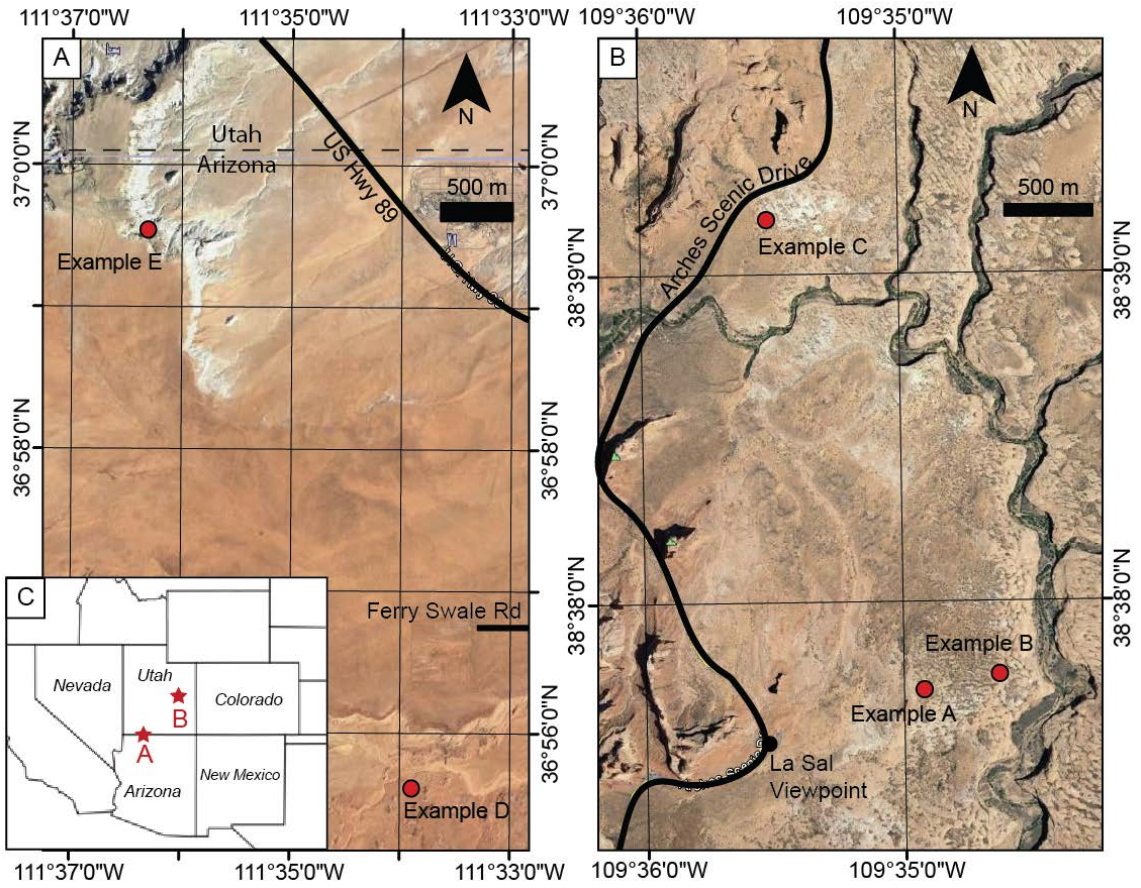

Figure 3.2: Context maps showing the locations of the five outcrops with interpreted examples of interaction architecture. (A) Interaction architectures identified in outcrops of Jurassic Entrada Sandstone (Example E) and Jurassic Page Sandstone (Example D) near the Utah-Arizona border. (B) Interaction architectures in outcrops of Jurassic Navajo Sandstone in Arches National Park. (C) Red stars show the approximate locations of (A) and (B) in the southwestern US.

trends in the dune transport direction (SE) and dips toward the SW (Fig. 3.3). In the transport direction, the surface then curves to the east to become parallel to the strike of the interpreted target set, at which point the two sets combine into one, and the interpreted interaction surface becomes indistinguishable laterally along strike (Criterion 4). Sinuosity along the northern portion of the interaction surface is attributed to local centimeter-scale relief that exposes the surface at different levels. Cross-strata in the

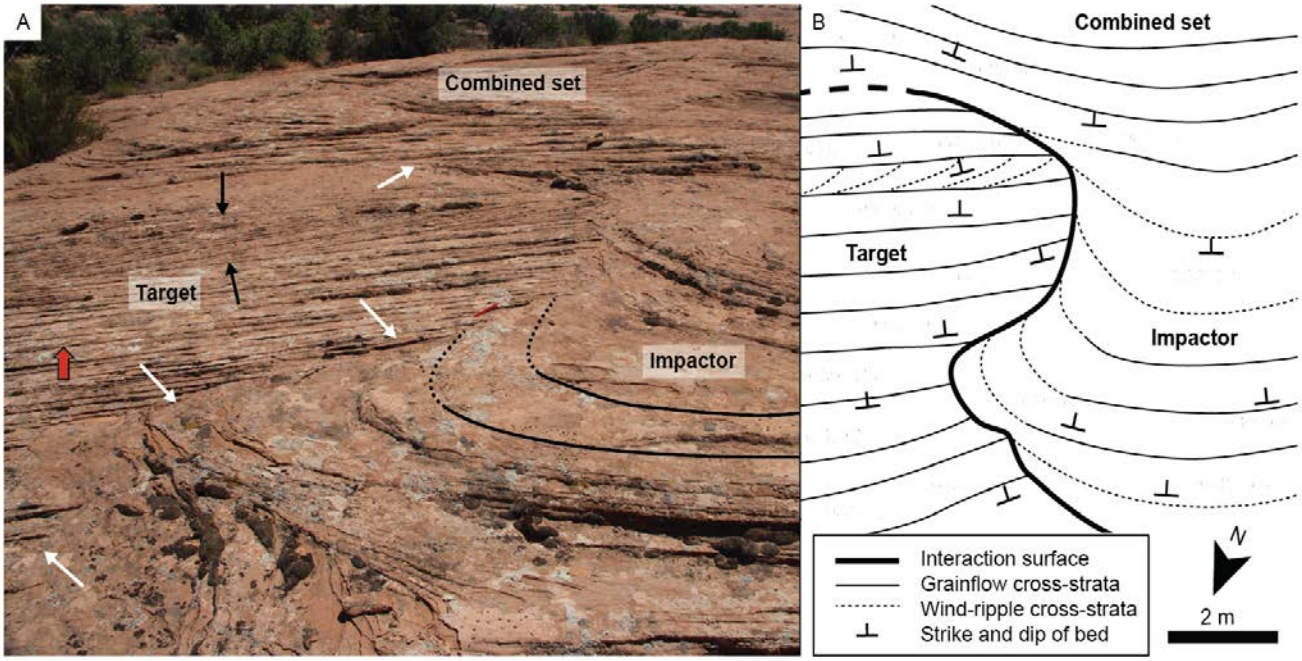

Figure 3.3: Interaction architectures in Example A: Navajo Sandstone. (A) This SE-facing view shows the interaction surface (white arrows) trending in the transport direction (southeast; red arrow) and then turning to the east to parallel the target strata (Criterion 4). Cross-strata in the target set dip to the SE and include a coset of compound cross-strata ~60 cm thick, which is bounded by second-order bounding surfaces (black arrows). In the foreground target grainflow strata are truncated by the interaction surface, and wind-ripple strata of the defect tangentially approach the surface (Criteria 1 and 3). (B) Plan-view schematic of the stratigraphic architecture measured at this example. The average divergence angle between the orientation of the impactor and target strata is 95° (Criterion 2). Foreground sinuosity in the interaction surface is attributed to centimeter-scale relief in the outcrop.

target dune set dip toward the SE (mean dip direction of 148°) and are dominated by 3-6 cm thick grainflow stratification (Criterion 3). The target set contains a single, thin (60 cm) compound set showing along-slope transport to the NE. Cross-strata of the target set are truncated by the interaction surface at an average angle of 75° (Criterion 1). Cross-strata of the interpreted impactor set range in dip direction from 149°-176° (mean of 161°), capturing the concave-southeast curvature of this interpreted dune defect. More central portions of the impactor set are dominated by wind-ripple laminae with some

grainflow cross-strata, but near the interaction surface the cross-strata consist exclusively of wind-ripple laminae (Criterion 3). These wind-ripple laminae curve and approach the interaction surface from the west with a mean incidence angle of 20° before curving and onlapping tangentially onto the surface (Criterion 1). Across the interaction surface, cross-strata of the target and impactor sets diverge by an average of 95° in orientation (Criterion 2). In the transport direction, the divergence angle decreases until the impactor and target cross-strata are parallel, and the combined set is dominated by grainflow cross-strata (Criterion 4). This architecture is consistent with an impactor defect that approached a SE-migrating target dune, attached, and combined with the target dune to form a composite brinkline.

3.4.2 Example B: Navajo Sandstone

Example B occurs over a 5 m x 5 m plan-view outcrop of Navajo Sandstone located 1 km east of the La Sal Mountains Viewpoint (Fig. 3.2B; Table 3.1). The interpreted interaction bounding surface trends to the south in the dune transport direction and dips to the east, before curving to the west to become parallel to the interpreted target cross-strata (Fig. 3.4; Criterion 4). The target cross-strata have a mean dip direction toward 165°, and are dominated by 2-4 cm thick grainflow stratification (Criterion 3). Within the target set is a third-order (reactivation) surface recording a reorienting of the lee face by less than 10°. Cross-strata of the target set are abruptly truncated by the interaction surface at an average angle of 76° (Criterion 1). Cross-strata of the interpreted impactor set have a mean dip direction of 140° and are dominated by wind-ripple stratification (Criterion 3). Impactor cross-strata tangentially approach the interaction surface (Criterion 1) from the east with a mean approach angle of 12°, but

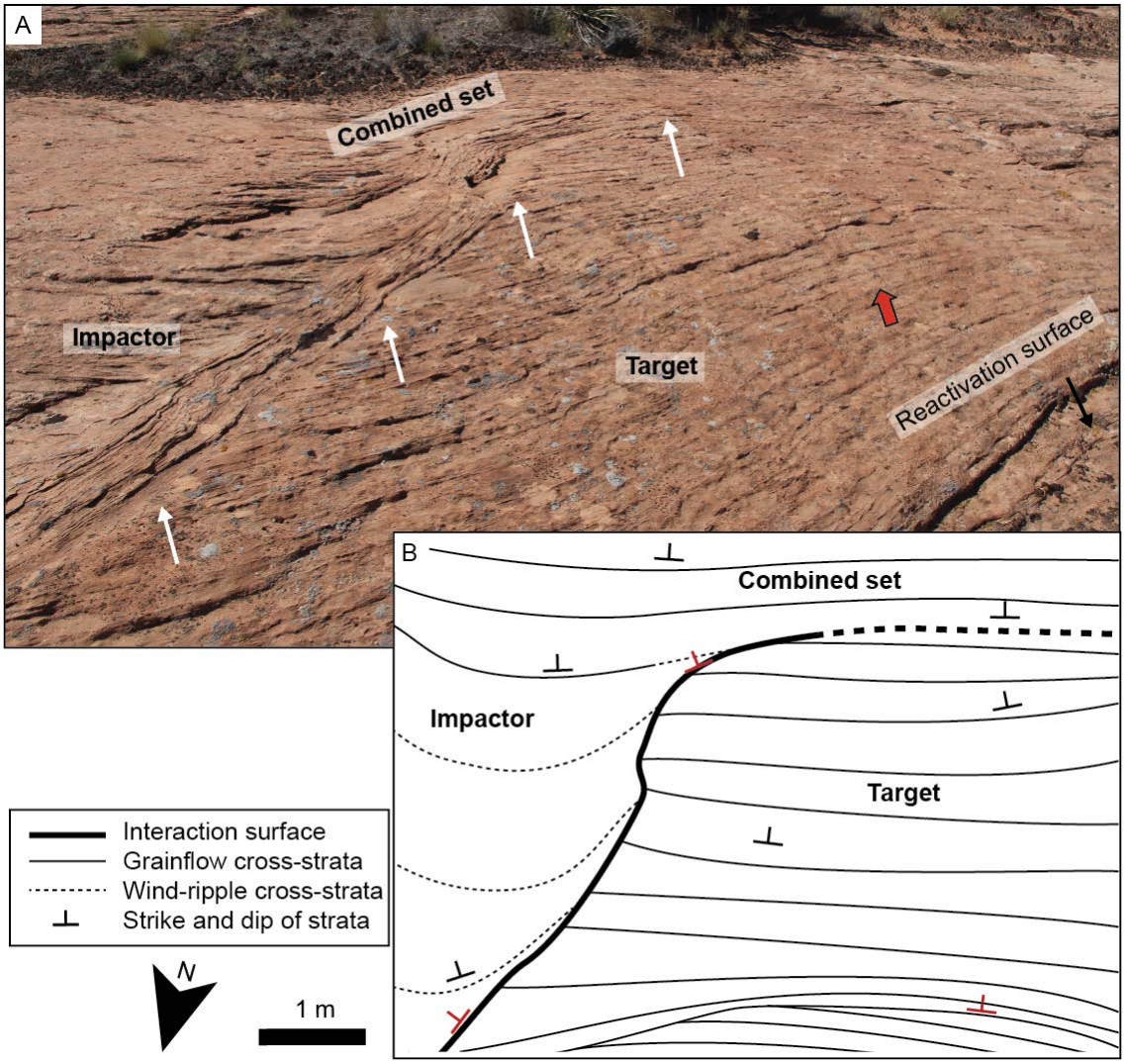

Figure 3.4: Interaction architectures in Example B: Navajo Sandstone. (A) This south-facing view of the interaction surface (white arrows) shows the surface separating impactor strata to the east from target strata to the west. The interaction surface trends in the transport direction (south) before curving to the west to parallel the strata of the combined set (Criterion 4). In the foreground wind-ripple laminae from the impactor tangentially approach the interaction surface that truncates target grainflow strata (Criteria 1, 3). The target also hosts a third-order (reactivation) surface. Red arrows (B) A schematic of the measured stratigraphic relationships shows the average divergence angle between target and impactor strata of 88° (Criterion 2). Red markers indicate the orientation of surfaces.

consist of grainflow cross-strata north of the trace of the interaction surface where the brinklines have recombined. The orientation of cross-strata from the target and impactor sets diverge across the interaction surface by an average of 88° (Criterion 2). This divergence angle tends to zero as the interaction surface curves to the west. Down-transport the target and impactor strata parallel the interaction surface and the two sets are indistinguishable.

3.4.3 Example C: Navajo Sandstone

Example C occurs over a ~25 m x 30 m outcrop of Navajo Sandstone east of Arches Scenic Drive (Fig. 3.2B; Table 3.1). This partially oblique outcrop captures both the downcutting and curvature of the interpreted interaction surface, which separates the impactor set to the east from the target set to the west (Fig. 3.5). Trending in the transport direction (south), the interaction surface cuts down across target strata at an apparent dip of 13° before curving to the west to parallel the trend of the target cross-strata where the outcrop becomes horizontal (Criterion 4). Target cross-strata dip toward the south (average dip direction of 184°), and are dominated by 1-3 cm thick grainflow strata that downlap onto the underlying set exposed to the west (Criterion 3). The surface truncates cross-strata of the target set at an average incidence angel of 81° (Criterion 1). Cross-strata of the impactor set dip to the south (average dip direction of 189°) away from the interaction surface, but toward the surface wind-ripple laminae curve to tangentially onlap the surface with a mean approach angle of 14° (Fig. 3.6; Criteria 1, 3). The divergence angle between the dip direction of target and impactor cross-strata across the interaction surface averages 95° (Criterion 2). Following the interaction surface to the south, the divergence angle tends to zero as the impactor and target cross-strata become parallel with one another and the interaction surface.

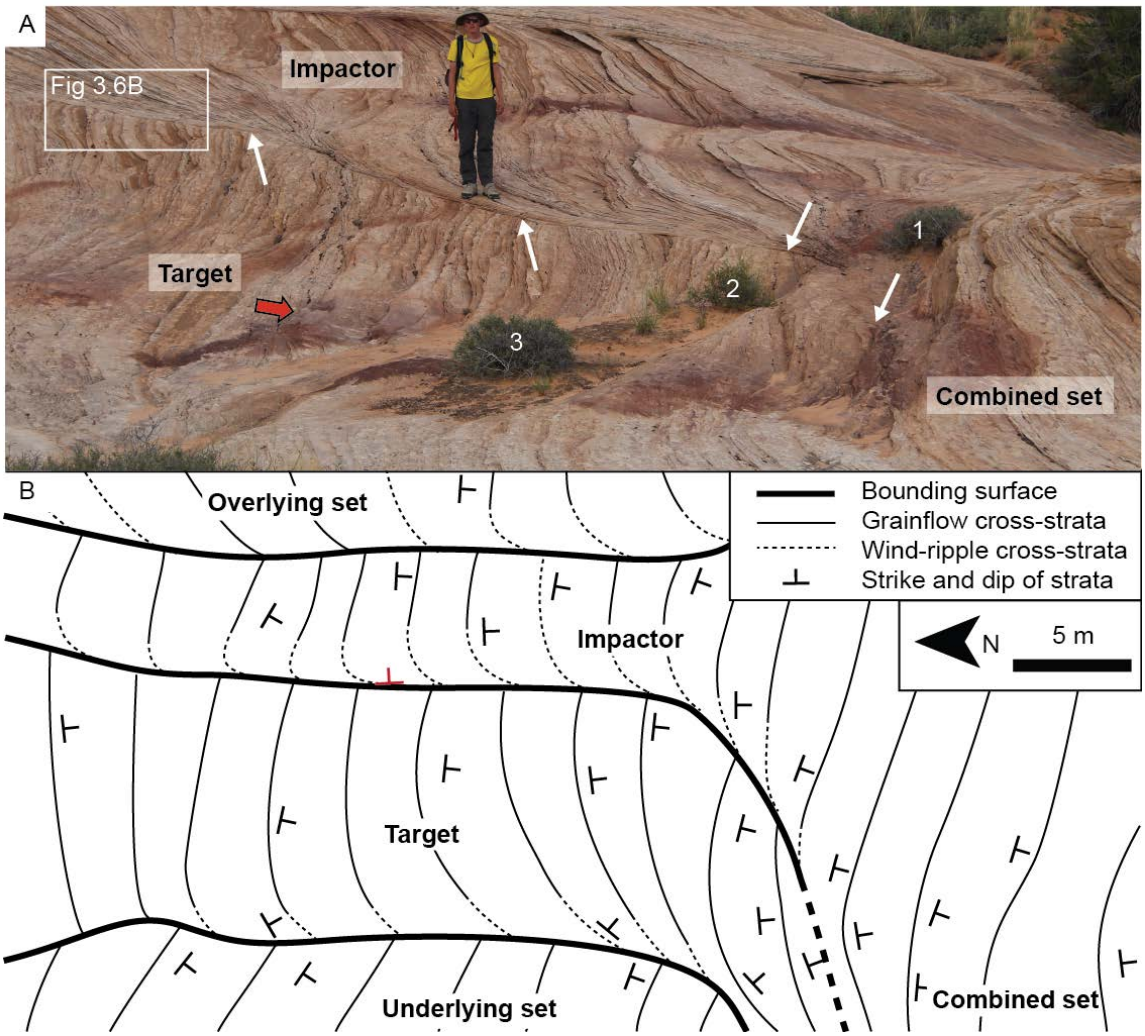

Figure 3.5: Interaction architectures in Example C: Navajo Sandstone. (A) This east-facing view of the partially oblique outcrop shows the interpreted interaction surface (white arrows) separating impactor strata above from target strata below. The surface trends in the transport direction (south) and curves to parallel the target and impactor strata between bushes (1) and (2). Wind-ripple strata in the impactor tangentially approach the interaction surface (Criterion 1). The underlying target grainflow strata are truncated by the interaction surface (Criterion 3). White box shows the extent of Fig. 3.6B. Labeling on shrubs matches Fig. 3.6A, which faces south. Red arrow marks the transport direction. (B) A plan-view schematic of stratigraphic architectures measured at this example. Red marker shows where the interaction surface was exposed in enough relief for a measurement on the surface rather than the strata. Impactor and target strata diverge in orientation by an average 95° (Criterion 2). Down-transport the two sets combine and the interaction surface is indistinguishable as it becomes parallel to the strata.

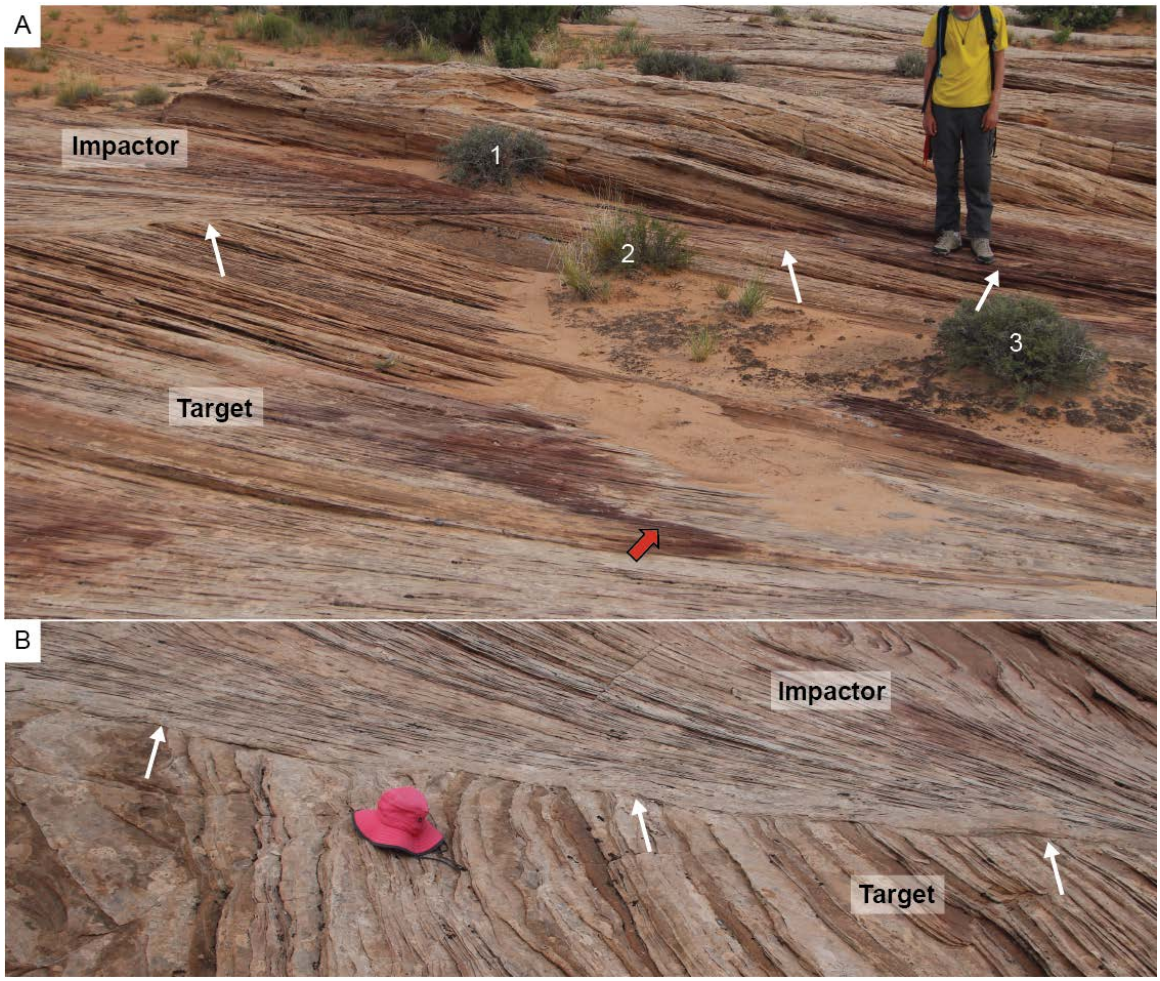

Figure 3.6: The interaction surface in Example C: Navajo Sandstone. (A) This south-facing view shows the interaction surface (white arrows) curve from trending in the transport direction (south) on the left to trending parallel to the strata (west) on the right. The surface passes between bushes (1) and (2), truncating the target strata at progressively lower angles until the two become parallel. Bushes are labeled as in Fig. 3.5. Red arrow indicates the transport direction in this oblique exposure. (B) Grainflow strata in the target set are truncated by the interaction surface (white arrows). Across the surface, wind-ripple laminae in the impactor set tangentially approach the surface, making the angle between target and impactor cross-strata an average 95°. Extent of this image is shown in Fig. 3.5A.

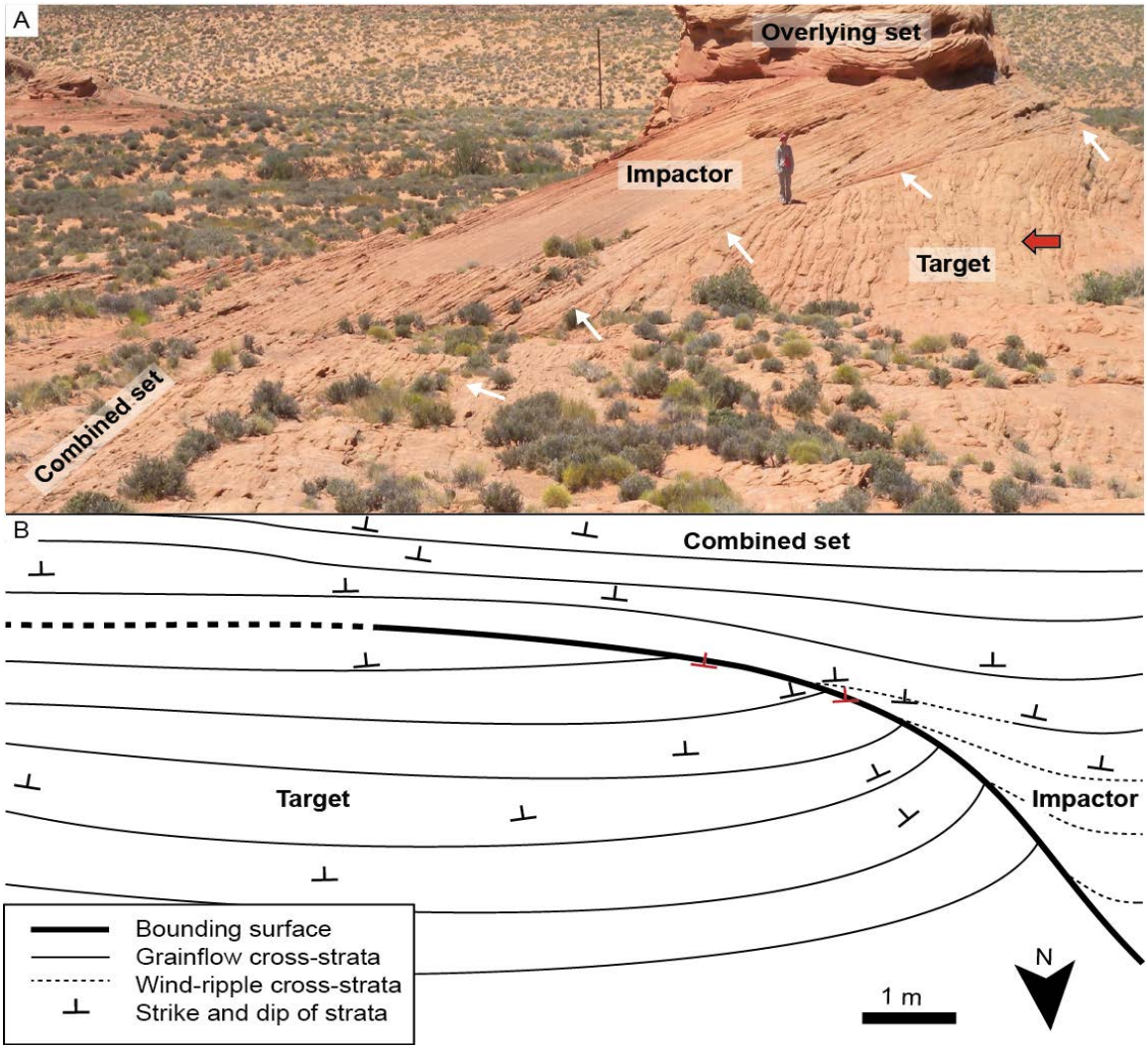

Figure 3.7: Interaction architectures in Example D: Page Sandstone. (A) This west-facing view shows the interaction surface (white arrows) cutting down across a resistant outcrop knob that exposes the architecture in partial oblique section. The interaction surface trends in the transport direction (SSE) across the knob, but curves to the east and parallels the target and impactor strata, which in the foreground are parallel and indistinguishable as separate sets (Criterion 4). Near the knob, grainflow strata in the target set are truncated by the interaction surface and wind-ripple strata in the impactor set tangentially approach the surface (Criteria 1 and 3). Red arrow shows the transport direction of the target set. (B) The plan-view schematic of the architectures of this example has been rotated 90° from (A) to better fit the page and to match schematics in other examples where transport is toward the top of the page. The target set is composed of thick grainflow strata, which are truncated by the interaction surface. To the west, impactor wind-ripple strata tangentially approach the interaction surface, and target and impactor strata diverge by an average 93° (Criterion 2).

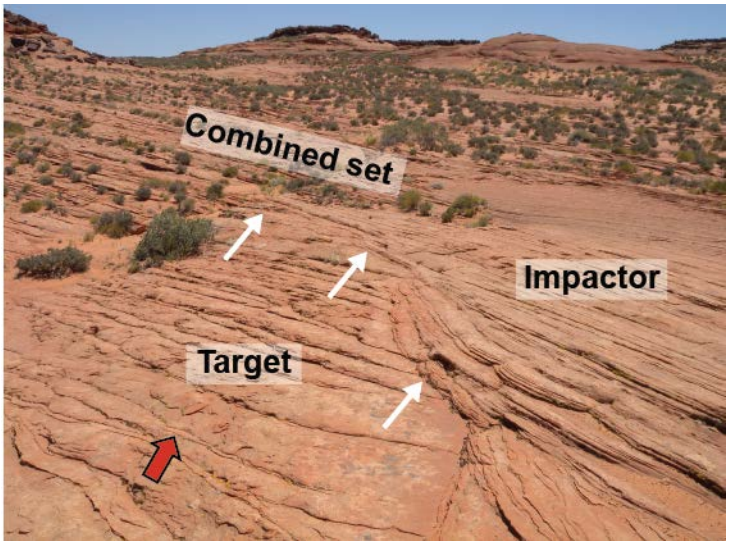

Figure 3.8: Interaction surface from Examples D in Page Sandstone. This SE-facing image looks down the trend of the interaction surface (white arrows), which curves to the left (east) to parallel the strata. In the foreground the surface separates thick truncated grainflow strata in the target set, and tangentially downlapping wind-ripple strata in the impactor. Red arrow indicates approximate transport direction of the target.

3.4.4 Example D: Page Sandstone

Example D occurs over a 10 m x 20 m outcrop of Page Sandstone, 1 km south of Ferry Swale Road (Fig. 3.2A; Table 3.1). A prominent bounding surface cuts across a resistant knob and separates the interpreted target set in the east from the impactor set in the west (Fig. 3.7). The resistant knob exposes the interpreted interaction bounding surface in partially oblique section as it downcuts across the target set. On the knob, the surface trends to the SE in the general transport direction with an apparent dip of 17° to the SW. The surface then curves to the east, paralleling the trend of the target and impactor cross-strata (Fig. 3.8; Criterion 4). At the up-transport margin of the area, vertical relief on the knob shows the target set is at least two meters thick (Fig. 3.7). The target set is dominated by 5-8 cm thick grainflow cross-strata (Criterion 3) dipping to the south (average dip direction of 175°). The lateral extent of the outcrop captures curvature

in the target set, which ranges from SE-dipping (195°) in the west to SW-dipping (145°) in the east. In the impactor set, wind-ripple laminations and grainflow strata dip toward the south with a mean dip direction of 170°. Near the interaction bounding surface, wind-ripple laminae tangentially approach the surface (mean approach angle of 15°) and overlie target grainflow cross-strata truncated at an average 78° by the interaction surface (Criteria 1, 3). Across the interaction surface, the strike of target and impactor strata diverges by an average of 93° (Criterion 2). Following the interaction surface to the south, the target and impactor strata become parallel along with the curving bounding surface and laterally the two sets become indistinguishable.

3.4.5 Example E: Entrada Sandstone

Example E occurs on a high bench of Entrada Sandstone outcrop roughly 10 m x 20 m in area, located 1.5 km west of US Highway 89 (Fig. 3.2A; Table 3.1). The bounding surface separates the interpreted impactor set in the SE from the interpreted target set in the NW (Fig. 3.9). In the up-transport position the interpreted interaction surface trends in the dune transport direction (SW) and dips toward the SE, but down-transport the surface curves to the NW to parallel the target and impactor strata (Criterion 4). Lateral to where the interaction surface turns to parallel the strata, the eroded outcrop provides a cross-sectional view of the surface as well as the target and the combined sets (Fig. 3.10). Although traced from the plan-view exposure, in cross-section the surface is subtle, as would be expected where the target and impactor set have combined. The cross-section, however, does well illustrate that the target and impactor sets have effectively combined into a single set. Within the target set, cross-strata dip toward the SW with a mean dip direction of 244°. The target set is dominated by 5-10 cm thick

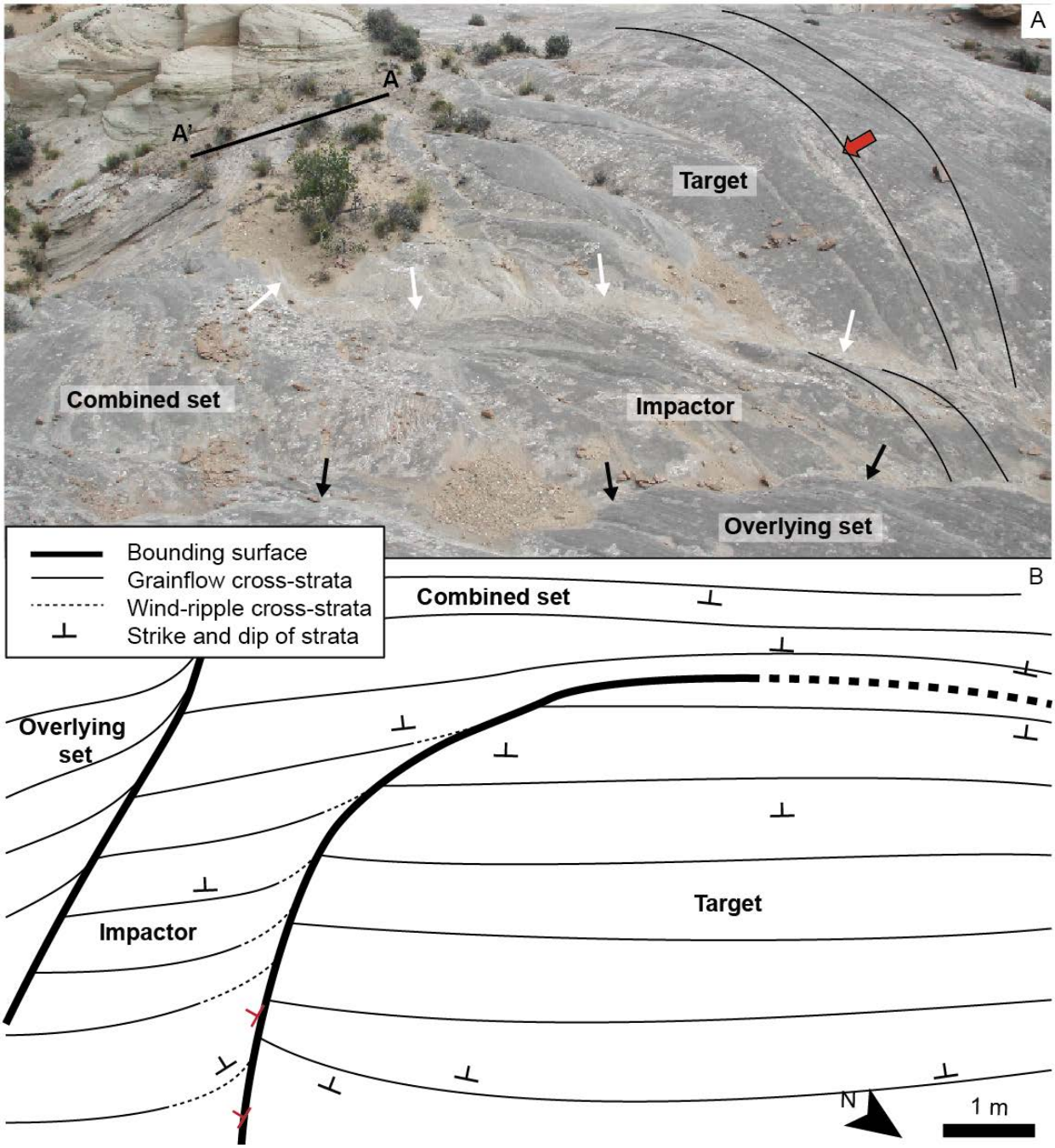

Figure 3.9: Interaction architectures in Example E: Entrada Sandstone.

Figure 3.9: Interaction architectures in Example E: Entrada Sandstone. (A) This NW-facing view shows the interpreted interaction surface (white arrows) trending in the transport direction (red arrow) and then curving toward the top of the page (NW) where it becomes parallel with the cross-strata (Criterion 4). Lines drawn in the up-transport margin of the image represent cross-strata and orient the viewer. To the SE the impactor set is covered by an overlying set separated from the impactor by a first-order surface (black arrows). Along the interaction surface, wind-ripple strata from the impactor set tangentially approach the surface. To the NW, cross-strata in the grainflow-dominated target set are truncated by the interaction surface (Criteria 1, 3). The outcrop is eroded to the NW such that strata are exposed in cross-section on either side of the interaction surface (line A-A'). This cross-section is shown in Fig. 3.10. (B) This schematic of the architectures associated with this interaction has been rotated so that the transport direction is toward the top of the page to match schematics for other examples. Across the interaction surface, target grainflow strata diverge from impactor wind-ripple laminae by an average of 100° (Criterion 2). Red markers indicate where measurements were taken on the surface rather than adjacent strata.

Figure 3.10: This SE-facing view of the outcrop shows a dip-section exposing strata on either side of the interaction surface (white arrow). Location is given in Fig. 3.9. The interaction was traced to this location, but it is indistinguishable in this cross-section. The target strata and combined set strata are parallel and no truncation from the bounding surface is evident between them, confirming that the surface becomes parallel to the strata when it curves to the NW. The absence or extreme subtlety of the surface is in keeping with the expected behavior of an interaction.

grainflow cross-strata. At the up-transport margin of the study area, 30° of curvature was measured on the target set, with dip directions varying from 260° in the SE to 230° in the NW. Target cross-strata are truncated by the interaction surface at an average angle of 75° (Criteria 1). Impactor cross-strata dip toward the south with a mean dip direction of 188°. Grainflow strata dominate the impactor set away from the interaction surface, but these yield to wind-ripple laminae that approach the south side of the interaction surface at an average incidence angle of 25° and onlap tangentially onto the surface (Criterion 1). Across the up-transport margin of the surface, the orientation of wind-ripple impactor strata differ from grainflow target strata by a mean divergence angle of 100° (Criteria 2, 3). As the bounding surface curves, this angle tends to zero and the impactor strata, target strata and interaction surface all align parallel (Criterion 4).

3.5 CONCLUSIONS

The objective of this work was to identify stratigraphic architectures in well-known aeolian units that are consistent with modern examples of interaction architectures documented at the White Sands Dune Field. Five examples presented here from Jurassic units in the western United States show criteria diagnostic of interaction architecture as distilled down from the White Sands examples. A contrary result - that interaction architectures are absent in the rock record would be more surprising given the ubiquity of interactions in modern systems. The results of this study suggest that interaction architectures have been overlooked or misidentified previously. For example, now that this type of interaction architecture has been recognized, it is found to be commonly expressed in plan-view exposures of dune accumulations at White Sands (Brothers et al., 2017). In hindsight, previously described ancient outcrops are plausibly reinterpreted as interaction architecture (e.g., Bristow and Hill, 1998; Bristow, per. comm. 2016).

This work focused specifically on defect-driven interactions, but there are several other types of interactions identified from modern dune fields, models and experiments (see review in Kocurek et al., 2010), and their stratigraphic architectures are undefined. In addition, the preserved frequency of interactions in the rock record is unknown. Dune interactions are most common during the early stages of dune-field pattern construction, and their frequency of occurrence is much greater than that of typical processes of accumulation and preservation. Moreover, strata deposited during early stages of dune-field construction are commonly cannibalized by growing dunes such that the aeolian rock record appears to be biased toward preservation of later stages of dune-field construction. These observations suggest that interaction architectures are present in the rock record, but that they are not spatially dense in units deposited by large dunes.

More broadly, the role of dune interactions in the dynamics of dune-field pattern evolution and sand flux exchange between bedforms is still being defined (e.g., Narteau et al., 2009; Eastwood et al., 2011; Worman et al., 2013; Genois et al., 2013; Gao et al., 2015). The most expeditious method for coupling dune surface dynamics with the generation of a stratigraphic record rests with an emerging generation of numerical models (e.g., Jerolmack and Mohrig, 2005; Gao et al., 2015; Swanson et al. 2016a), which simulate interaction and other complex stratigraphic architectures. Results from these models can then be field tested in the stratigraphic record of modern and ancient dune fields.

3.6 Acknowledgments

The authors thank S. Brothers, T. Swanson, J. Day, A. Pedersen, J. Mason, and C. Lopez-Gamundi for their assistance with data collection in the field. This work was

supported by the National Science Foundation Graduate Research Fellowship Program under grant no. DGE-1110007.

Chapter 4: What is Preserved in the Aeolian Rock Record? A Jurassic Entrada Sandstone Case Study at the Utah-Arizona Border

4.1 INTRODUCTION

The fundamental boundary conditions for aeolian dune-field development are sand supply, the availability of this supply for wind transport, and a wind transport capacity sufficient to mobilize the grains (i.e., "sediment state" of Kocurek and Lancaster, 1999). As seen in nature (Cooper, 1958; Kocurek et al., 1992; Lancaster, 1996; Nield and Wiggs, 2011; Elbelrhiti, 2012), experiments (Endo et al., 2004; Hersen and Douady, 2005; Ping et al., 2014), and models (Werner, 1995; Bishop et al., 2002; Diniega et al., 2010; Eastwood et al., 2011; Swanson et al., 2016a), where dune fields originate on a planar surface, protodunes initially form and these evolve into a field of small dunes. Dune-field patterns emerge through the autogenic process of dune interactions, and a field of many small dunes evolves (coarsens) toward one with fewer, larger, and more widely spaced dunes (e.g., Ewing and Kocurek, 2010b; Kocurek et al., 2010; Gao et al., 2015). Alternatively, a change in boundary conditions may initiate a new constructional phase of dunes upon an existing (antecedent) dune pattern. The existing dunes serve as the available sand supply and are reworked into a new pattern, again through a series of interactions (Werner and Kocurek, 1997; Kocurek and Ewing, 2005).

The development of a stratigraphic record from a dune field firstly requires that the dunes leave an accumulation or a body of strata. Most dune fields leave no stratigraphic record. Rather, dunes bypass along a surface or are reworked by subsequent environments. Where accumulations form, autogenic processes operating within dune

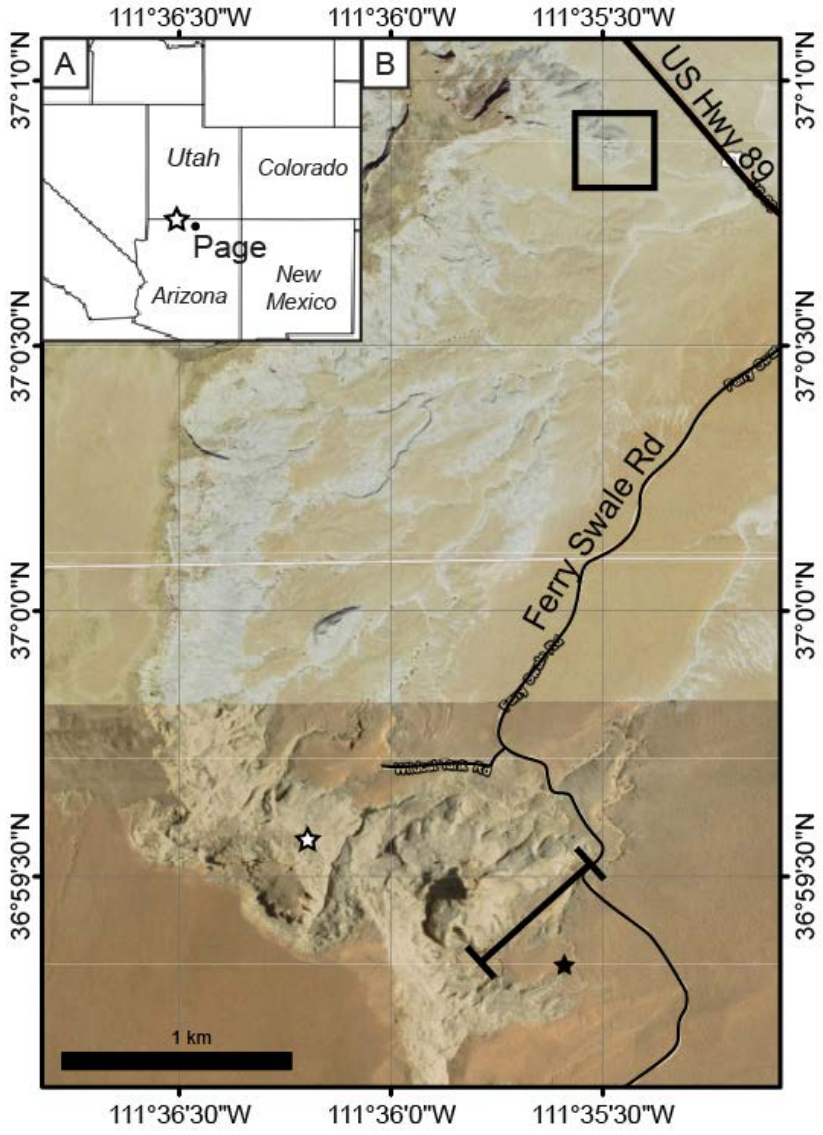

Figure 4.1: Study area. (A) Approximate location of the study area just northwest of Page, Arizona. (B) Satellite image of the study area (Esri global basemap) showing light-toned exposures of Jurassic Entrada Sandstone along ~ 5 km of cliffs. The primary outcrop is a ~ 500 m exposure (black line) trending 060°. Brackets show the extent of the combined photomosaics in Figs. 2A and 2B, which overlap in the middle of this extent. Black star indicates the approximate location of the viewer for Fig. 4.2. The upper sabkha bed described in the text was not accessible along the wall and was instead measured to the northwest (white star). The large compound set was additionally studied at the secondary outcrop (black box) near US Highway 89. Accessible portions of the section between the primary and secondary outcrops were studied to supplement unit characterization.

fields may preclude a complete record of dune-field construction. Especially in the early stages of dune-field construction, dune interactions occur at a much higher frequency than processes of accumulation. Dunes and their stratigraphic record of interactions are consumed during pattern evolution. Depths of scour in interdune troughs vary, and a deeper trough may erode the accumulations of earlier dunes (Paola and Borgman, 1991; Bridge and Best, 1997). Furthermore, growing dunes derive sediment from underlying plane sources, and upwind line or point sources (Ewing and Kocurek, 2010a), but growing dunes may also cannibalize earlier dune-field accumulations.

At the basin scale, allogenic boundary conditions that favor accumulation are not the same as those that give rise to dune-field construction. Although accumulation may occur because of a number of parameters, these can be broadly coupled with types of dune fields (Kocurek and Havholm, 1993; Kocurek, 1999; Mountney, 2012). Within "dry systems," accumulation is typically caused by flow deceleration as a function of topography (e.g., flow into a topographic basin) or wind patterns (e.g., flow convergence or a change in surface roughness). Within "wet systems," accumulation results from a rise in the capillary fringe through the deposits. Within "stabilizing systems," accumulation is coupled to surface stabilizing factors such as vegetation.

Preservation of these accumulations further requires that the accumulations are not subsequently removed. Kocurek and Havholm (1993) distinguished between accumulation and preservation, which parallels the earlier distinction by Sadler (1981) that some deposits are temporary and subsequently removed, whereas other deposits are permanent and contribute to the stratigraphic record. For example, ~ 10 m of accumulations were deposited by migrating dunes at the White Sands Dune Field, New Mexico, but those accumulations that are above the water table are currently being

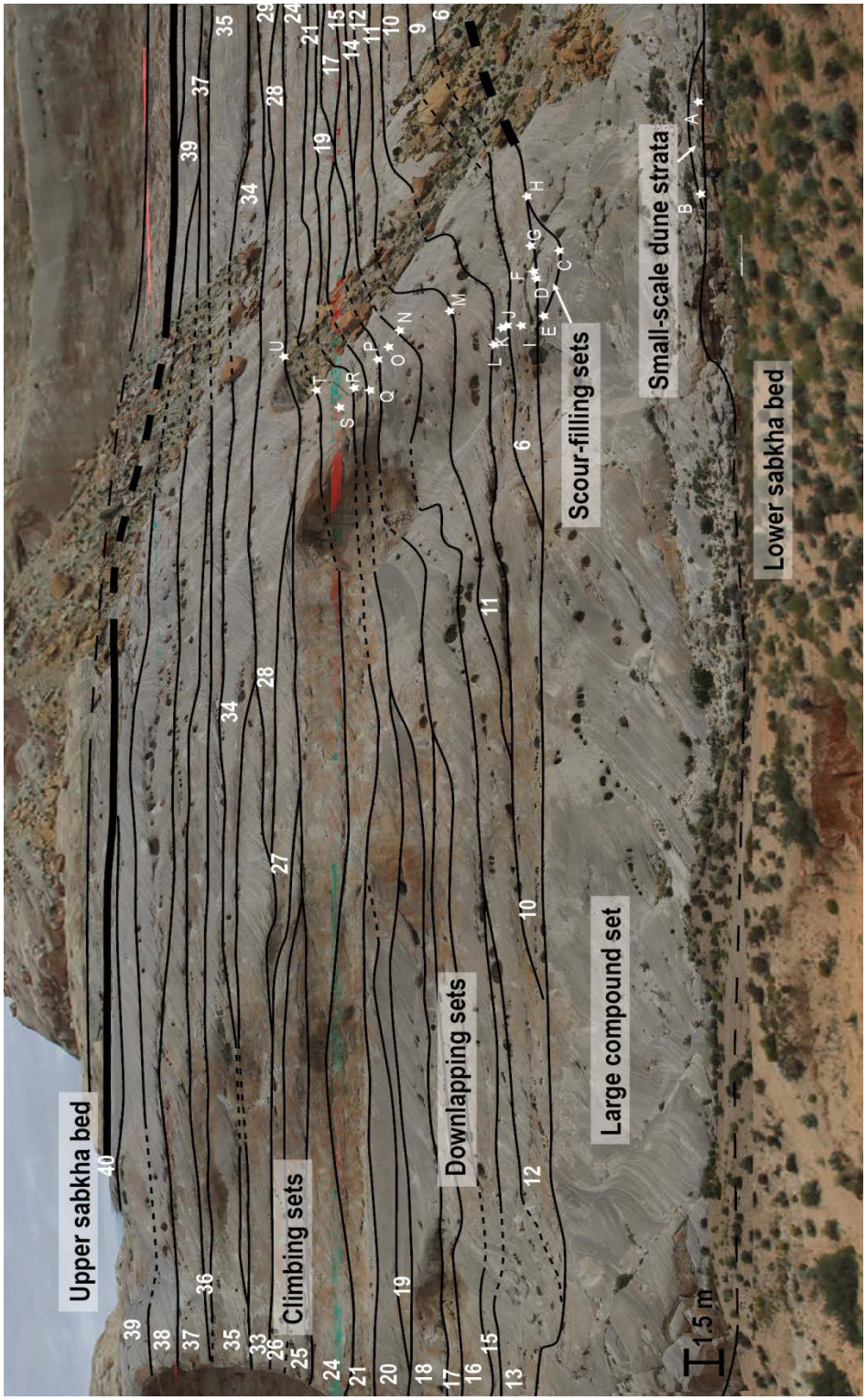

Figure 4.2A: Photomosaic of the primary outcrop (left hand side)

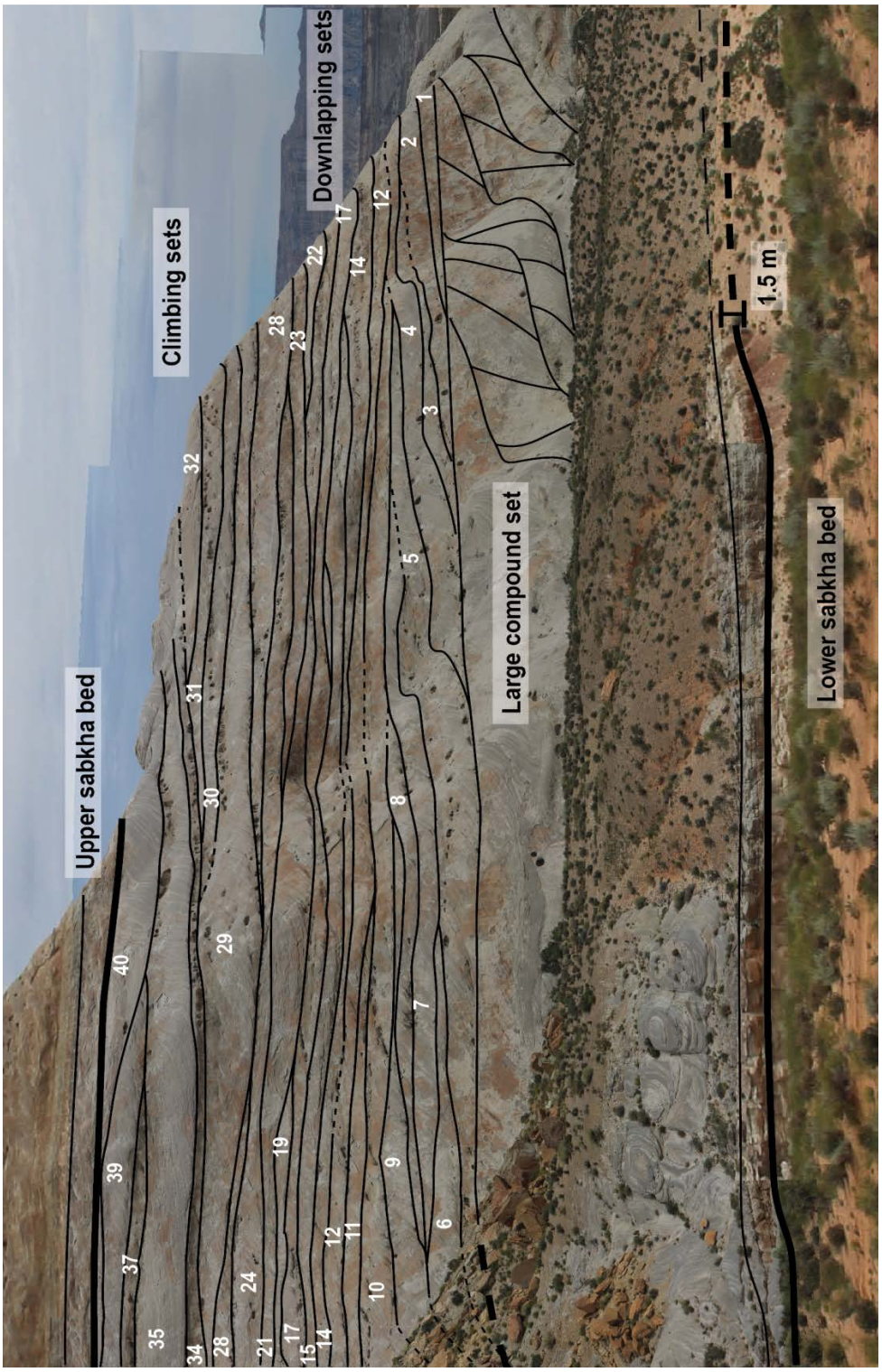

Figure 4.2B: Photomosaic of the primary outcrop (right hand side)

Figure 4.2: Photomosaic of the primary outcrop (location given in Fig. 4.1B). (A) Left hand (southwest) ~ 250 m of the outcrop. (B) Right hand (northeast) ~ 250 m of the same wall. Approximately 10% of the right side of (A) overlaps with ~ 10% of the left side of (B) to aid the reader in tracing strata across the two images. Individual dune sets were mapped on this combined photomosaic whose full resolution is < 1 cm/px. Thin lines indicate set boundaries, and bold lines trace the sabkha beds that define the boundaries of the studied interval. Each set above the large compound set is numbered chronologically as interpreted by superposition with set #1 on the far lower right preserving the earliest preserved set, and set #40 in the upper left preserving the latest. Set boundaries measured in a transect up the outcrop (white stars) and were used to determine the reported set thicknesses. Above the apex of the talus deposit (point U) the outcrop was too shear to access. Images have been rotated to remove an apparent dip of 1.16° along the outcrop trend.

cannibalized along the upwind margin of the dune field because of a diminished sand supply (Kocurek and Ewing, 2017). Preservation commonly occurs when continued sedimentation buries aeolian accumulations within a subsiding basin, or when there is a continued relative or absolute rise of the water table through the accumulations (Kocurek and Havholm, 1993). In more exotic cases, preservation is geologically instantaneous, such as burial of dunes by lava flows (Jerram et al., 2000; Scherer, 2002; Waichel et al., 2008), or rapid marine/lacustrine flooding accompanied by subaqueous deposition (Vincelette and Chittum, 1981; Benan and Kocurek, 2000).

Given the complex interplay between autogenic processes and differing boundary conditions for dune-field development, accumulation and preservation, the question is what stages of evolving aeolian dune fields are represented in the rock record? Measured sections through aeolian units are numerous, but there are significantly fewer outcrop-scale examples in which the evolutionary stages of dune fields can be interpreted from the architecture of the sets and bounding surfaces (e.g., Crabaugh and Kocurek, 1993; Mountney and Jagger, 2004; Mountney, 2006a). In addition, focus is typically upon the preserved accumulations, whereas the bounding surfaces that truncate intervals of strata

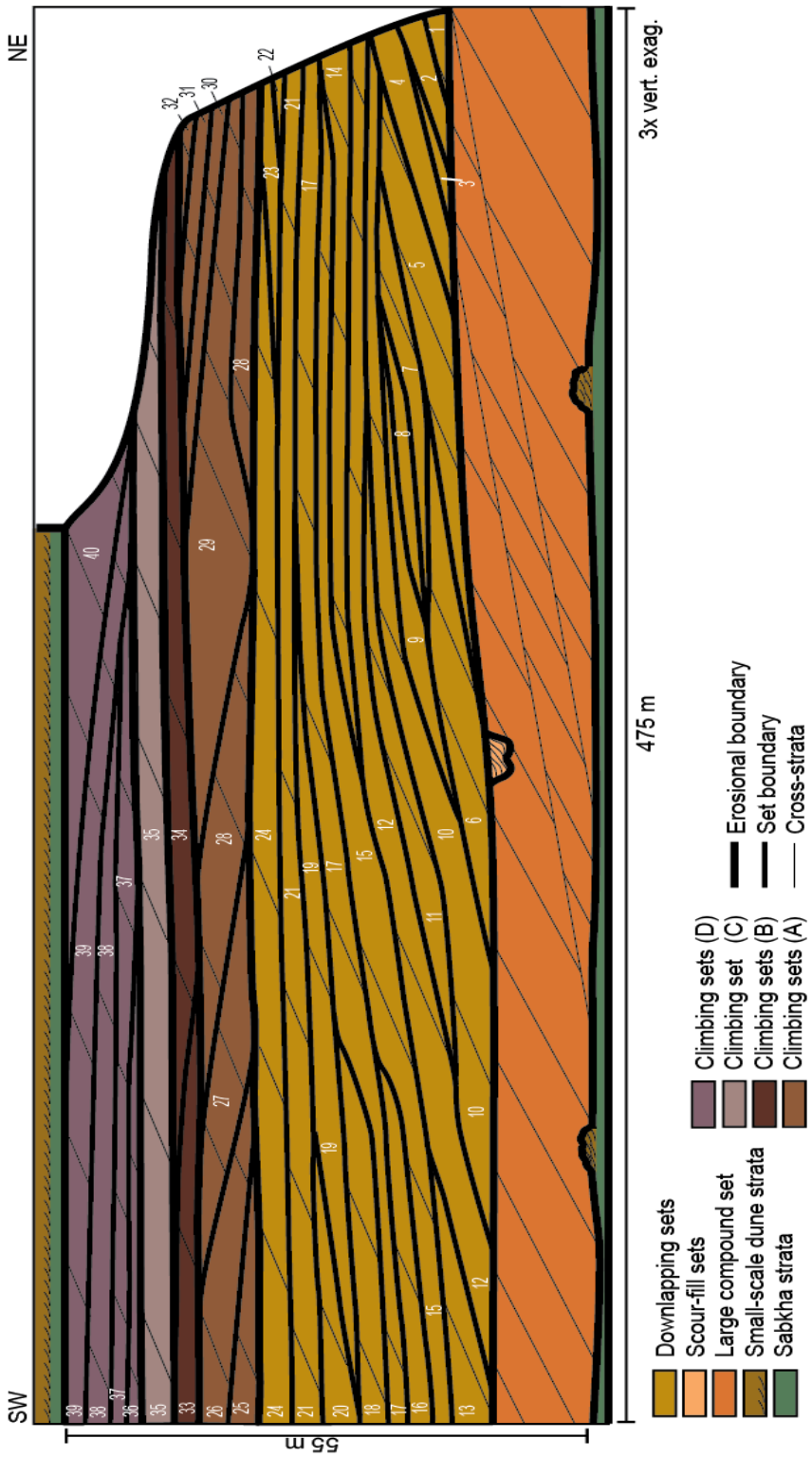

Figure 4.3: Sets mapped in the outcrop wall

Figure 4.3: Sets mapped in the outcrop wall (Fig. 4.2) as projected onto a vertical plane trending toward 060°. Color-coded units correspond to descriptions and interpretations in text. The outcrop has been three times vertically exaggerated to show details, but the cross-strata, drawn in for schematic purposes, have not been exaggerated and dips shown are the calculated apparent dips for the wall orientation based on measured actual dip values.

receive less attention. These surfaces, which define the limits of the preserved accumulations, may represent longer spans of time than the strata, and significant dune-field events are collapsed into the surface (Loope, 1984; Talbot, 1985; Kocurek, 1988; Mountney, 2006b). This case study of a section of the Middle Jurassic (Callovian) Entrada Sandstone on the Arizona-Utah border utilizes outcrop-scale architectures to identify what stages of dune-field construction were preserved, but also speculates on what stages have not been preserved. This study is based upon gross bounding surface and set architectures, and a detailed reconstruction of the Entrada dunes, the wind regime, and regional allogenic forcing is beyond the scope of this study.

In the spectrum of preserved sand seas within the rock record, the Entrada Sandstone is a near end-member (Allen et al., 2000). Reaching up to 300 m in thickness, the Entrada Sandstone and its correlative aeolian units extend from Wyoming-Utah in the north to northern Arizona-New Mexico-Texas in the south (Blakey et al., 1988, their fig. 27A). The Entrada Sandstone was deposited within the foreland basin that characterized western North America during the Jurassic (Busby-Spera, 1988; Bjerrum and Dorsey, 1995). Within this strongly asymmetric basin, the Entrada Sandstone thins eastward toward the craton and elements of the Ancestral Rockies, and thickens markedly westward (Blakey et al., 1988, their fig. 27A) to correlative thick (~ 400 m) deposits of the restricted marine Preuss and Arapien formations in the Utah-Idaho Trough (Imlay, 1952; Hansen, 1965; Hileman, 1973). Eastern facies of the Entrada are aeolian-dominated, but interbedded red silty sandstone representing a sabkha facies become

increasingly common westward as the Entrada transitions to the Preuss Formation (Blakey, 1988, his fig. 12; Blakey et al., 1988, their fig. 27B). Our study area lies within the maximum depo-center of aeolian facies for the Entrada Sandstone. Whereas Preuss sediments were sourced from the uplands to west (Hileman, 1973; Kocurek and Dott, 1983), the quartz-rich sands of Entrada were derived from deflation of floodplains of transcontinental fluvial systems originating in the Appalachian Mountains (Dickinson and Gehrels, 2009; Dickinson and Gehrels, 2010). Regional cross-strata orientations show a general southward dune migration direction, with southwestward transport in the study area (Peterson, 1988, his fig. 13). Ultimately, the Entrada Sandstone was transgressed by a variety of marine environments (e.g., Curtis, Stump and equivalent units, Blakey et al., 1988, their fig. 2) and buried within the subsiding basin.

4.2 Study Area and Methods

The study area consists of exposures of Entrada Sandstone outcropping along 5 km of cliffs in the Glen Canyon Recreation Area northwest of Page, AZ (Fig. 4.1). The studied interval consists of ~ 60 m of section between two interpreted sabkha beds (see below). The contact of the Entrada Sandstone with the underlying Carmel Formation is covered in the immediate study area, but it is visible to the east along the shores of Lake Powell. Based upon elevations from Google Earth, the lower sabkha bed is ~ 115 m above the contact. Approximately 85 m of Entrada Sandstone rise above the upper sabkha bed, and are largely expressed as near-vertical outcrop faces. Accessible areas of much of the outcrop were studied in order to characterize the unit, but the focus was upon a ~ 500 m long section (black line in Fig. 4.1), and secondarily upon a section exposed near highway US 89 (black box in Fig. 4.1). A photomosaic of the primary outcrop was constructed. Sets of cross-strata and the bounding surfaces on this outcrop were surveyed

for use as control points using a total station theodolite in a transect up the outcrop as far as slope steepness allowed. Additional elevation data points for the primary outcrop were derived from Google Earth. Sets of cross-strata mapped in the photomosaic were then projected onto a vertical plane trending parallel to the outcrop (060°) in order to remove distortion associated with small-scale topography and sinuosity of the wall. The 060° trend of the outcrop provides an approximately transport-parallel view of the sets, which show cross-strata dip directions toward the southwest.

Although tectonic tilt of the outcrop is very minor, because characterization of set and bounding surface architecture may include very low angles (i.e., angle of climb), a datum was established and the final mapping results were rotated with respect to this horizontal. The lower and upper sabkha beds were taken as the most robust indicators of the original depositional surface. The base of the lower sabkha bed was surveyed along the primary outcrop, and these points were fitted to a plane using a least-squares orthogonal regression. The resulting plane fit indicated a slight tilt (1.2°) to the northeast (044°) with a root-mean-squared error of fit of 0.26 m. The upper sabkha bed was similarly measured, but along a much more limited accessible area (Fig. 4.1), and fitted to a plane, yielding a tilt of 1.8^{o} toward the north (005^{o}) with a root-mean-squared error of fit of 0.14 m. For comparison, the Carmel/Entrada contact along Lake Powell (12-20 km northeast of the study area) was measured using elevations from Google Earth. The best-fit plane indicated a tilt of 1.2^{o} to the north-northwest (340^{o}) with a root-mean-squared error of fit of 17.5 m. Overall, tectonic dip of about one degree toward the north characterizes these outcrops. Given that elevations from Google Earth are accurate only to the nearest meter and the best outcrop measurements are from the lower sabkha bed, the base of the lower sabkha bed was defined as datum, and images of the outcrop have been rotated to correct for an apparent dip of 1.16^{o} along this 060^{o} trending wall.

4.3 STRATIGRAPHIC UNITS

The primary section between the lower and upper sabkha beds was divided into stratigraphic intervals in which each interval is characterized by a set architectural style and bounded by an outcrop-scale erosional surface. Figure 4.2 shows the photomosaic in which the stratigraphic intervals are identified, sets of cross-strata numbered, and bounding surfaces between sets traced. The lower and upper sabkha beds are traced with bold lines. Figure 4.3 shows the diagrammatic section projected into a vertical plane trending 060^{o}, with color-coded stratigraphic intervals bounded by outcrop-scale erosional surfaces identified in Figure 4.2.

4.3.1 Lower and upper sabkha beds and transition to small-scale aeolian cross-strata

4.3.1.1 Description

The lower and upper beds that bound the studied stratigraphic intervals are approximately parallel in orientation (see above), continuous across the outcrop, composed of a silty fine-grained sandstone, and very similar to one another in sedimentary structures. The lower bed overlies a polygonally fractured, outcrop-scale surface truncating large-scale Entrada cross-strata (Fig. 4.4A). The upper bounding bed overlies the outcrop-scale surface that truncates the uppermost cross-stratified interval within the studied section. Both the lower and upper beds are recessional, show local reduction to a green color, and are predominately characterized by wavy, brecciated and crinkly laminations (Fig. 4.4A-C). Intercalated with these laminations, especially higher in the beds, are centimeter-scale subaqueous ripple cross-strata, low chevron-style ripple cross-strata that suggest wave ripples, and parallel laminae of probable subaqueous sheet-flow origin. In addition, intervals of aeolian wind-ripple laminae and small sets of cross-

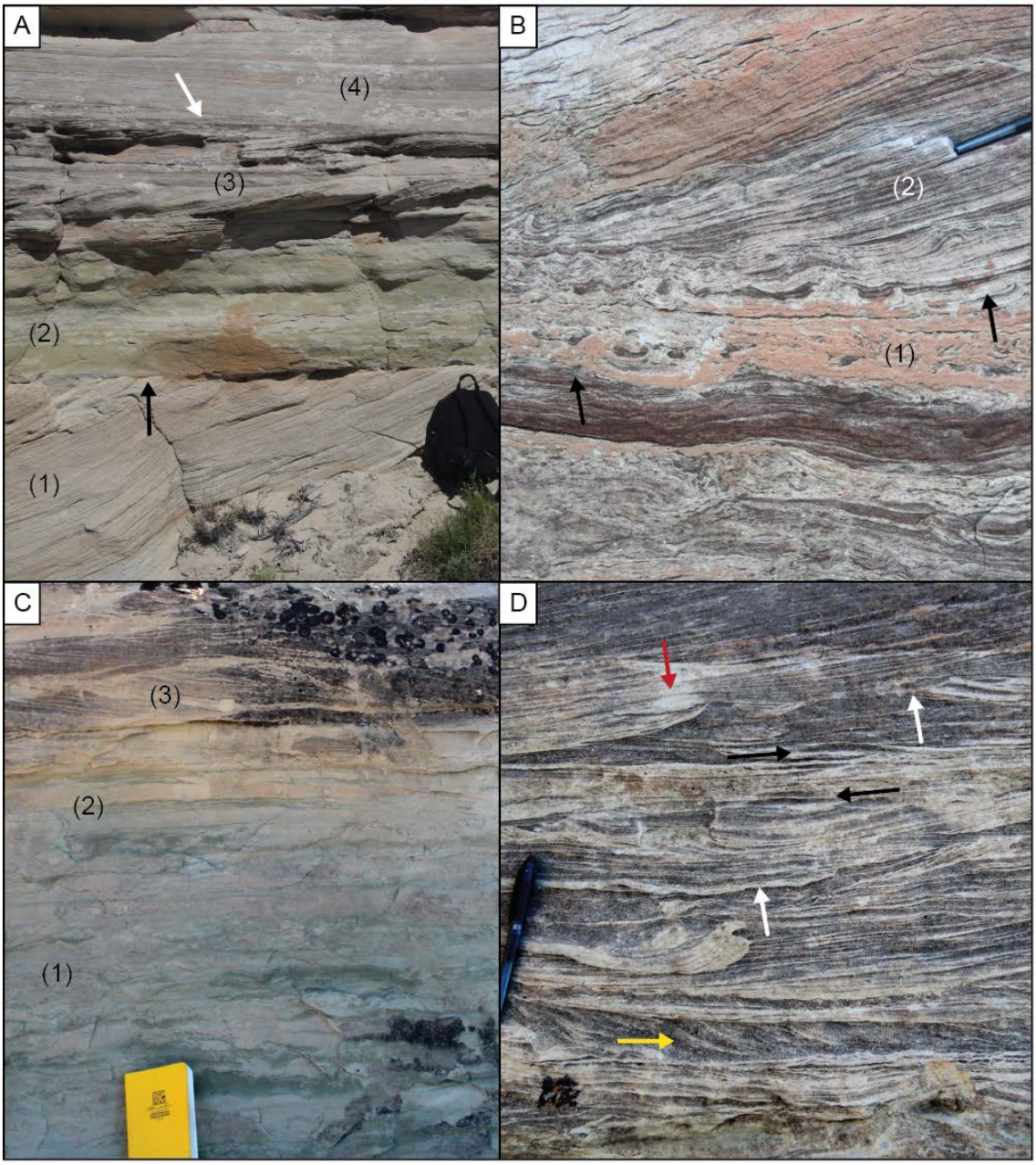

Figure 4.4: Sabkha and small-scale aeolian facies.

Figure 4.4: Sabkha and small-scale aeolian facies. (A) The lower sabkha bed rests upon a surface (black arrow) that truncates large-scale aeolian cross-strata (1). Above the sabkha bed (2), there is a transition to small-scale aeolian dune sets (3), which are, in turn, truncated by the surface (white arrow) upon which the large compound set (4) rests. Where the erosional remnants of the small sets are absent, the large compound set overlies the sabkha bed. (B) Contorted, brecciated and crinkly bedding in the interpreted lower sabkha interval (1) is overlain by a small set of aeolian cross-strata (2) that degenerates down-dip into contorted strata. Dune and some sabkha surfaces are corrugated (black arrows). Note pen in upper right corner for scale. (C) The upper sabkha bed (1) characterized by crinkly and brecciated laminae transitions to small-scale aeolian sets (2), which increase in size gradually up the section (3). (D) Small-scale aeolian sets above the upper sabkha bed. Sets are dominated by wind-ripple cross-strata, but also contain thin grainflow cross-strata (yellow arrow). Surfaces bounding the sets are commonly corrugated (white arrows), irregular topography is draped by wind-ripple laminae (red arrow), and preserved ripple forms show reversed migration directions (black arrows).

strata occur. A prominent example within the lower unit consists of aeolian cross-strata that degenerate down-dip into contorted bedding (Fig. 4.4B).

Above both the lower and upper bounding beds, the section transitions into a fine- to medium-grained sandstone aeolian facies characterized by wind-ripple laminations, preserved ripple forms, and small sets of aeolian cross-strata (Fig. 4.3). Above the upper bounding bed this facies forms a fairly continuous horizon of aeolian strata marked by increasing set size and increasing grainflow cross-strata thickness (Fig. 4.4C). Sets are typically discontinuous with distinctly corrugated upper surfaces, and erosional depressions are infilled by downlapping and draping wind-ripple strata (Fig. 4.4D). Above the lower bounding bed, however, the aeolian facies occurs only as erosional remnants that project vertically up to ~ 1 m and extend laterally for only 3-7 m before being eroded by the surface upon which the overlying compound set (see below) rests (Figs. 4.2, 4.3, 4.4A). More typically this surface downcuts to the level of the basal silty, fine-grained sandstone bed. Where the erosional remnants remain, sets range up to 20 cm in thickness with a mean foreset dip direction toward 194°.

4.3.1.2 Interpretation

The lower and upper bounding beds are interpreted as sabkha deposits with periodic subaqueous flooding and aeolian intervals. The dominant wavy, brecciated and crinkly laminae of the basal beds were first recognized as characteristic of sabkhas within interdune areas or occurring as extensive flats in modern desert settings by Glennie (1970), subsequently documented in other modern sabkhas (Ahlbrandt and Fryberger, 1981; Fryberger et al., 1983; Kocurek and Nielson, 1986), and are abundantly present in the Entrada and other Jurassic aeolian units within the foreland basin (e.g., Kocurek, 1981; Crabaugh and Kocurek, 1993; Havholm and Kocurek, 1994). Periodic flooding of the salt-encrusted flats is implied by the subaqueous ripple and sheet-flow deposits, and wave ripples argue for periods of standing water. The upward transition of sabkha deposits into aeolian strata depicts a drying-upward trend. Set size and grainflow strata thickness indicate small dunes (Kocurek and Dott, 1981), and the corrugated surfaces are caused by deflation of a damp or evaporite-cemented substrate (Cooper, 1958; Kocurek, 1981; Hummel and Kocurek, 1984; Simpson and Loope, 1985). The depositional environment of the aeolian facies is interpreted as a wet system, in which the water table is near the surface, and the behavior of the water table over time controls the accumulation/deflation of the deposits (Kocurek and Havholm, 1993).

The lower and upper bounding intervals are significant in showing a water-table control on strata accumulation and preservation. Evidence for a water-table control includes: (1) deflation of aeolian strata to the quasi-planar surfaces (Loope, 1984; Kocurek, 1988), (2) development of polygonal fractures on the lower surface, which are interpreted as thermal fracturing of an evaporite-cemented surface (Kocurek and Hunter, 1986), (3) accretion of sabkha deposits within the capillary fringe (Warren, 2016), and (4) the presence of aeolian wet-system accumulations (Kocurek and Havholm, 1993;

Mountney and Thompson, 2002; Mountney, 2006a). The lower and upper outcrop-scale bounding surfaces marking the bases of these intervals are interpreted to represent the ending of an aeolian constructional event attributed to diminishing sand supply and migration of dunes from the area, followed by deflation of dune strata to intersect the water table. The polygonal fractures on the lower surface require an exposed surface for formation. The overlying sabkha strata indicate that the deflationary event and surface formation were followed by continued rise of the water table under limited sediment-availability conditions. Continued accumulation of the overlying wet-system aeolian deposits implies a renewed influx of sand, but also a continued rise in the capillary fringe. Very similar stratigraphic relationships are common in Jurassic aeolian units within the region and these have been similarly interpreted (e.g., Havholm et al., 1993; Carr-Crabaugh and Kocurek, 1998).

Whereas the sabkha-to-wet-aeolian-system transition is an "expected" stratigraphic evolution associated with the initiation of an aeolian constructional event, the large compound set (see below) directly overlying the lower sabkha bed or the small sets within the erosional remnants is not. The erosional remnants of aeolian strata within the lower interval provide a stratigraphic window into a once thicker, continuous aeolian unit. Given the preservation of the sabkha and initial wet aeolian system accumulations by a rising water table, erosion is thought to have occurred during a relative drop in the water table, which would have made the sediment available for deflation.

4.3.2 Large compound set

4.3.2.1 Description

The large compound set overlying the lower sabkha bed and erosional remnants was studied in the primary section (Figs. 4.2, 4.3), and because of its size and weathering

profile, the unit is traceable along the outcrop cliff to the secondary highway outcrop (Fig. 4.1). The compound set at the highway outcrop was earlier described by Rubin and Hunter (1987b, their stop 2). The compound set ranges in thickness from 10-35 m as a function of deep erosion along its upper contact, which yields significant paleo-topographic relief along the surface. Along the primary outcrop wall, the compound set is 15 m thick in the northeast and 10 m thick in the southwest (Fig. 4.3). Northward from the primary outcrop, the upper surface falls along the outcrop wall toward the highway outcrop (Fig. 4.5A). Within the immediate vicinity of the highway outcrop ~ 25 m of relief occurs on the surface (Fig. 4.5C).

As diagrammatically shown in Figure 4.3, the unit manifests with either simple cross-strata or compound cross-strata (Fig. 4.5B). Grainflow strata dominate the simple cross-strata with a mean dip angle of 25^{o} toward 215^{o}. Individual cross-stratum range from 15-20 cm in thickness. Wind-ripple laminae separate grainflow strata, and additionally occur as bottomsets. Along the primary outcrop wall, the compound cross-strata manifest as cosets bounded by superposition (Kocurek 1996) or second-order (Brookfield, 1977) surfaces dipping to the southwest (Fig. 4.2). Better exposed at the highway section, cosets are ~ 4 m thick (Fig. 4.5B). Bounding surfaces have an average dip of 15^{o} toward 180^{o}, whereas the cross-strata dip on average 26^{o} toward 205^{o}. Cosets are dominated by grainflow cross-strata (2-4 cm in thickness) with intercalated wind-ripple laminae.

4.3.2.2 Interpretation

Although detailed reconstruction of the bedform that resulted in the large compound set is not an objective of this paper, the bedform can be broadly interpreted. Manifestations of the unit as either simple or compound are thought to reflect changing

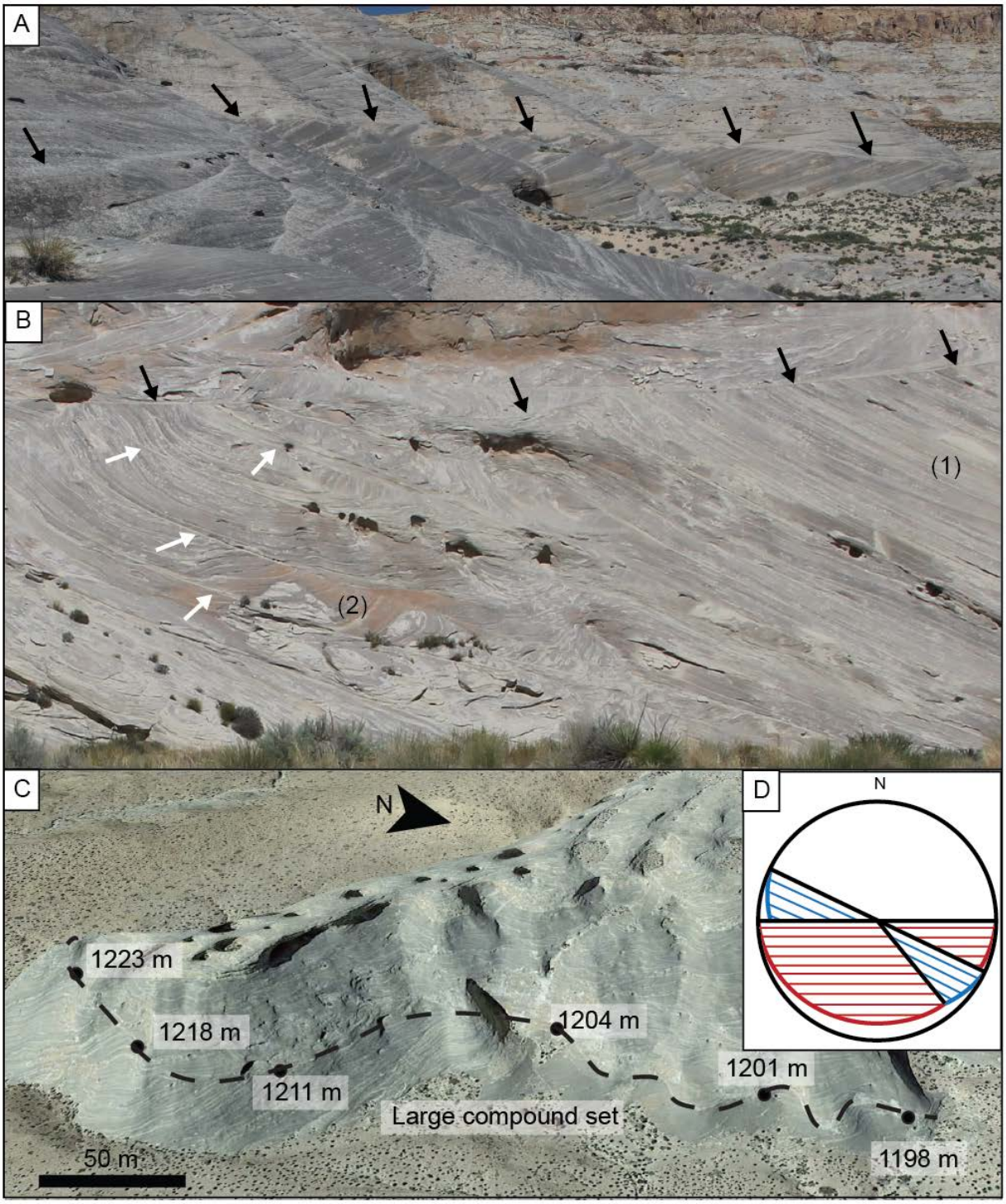

Figure 4.5: Features of the large compound set.

Figure 4.5: Features of the large compound set. (A) The top erosional surface of the set (black arrows) can be traced across the outcrop, and in this west-facing image the surface dips to the right (north). (B) Secondary highway outcrop (Fig. 1, black box) showing both simple (1) and compound (2) cross-stratification. Simple cross-strata are dominated by thick grainflow cross-strata, and compound sets are bounded by superposition surfaces (white arrows). Note relief along the upper erosional surface (black arrows). (C) The top erosional surface of the large set (dashed line) shows ~ 25 m of paleo-topographic relief at the secondary highway outcrop. At this outcrop the surface falls in elevation to the north, whereas along the primary outcrop (Figs. 2, 3) the surface falls in elevation to the south. Image courtesy of Google Earth. For scale, shrubs at the base of the outcrop are ~ 1 m high. (D) Stereonet showing the orientation of superposition bounding surfaces (red) and cross-strata (blue) as measured at (B). The line of intersection of the planes gives the trend of the superimposed dunes as 320^{o}.

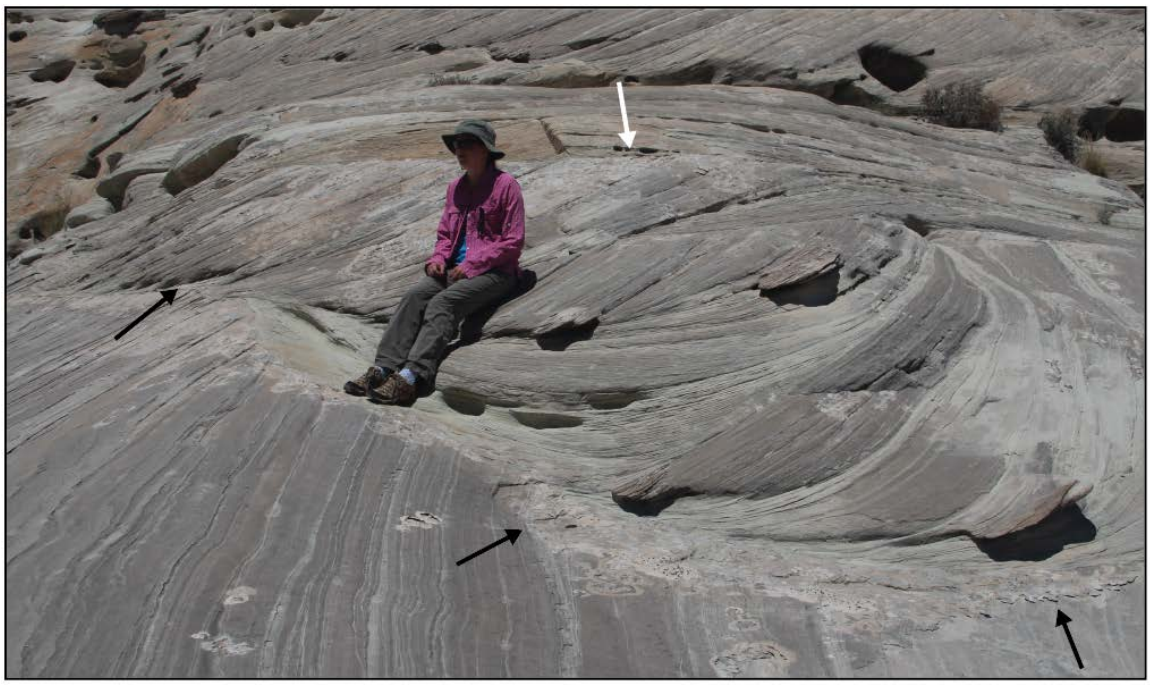

Figure 4.6: Compound cross-strata filling a local deeper scour into the underlying large compound set. The filling set conforms to the irregular shape of the scoured surface (black arrows), suggesting that it was cut by the migrating dune. The scour-fill is truncated by the surface that truncates the large compound set laterally (white arrow).

lee-face configurations along sinuosity of the main bedform. As determined along the curving outcrop, simple cross-strata dominate where the dip direction is toward the southwest (210^o-230^o), but as the dip direction becomes more southward, compound cross-strata occur. Simple cross-strata dominated by grainflow are interpreted to represent a slipface where the brinkline, trending roughly at 305^o or normal to the mean cross-strata dip direction (215^o), was transverse to wind from the northeast (Eastwood et al., 2012). The compound cross-strata are interpreted to represent deposition by dunes superimposed upon the lee face of the main bedform (Brookfield, 1977; Rubin and Hunter, 1983; Rubin, 1987). Using the stereonet method of Rubin and Hunter (1983), the intersection of the planes formed by the bounding surface and the cross-strata (Fig. 4.5D) defines the trend of the superimposed dunes as 320^o with migration normal to this trend (toward 230^o). Given the onset of compound cross-strata as the dip direction changes from southwest to south, and the mean dip direction of the superposition surfaces toward 180^o, portions of the main dune lee face marked by superimposed dunes were oriented roughly east-west (and dipping southward) and the superimposed dunes migrated obliquely down the lee face toward the southwest. Although only general trends for the surfaces and cross-strata are given by Rubin and Hunter (1987b), our reconstruction is in general agreement with this earlier one, except that our reconstruction indicates an oblique downslope migration to the southwest for the superimposed dunes, whereas Rubin and Hunter (1987b) indicated an alongslope migration to the west. The oblique downward migration is more realistic given the downward slant of the superposition surface in the primary outcrop (e.g., Rubin, 1987, his fig. 25), which trends in the general transport direction of the main bedform.

Stratigraphically, the compound set is a singular feature between two erosional, outcrop-scale bounding surfaces. Cross-strata downlap onto the erosional surface that

bounds the lower sabkha bed or erosional remnants of the initial wet-system dune field. The upper bounding surface of the compound set shows up to 25 m of paleo-topographic relief. Because of this relief and the absence of polygonal fractures or overlying sabkha deposits, the upper bounding surface does not appear to be associated with a water table. The paleo-topography may represent some degree of preserved dune topography, but the irregularity of the paleo-topography locally (Fig. 4.5C) implies that aeolian deflation significantly contributed to development of the relief on the upper bounding surface.

Given the size of the preserved set/coset and the thickness of the grainflow cross-strata (Kocurek and Dott, 1981), the main bedform was a very large feature that migrated across the area leaving a continuous set for at least a few kilometers. The presence of a large compound bedform implies a very mature dune field in which a pattern of large compound dunes evolved from smaller and simpler dunes. The contrary view requires a pattern of large compound dunes to initially evolve on a surface with sand transport and no antecedent dune-field development. Whether the large compound dunes evolved in the immediate area, or upwind and thence migrated into the study area, there is no record of earlier dune-field evolution in the study area.

4.3.3 Local scour-filling sets along surface bounding large compound set

4.3.3.1 Description

Locally present along the erosional surface that bounds the set of large compound cross-strata is a deeper scour filled by a set of compound cross-strata (Figs. 4.2, 4.3). As shown in Figure 4.6, the depression is ~ 2 m deep and extends along the outcrop for ~ 5 m. The compound set filling the scour is then truncated to the level of the main bounding surface laterally. The irregular scour base appears to conform with the architecture of the overlying set (Fig. 4.6), suggesting that the scour was created with dune migration. The

scale of this irregular scour into the compound set is similar to other scours evident along portions of the bounding surface at the highway outcrop (Fig. 4.5C). The compound set shows an irregular alternation of centimeter-scale grainflow and wind-ripple cross-strata separated by a bounding surface.

4.3.3.2 Interpretation

Although it is possible that the scour-fill represents the basal portions of another compound dune in the same field as the underlying large compound set, this interpretation is thought unlikely because of differences in the architectural styles of the sets and scale of bedforms as inferred by the thickness of the grainflow cross-strata. Rather, given its singular occurrence scouring into the large compound set, the scour-fill feature is potentially a stratigraphic window into the dynamics that gave rise to the surface that bounds the large compound set. As discussed above, relief on this bounding surface may reflect some degree of relict dune topography, but wind erosion of the surface without a water-table control must have been significant. Interpretation of the scour-fill structure as created by migrating dunes argues that erosion of large compound dune strata occurred by negatively climbing dunes that derived their sand from cannibalization of the substrate. The scour-fill feature itself would then represent the unusual occurrence where accumulations of the cannibalizing dunes were locally preserved in an especially deep-scoured depression.

4.3.4 Downlapping sets filling paleo-topographic depressions

4.3.4.1 Description

Overlying the erosional surface bounding the large compound set is a ~ 20-25 m thick interval consisting of 1-3 m thick sets bounded upward by an outcrop-scale erosional surface (sets 1-24 in Figs. 4.2, 4.3). Cross-strata within the sets have a mean dip

direction of 229^{o} and consist of intercalated grainflow and wind-ripple laminae. Given the dune transport direction, the primary section (060^{o}) is oriented nearly transport-parallel. Outcrops north of the primary wall and oriented approximately normal to the transport direction show set troughs with an average width of ~ 12 m (Fig. 4.7).

The most distinctive aspect of the sets on the primary outcrop wall is their downlapping architecture (Fig. 4.3). Where best defined by sets with the greatest lateral extent (sets 10-15), from northeast to southwest, sets transition from inclining slightly upward to curving downward to downlapping onto the lower bounding surface. The

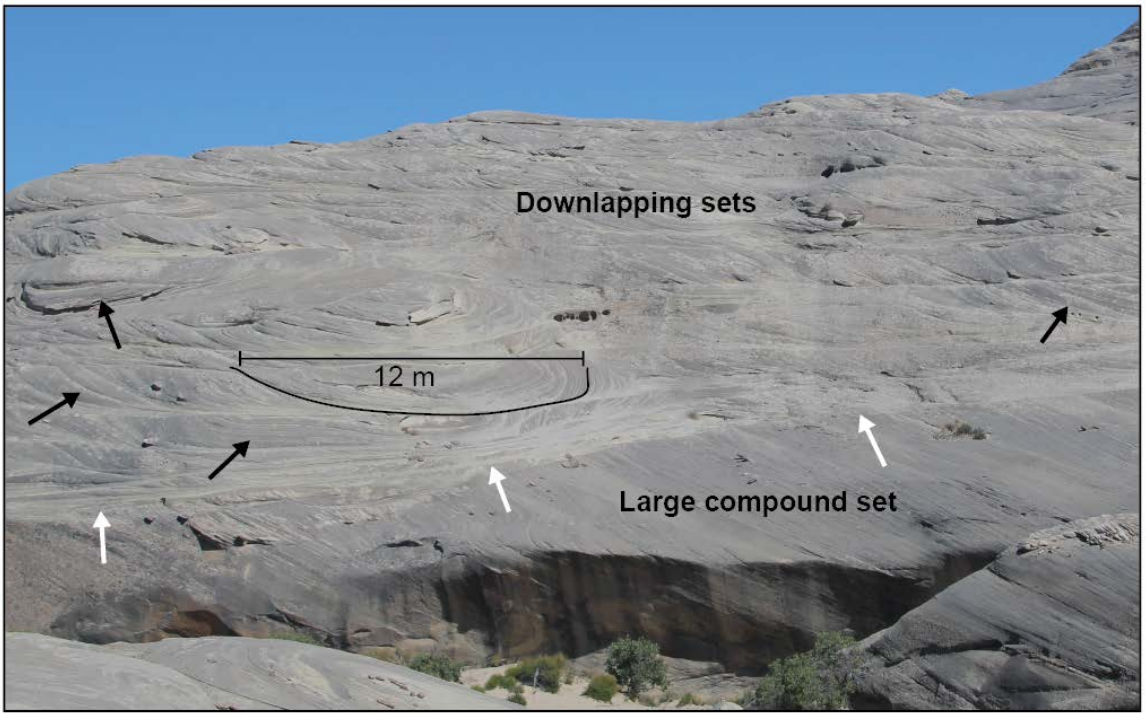

Figure 4.7: Trough cross-stratification of the downlapping sets. Viewed facing SSW, this outcrop exposes many troughs (black arrows) with an average width of ~ 12 m. These dunes are interpreted to have filled in paleo-topographic relief on the eroded top surface (white arrows) of the large compound set.

downward curvature occurs above the break in slope of lower bounding surface to a lower elevation (Fig. 4.3). The mean downward inclination of the set bounding surfaces is ~ 2^{o} as measured from the lower bounding surface. The overall architecture of these cosets has the appearance of a prograding body in which the sets climb over and then down the larger form, essentially forming topsets and foresets (Fig. 4.3). Variation in this set architecture evident in Figure 4.3 is thought to reflect both progradation of the overall sand body, and local variation in scour and accumulation. Sets 1-6 progressively downlap onto the lower surface, but sets 5-6 are truncated upward by subsequent sets, and sets 7-9 infill scour and prograde. Set 10 is the first set to define the topset and foreset of the larger sand body. Set 11 falls short of the basal surface and is truncated by continuous set 12. Upward, continuous sets largely alternate with more leeward sets that are scoured into lower continuous sets, and are then truncated by overlying continuous sets. Uppermost sets 21-24 are largely planar and thought to represent the topset portions of the sand body which prograded through the outcrop.

4.3.4.2 Interpretation

The architecture of a coherent coset of trough-shaped sets in the strike section that prograde and downlap in the dip section could be interpreted as a compound dune consisting of sinuous dunes migrating over and down the larger host bedform (e.g., Rubin, 1987, his fig. 65). However, this interpretation is rejected given the: (1) documented paleo-topographic relief on the lower bounding surface that truncates the underlying large compound dune, (2) similarity between thickness of the coset and relief of the paleo-topography, (3) curvature of the continuous sets from topset to foreset over the break in slope of the lower bounding surface, and (4) presence of the topsets that would indicate unlikely supercritical climb. Rather, the downlapping sets are interpreted

as filling a paleo-topographic depression present on the surface that bounds the underlying compound set. The general nature of the coset with its topset and foreset architecture indicates that the dunes formed a coherent sand body that progressively prograded and filled the depression. The end of deposition of the downlapping interval may simply represent completed filling of the local topographic depression. Subsequent dune-field development may have occurred, but the depression constituted the local accumulation space. Dunes above this level either bypassed or their accumulations were subsequently eroded. In the broader interpretation, the period of negatively climbing dunes and substrate deflation that gave rise to the erosional paleo-topography was followed by filling of depressions along this surface. It is possible that sand to fill this depression was derived from upwind scour of the surface, but the volume of sand represented by the downlapping sets seems best attributed to a renewed influx of sand to the area. The preserved record of this event, however, resides largely in the filled depressions.

4.3.5 Climbing dune sets

4.3.5.1 Description

The upper ~ 20 m of the primary outcrop consists of four intervals of sets of cross-strata that originate upon a lower planar surface, show a distinct rise (i.e., climb), and are truncated by an upper planar surface (Figs. 4.2, 4.3). This architecture is characteristic of accumulation by climbing bedforms, as first recognized for subaqueous bedforms (Sorby, 1869; Walker, 1963; Allen, 1970) and more recently for large aeolian dunes (Brookfield, 1977; Rubin and Hunter, 1982).

The first ~ 7 m thick interval (sets 25-32 in Figs. 4.2, 4.3) is bounded below by the surface defining the top of the downlapping sets (see above), and above by the next

outcrop-scale truncational surface. Sets 25-28 originate on the lower surface, and it is assumed that the younger sets also originated on this surface as projected to the northeast. Set 29 shows variation in scour depth and nearly downcuts through underlying set 28. Sets 26-32 are truncated by the upper surface. The apparent angle of climb as measured from the lower bounding surface, which is taken as the accumulation surface, is ~ 2^{o}. Sets average 2.5 m in thickness.

The second interval is ~ 2 m thick and consists of only two sets (sets 33-34 in Figs. 4.2, 4.3), which nevertheless show a climbing architecture. Both sets originate from the surface truncating the first interval of climbing sets, and are truncated by the next surface upward.

The third interval is ~ 3 m thick and consists of a single thick set (set 35 in Figs. 4.2, 4.3). The interval is defined by the surface truncating the sets below, and by an upper surface upon which the fourth interval of climbing sets originates. Although climbing of set 35 cannot be demonstrated, this interval is included herein because of its position and similarity to the underlying and overlying intervals.

The fourth interval (sets 36-40 in Figs. 4.2, 4.3) is ~ 7 m thick and truncated by the surface upon which the upper sabkha bed rests. Sets, with the exception of set 38, which is truncated by set 39, originate on the lower bounding surface. The apparent angle of climb is 0.9^{o} and average set thickness is 1.8 m.

As seen along the primary outcrop where outcrop trend is about parallel to the southwest dune migration direction, the sets within all the climbing intervals are simple, and dominated by grainflow cross-strata punctuated by wind-ripple laminae (Fig. 4.2). Although a detailed analysis of the bedforms and wind regime is beyond the scope of this paper, a rich diversity of sedimentary features occurs along the outcrop between the primary and highway sections (Fig. 4.8). Variation in scour depth occurs, and although

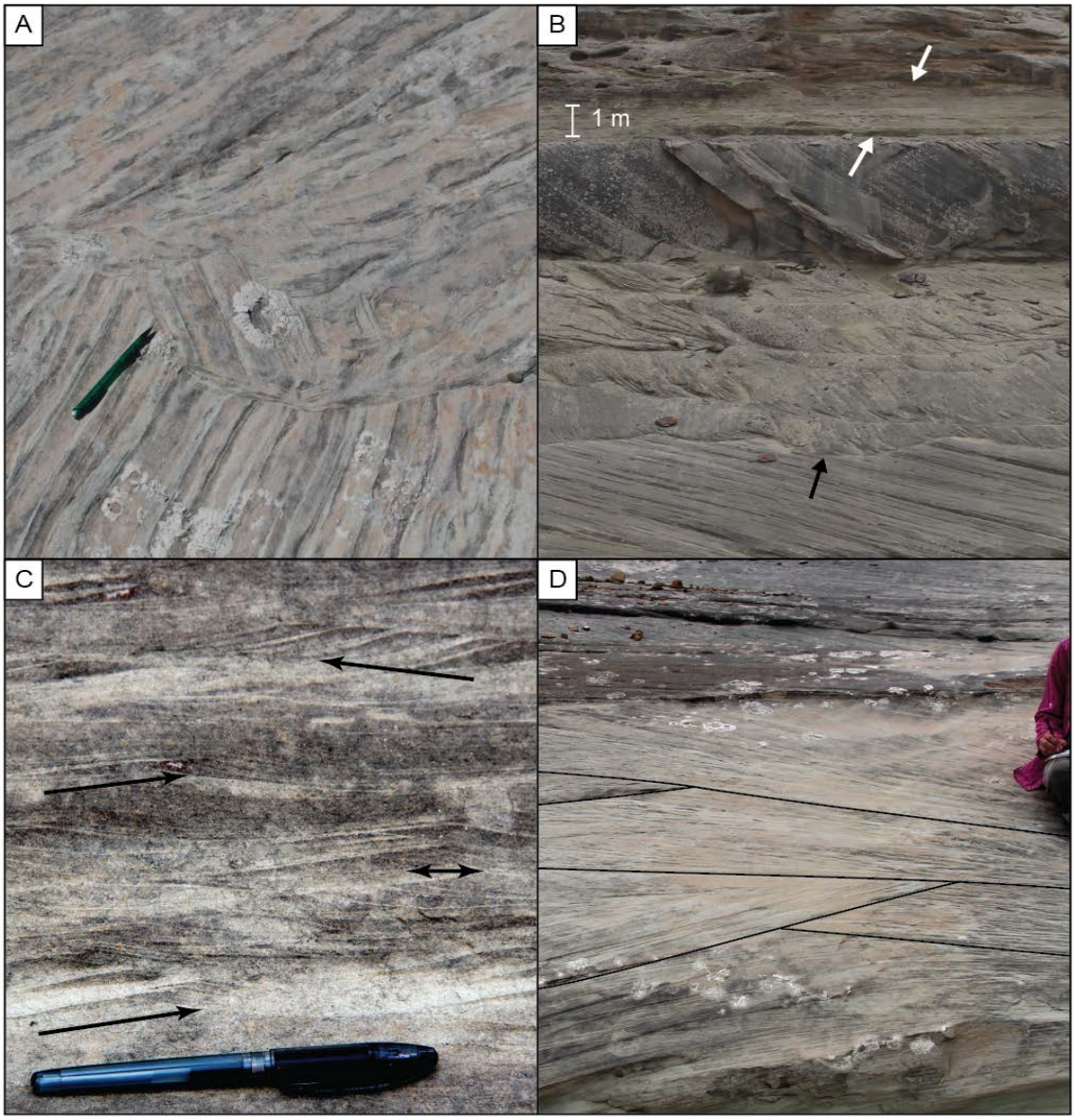

Figure 4.8: Sedimentary features in the climbing dune sets. (A) Brecciated and rotated block of aeolian cross-strata and associated corrugated bounding surface demonstrate at least intermittent wet periods during this depositional phase of the Entrada. (B) The climbing dune sets are truncated by the surface upon which the upper sabkha bed (white arrows) rests. Several meters below the sabkha bed, variation in scour depth is evident along the bounding surfaces between sets (e.g., black arrow), and the steep relief on some surfaces further indicates wet-system accumulation. (C) Near-critically climbing ripple strata within the climbing sets show rapid deposition and a reversal of transport direction (arrows). (D). Cross-strata exposed in plan-view "zig-zag" across the outcrop. The change in orientation (by ~ 30^{o}) is interpreted to be in response to changes in wind direction and the readjustment of a convex nose of the dune.

most bounding surfaces between sets are smooth, others are corrugated, indicating deflation of a damp surface (Fig. 4.8B), and rotated blocks of dune cross-strata occur (Fig. 4.8A). Locally sets are compound, and reactivations surfaces are relatively common. Plan-view outcrops were found showing reversals in asymmetry of convex-downwind dune segments (Fig. 4.8D), and preserved wind-ripple forms with reversing migration directions are relatively common (Fig. 4.8C).

4.3.5.2 Interpretation

The four intervals of preserved climbing sets are interpreted to represent pulses of dune accumulation that were subsequently truncated to a planar surface. Although no sabkha strata were identified, the planar truncational surfaces bounding each interval of climbing sets suggest a water-table-controlled level of deflation. The corrugated surfaces between sets, as well as the brecciated strata, suggest that these dune fields were at least partially wet systems. The bi-directionality observed in the cross-strata, as well as the common reactivation surfaces, indicate that the wind regime was not unimodal, albeit net dune transport was to the southwest, as indicated by the overall cross-strata orientation. Although each interval of climbing sets originates upon a planar, deflationary surface, no interval shows a basal portion representing dune-field initiation, in which small sets occur and evolve into the meter-scale sets preserved.

Because the architecture of climbing bedforms is relatively well known, dune parameters can be estimated for the first and fourth intervals where multiple sets occur between the outcrop-scale bounding surfaces. The relationship between set thickness (s), dune spacing (l), and angle of climb (δ) is given by:

$$s = l\ tan\delta \tag{4.1}$$

(Brookfield, 1977; Rubin and Hunter, 1982; Bridge and Best, 1997). For the first climbing interval, with an average set thickness of 2.5 m and an apparent climb angle of 2^{o}, this equation yields a dune spacing of ~ 72 m. For the fourth interval, the apparent angle of climb is 0.9^{o} and average set thickness is 1.8 m, yielding a dune spacing of 114 m. Given the calculated dune spacings and assuming a range of 10-20 for the bedform index (spacing / height; Lancaster, 1988), calculated dune heights for the first interval are ~ 4-7 m, and ~ 6-11 m for the fourth interval. The relatively thick sets in comparison to dune height are consistent with the high angles of climb. Dune migration rate is a function of dune size and wind regime, the latter of which is unknown for the Entrada. However, dunes in the White Sands Dune Field, New Mexico, average ~ 5 m in height (Baitis et al., 2014) and migrate ~ 3 m/yr (Pedersen et al., 2015). Assuming a conservative slower migration rate of 2 m/yr for the larger Entrada dunes, and using the calculated dune spacing and the observation that in the first and fourth intervals the greatest number of sets stacked vertically is four, the time represented by each of these intervals is on the order of centuries (144 yr for the first interval, 228 yr for the fourth interval). This minimum time does not include any cannibalized lower record, sets totally removed within the climbing sequence owing to scour-depth variation, or sets removed during formation of the upper erosional bounding surface. However, given the minimum time recorded and the high angle of climb, the climbing intervals most likely represent geologically brief pulses of sediment influx and dune-field construction.

4.4 DISCUSSION

Figure 4.9A is an outcrop-scale Wheeler diagram in which the strata shown in Figure 4.3 are plotted as a function of their spatial extent and interpreted time, bounding surfaces are represented as gaps in time, and speculation is given as to “missing” portions

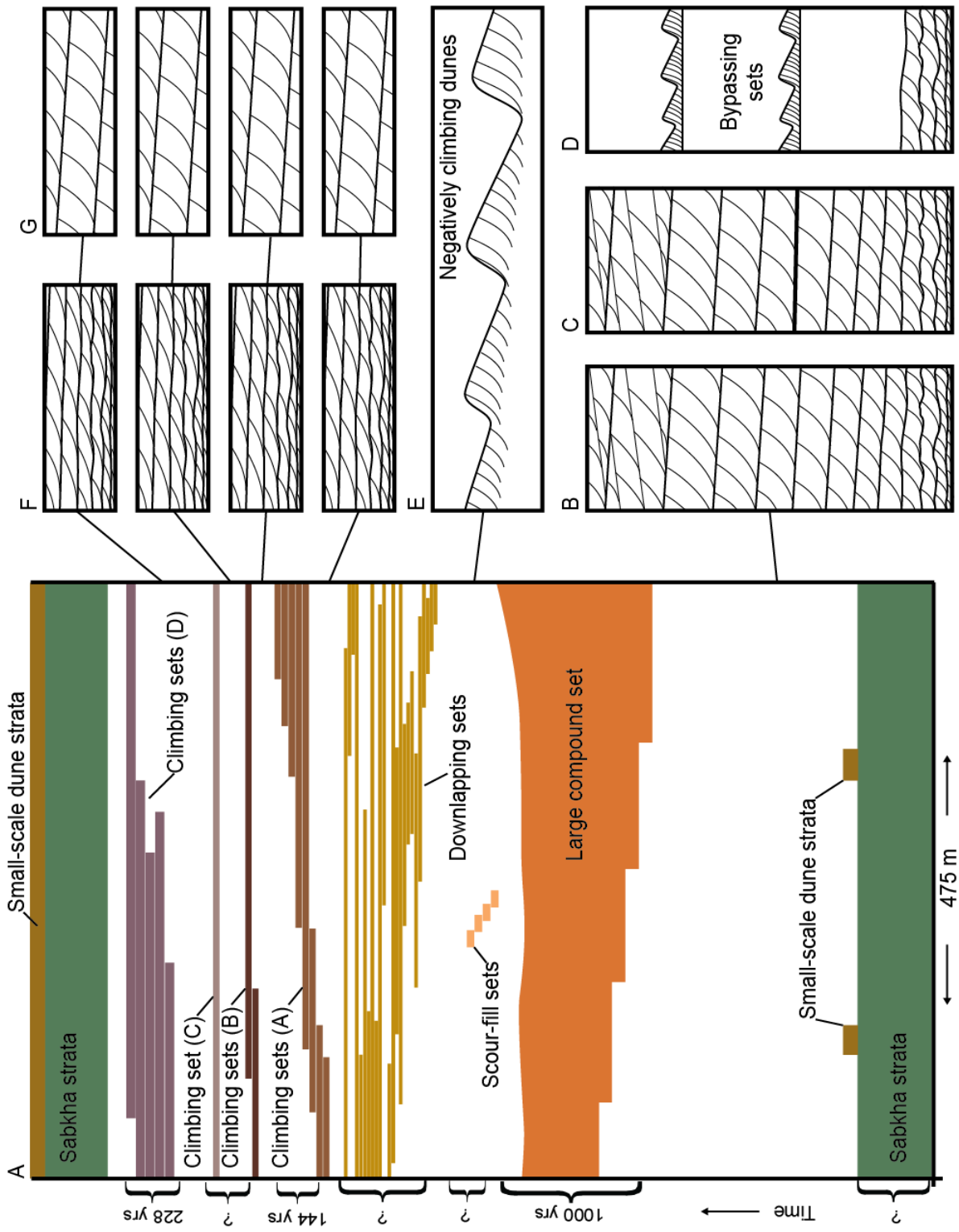

Figure 4.9: Outcrop-scale Wheeler diagram

Figure 4.9: Outcrop-scale Wheeler diagram of the diagrammatic section in Fig.3, and speculation about “missing” strata. (A) Preserved accumulations are shown and outcrop-scale bounding surfaces are represented as gaps in time. Time is not to scale, but some time spans presented in the text are given for individual intervals. (B) – (G) show possible scenarios for time gaps, as discussed in the text.

of the section within these time gaps. This diagram is entirely interpretative and intended to explore aspects of development, accumulation, and preservation of aeolian and related facies.

The lower, predominately sabkha bed is interpreted to represent accumulation with a relatively slow rise of the capillary fringe under sediment-limited conditions (i.e., the unit is shown thicker in Fig. 4.9A than its actual thickness in Fig. 4.3). Initial preservation processes included the continued rise of the water table, and burial by accumulations of the wet-system dune field represented by the erosional remnants. With the interpreted fall in the water table and deflation of most of the overlying cross-strata, resistance to scour because of evaporitic cements may have preserved the sabkha bed until subsequent burial by the overlying compound set.

The extent of development of the dune-field represented by the erosional remnants is not known, nor is dune-field construction that culminated in the overlying large compound dunes. This record is collapsed into the bounding surface separating the units. Speculation given for this time gap in Figure 4.9A considers just three scenarios arising from considering whether the erosional remnants and the large compound set are genetically related or not; in truth, any number of events could have occurred. Where the erosional remnants are taken as representing the initial dune field that culminated in the large compound dunes, missing strata are sets that represent increasingly large dunes, which ultimately became compound dunes (Fig. 4.9B). These strata could have been progressively cannibalized by growing dunes that were, in turn, cannibalized by the

growing compound dune as the dune field evolved. Alternatively, the deep scour trough that now houses the compound set could have downcut through most underlying strata to the level of the sabkha bed. Where the erosional remnants and the large compound set are taken as unrelated, the erosional remnants represent a dune-field constructional event, the termination of which was marked by surface development that may have downcut to create the erosional remnants as seen today (Fig. 4.9C). A subsequent, probably major, dune-field construction event followed that culminated in large compound dunes. As with the first scenario, growing dunes cannibalizing the substrate or deep scour associated with the compound dunes ultimately gave rise to the large compound set overlying the sabkha bed and erosional remnants. In a third scenario, the erosion that gave rise to the erosional remnants occurred soon after their deposition, and no accumulation occurred thereafter until the deposition of the large compound set, with all sand being incorporated into the growing dunes that gave rise to the compound dunes. A prolonged period of growing dunes that bypassed or mined the substrate culminated in the accumulation of the large compound set.

The large compound set in Figure 4.9A is shown with a lower stair-step pattern in the migration direction in order to represent the slow progressive migration of the bedform along the primary outcrop. Given the interpreted large dune size and assuming some comparatively slow migration rate (e.g., 0.5 m/yr), on the order of 1000 yrs is needed for the bedform to migrate the 475 m length of the primary outcrop. The pronounced erosional relief on the upper bounding surface of the set, coupled with the local deeper scour filled by the small compound sets (Fig. 4.3), is interpreted to represent surface deflation of possible relict dune topography by negatively climbing dunes during a period of diminished sand supply. The bounding surface, therefore, is interpreted to represent a time gap during which dune strata (with the exception of the singular scour-

fill) were not accumulating, but rather negatively climbing dunes cannibalized the underlying strata (Fig. 4.9E). The overlying downlapping sets are interpreted to be intricately related to the erosional bounding surface by filling depressions that existed along the surface during a subsequent influx of sediment. Whereas the scour-fill inset into the compound set may represent filling of an unusually deep migrating scour trough, the downlapping sets represent filling of an erosional depression of an order of magnitude wider and at the landscape scale.

The upper interval of climbing sets (climbing sets A-D in Fig. 4.9A) are interpreted as geologically brief periods of accumulation followed by surface planation, most probably to the water table. The absence of strata showing any initial dune-field construction, as well as strata removal associated with formation of upper bounding surfaces underscore the differences in dune-field construction, accumulation, and preservation. As given in Figure 4.9F, in one scenario dune fields could have been evacuated from the area with formation of each truncational bounding surface. Each interval of climbing sets would have then initiated with small dunes that evolved into the meter-scale dunes represented by the accumulated and preserved sets. The absence of this initial dune-field record implies that any strata from these early dunes were cannibalized by the growing dunes or scoured by the passage of deeper migrating interdune troughs. In a second scenario, dunes existed continuously, perhaps since the depression-filling downlapping sets, but rather accumulation was episodic and punctuated by periods of dune bypassing or negative climbing with scour to the water table (Fig. 4.9G). The first scenario is compatible with an Entrada depositional system in which dune fields temporally waxed and waned as a function of sand supply, or in which dune fields were separated spatially and progressively migrated across the area. The second scenario envisions a depositional environment with continuous dune coverage where episodes of

accumulation may have resulted from temporary relatively higher rates of sediment influx, with subsequent deflation to the rising water table during times of diminished flux. In any scenario, truncation of the intervals of sets by an upper bounding surface indicates that there were dune accumulations that were not preserved. Truncation of the uppermost interval of climbing sets (climbing sets D in Fig. 4.9A) was to the water table, and followed by slow sabkha accretion in a rising capillary fringe.

As is often inferred from the rock record (e.g., Carr-Crabaugh and Kocurek, 1998; Mountney, 2006a), interpretation of the Entrada interval studied here indicates that the preserved accumulations represent geologically brief spans of time, and that significantly greater spans of time are represented by the outcrop-scale bounding surfaces. This is especially true for climbing sets A and D (Fig. 4.9A), where the calculated century-time scale to emplace the sets (see above) is not compatible with much slower rates of water-table rise or subsidence associated with accumulation and preservation. The implications are that accumulations occurred during major, but geologically brief sand pulses, that original total accumulations were significantly thicker than those preserved, and that surfaces within the preserved accumulations represent a level of deflation defined by a slower-paced rise in the water table and subsidence. Given this reasoning, the outcrop-scale truncational surfaces are best interpreted as areal-to-regional surfaces described elsewhere (e.g., Loope, 1984; Kocurek, 1988; Kocurek and Havholm, 1993; Mountney 2006a) at the time scale of parasequences (e.g., Van Wagoner et al., 1990). Because neither the parasequences nor the surfaces that bound them have not been traced beyond the study area, it is unknown whether these represent regional allogenic forcing, or more local impacts of sediment sourcing coupled with water-table behavior and continued subsidence.

4.5 CONCLUSIONS

The initial question posed in this paper asked what stages of dune-field construction are preserved in the rock record? In this case study of an interval of the Jurassic Entrada Sandstone, analysis of the gross architecture of preserved accumulations and their bounding surfaces demonstrated that the studied interval does not represent continuous sedimentation within a single, long-lasting sand sea. Rather, three of the intervals (large compound set, the scour-fill sets, downlapping sets) appear associated with filling of deep scoured troughs or landscape-scale erosional depressions, two intervals of sabkhas and overlying initial wet systems appear associated with a rising water table, and only the upper intervals of climbing sets approach the common model of accumulation by climbing dunes. Speculation about missing strata represented by the major bounding surfaces most commonly gravitates toward cannibalization of the early record of dune-field construction, and removal of significant volumes of strata resulting in the formation of these erosional surfaces. In nearly all cases, later deposits were strongly influenced by antecedent conditions and surface configuration. The time represented by the preserved accumulations appears to be considerably less than the time represented by the erosional surfaces.

Although the autogenic processes influencing dune fields (e.g., dune-field evolution through dune interactions) that occurred in the Entrada system are common to dune fields in general, the set of allogenic boundary conditions in which the Entrada system evolved are, in detail, unique to that system. Low-frequency allogenic boundary conditions (e.g., tectonism, climate, sea level) are thought to “trickle down” to the depositional environment and influence autogenic processes (Kocurek and Ewing, 2017). In this regard, the Entrada record described here most likely represents a point on a

spectrum of preservation styles in the aeolian stratigraphic record. The breadth of this spectrum can be best approximated with more examples.

4.6 Acknowledgments

The authors thank the Glen Canyon National Recreation Area for permission to conduct this study. In particular, Dr. John Spence was exceptionally helpful with permitting and field equipment. Fieldwork was supported by Shell Exploration and Production Company, and the National Science Foundation Graduate Research Fellowship Program.

Chapter 5: Carving intra-crater layered deposits with wind on Mars[1]

5.1 INTRODUCTION

Layered sedimentary rocks preserve the record of ancient environments and climate on Mars, as well as any potential astrobiological record. The thickest accumulations of sedimentary rocks on Mars are housed within crater basins, including Gale crater, the current exploration site of the rover Curiosity (Wray, 2013). Observations thus far by Curiosity have led to the discovery that the basal portions of the 5 km stack of sedimentary rocks were deposited predominately by streams and deltas flowing into a crater lake (Grotzinger et al., 2015; Williams et al., 2013a). Upper portions of the stack are thought to represent aeolian deposition (Anderson and Bell, 2010; Bennett and Bell, 2016; Grotzinger et al., 2015; Milliken et al., 2014). Subaqueous deposition overlain by aeolian deposition has also been invoked to explain the strata of other intra-crater layered mounds (Howard, 2007; Schon et al., 2012; Wilson et al., 2007). Layered strata within craters are typically found near the center of the craters, and show a spectrum of morphologies ranging from small low-relief hills, to large central mounds such as in Gale crater, to crater-filling with moats circumscribed by the crater rim (Fig. 5.1A-D) (Malin and Edgett, 2000). Although it has been suggested that mounds grew in-place (Kite et al., 2013), the general consensus is that mound morphologies represent a spectrum of advancing stages of wind erosion of once-filled craters (Bennett and Bell, 2016; Grotzinger and Milliken, 2012; Grotzinger et al., 2015). Despite the widely-ranging significance of this interpreted succession of wind-eroded forms, the dynamics that would yield mounds and moats within craters have not been demonstrated. This study utilizes simple wind tunnel experiments and LES flow modeling to explore wind erosional

[1] This chapter was published in Geophysical Research Letters in 2016. Citation: Day, M., Anderson, W., Kocurek, G., and Mohrig, D., 2016, Carving intracrater layered deposits with wind on Mars: Geophysical Research Letters, v. 43, no. 6, p. 2473-2479.

patterns within filled craters, and illuminates the dynamics that create an expanding moat and retreating mound morphology consistent with orbital and ground observations. The location of these mounded sedimentary deposits on Noachian terrain has implications for the timing of global climatic change on Mars and a restructuring of the martian sedimentary cycle.

5.2 WIND TUNNEL EXPERIMENTS

To simulate the morphological evolution of craters filled with sedimentary layers and then subjected to wind erosion, physical models of martian craters were filled with damp, cohesive sand and subjected to a unidirectional wind in a wind tunnel until all sediment-fill was removed (see section 5 for more details). No sand was introduced upwind of the crater, and although some drying did occur, images taken during the experiment confirm that this was relatively limited. Successive digital elevation models were made to capture the morphological evolution of the interior deposit. Erosion of the interior first began just inside the crater rim, creating a shallow moat. This pattern of erosion then continued as flow was preferentially focused adjacent to the rim, deepening the moat and sculpting the remaining deposit into a central mound. As the moat eroded down to the crater floor, the central mound shrank to the size of a small remnant hill, until that too was entirely removed (Fig. 5.1E-H). Although this simple wind tunnel experiment is not intended as a scaled model of martian conditions, it does demonstrate a pattern of moat creation and retreating mound caused by wind erosion that is qualitatively similar to the spectrum of morphologies observed on Mars.

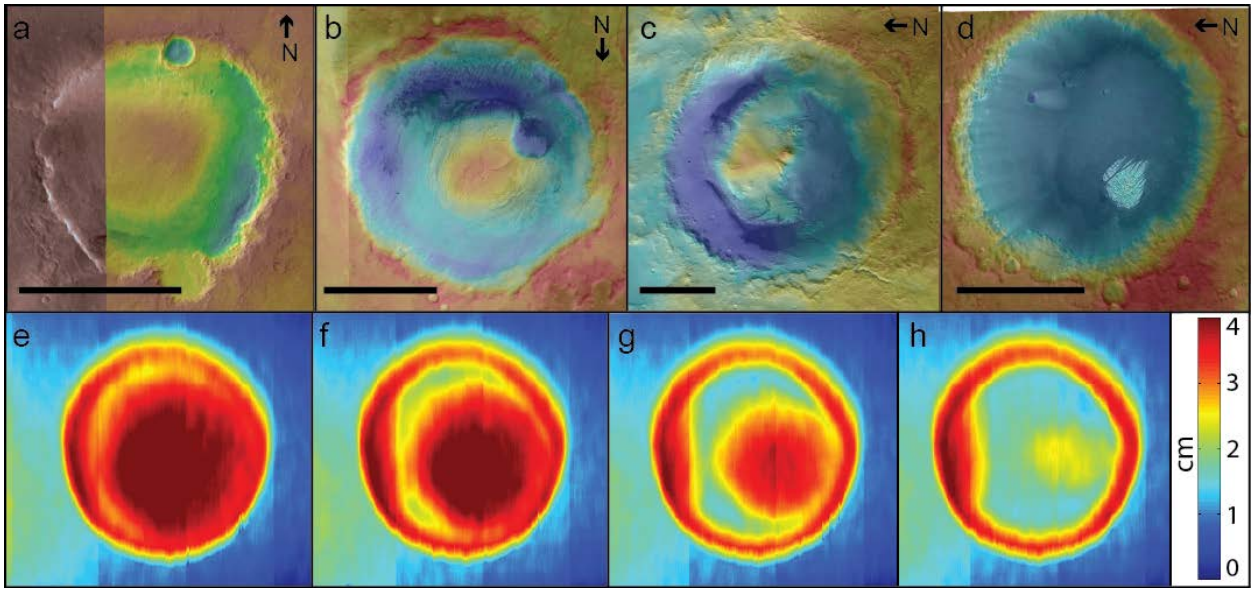

Figure 5.1: Spectrum of intra-crater mound morphologies. (a-d) Martian craters showing the spectrum of intra-crater layered deposit morphologies from (a) initial moat (unnamed crater at 6.7°E, 12°N), to (b-c) expanding moat with retreating central mound (Firsoff and Gale craters), to (d) remnant isolated hill (Pollack crater). Images and DEMs from High Resolution Stereo Camera with DEMs differentially stretched to bring out the relief in each crater (warm colors reflect high elevation, and cool colors low elevation). Scale bar is 50 km. Craters in (b), (c), and (d) have been rotated for better comparison with wind tunnel analogs with north as indicated. (e-h) DEMs from wind tunnel experiments showing progressive stages of crater fill erosion hypothesized to correspond with the martian morphologies in (a-d). Model diameter is 30 cm with 1:10 depth-to-diameter geometry. Note colorbar for relief. Wind is from left to right.

5.3 LARGE-EDDY SIMULATION OF FLOW FIELD

Four topographies chosen based on wind tunnel experiments and martian observations were formed using superimposed Gaussian curves and served as boundary conditions for large-eddy simulation (LES) modeling of flow fields. These four topographies represent different stages of the morphological spectrum; filled crater, filled crater with initial interior moat, crater with wide moat and retreating mound, and empty crater. In each case, a pattern of secondary flow originates via flow separation at the upwind crater rim. Vortical structures originating at the upwind rim undergo a spatial

realignment owing to vortex “stretching and tilting” mechanisms, travel parallel to the rim’s inner walls, and exit the crater at its downwind flank (Fig. 5.2). Secondary flow patterns from LES show that flow is deflected around mound topography and vorticity near the rim intensifies as the moat deepens from one erosional stage to the next, indicating a positive feedback between surface morphology and sediment erosion. Sand transported in these vortices would abrade and further erode the moat, creating a deeper channelizing pathway for flow, and explaining the tendency for these deposits to retreat to the crater center.

The present application of LES is underpinned by presumption of aerodynamically “fully rough” conditions, thereby enforcing Reynolds number dynamic similarity on the problem even as the geometric scale is varied (Jimenez, 2004). Here, therefore, we argue that LES captures the dynamically important crater flow scales of motion because the prescribed domain depth, H, is set to be the depth of the planetary boundary layer (Shao, 2000) and exceeds the crater rim height (Michaels and Rafkin, 2004; Petrosyan et al., 2011).

5.4 RESULTS AND IMPLICATIONS

5.4.1 Moat erosion and mound retreat

Distributions of shear stress resulting from LES were used to estimate the largest mobile grain size in the modeled topographies for a range of martian wind speeds. For all morphological stages, the largest grains were mobilized where flow accelerated over positive slopes: on the upwind exterior of the crater; on the downwind interior rim; and on the upwind interior mound (Fig. 5.3). Shear stress on the mound was higher on the upwind side than the downwind side, accounting for the up-to-downwind asymmetry in observed martian mounds. Crescent-shaped zones of high shear stress and increased

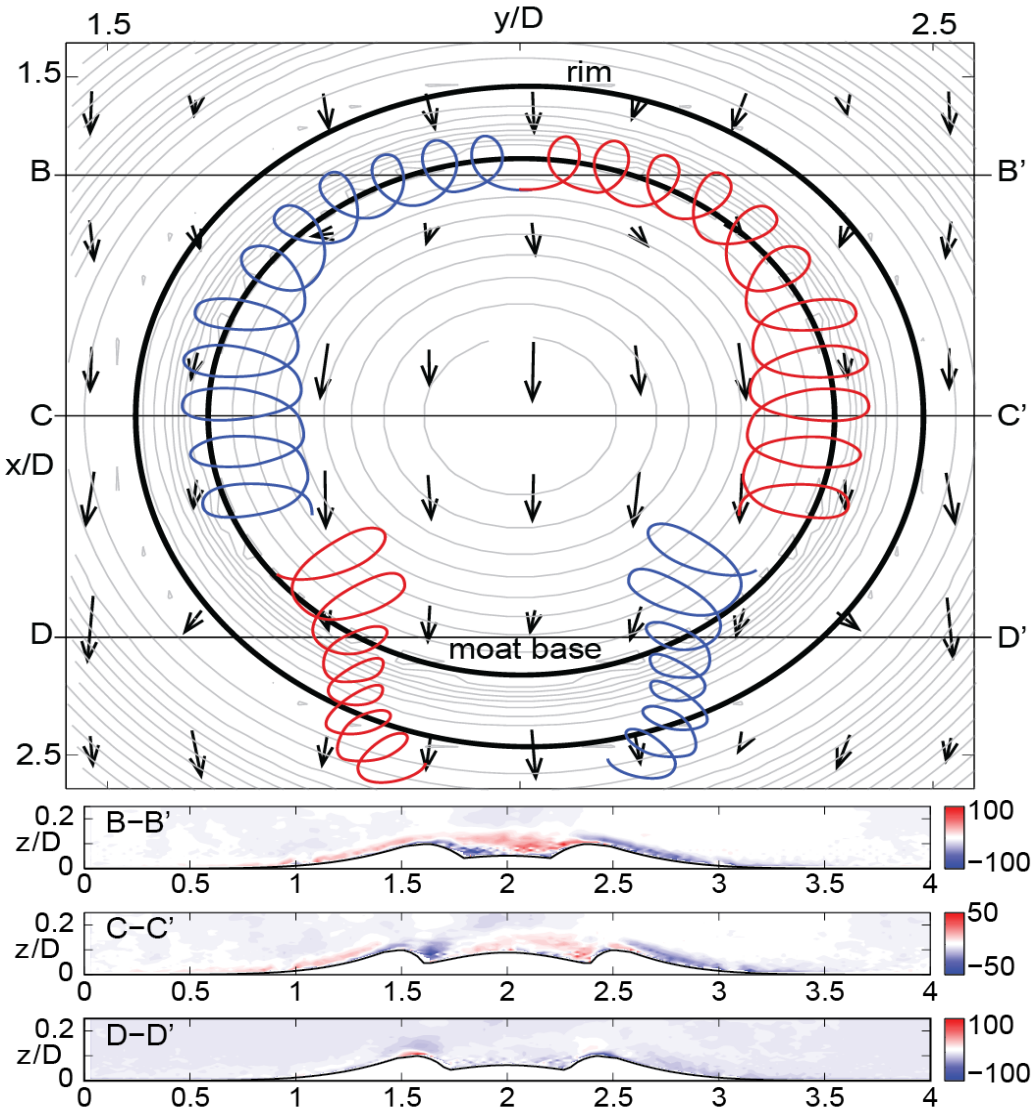

Figure 5.2: Secondary flows responsible for early-moat erosional stage crater. Top image is a sketch of plan-view crater topography (indicated by thin gray elevation contours with dark black lines defining the rim (outer) and moat bottom (inner)). Arrows added to illustrate the time-averaged vector field of flows across the crater. Flow is relatively streamlined, but deflected slightly around the mound on both upwind and downwind sides. Schematic of counter-rotating, quasi-streamwise vortices flanking the mound are superimposed, showing how helical spirals establish in the widening moat (lines colored by anticipated streamwise vorticity, where red and blue denote positive and negative, respectively). x, y, and z are normalized by the crater diameter (D). Note also that top panel includes transects B-B' C-C' and D-D'. The bottom panels show associated cross-sections with time-averaged streamwise vorticity from LES. Color contours indicate sign and magnitude of streamwise vorticity. These and other visualizations were used to develop the conceptual model of vortical, secondary flows associated with aeolian erosion driving deflation of the moat.

transport form in the crater interior, suggesting erosion would proceed along the rim. Because mobile grain size was always higher in crater interiors than on the downwind exterior, sediment of a given grain size would not be transported smoothly from interior to exterior, but only during high winds could the largest grains be evacuated out and away from the crater. Until these high wind events, sand would remain mobile in the crater interior, eroding existing strata, eroding grains themselves, and organizing sand into bedforms. In the modeled stages with mounds, grain mobility was lowest in the lee of the mound. This would be the expected location of any sediment accumulation.

Differences in competence between the erosional stages further demonstrate a positive feedback between erosion and morphological evolution of the interior layered deposit (Fig. 5.3). As the interior layered deposit erodes, the grain size that can be mobilized around the deposit increases, allowing for more abrasion and erosion. Competence on the downwind crater exterior also increases with progressive erosional stage, allowing for new sediment generated by abrasion to be transported away from the crater. Were mobile grain sizes to decrease as erosion progressed, the simulations would indicate a stabilizing feedback of decreased excavation, and aeolian erosion would become an unlikely mechanism for the observed morphological change. Instead, the simulation suggests erosion is initiated near the crater interior rim, creating a moat that concentrates deflected flow. Turbulent vortices trap and transport sand through the moat, abrading the central deposit and causing it to become a streamlined mound that retreats to the center until all material is eroded away.

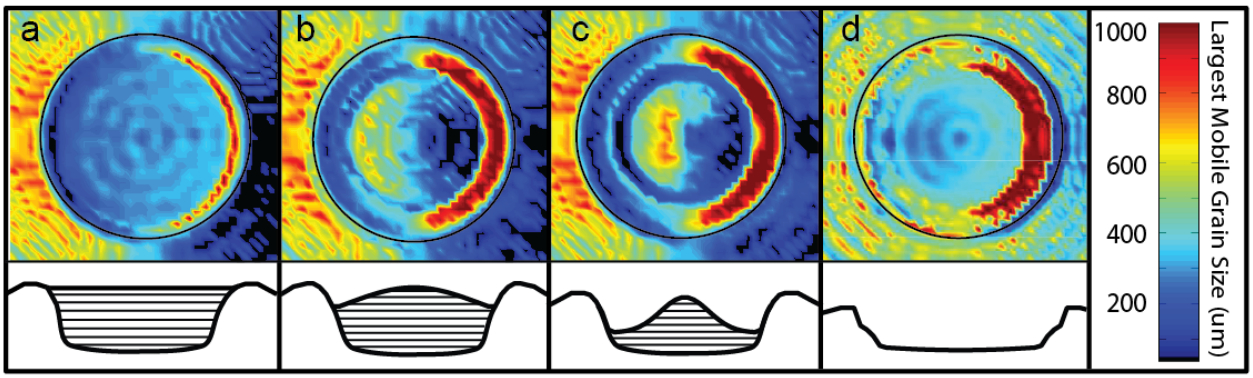

Figure 5.3: LES-derived Competence maps for representative erosional stages. The largest grain size transported in 15 m/s winds at 1 m bed-elevation was calculated for the spectrum of modeled morphologies. Schematic cross-sections of each stage are shown below plan-view competence maps. For reference, the crater rim is shown in black circle in upper panels. Wind is from left to right. Transport is highest where flow accelerates over positive slopes. Crescent-shaped zones of increased transport suggest erosion is concentrated initially around the rim, carving out a moat. As erosion progresses (a-c) larger grains become transported, increasing potential erosion and creating a positive feedback between morphology and excavation.

5.4.2 Comparison to orbital and ground observations

Layered mound deposits of probable sedimentary origin were identified in 30 martian craters between 19 and 246 km in diameter (Fig. 5.4). While more than 30 intra-crater mounds have been identified in the literature (Bennett and Bell, 2016; Grotzinger and Milliken, 2012; Malin and Edgett, 2000), craters in this study were limited to those that exhibited a layered interior deposit with morphology along the spectrum of erosional topography (Table 5.1) (Malin and Edgett, 2000). All of the identified mounds were found on Noachian southern highland terrain. Five examples of wind-carved mounds were found in craters on Amazonian terrain, but these deposits did not exhibit layering consistent with sedimentary deposits. Instead, these craters are interpreted as a distinct class filled by more recent activity. It is noted that the erosional texture of these yardang-

cut mounds matches that of the nearby Medusae Fossae Formation (K L Tanaka, 2000), a deposit whose origin is still debated (Kerber et al., 2011; Mandt et al., 2008; Williams et al., 2013b). Potential mounds obscured by superimposed craters or their ejecta, and mounds thought to be dominantly central uplift peaks (Melosh and Ivanov, 1999) were not considered. Latitudes were confined to ±60° to exclude intra-crater mounds formed by cold-trapping ice accumulation (Conway et al., 2012) (e.g., Korolev crater; Armstrong et al., 2005), which are morphologically and genetically distinct from equatorial mounds.

Three geomorphic features serving as proxies for erosional wind regime were analyzed in this study. Yardangs, elongate forms carved into bedrock by aeolian erosion (Ward, 1979), orient parallel to the average wind direction and were found on 22 of the layered deposits. Forming over shorter time scales, dunes were found in 16 of the studied craters. Dune slipfaces are a proxy for the net-transport direction of recent winds (Rubin and Hunter, 1987a), and in 13 of the craters dunes were found at the downwind floor of the crater, consistent with LES predictions for the location of any sediment accumulation. Wind streaks form when sediment exiting craters at downwind rims produce elongate flow-parallel features identified by their albedo contrast with surrounding terrain (Edgett and Malin, 2000). Wind streaks were found associated with 13 of the studied craters, and nine of the streaks seem to originate from crater-interior dune sands. In each of the 11 craters that exhibited yardangs, dunes, and a wind streak, the recorded wind direction was in agreement across all three features. In the five craters where only two of the feature types were present, recorded wind direction was also in agreement.

The most detailed analysis of wind-generated features exists for Gale crater, where both orbital and ground data have been merged to reconstruct the wind regime (Day and Kocurek, 2016). Statistical analysis of Gale yardangs affirmed that flow was deflected around central mound topography, as here predicted by LES. While dunes in

Gale occur both upwind and downwind of the mound, and show morphologies indicating the influence of more recent katabatic winds (Day and Kocurek, 2016), their overall southward migration is in agreement with the yardang and south-extending wind streak orientation. Furthermore, ventifacts (Bridges et al., 2014), streamlined bedrock nodules (exhumed diagenetic concretions) (Stack et al., 2014), and sand shadows (Blake et al., 2013) supported inferences about wind regime made from orbital observations.

5.4.3 Global change in climate and sedimentary cycle on Mars

Over the time scale of martian geologic history, the role of craters in the sedimentary cycle of Mars has changed. Craters have evolved from being basins that served as sedimentary depocenters, trapping subaqueous and then aeolian sediments, to sediment source areas from which sand and dust are eroded and then transported out of the craters (Grotzinger and Milliken, 2012). The juxtaposition of subaqueous strata and the aridity of modern Mars invoke a dramatic change in planetary boundary conditions. More specifically, the sequence of subaqueous deposition of basal strata, followed by aeolian deposition of upper mound strata, followed by a final stage of crater-scale erosion is consistent with global desiccation.

Planet-scale desiccation would herald a period of aeolian construction as dried sediment becomes available for transport by the wind. Exposed subaqueous deposits would be reworked by the wind within craters, and sand-transporting global winds would decelerate upon entering crater topographic basins, thereby supplying the external sediment required to fill craters with aeolian strata. Over time, with available sediment increasingly housed within craters and other sinks, and sediment supplies from subaqueous deposits exhausted, winds become increasingly under-saturated and the wind regime shifts from depositional to erosional (Grotzinger and Milliken, 2012). Moreover,

with the onset of aridity, chemical weathering greatly diminishes and slow physical weathering dominates, resulting in a reduction of global sediment production. Within these new planetary boundary conditions, erosion of strata housed in craters begins through abrasion by grains in transport, with sediment transported from craters and with increasing loading of the global dust budget. This progression is common in terrestrial basins (Kocurek and Lancaster, 1999), but would represent a planet-scale event on Mars.

The timing of the postulated global desiccation event can be bounded using the distribution of the observed deposits. Intra-crater layered mounds of probable sedimentary origins are distributed across all longitudes of the southern highlands, but limited to Noachian terrain (Fig. 5.4) (Tanaka et al., 2014). While the deposits themselves are difficult to date, the exclusive presence of these features on Noachian terrain suggests that the planetary phase of crater filling by sedimentary strata was not active in the Hesperian or Amazonian. This bounds the transition to some time near the late Noachian, at which point Mars is hypothesized to have transitioned from a wet planet to being aeolian dominated (Craddock and Howard, 2002; Warner et al., 2010). The presence of mound morphologies within the younger class of Amazonian craters demonstrates that the dynamic processes carving mounds are characteristic of wind and not unique to a time period on Mars. Carving the observed layered mounds via ~3 Ga of aeolian erosion is in keeping with the broader context of martian history, and explains the full range of observed deposit morphologies.

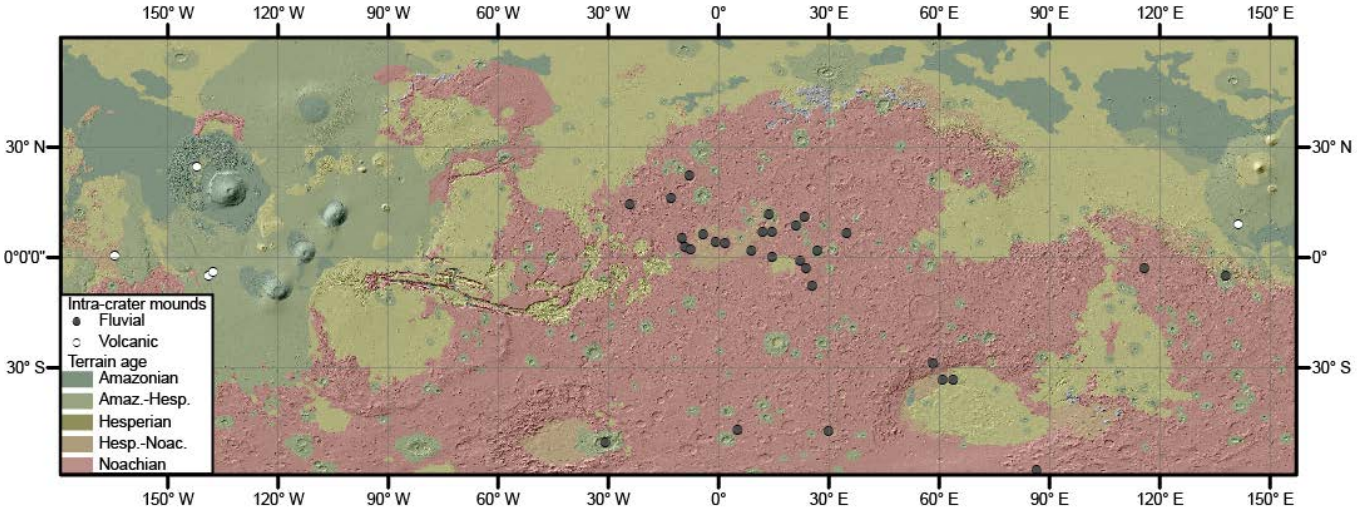

Figure 5.4: Distribution of intra-crater mounds across terrain of different ages. The most recent geologic map is color-coded by terrain age and overlain on MOLA hillshade to highlight the bimodal distribution of intra-crater mounds on Noachian (red) and Amazonian (green) terrain. Amazonian-terrain mounds are morphologically distinct from their highland counterparts.

5.5 METHODS

Martian craters with intra-crater layered deposits and mounds were identified using Viking color images, a CTX global mosaic, and HiRISE images with guidance from existing literature (Bennett and Bell, 2016; Grotzinger and Milliken, 2012; Malin and Edgett, 2000). Both wind tunnel and LES modeling analyzed crater geometries with depth-to-diameter ratios of 1:10 and 1:30 corresponding approximately to 15 km and 150 km diameter craters, respectively (Robbins and Hynek, 2012). Crater topography was modeled using smooth curves. The effects of central uplift peaks (Melosh and Ivanov, 1999) were not modeled, but uplifts would be all or mostly covered during filled, moat, and mound stages of the erosional spectrum (e.g., Gale crater). Physical experiments were conducted in a 3 x 1.5 x 0.5 m wind tunnel with 30 cm and 60 cm diameter models made from an unerodable substrate. Filled to the height of the rim with 100 μm sand (dampened for cohesion at 7:1 sand-to-water), crater models were subjected to a

Table 5.1: Craters discussed in this study

Lat (°N)	Lon (°E)	Diameter (km)	Name	Interpreted Age
24.42	217.82	29		Amazonian
21.98	351.97	148	Becquerel	Noachian
16.07	346.97	138	Trouvelot	Noachian
14.29	335.62	31		Noachian
11.49	13.49	74		Noachian
10.84	23.34	165	Henry	Noachian
8.93	141.27	50		Amazonian
8.54	20.93	73		Noachian
6.70	11.82	76		Noachian
6.56	14.33	63	Capen	Noachian
6.49	34.74	92		Noachian
5.91	355.55	53	Vernal	Noachian
5.04	349.86	104	Crommelin	Noachian
3.92	359.02	50		Noachian
3.81	1.56	54		Noachian
2.69	350.63	79	Firsoff	Noachian
2.12	352.16	50		Noachian
1.68	8.81	43		Noachian
1.56	26.71	93		Noachian
0.19	195.55	100	Nicholson	Amazonian
-0.16	14.35	42		Noachian
-1.12	22.11	65		Noachian
-3.02	115.74	72		Noachian
-3.12	23.64	93		Noachian
-4.27	222.28	28		Amazonian
-5.23	221.14	37		Amazonian
-5.29	137.83	155	Gale	Noachian
-7.80	25.25	90	Pollack	Noachian
-29.11	58.21	20		Noachian
-33.41	63.77	19		Noachian
-33.43	60.84	26		Noachian
-47.04	4.97	66	Asimov	Noachian
-47.59	29.76	156	Proctor	Noachian
-50.58	329.05	246	Galle	Noachian
-57.97	86.41	66	Spallanzani	Noachian

unidirectional 7 m/s wind until all filling sand was removed. LES was conducted on topographies chosen as representative of the full morphological spectrum. Resulting distributions of shear stress were then used to estimate competence using established relationships (Coles, 1956; Garcia, 2008; Kok, 2010; Shao and Lu, 2000). Because of the effects of electrostatic cohesion associated with dust transport ($d < 50$ μm) (Kok, 2010), only sand grain sizes were considered when calculating competence. See Appendix B for a detailed explanation of post-processing of LES datasets to infer aeolian processes.

5.6 Acknowledgments

This material is partly based upon work supported by the National Aeronautics and Space Administration, under Contract No. 1450036 issued through the MSLPS Program, and the National Science Foundation Graduate Research Fellowship under Grant No. DGE-1110007. High-performance computing resources were provided by Academic and Research Computer Services at Baylor University and the Texas Advanced Computing Center at the University of Texas at Austin. Authors acknowledge support from the University of Texas at Dallas, and thank Kenneth Christensen for help in early stages of this work.

Chapter 6: Observations of an aeolian landscape – from surface to orbit in Gale crater[2]

6.1 INTRODUCTION

On Earth, landscapes evolve through the interplay between tectonics, and water-dominated erosion and deposition. In contrast, Mars has generally been regarded as the most aeolian-dominated planet in the solar system (e.g., Sagan and Bagnold, 1975; Arvidson et al., 1979; Greely et al., 1999). On Earth, landscapes fashioned solely by wind action are rare. For example, although extensive aeolian dune fields blanket the modern Sahara Desert of North Africa, even a cursory examination of this landscape reveals uplands marked by erosional dendritic fluvial networks, and lowlands marked by mid-Holocene lakes and fluvial systems (e.g., Bouchette et al., 2010). Uniquely aeolian erosional and depositional features such as yardangs and dunes are well known, but sand dunes are nearly universally sourced by contemporaneous or earlier wet period fluvial systems (Kocurek and Lancaster, 1999), and yardangs are typically fashioned from lacustrine deposits (Wang et al., 2011). Similarly, although the Dry Valley of Antarctica displays a rich variety of cold-climate aeolian features (Gillies et al., 2013), the fundamental fabric of the landscape is glacial-dominated. While fluvial-dominated and glacial-dominated processes and their landscapes are well described and modeled, with the paucity of aeolian-dominated Earth landscapes, there is no comparable body of work describing landscapes that evolve where wind is the prime or sole geomorphic agent. Resurfacing by aqueous processes and tectonism on Earth precludes the formation of aeolian landscapes over geologic spans of time.

[2] This chapter was published in Icarus online in 2015 and printed in 2016. Citation: Day, M., and Kocurek, G., 2016, Observations of an aeolian landscape: From surface to orbit in Gale Crater, Icarus, http://dx.doi.org/10.1016/j.icarus.2015.09.042.

On Mars, landscapes and strata formed in fluvial, deltaic and lacustrine environments are well known from the most ancient Martian surfaces. However, beginning with global climatic change at ~ 3.5 Ga (Bibring et al., 2006), aeolian processes have increasingly dominated. In the absence of liquid water at the surface, wind emerges as the "default" global geomorphic agent, with more localized geomorphic change caused by impacts, ice, and gravity-driven slope retreat, all imprinting over a background of very slow physical weathering. Mars, therefore, may be the best natural laboratory in which to delineate the attributes of an aeolian landscape. In this study we use satellite and surface images to explore the extent to which the landscape of Gale crater is aeolian dominated, thus helping to define the attributes of such a system. The collection of aeolian features associated with Gale crater also serves to reconstruct the history of the wind regime over orders of magnitude of time.

6.2 GALE CRATER STUDY AREA AND DATA SET

The impact that formed Gale crater is estimated to have occurred ~3.6-3.8 billion years ago (Thomson et al., 2011; Le Deit et al., 2013). At 155 km in diameter, Gale crater sits just south of the dichotomy boundary near Aeolis Mensae (Fig. 6.1) (Wray, 2013). The interior of Gale is dominated by the central mound Mount Sharp (Aeolis Mons), which stands roughly 5 km high, or three times the depth of the Grand Canyon. The mound and surrounding features have been extensively mapped (e.g., Anderson and Bell, 2010; Hobbs et al., 2010; Thomson et al., 2011) and are similar to other intra-crater mounds found across Mars (Grotzinger and Milliken, 2012).

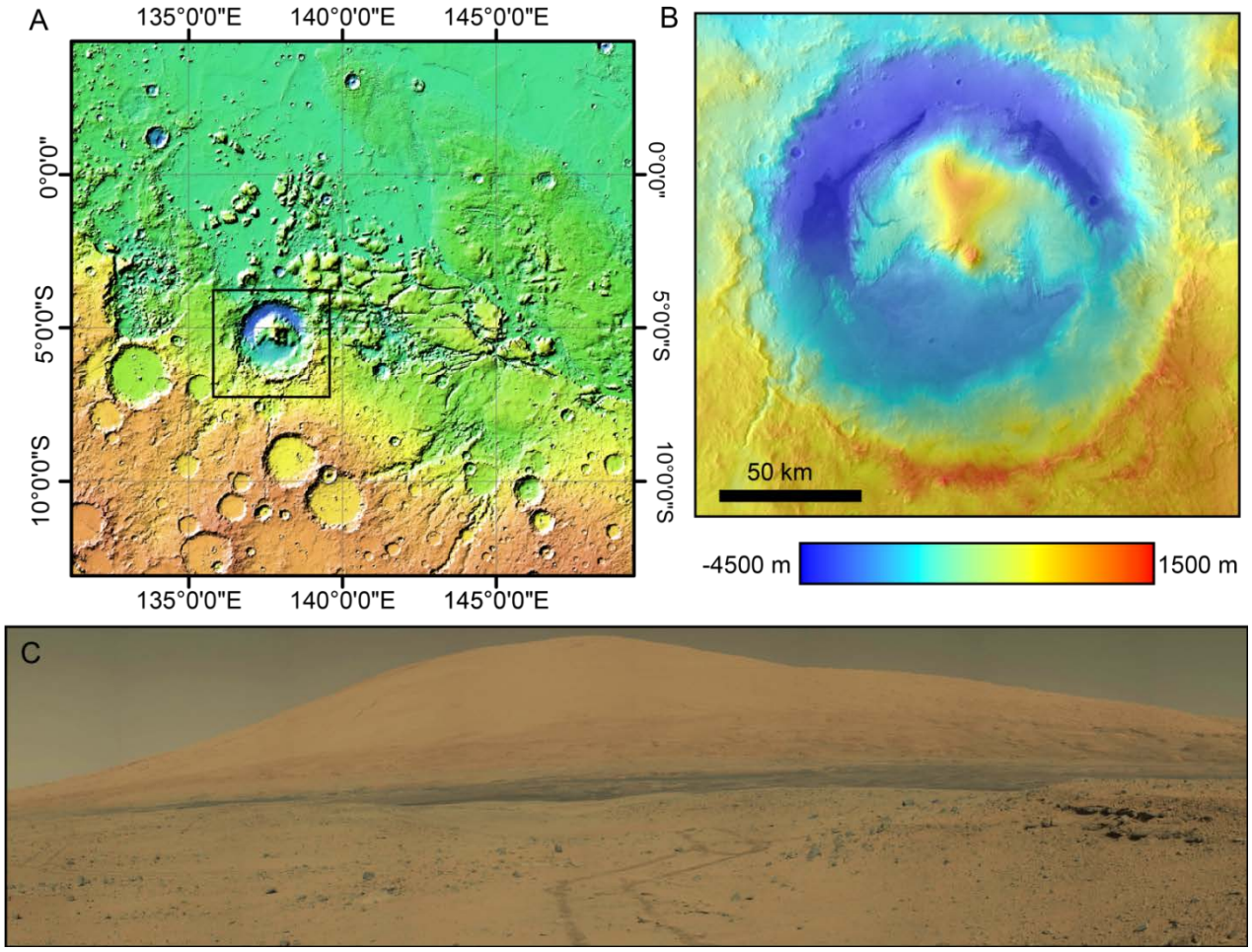

Figure 6.1: Gale crater context. (A) Mars Orbiter Laser Altimeter (MOLA) colorized elevation map showing context of Gale crater (boxed). Note the change from high elevation in the south to low elevation in the north associated with the global topographic dichotomy. (B) Gale crater shown with HRSC-derived DEM superimposed on HRSC visual basemap. The crater interior is dominated by Mount Sharp (Aeolis Mons). (C) Mount Sharp as seen from the surface by Curiosity. Foreground wheel tracks are 30 cm wide, and the total relief on the mound is ~5 km (sol 530, Mastcam mosaic starting at frame 0530ML0021050000203319E01_DRCX; all MSL data can be accessed through the JPL PDS archive).

In association with the ongoing Mars Science Laboratory (MSL) mission, an unprecedented number of images have become available for the study of Gale crater. To date, the rover Curiosity has spent over 1,000 Martian sols traversing the floor of Gale,

taking images at resolutions down to 15 μm/px (Edgett et al., 2012). Using the full range of available scales, for this study features were first mapped in orbital images using a High Resolution Stereo Camera (HRSC) basemap, overlain with higher resolution Context Camera (CTX) and High Resolution Imaging Science Experiment (HiRISE) images. Resolution ranged from 25 cm/px in HiRISE coverage, to ~10 m/px in HRSC. Surface images were then used to sample aeolian features along the Curiosity rover traverse from Bradbury Landing to Pahrump Hills (sols 1-960). Sampling every 200 to 300 m, Navigation Camera (Navcam) mosaics were used to document aeolian features in the landscape. Mast Camera (Mastcam), and Mars Hand Lens Imager (MAHLI) images were used to support identification and characterization of the aeolian features discussed below.

6.3 NON-AEOLIAN ACTIVITY IN GALE CRATER

Gale crater is fundamentally an impact crater. Smaller-scale cratering blankets the crater interior (Le Deit et al., 2013), disrupting the morphology of aqueous and aeolian features alike. Subaqueous erosional and depositional processes clearly dominated during the early crater history. Although upper portions of Mount Sharp have been speculated to be aeolian in origin (Anderson and Bell, 2010), basal portions of Mount Sharp thus far investigated are interpreted as subaqueous (lacustrine) in origin (Grotzinger et al., 2014). Moreover, the trek of Curiosity from its landing site to the base of Mount Sharp revealed deposits of conglomerates, sandstones and mudstones of interpreted fluvial, deltaic and lacustrine origins (Williams et al., 2013a; Grotzinger et al., 2014). The crater rim is characterized by dendritic channel systems, which give rise to alluvial fans (Anderson and Bell, 2010; Palucis et al., 2014). Similarly, entrenched channels emanating from Mount Sharp evidence subaqueous erosion on Mount Sharp

(Thomson et al., 2011). Subaqueous erosion and backwasting of the crater rim and central uplift, in addition to a few drainage networks that breach the crater rim, are thought to have sourced the subaqueous strata within Gale crater through a series of fluvial-deltaic systems and basinal lacustrine body (Grotzinger et al., in press).

The subaqueous history of Gale crater, however, records an ancient period on Mars with the presence of liquid water and a denser atmosphere. Crater counts suggest that the subaqueous sedimentary strata were emplaced before 3.2-3.3 Ga (Grant et al., 2014; Newsom et al., 2014). For the subsequent ~3 Ga, Gale crater has arguably been under the domain of aeolian processes, gravity-driven slope processes, and cratering. All subaqueous features are in a current state of erosion. For example, channel networks show a high albedo indicating dust mantling, inverted channels have been exhumed through wind deflation, and fan surfaces are heavily cratered (Palucis et al., 2014).

6.4 Exhumation of Mount Sharp

Although a depositional origin for Mount Sharp has been suggested (Kite et al., 2013), consistent with observations presented here, most works interpret Mount Sharp as a remnant morphology from the exhumation of a once totally filled crater (e.g., Malin and Edgett, 2000; Grotzinger et al., in press). Gale crater is one of many craters to host an intra-crater mound separated from the rim by an interpreted erosional moat (Grotzinger and Milliken, 2012). The streamlined morphology of Mount Sharp argues for N-S net transport by wind. The amount of sediment removed by aeolian deflation to yield current Mount Sharp topography can be estimated using the HRSC-derived digital elevation model (DEM). Assuming the crater was once filled to the maximum height of Mount Sharp, the removed volume was calculated as 6.34×10^4 km^3. This does not include the

volume of loose sediment in dune fields, sand sheets, transverse aeolian ridges (TARs), and dust.

Loose sediment in Gale crater is taken as largely derived from erosion of Mount Sharp and the crater rim, consistent with Tirsch et al., (2011) who suggest that intra-crater dune fields are sourced primarily from landscapes within the crater. However, because craters act as temporary depo-centers, the crater has also likely received an unknown quantity of sediment transported into the crater from external sources. Dust would be created with erosion internal to the crater, but the crater must also house dust derived from the global dust budget. In order to estimate the total volume of sediment housed in dune fields, TARs, and sand sheets, major deposits of these were mapped in the crater interior (Fig. 6.2). The total mapped surface area was multiplied by an assumed average depth (Table 6.1) and, neglecting porosity, yielded a volume on the order of 10 km^3. This volume is dominated by dune sediment, so assumptions of equivalent sand depth are not trivial. The largest and smallest barchan dunes and linear dunes in the Bagnold Dune Field were used to bracket estimates of equivalent sand thickness in the dunes. Lee slopes in this field were measured as ~30º (Atwood-Stone and McEwen, 2013; Silvestro et al., 2013) and assuming 10º stoss slopes, equivalent sand depths ranged from 3-17 m. Dune spacing is variable and exposed bedrock in interdune areas is estimated to account for ~10% of the mapped area. Taking the average estimated sand depth of 10 m and subtracting the 10% interdune area, the total sand volume is estimated as 6.44 km^3. Similar considerations were applied to TARs (5.31×10^{-2} km^3) and sand sheets (1.85×10^{-2} km^3). Varying estimates of depth and total coverage can alter the total estimate by a scaling factor, but the order of magnitude of the sand volume is estimated to remain the same. In any estimate, the amount of potentially mobile sand housed in Gale crater is relatively minor, and the crater represents an overall sand-starved system.

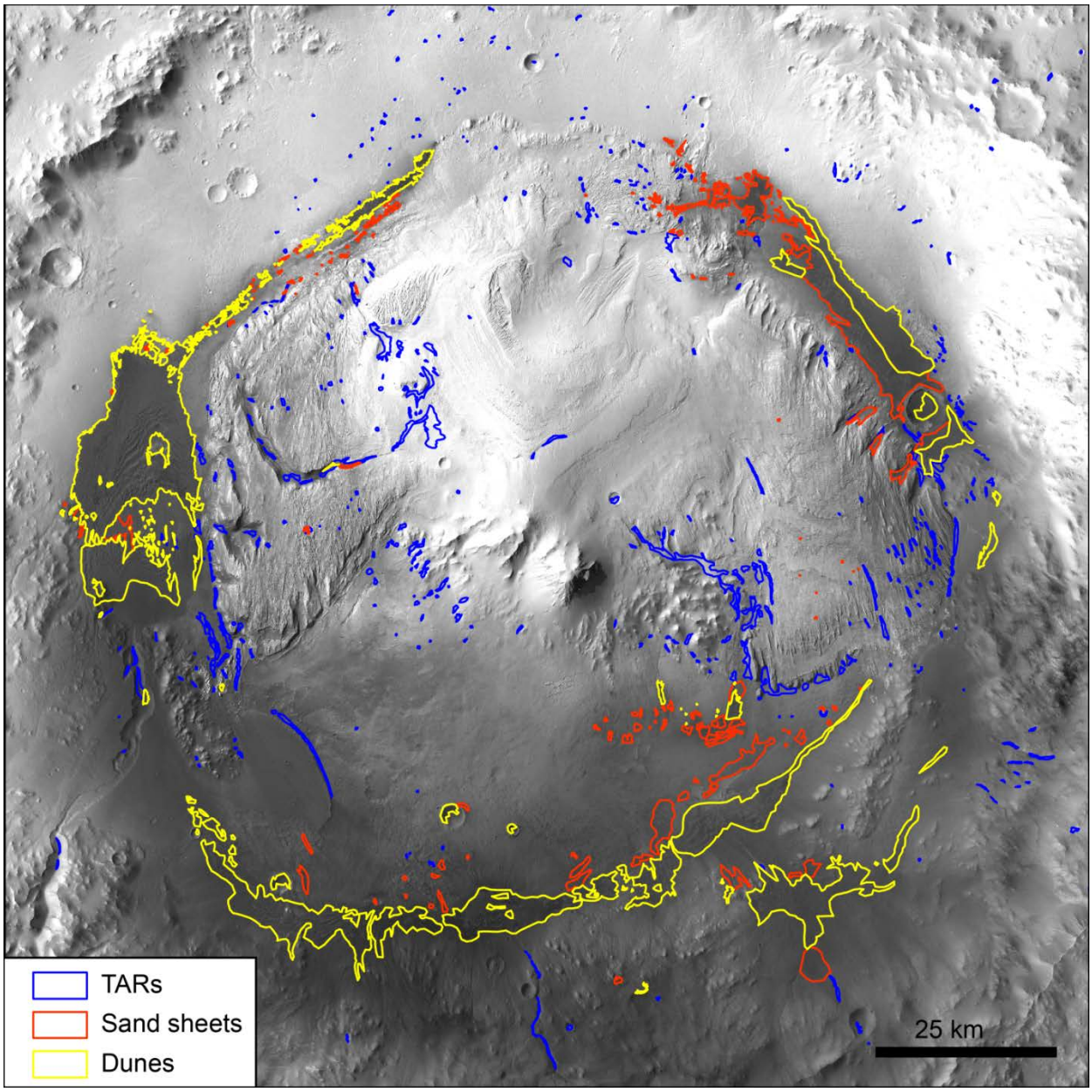

Figure 6.2: Mapped areas of dunes, sand sheets and TARs in Gale crater. Estimated total sediment volume is of order 10 km^3. See Table 6.1 for assumed average depths and surface areas. North-up oriented background HRSC mosaic of Gale crater is also used in subsequent figures (h1916_0000, h1927_0000, h4235_0001).

Estimating the volume of dust in Gale crater is less straightforward. A simple estimate can be made assuming a 1 mm thick mantling of dust across the entire surface area approximated by πr^2. This simple calculation yields a volume of 7.6 x 10^{-2} km^3, but does not take into account any surface roughness. Here roughness contributions come at a range of scales from the topography of Mount Sharp, to individual grain coatings. The total contribution of dust in Gale could be orders of magnitude higher than this simple calculation, which is given here as a conservative lower bound to the dust mantle volume.

Table 6.1: Gale crater interior loose sediment volume estimates

Sediment Type	Measured surface area (km^2)	Assumed average thickness (m)	Total volume (km^3)
Dunes	715	9	6.44
TARs	106	0.5	5.31 x 10^{-2}
Sand sheets	185	0.1	1.85 x 10^{-2}
		Total volume:	6.51

Assuming a horizontal crater floor (DTM-derived slope is <1º), the gross volume of Mount Sharp is estimated as 1.25 x 10^4 km^3. Volume occupied by a central uplift peak created during impact is unknown and here included in the Mount Sharp volume. This estimate yields a total crater interior volume of ~7.59 x 10^4 km^3, with Mount Sharp occupying 16% of the interior volume, and the remaining 84% removed. The time over which the postulated exhumation of Mount Sharp occurred is unknown, and erosion rates are expected to have varied, with significantly greater rates early in crater history (Warner et al., 2010; Grotzinger et al., in press) and very low rates currently (Golombek et al., 2010; Farley et al., 2014). An assumption of 3 Ga of excavation yields an average annual flux of 2 x 10^4 m^3/yr, whereas assuming 1 Ga yields 6 x 10^4 m^3/yr. The Namib

Sand Sea on the west coast of southern Africa houses roughly 1.02 x 10^3 km^3 of sand, with modern sand influx rates of approximately 4 x 10^5 m^3/yr (Lancaster, 1989a). Over the past 3 Ga on Mars, 60 Namib Sand Seas worth of sediment have been excavated from Gale crater, at average rates of excavation an order of magnitude lower than modern sediment influx rates seen on Earth.

6.5 ORBITAL OBSERVATIONS

Ripples, dunes, TARs, yardangs, and crater wind streaks can all be observed from orbit in Gale crater. These features exhibit morphologies characteristic of their formative wind regimes, and cover a wide range of temporal and spatial scales. Considered together, these aeolian features can be used to explore the history of sand-transporting winds spanning a significant period of the geologic past of Gale crater. Although absolute time scales of formation are unknown, relative time scales can be inferred from superposition of these features (Fig. 6.3). Ripples orient to a particular wind quickly and can be seen on dune stoss and lee slopes (Howard, 1977). Dunes, in turn, are seen migrating over TARs, which commonly form between yardangs. Finally, yardang morphology is influenced by channel topography, requiring that the channels formed first. Small crater wind streaks also serve to indicate wind direction, but were not observed in superposition with any other features. Each feature is here discussed in turn, and analyzed for a record of formative wind direction.

6.5.1 Crater wind streaks

Gale crater exhibits a low albedo wind streak that extends from the southern rim of the crater onto the surrounding plains and into Lasswitz crater (Fig. 6.4). This wind streak is ~150 km wide and ~370 km long, and is interpreted to have formed from dune sands excavated from the crater interior by northerly winds (Edgett and Malin, 2000;

Wray, 2013). Its low albedo contrasts with the bright surfaces seen in the surrounding area (Christensen, 1986), and is interpreted as an absence of dust mantling and an indication of active transport processes (Veverka, 1975). Bedforms (i.e., ripples or dunes) are not visible on the wind streak, arguing that sediment on wind streak represents a veneer too thin to be organized into bedforms visible at CTX resolution. In addition, wind speeds needed to overcome the topography of the rim and transport sand out of large craters likely occurs only during rare high-speed wind events. Given the size of the wind streak, therefore, wind streak construction must have occurred over significant time.

A separate population of much smaller wind streaks emanate from small craters (d < 0.5 km) on the southern rim of Gale crater (Fig. 6.5). These bright albedo wind streaks contrast with dark dune sands from the Southern Dunes, and are thought to form by the collection of air-fall dust in the sheltered lee of craters (Fig. 6.6) (Sagan et al., 1972). Similar wind streaks, observed near the Mars Exploration Rover (MER) Opportunity landing site in Meridiani Planum, reversed direction before and after a dust storm, suggesting constructive time scales of weeks to months (Sullivan et al., 2005). On the north, west and east Gale crater rim, where no streaks are observed, rim deposits are homogenous in their light tone, thus preventing definition of any dust-mantle wind streaks. On the south rim, measurements of 180 high albedo wind streaks yielded an average orientation of 351° interpreted to form from southerly (171°) winds (Fig. 6.6B, Table 6.2). The southerly winds recorded by these features are counter to the dominance of northerly winds observed elsewhere, but match observations in the Southern Dunes discussed below.

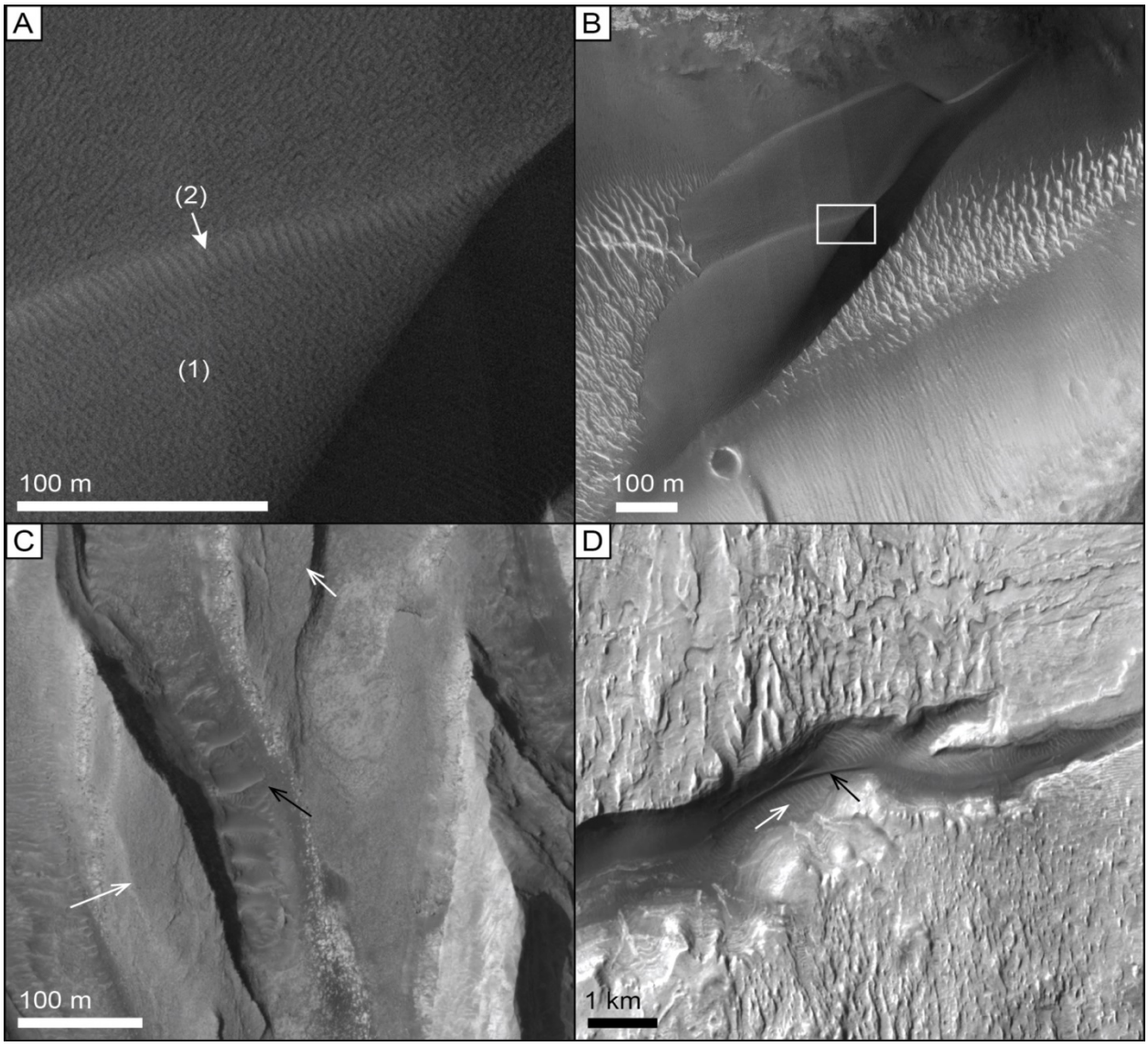

Figure 6.3: Superposition of aeolian features. (A) Ripples superimposed upon the stoss (1) and lee (2) surfaces of a dune. (B) The same dark dune migrating over light toned granule ripples or small TARs. White box indicates position of (A). HiRISE image PSP_006143_1745. (C) TARs (black arrow) positioned between yardangs (white arrows), transverse to the yardang-formative north-south wind direction. HiRISE image EPS_019698_1750. (D) Yardang field formed across a channel valley. Yardang scale and spacing changes dramatically from north to south sides of valley, suggesting that flow disturbance associated with valley topography affected yardang formation. The valley topography, therefore, necessarily predates the associated yardangs. Note also the intra-valley linear dune (black arrow) covering light toned intra-valley TARs (white arrow). HiRISE images ESP_012195_1750 and PSP_008147_1750. (A) and (B) have been contrast-stretched to increase feature definition. Locations are indicated in Figure 6.5, and north is up in all images.

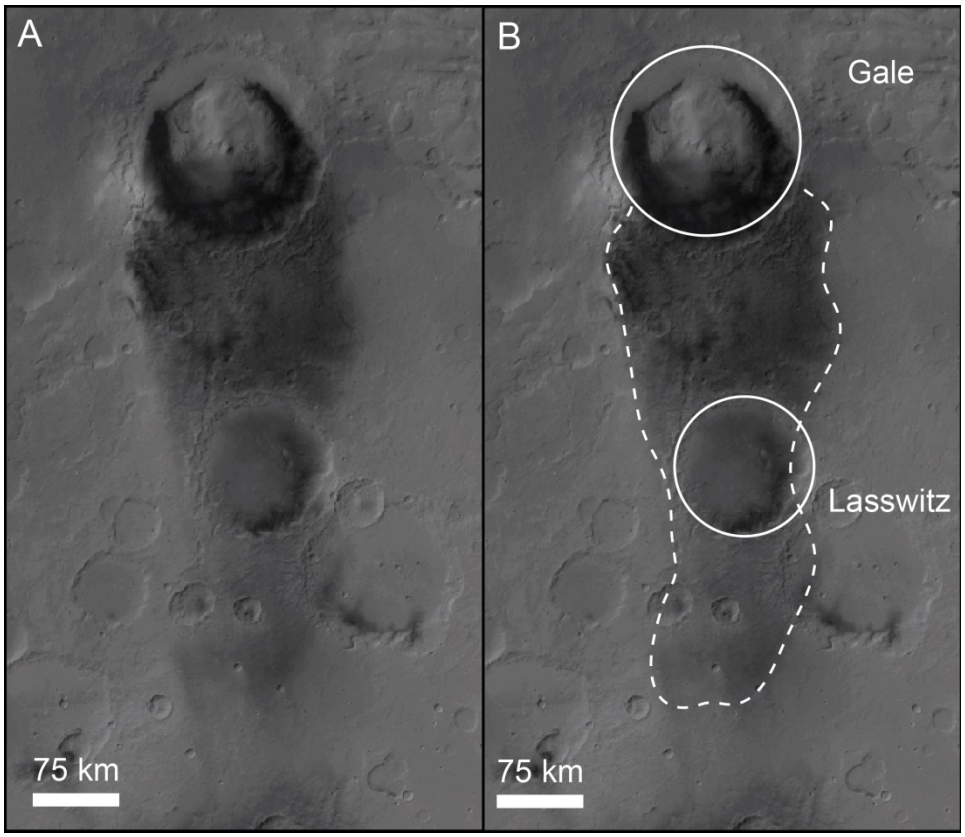

Figure 6.4: Gale crater wind streak. (A) Gale crater with its low albedo wind streak extending into Lasswitz Crater to the south. (B) Same image as (A), but with extent of the wind streak and craters shown by dashed and solid lines. North-up oriented Mars Orbiter Camera (MOC) wide angle mosaic from Aeolis (MC-23) quadrangle.

6.5.2 Yardangs

Yardangs form from persistent aeolian erosion by abrasion, causing elongate flow-parallel features to be carved out of the bedrock (Hedin, 1903). Typically occurring as fields, yardangs form slightly asymmetric morphologies, with the upwind end of the feature blunted into an inverted boat-hull shape. Because some fluvial and mass wasting processes can generate morphologies similar to yardangs (Ward, 1979), features associated with sinuous channels, or headward eroding canyons were not included in this study. Positive relief on both sides of the feature was also required to prevent misidentification of linear textures in layered terrain as yardangs. A perfect yardang

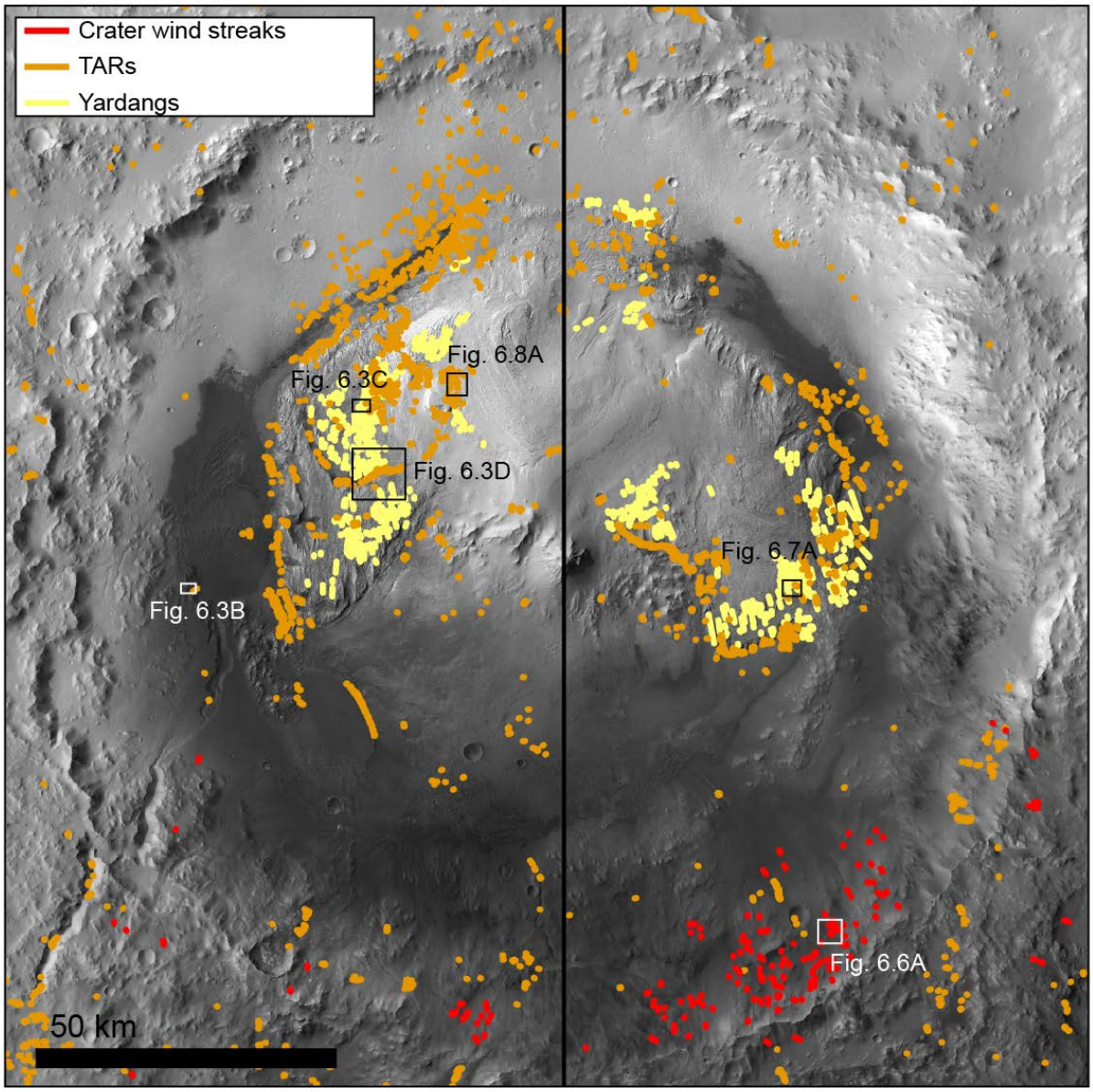

Figure 6.5: Distribution of mapped yardangs, TARs, and crater wind streaks. Yardangs are found only on Mount Sharp, and crater wind streaks are seen only on the southern crater rim. Black axial line denotes where yardangs orientations (Fig. 6.7) were divided between the two halves of the mound. Boxes over HRSC background denote the locations of panels in other figures as indicated. See Table 6.2 for detailed statistics and sample sizes of each dataset.

Table 6.2: Wind indicator sample statistics

Feature	Mean orientation (°)	Standard deviation (°)	Min length (m)	Max length (m)	Mean length (m)	Standard deviation (m)	Sample size (n)
Crater wind streaks	351	33	66	962	206	141	180
Yardangs – east	347	24	60	4340	530	508	329
Yardangs – west	359	13	33	1320	349	240	440
TARs total	88	47	9	876	124	103	3222
TARs major	71	24	9	721	125	106	2047
TARS minor	337	22	10	650	93	89	1175
Sand shadows	189	0.5	0.12	3.74	0.59	0.34	69

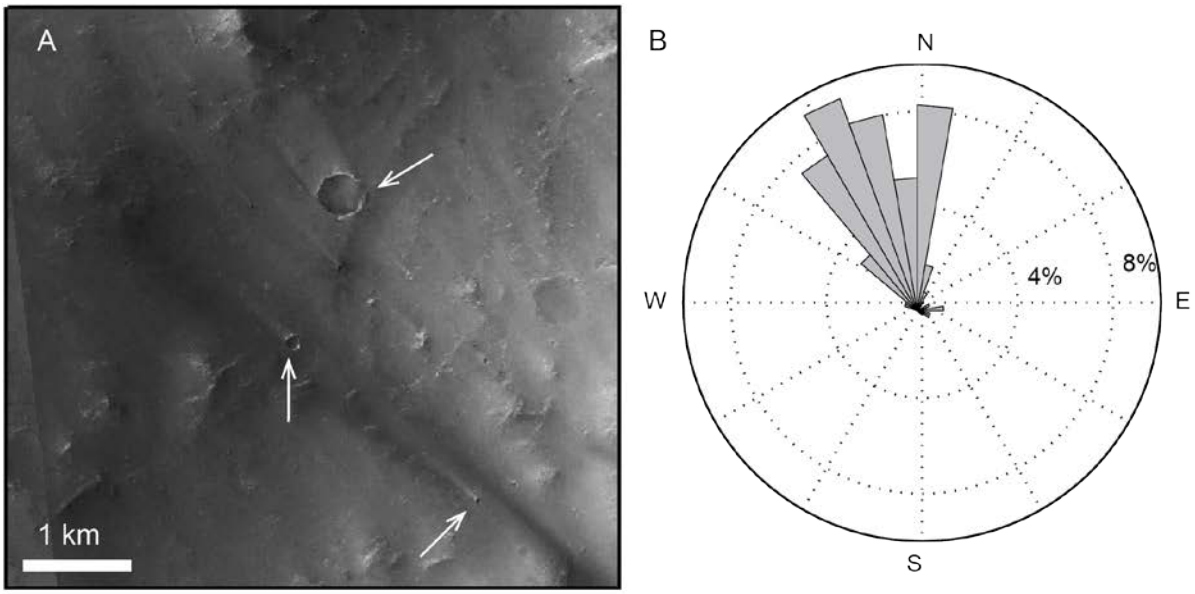

Figure 6.6: Southern rim wind streaks. (A) Small crater wind streaks on the southern Gale crater rim. Arrows indicate just a few of the craters with NW trending streaks in this scene. Image is contrast-stretched to make streaks more visible (CTX image P01_001554_1745_XI_05S221W, north-up oriented). (B) Histogram of orientations of mapped crater wind streaks. Mean orientation (351º) is interpreted to form from southerly (171º) winds.

would indicate an absolute wind azimuth with its blunted upwind hull, but the yardangs observed on Mars commonly do not exhibit this classical asymmetry (Fig. 6.7). This study, therefore, considers yardangs to be 180º ambiguous indicators of wind direction.

Locations and distributions of yardangs mapped in this study (Fig. 6.5, Table 6.2) correspond well with independent mapping of Mount Sharp (Anderson and Bell, 2010; Thomson et al., 2011). The presence of yardangs on Mount Sharp and the general absence of well-defined yardangs elsewhere imply that the strata of Mount Sharp are fine-grained and not strongly cemented. Ranging from 33 m to 4.3 km in length, yardangs are elongated N-S with a mean orientation of 354°. Dividing yardangs between the east and west sides of Mount Sharp (Fig. 6.5) yields two statistically distinct populations of yardangs with means differing by 12° (Fig. 6.7, Table 6.2, t-test, $\alpha < 0.01$). This variation could be explained by large-scale flow divergence of northerly winds around Mount Sharp.

6.5.3 Transverse aeolian ridges

The term “transverse aeolian ridge” (TAR) describes Martian bedforms with size and morphology intermediate between ripples and dunes (Fig. 6.8) (Wilson and Zimbelman, 2004). Most commonly found in Martian equatorial regions, TARs form symmetric linear ridges with wavelengths between 20 and 60 m (Wilson and Zimbelman, 2004; Zimbelman, 2010). TARs are distinguished from dunes by high albedo, linear crests, lack of activity, and symmetric cross-sectional profiles (Shockey and Zimbelman, 2013). TARs are distinguished from sand shadows by scale and lack of an upwind obstacle, and from ripples by scale, context, and albedo. TARs are commonly found in topographic lows, and are thought to align normal to their formative wind direction (Balme et al., 2008). The formation mechanism of TARs is still debated, with

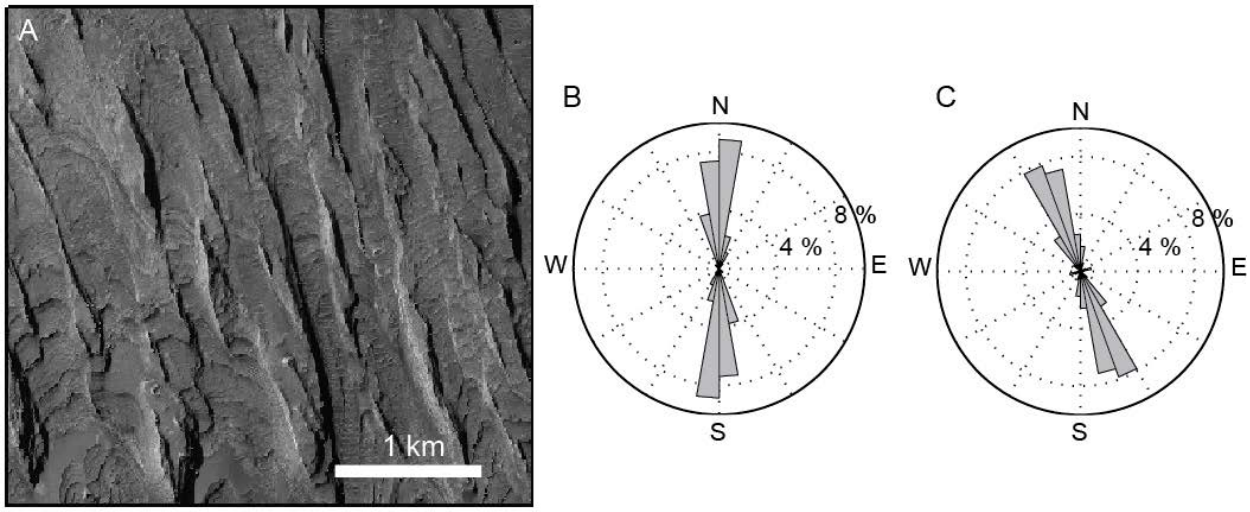

Figure 6.7: Yardangs. (A) Yardangs in Gale crater. These elongated erosional forms have tapered ends and typically form in groups (Ward, 1979). HiRISE image ESP_018643_1745 is oriented north up. (B-C) Yardang orientations measured on the west (B) and east (C) sides of Mount Sharp (Fig. 6.5). Orientations are shown symmetric to account for 180º ambiguity in formative wind direction. The two sides are statistically distinct and the 12º difference in mean orientation is interpreted to result from flow divergence around Mount Sharp topography.

hypothesized terrestrial analogs including granule ripples, reversing transverse dunes (Zimbelman and Scheidt, 2014), anti-dunes (Geissler, 2014), and megaripples (de Silva et al., 2013; Sullivan et al., 2014). To date, lateral migration of TARs has not been observed. Recent work on armored granule ripples in South America has suggested that TARs may be aggrading through the capture and infiltration of dust (de Silva et al., 2013; Bridges et al., 2015). Gravels armoring terrestrial "megaripples" are too large to be transported off the bedform by wind, but can still trap passing finer material. These fines are kinetically sieved downward as gravels vibrate during wind events, raising the bedform surface. This process is suggested as an analog for TAR aggradation on Mars.

Mapping of TARs in Gale crater (Fig. 6.5, Table 6.2) found that they most commonly form in local topographic lows (e.g., in channels, between yardangs, and in small craters) where flow is directed by topography. TAR morphologies were dominantly simple (linear) and forked (Balme et al., 2008), but networked morphologies, marked by a plaid pattern of crossing ridges, were seen in HiRISE at the northern base of Mount Sharp. The observed TARs were predominantly confined, enclosed on all sides by topography, or controlled, forming in association with less than circumferential topography (Balme et al., 2008). Some TARs formed on the crater floor and smooth reaches of Mount Sharp, independent of local topography. Ranging from 9 to 876 m long, TARs cover approximately 1% of the Gale crater interior surface, and are oriented in all directions. To prevent a premature genetic interpretation, TARs are here considered 180° ambiguous indicators of formative wind direction. The mean orientation of all bedforms is 88°, but the set of sampled TARs can be modeled as two overlapping normally-distributed populations, with mean orientations of 71° and 337° for major and minor signals, respectively (Fig. 6.8, Table 6.2). These are interpreted to correspond with primary northwesterly and subordinate northeasterly winds.

6.5.4 Dunes and ripples

6.5.4.1 Approach

Dune fields in Gale crater occur within the moat between Mount Sharp and the crater rim. These dune fields have been extensively characterized by Hobbs et al. (2010). Here we more broadly identify four morphologically distinct regions (Fig. 6.9), and independently map the orientations of dunes and dune brinklines in order to further reconstruct the wind regime in the crater interior. The most detailed analysis is for Bagnold Dune Field because of extensive HiRISE coverage (Silvestro et al., 2013).

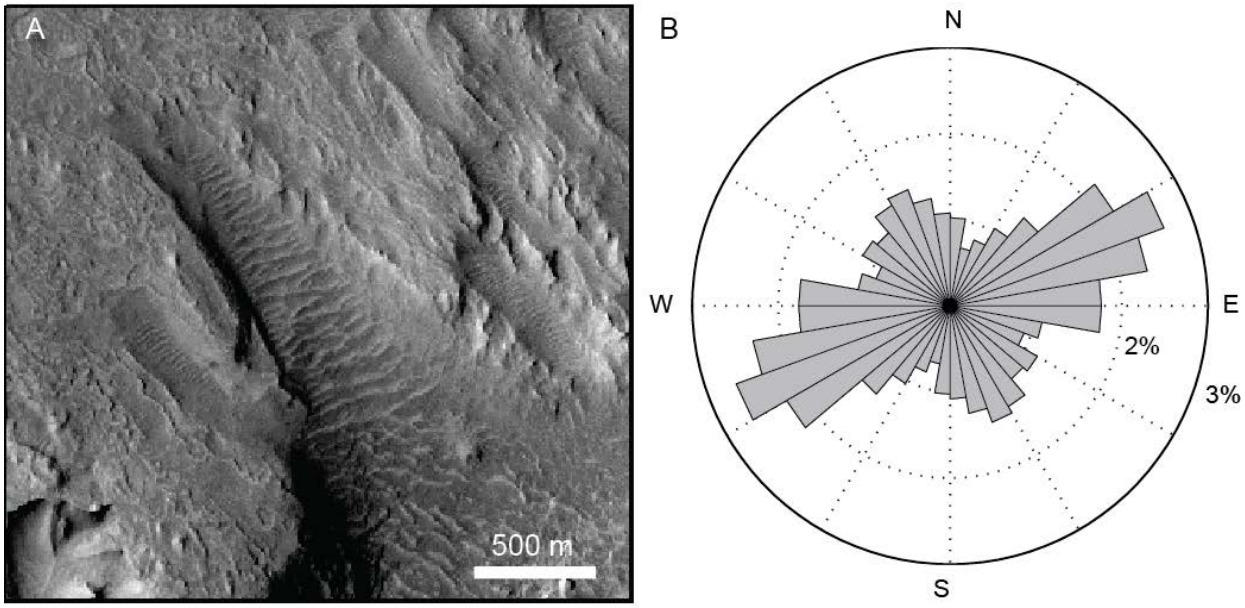

Figure 6.8: Transverse aeolian ridges. (A) TARs confined to a valley on Mount Sharp, and oriented normal to valley walls. TAR orientation is clearly dependent on local topography, making TARs poor indicators of regional-scale winds. These TARs show simple linear and forked morphologies. HiRISE image ESP_031948_1750 is oriented north up. (B) Orientations of all TARs mapped in Gale crater, symmetric to account for 180º formative wind ambiguity. Two overlapping populations of TAR orientations were modeled to have mean NE (71º) and NW (337º) trends. These are interpreted to form from dominant northwesterly (341º) and subordinate northeasterly (67º) winds similar to winds interpreted in the Bagnold Dune Field.

Analysis for the other regions is necessarily less comprehensive because of the incomplete HiRISE coverage of these fields.

This work largely concurs with the conclusions of Hobbs et al. (2010) that northerly winds dominated Gale crater and that these winds are strongly channeled by crater topography. Because dunes and ripples form from mobile sand, their morphology and orientation are thought to reflect the current wind regime in Gale crater, in contrast to features such as yardangs that require orders of magnitude more time to form. Where sand availability is not restricted and dune reconstitution time is longer than cycles in the wind regime, dune crestlines are oriented to be as perpendicular as possible to all components of the wind regime, the gross bedform-normal orientation of Rubin and

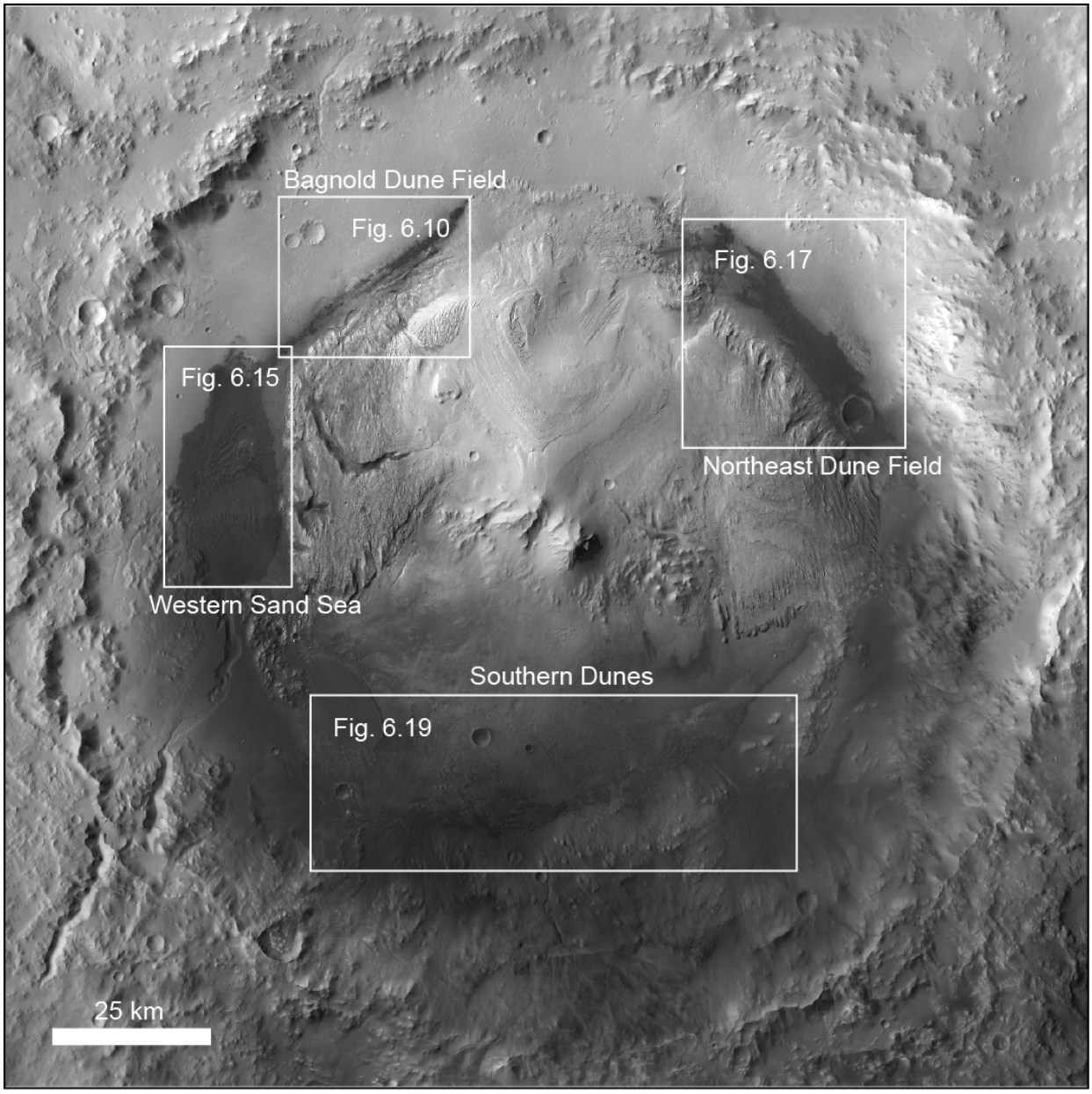

Figure 6.9: Morphologically distinct dune regions discussed in Section 6.5.4. White boxes indicate the named dune fields and extent of corresponding context images. Note that the fields are all circumferential to Mount Sharp and associated with steep slopes of either Mount Sharp or the southern crater rim. Background HRSC mosaic.

Hunter (1987). Where sand availability is restricted, as is commonly the case on Mars, dunes elongate in the mean transport direction from a local sand source (Courrech du Pont et al., 2014). In either case, dune crestline trend reflects the total wind regime and net dune migration direction, and not a specific wind direction except where the wind regime is essentially unimodal. Wind ripples, because of their small size and shorter reconstitution times, are more apt to show the last significant wind event, but their orientation is also strongly affected by dune topography (Howard, 1977).

6.5.4.2 Bagnold Dune Field

The Bagnold Dune Field is situated along the upcoming Curiosity traverse, and will be the location of the first surface observations of active Martian dunes. Orbital measurements yielded ripple and dune migration rates in this field of 0.66 m/yr and 0.4 m/yr, respectively (Silvestro et al., 2013). This long and thin field runs 30 km along the northwest basal margin of Mount Sharp, and averages 1 km wide. Following the field from NE to SW, the dune field features a 16 km long main section of well-defined duneforms, followed by a 9 km stretch of bypass where dunes are mostly absent, finally ending in a 5 km long set of re-formed barchan dunes (Fig. 6.10A).

Dune morphologies in the Bagnold Dune Field range from barchans along the NW margin to linear dunes in the interior (Fig. 6.11). Small symmetric barchans (100-150 m wide), seen in isolation at the NE end of the field, laterally link with other barchans as they migrate downwind, forming asymmetric dunes as one arm elongates to the SW (Fig. 6.12A). These elongate arms extend and connect with other defect arms downwind to form chains that coalesce into the SW-NE trending linear dunes (Fig. 6.12C). Near the beginning of the field these linear dunes (0.5-1.5 km long) are asymmetric, with steep SE-facing slopes (Fig. 6.12C). To the SW, morphologies grade

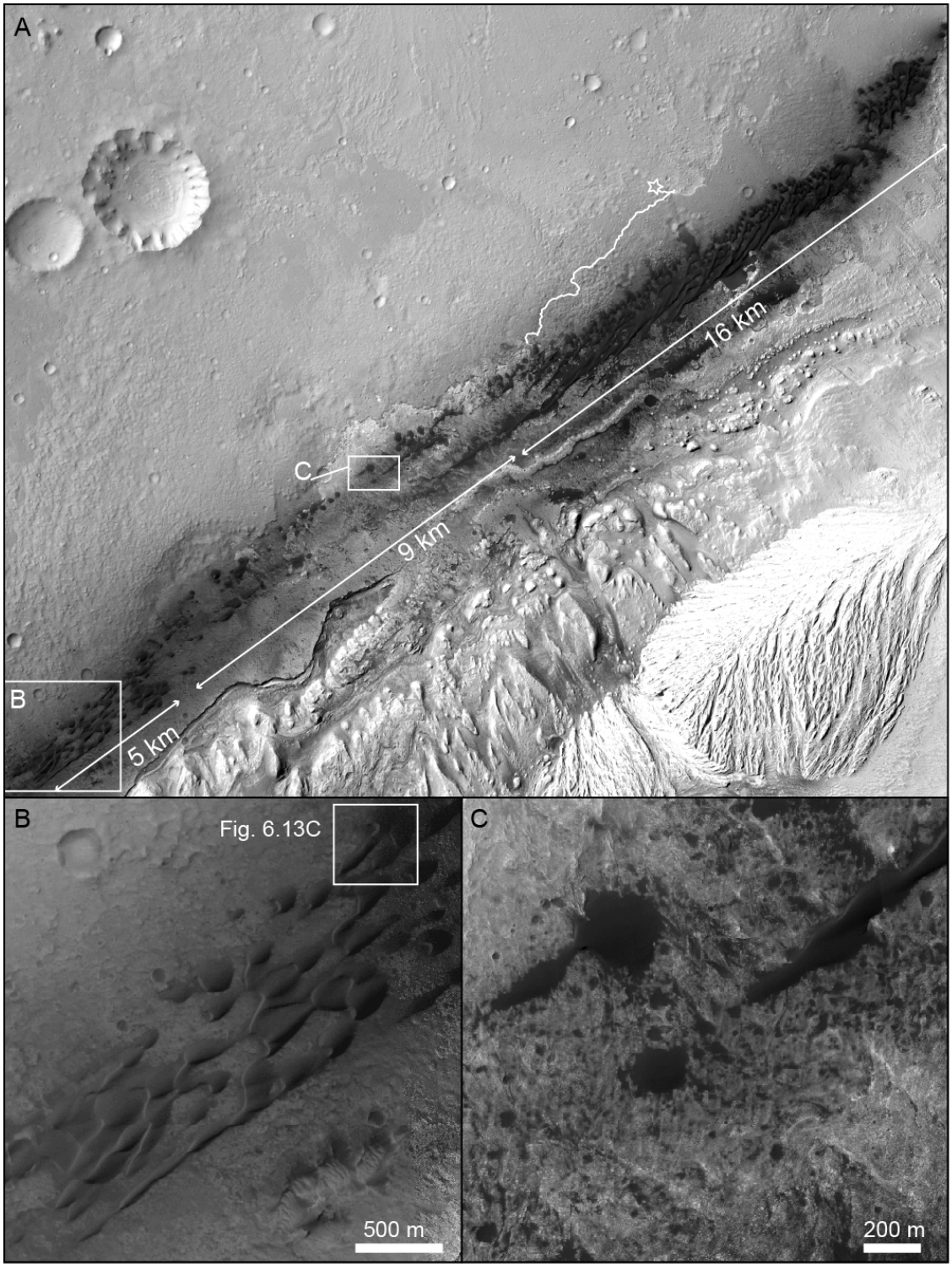

Figure 6.10: Bagnold Dune Field

Figure 6.10. Bagnold Dune Field. (A) HiRISE mosaic of the Bagnold Dune Field showing three regions discussed in Section 6.5.4.2. The main area is 16 km long and houses the majority of the dunes. The middle 9 km region is sediment-starved, featuring only sparse bedforms and sand sheets that fill topographic lows. The final 5 km is dominated by asymmetric barchans interpreted to have reformed from sediment sourced from the main field. White boxes show the locations of (B) and (C). The Curiosity landing site and traverse through sol 960 are given by the star and white line, respectively. (B) Southwest end of the Bagnold Dune Field where SW-facing (Population 2) slipfaces dominate and SE-facing slipfaces (Population 1) are mostly absent. White box shows the location of Figure 6.13C (HiRISE images ESP_025790_1750 and ESP_012841_1750). (C) Sand-starved duneforms in the middle region of sediment bypass. This contrast-stretched image shows the tail end of a linear dune (right) and a tear-drop dune (left) dying out as they migrate to the southwest. Circular dark patches in the image are sand sheets filling small craters (HiRISE image ESP_028823_1755). North is up in all panels.

into symmetric linear dunes (Fig. 6.12B), and even reverse to have sharper NW-facing slopes (Fig. 6.12D), arguing for formation by barchan arm elongation in bimodal winds (Bourke, 2010). Rippled sand sheets make up the interdune areas between linear dunes, and ripples observed on linear dunes crests are parallel to the dune ridge (Fig. 6.12E).

Focusing on the barchan dunes, in all regions the interdune areas between barchans are dominated by exposed bedrock and light-toned granule ripples (Fig. 6.13A). The isolated symmetric barchans near the beginning of the field exhibit a single sharp brinkline and SE-facing slipface. If the reconstitution time of the barchan dunes is longer than the wind alternation time, multiple slipface orientations could be preserved on a single barchan form. The “tear drop” morphology, where two slipfaces are bisected by an elongating arm, has been modeled to form in bimodal wind regimes with a divergence angle of at least 100º (Parteli et al., 2009), and is seen in abundance on Mars (Hayward et al., 2014). In the Bagnold Dune Field, tear-drop dunes form downwind of symmetric barchans in the main section of the field with SE- and SW-facing slipfaces (Fig. 6.13A). SE-facing slipfaces (Population 1) have sharp brinklines and smooth (non-rippled) lee

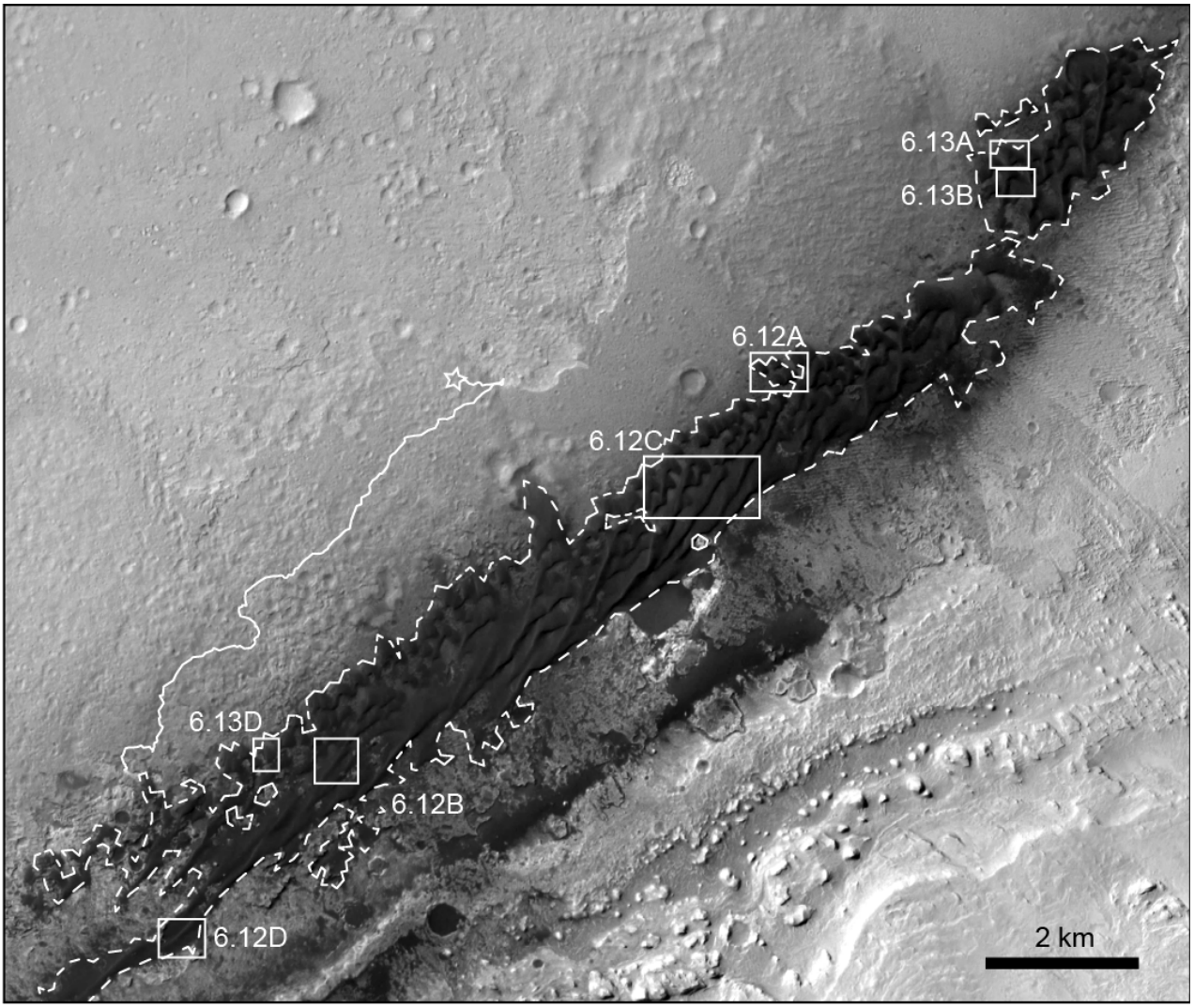

Figure 6.11: Northern Bagnold Dune Field. This north-up oriented HiRISE mosaic of the main section of the Bagnold Dune Field shows locations of panels in Figures 6.12 and 6.13. White star and line indicate the Curiosity landing site and traverse. Dashed line corresponds to the dashed line in Figure 6.14 and marks the dune-dominated surface used in this region to estimate loose sediment volume (Table 6.1).

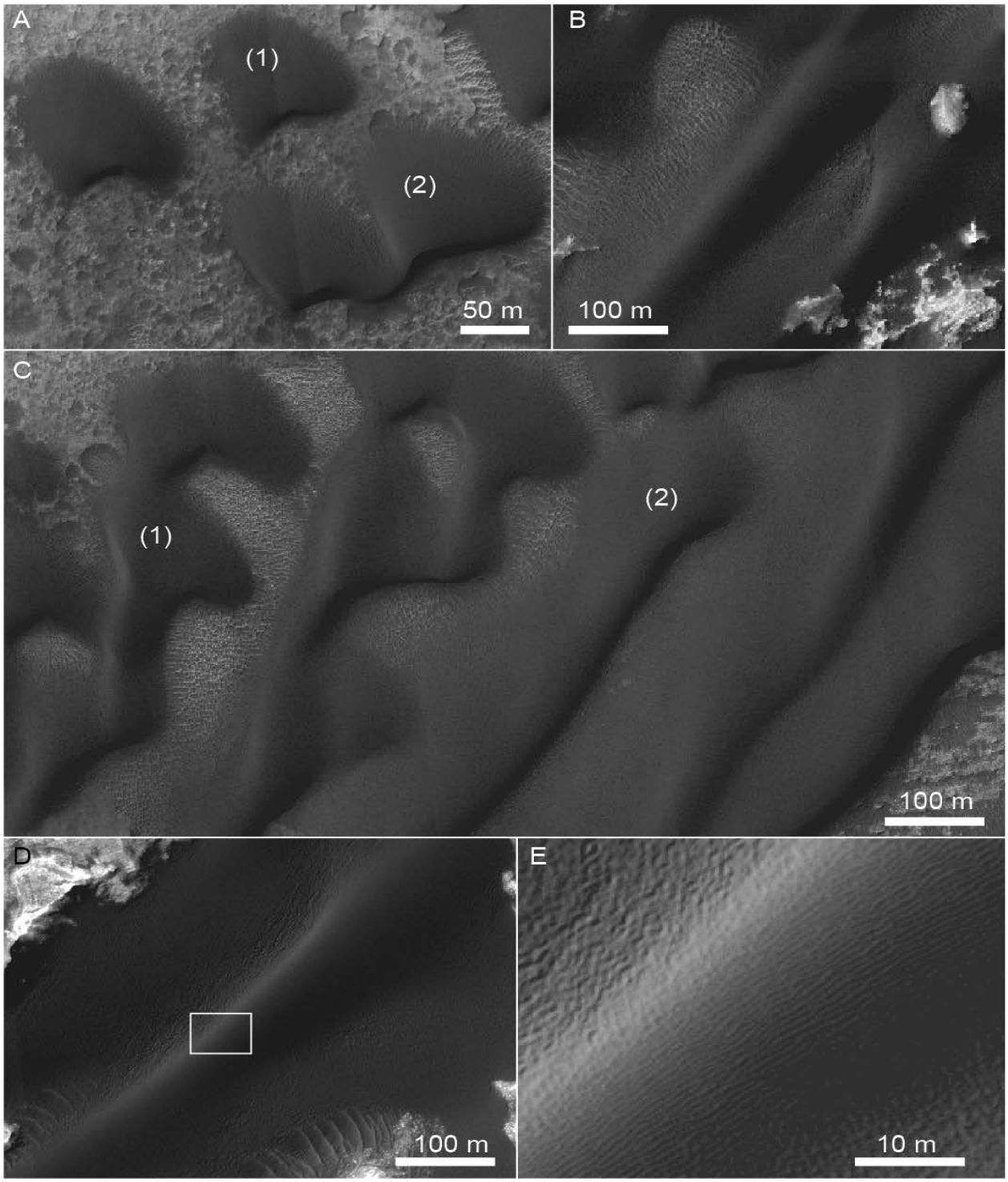

Figure 6.12: Dune morphologies in the Bagnold Dune Field.

Figure 6.12. Dune morphologies in the Bagnold Dune Field. (A) Symmetric barchans (1) migrate and link to become asymmetric barchans (2). (B) Symmetric linear dune from the middle of the main section with equally defined slopes to each side of the crestline. (C) Progression of dune morphology from west to east in the dune field. Barchans link defect arms downwind to form chains of elongations to the south and southwest (1). Chains become linear dunes, here asymmetric with SE-facing steeper slopes (2). Note how the linear dunes become detached from formative barchans. (D) Reversal on linear dune in the SW of the field to have a sharper NW-facing slope. White box shows the location of (E). (E) Ripples on the linear ridge aligning parallel to ridge direction. Images have been contrast stretched to bring out albedo variation, and north is oriented up in all panels. HiRISE images ESP_024023_1755 (A and C), ESP_033649_1750 (B, D and E).

surfaces interpreted as grainflow deposits and are hereafter designated the primary slipface population (Fig. 6.13B). The grainflows seen on these slipfaces indicate formation transverse to flow (±20º) (Eastwood et al., 2012). Ripple orientations on dune stoss slopes align roughly parallel near the dune crest with these sharp slipfaces (Fig. 6.14A). The SW-facing slipfaces (Population 2) are distinctly different. Hereafter referred to as the secondary slipface population, these slopes exhibit superimposed ripples migrating across and reworking the steep deposit (Fig. 6.13B). Sharp brinklines are absent on secondary lee faces, and no grainflow deposits were observed.

The relationship between the two slipfaces changes along the dune field. The primary slipfaces are the most prominent in the NE of the field, and the secondary slipfaces become dominant as one follows the field to the SW (Figs. 6.13D, 6.13C). Rather than a sharpening of the secondary lee faces, this transition occurs as a gradual disappearance of the primary lee faces, which become more subdued to the SW (Fig. 6.13D). The decay of primary slipfaces roughly corresponds with a reversal of the dominant slope on the linear dunes described above. At the very SW end of the dune field, the final group of barchans is clearly dominated by the secondary slipface population. Here, SE-facing lee slopes are all but absent, and the teardrop morphology is

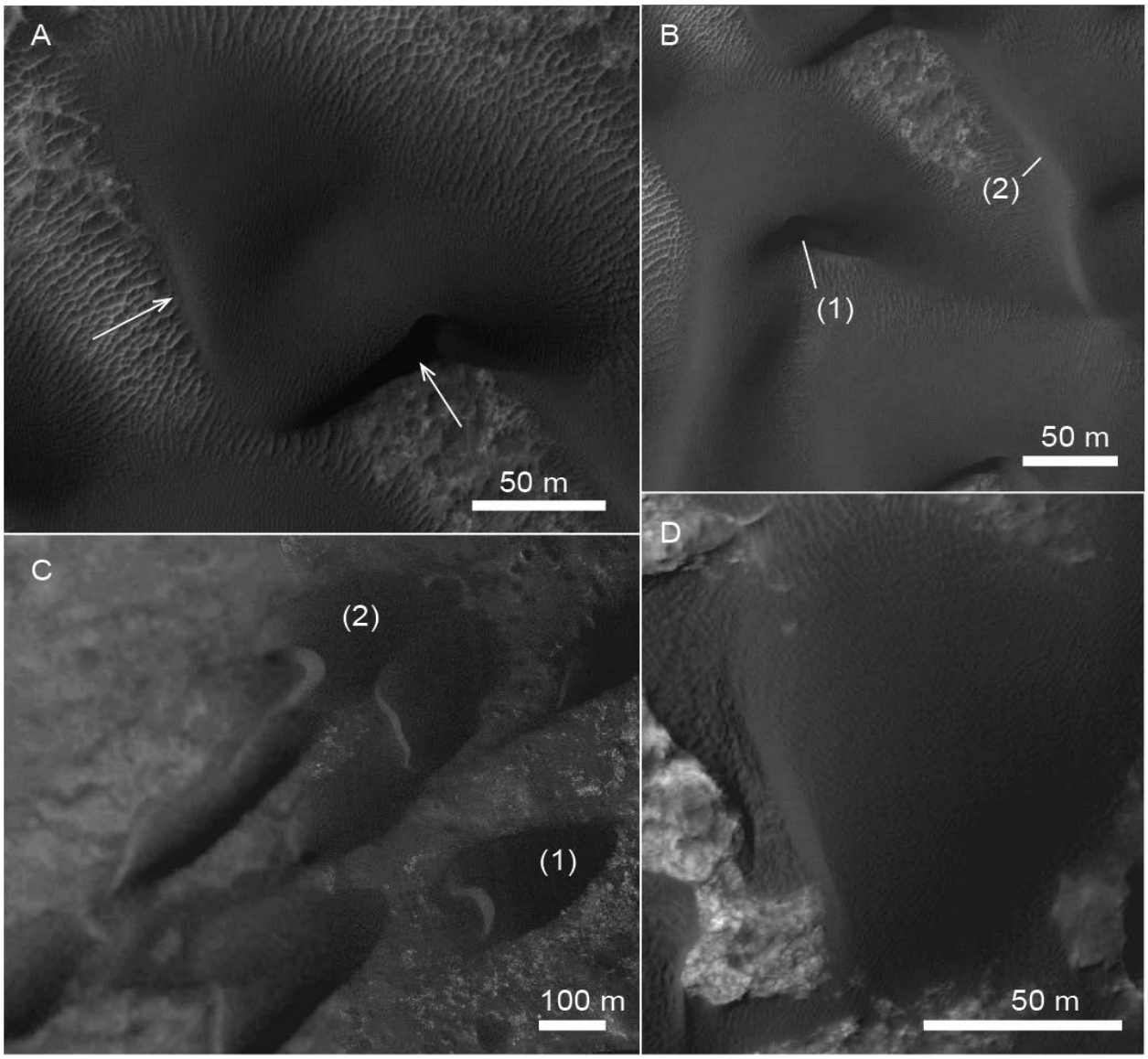

Figure 6.13: Slipfaces on Bagnold Dunes. (A) Tear-drop dune with two steep slipfaces (arrows) bisected by an elongating arm. Note the exposed bedrock and light toned granule ripples in the interdune areas. (B) Primary (1) and secondary (2) slipfaces in the NE end of the dune field (Fig. 6.11). Note the sharp brinkline in the primary face and the subdued brinkline on the secondary face. Crest and ripple orientations are mapped on this image in Figure 6.14A. A and B taken from HiRISE image PSP_009861_1755. (C) SW-migrating barchans in the SW end of the dune field. Note the symmetric (1) and asymmetric (2) morphologies and the SW-elongating arm that indicates the presence of a northeasterly wind. (See Fig. 6.10 for location) (D) Barchan dune from the middle of the field (Fig. 6.11) with no observed primary slipface, and secondary slipface similar to the morphology observed in (B). HiRISE image ESP_033649_1750. All images are contrast-stretched to bring out the variation in these dark features, and north is up in all panels.

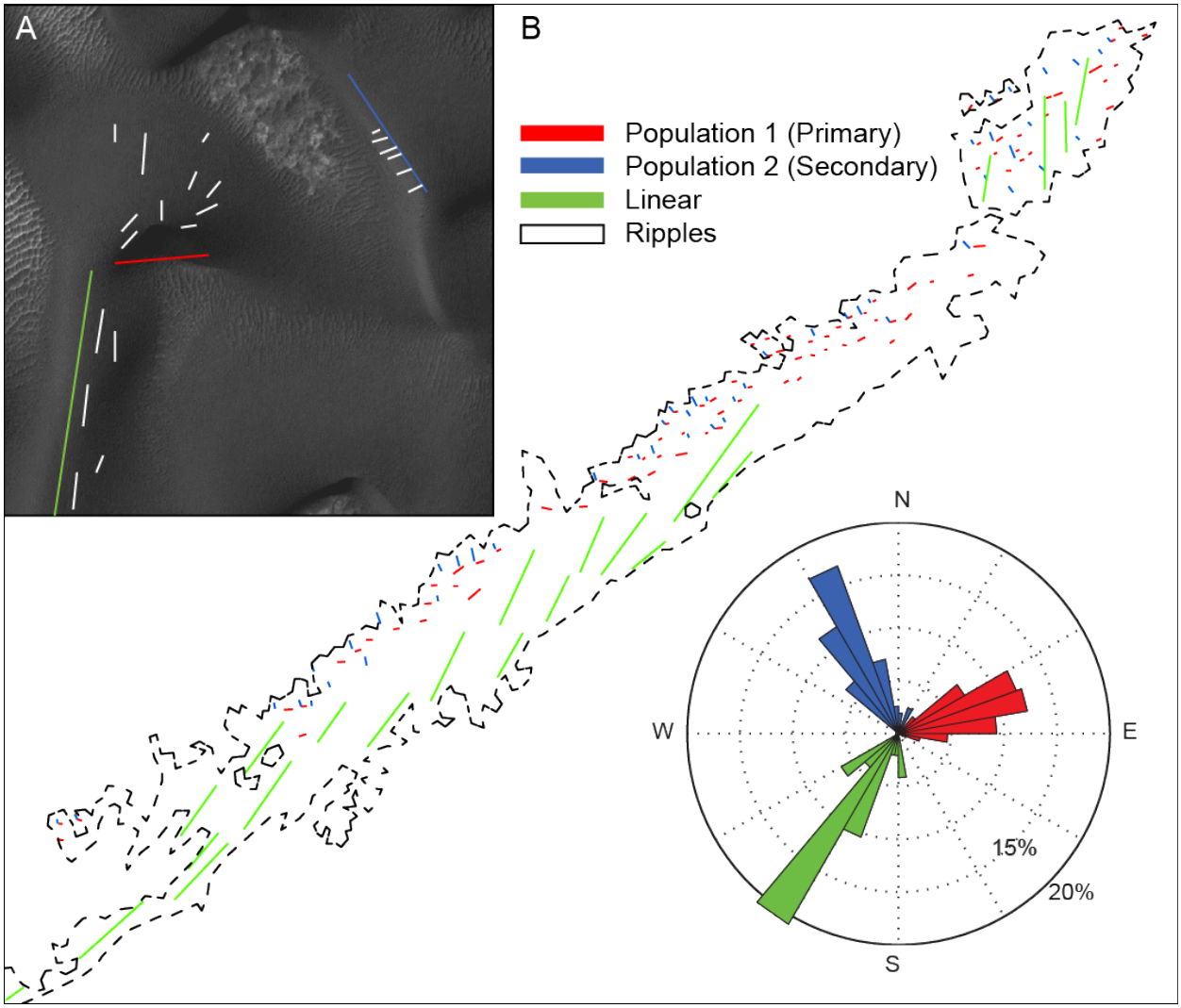

Figure 6.14: Bedform mapping in the Bagnold Dune Field. (A) Example mapping superimposed on the same image seen in Figure 6.13B. Primary brinkline trend is defined by the sharp south-facing slipface (red). Secondary trend is defined by steep lee slopes, reworked by ripples (blue). Linear dune trend is shown stemming from an elongating barchan (green). Ripple trends are shown for schematic representation of the variation in orientation with position on the dune. (B) Bedforms mapped in the main section of the Bagnold Dune Field with the same lateral coverage shown in Figure 6.11. Asymmetric barchans were also mapped in the extreme southwest, but were relatively few and are not shown here. Populations of orientations are shown in the rose diagram. Note that the primary and secondary orientations are interpreted to form transverse to winds with upwind azimuths of ~344º and ~67º, respectively.

no longer observed. Small symmetric barchans are seen migrating to the SW, and a new morphology of asymmetric barchans dominates. The southern defect arm of SW-migrating crescentic barchans elongates in the transport direction to the SW creating an asymmetric barchan with a short northern and long southern defect arm (Fig. 6.13C). The morphology of these elongated arms requires that the originally dominant northwesterly wind be still present, but now this wind is clearly subordinate to the northeasterly wind (Tsoar et al., 2004).

The orientations of the two populations of slipfaces and of the linear dunes were mapped across the Bagnold Dune Field (Fig. 6.14, Table 6.3). The average orientation of the linear dunes roughly bisects the average upwind azimuth inferred from the two slipface populations. In bimodal winds, barchan arms tend to elongate in the direction of the resultant wind vector (Tsoar, 1989). Assuming the two slipface orientations are approximate indicators of wind direction (±20º), an inversion of the theory of gross bedform normal (Fenton et al., 2014; Rubin and Hunter, 1987a), yielded a ratio of the two wind directions of ~1.3. The dominant wind direction is therefore interpreted to be from the NW (337º), and the subordinate direction from the NE (74º). This interpreted bimodality is consistent with recent modeling results of barchan morphologies formed in bimodal winds (Parteli et al., 2014), and with the populations of mapped ripples and dunes in the Bagnold Dune Field (Hobbs et al., 2010; Silvestro et al., 2013). This simplification considers only the mapped brinkline orientations and not the observed morphological shift that suggests a change in wind dominance from one end of the field to the other.

The Bagnold Dune Field is clearly an availability-limited system (Kocurek and Lancaster, 1999). The asymmetric morphologies are consistent with bedform formation in the sand-starved “fingering mode” identified by Courrech du Pont et al. (2014).

Barchan and linear dunes have low equivalent sand thicknesses relative to other dune types (Lee and Thomas, 1995), and barchan dunes characterize areas of limited sand supply. The 9 km break in the dune field further reflects the limited sand supply in this system (Fig. 6.10C). In this zone, the dunes lose definition, shrink to small domes, and decay into sand sheets. Although the dunes evidence a clear history of sand transport, on the whole sands are being transported through this region and into the Western Dune Field, making the Bagnold Dune Field a bypass dune field rather than an ultimate sand sink.

Table 6.3: Summary of brinkline and linear dune measurements

Dune Field	Bagnold Dune Field	Western Dune Field	Northeastern Dune Field	Southern Dunes
Population 1 – Mean brinkline orientation (º)	67 - primary	35	18	339
Standard deviation (º)	15	27	33	28
Number of samples	97	553	38	120
Population 2 – Mean brinkline orientation (º)	344 - secondary	336	324	49
Standard deviation (º)	17	29	23	14
Number of samples	77	246	46	122
Population 3 – Mean brinkline orientation (º)	-	88	50	55
Standard deviation (º)	-	22	14	20
Number of samples	-	105	9	25
Mean linear dune orientation (º)	32	4	327	5
Standard deviation (º)	15	32	16	32
Number of samples	24	76	14	17

6.5.4.3 Western Dune Field

The Western Dune Field extends along the western margin of Mount Sharp, and is the largest body of sand in Gale crater (Fig. 6.15) (Hobbs et al., 2010). This dune field is ~34 km long and is 15 km at its widest. As indicated on Figure 6.15B, the northern region of the dune field (20 km long) is separated from the southern region (10 km long) by a 4 km region of bypass spanning the width of the field. Dunes funnel in and around antecedent topography associated with nearly 700 m of elevation rise across the field (north to south). A mound of exposed layered bedrock can be seen in the middle of the northern section just north of a 1.8 km diameter crater, currently filled with dune sands (Fig. 6.15B). A dissected ridge marks the boundary between the southern area and the region of bypass, and is associated with a slope break in the local elevation (Hobbs et al., 2010, Fig. 6.5). Clearly deriving sands from the Bagnold Dune Field (Fig. 6.9), northern reaches of the Western Dune Field align with a retreating scarp (Fig. 6.16B), possibly laterally equivalent to the "Cratered Surface" terrain unit encountered by Curiosity (Anderson and Bell, 2010; Grotzinger et al., 2014). Initiation of the dune field at this scarp may reflect flow deceleration associated with the negative topography, but erosion of this strata may be an additional sediment source for the Western Dune Field.

Dune morphologies observed in the Western Dune Field are more diverse than those in the Bagnold Dune Field. Starting in the north, the field is defined by a rampart of peripheral barchans that coalesce to form crescentic and linear dunes with apparent migration toward the center of the dune field (Fig. 6.16B). Barchans on the western edge of the dune field (Fig. 6.16A) have well-defined SE-facing slipfaces, whereas barchans on the eastern edge (Fig. 6.16E) have SW-facing slipfaces. Both sets of slipfaces face the field interior, and elongating barchan arms are always on the north side. Barchans on the western edge coalesce into crescentic dunes (Fig. 6.16A), but lose definition as they

migrate inward toward a zone of markedly smooth topography that forms a halo around the dune field interior (Fig. 6.15B). Barchans on the eastern edge also coalesce and develop extended arms (Fig. 6.16E), but this pattern yields to subdued linear dunes in the interior on the eastern side of the filled crater (Figs. 15B). The central interior of the northern region shows a complex dune pattern. Large primary linear dunes trend northeast, but superimposed bedforms similar to terrestrial zibars (Nielson and Kocurek, 1986) occur in the interdune areas and intersect the primary linear dunes at a high angle (Figs. 15B, 16C). This complex pattern is reminiscent of star dunes formed in converging flows (e.g., Lancaster, 1989b; Zhang et al., 2012).

The middle bypass region (Fig. 6.15B) is devoid of bedforms, except for scattered barchans that range from 80-260 m in width (Fig. 6.16D). First observed at the dissected ridge, these symmetric barchans are oriented to migrate north across the exposed plain, and rejoin sands in the northern region of the field.

In the southern region (Fig. 6.15B), barchan dunes link and coalesce to form a morphological continuum between barchan and crescentic dunes (Fig. 6.16F). Dunes in this region exhibit north-facing slipfaces (Fig. 6.16F), matching those of the symmetric barchans in the middle bypass region. Slipfaces on crescentic and barchan dunes become less defined toward the eastern edge of this region where dunes abruptly yield to a sand-free plain (Fig. 6.16F). Elongating defect arms along this eastern edge terminate before forming symmetric linear dunes.

Slipface orientations of the barchan and crescentic dunes and the trends of linear dunes were mapped in the Western Dune Field (Fig. 6.15A, Table 6.3), yielding three populations of barchans/crescentic dunes and a population of linear dunes (Fig. 6.15C). Population 1 largely consists of the dunes on the western side of the dune field, where

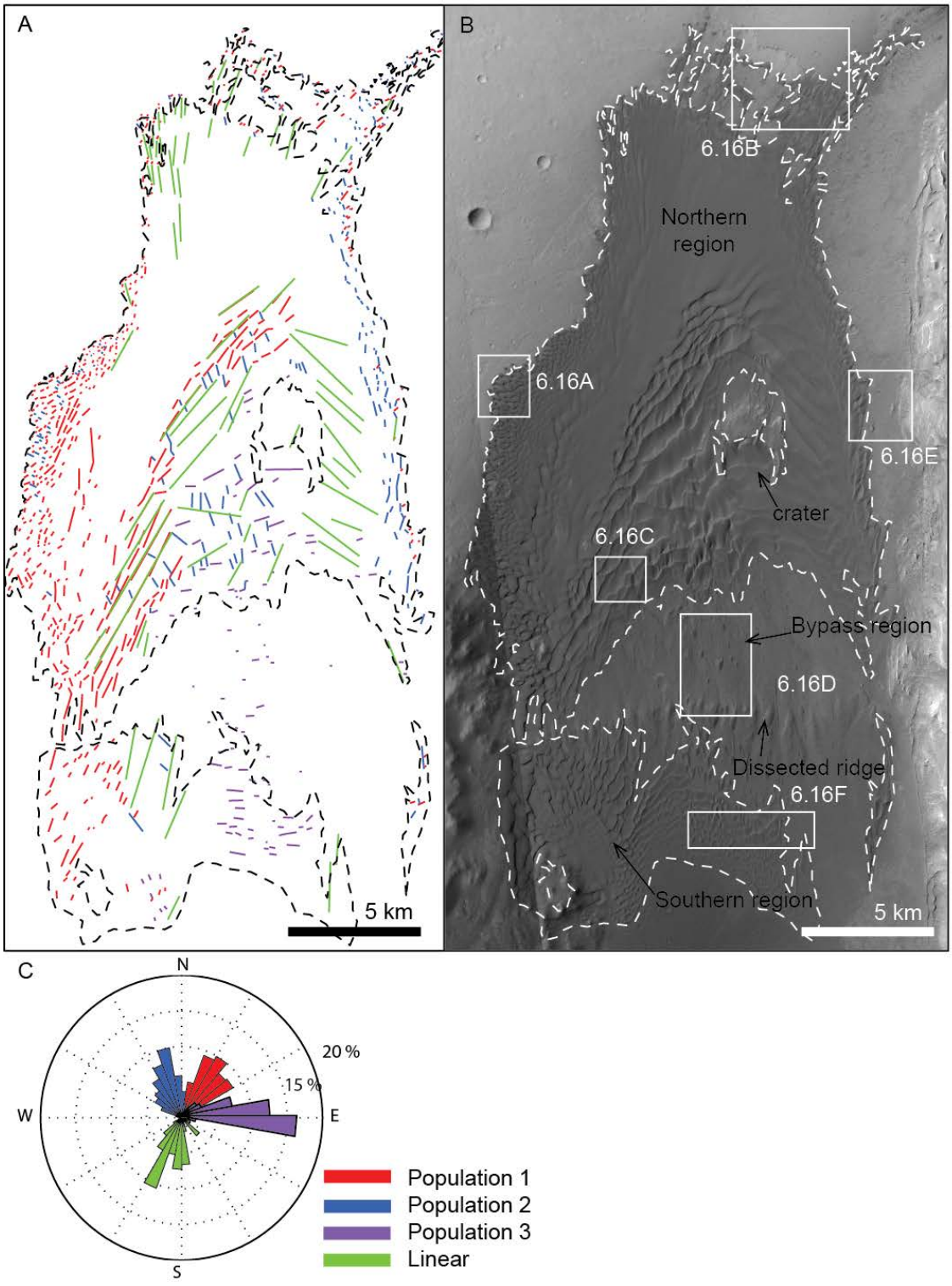

Figure 6.15: Western Dune Field.

Figure 6.15: Western Dune Field. (A) Bedform mapping in the Western Dune Field. Three populations of slipface orientations were mapped in addition to trends of linear dunes. (B) Western Dune Field at the base of just visible light toned Mount Sharp strata to the east. Dashed white line marks the edge of dune-dominated surfaces used in this area to estimate the volume of loose sediment. The three regions discussed in Section 6.5.4.4 and the filled crater are indicated (black arrows). White boxes and annotations indicate the location of panels in Figure 6.16. CTX image P13_006143_1745_XN_05S223W is oriented north-up. (C) Rose diagram of populations of slipfaces and linear dunes corresponding to measurements in (A). Populations 1 and 2 are shown by convention in the northern hemisphere, but Population 3 is shown together to prevent splitting of the population.

their brinklines trend NE (35^{o}) and dune orientation shows migration toward (125^{o}) the dune-field interior. Population 2 largely consists of the dunes on the eastern side of the dune field, where their brinklines trend NNW (336^{o}) and also show migration toward (246^{o}) the dune-field interior. Population 3 characterizes dunes in the southern and bypass regions, where brinklines trend E-W (88^{o}) and dunes are oriented to migrate north toward (358^{o}) the dune-field interior. The entire population of linear dunes trends N-S (04^{o}), but those in the western interior trend NE, parallel to Population 1, whereas the more subdued linear dunes in the east and superimposed in the west trend NW, parallel to Population 2.

The dune morphologies, their orientations, and the spatial abundance of sand all indicate that wind patterns create a convergence toward the interior dune field in the northern region. Peripheral areas of the dune field show dunes largely resting upon exhumed bedrock (Figs. 16A-E), but in the central interior, dunes are their largest and interdune areas are sand-covered (Fig. 6.16C). The flow convergence toward the central interior is further manifested by the complex superimposed dune trends.

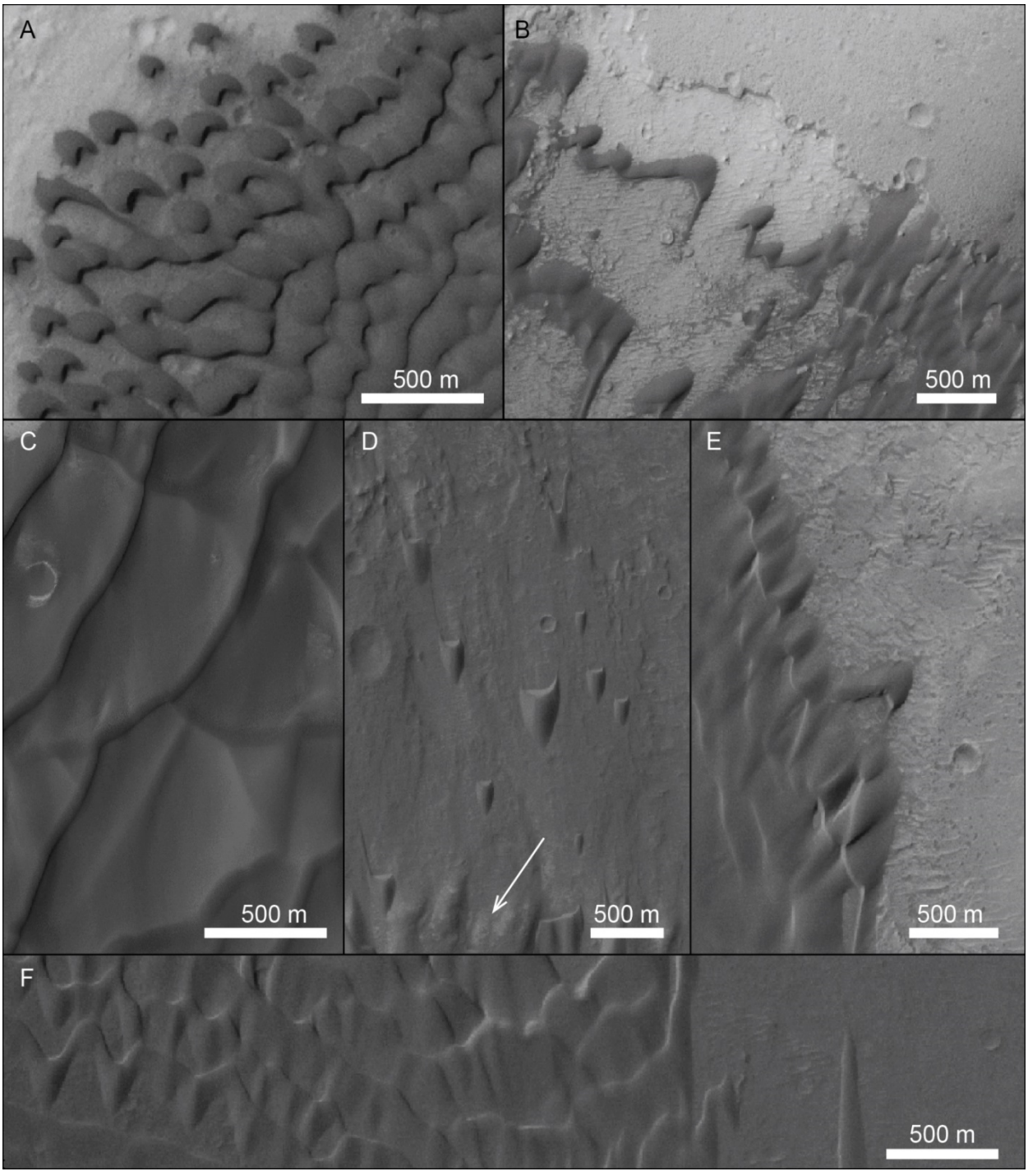

Figure 6.16: Dune morphologies in the Western Dune Field.

Figure 6.16: Dune morphologies in the Western Dune Field. (A) Peripheral symmetric barchans on the west edge of the Western Dune Field. Barchan dunes link with other barchans as they migrate to the SE, becoming increasingly asymmetric and forming crescentic ridges. Slipfaces on these dunes form Population 1 (Fig. 6.15A). (B) Asymmetric barchan dunes at the northern edge of the dune field form just downwind of a scarp, hypothesized to source some of the dune sands. (C) NE-trending linear dunes with superimposed NW-trending crestlines, forming morphologies similar to star dunes. This morphology argues for convergent flows in this region. (D) North-migrating symmetric barchans crossing the sand-starved bypass region. Slipfaces are oriented east-west (Population 3) and interpreted to form from southerly winds. Note the dissected ridge (arrow). (E) Asymmetric barchans on the eastern margin of the dune field, opposite barchans in (A). SW-facing slipfaces from Population 2 are sharpest in this area. (F) Barchans and crescentic dunes in the southern region terminate in bedrock plains to the east. The elongated barchan arm (just left of the scale bar) ends before becoming a linear dune. All images have been contrast stretched to bring out variation in the scene, and north is up (CTX image P13_006143_1745_XN_05S223W).

6.5.4.4 Northeastern Dune Field

The northeast quadrant of Gale crater hosts a dark streak indicative of actively transported aeolian sand that stretches 37 km along the northeast basal margin of Mount Sharp and averages ~5 km wide (Fig. 6.17). High resolution coverage in this dune field is particularly limited, but the area appears to be a mix of dunes, and sand sheets. Following the field from NW to SE, the beginning of the field is marked by symmetric barchans with well-defined east-facing slipfaces. These dunes grade into asymmetric dunes with southern arms elongating to the SE, roughly parallel to the dune field trend (Fig. 6.18A). Continuing to the south, barchans on the western edge lose definition and grade into apparent sand sheets, such that only about half of the ~5 km width of the dark streak appears to house enough sand to give rise to visible dunes (Fig. 6.17B). Linear streaks within the sand sheets are oriented parallel to the dune field trend. Further south, bedforms make up increasingly more of the low albedo width. Asymmetric barchans form a rampart margin on the eastern edge of the dune field (Fig. 6.18B), but their

slipfaces are subdued in comparison to the dunes in the north. Where resolvable, these dunes have brinklines trending NW with steep slipfaces toward the interior. Apparent linear dunes also occur within the main dune field, but their symmetry is difficult to determine with the limited resolution available. About 27 km from its northern margin, the dune field is interrupted by a 4.8 km diameter crater (Fig. 6.17B). Dune sands fill the crater with a crescentic "bullseye" morphology commonly observed in Martian craters (Hayward et al., 2014). Dark sands are also seen streaming around the exterior of the uplifted crater rim. Finally, at the SE end of the dune field, sands coalesce into several large crescentic dunes with steep SE-facing slopes (Fig. 6.18C). Ripple orientations on these dunes strongly follow the ridgeline orientation, with interference patterning near the crest attributed to changes in bedform slope (Fig. 6.18D).

Mapped brinkline orientations north of the 4.8 km crater define three barchans/crescentic dune populations that, as with the Western Dune Field, suggest that the dune field formed by flow convergence (Fig. 6.17A, Table 6.3). Population 1 brinklines, characterizing the dunes in the NW (Fig. 6.18A), trend NNE (18^{o}) with dune migration toward (108^{o}) the interior. Population 2 brinklines, characterizing the eastern periphery dunes, trend NW (324^{o}) with dune migration again toward (234^{o}) the interior. Population 3 brinklines characterize only dunes in the southern reaches of the field, and these trend NE (50^{o}) with dune migration toward (340^{o}) the interior. Linear streaks in the sand sheets and linear dunes in the main dune field trend 327^{o}, roughly parallel to the dune field and potentially define the mean transport direction that gives rise to the migration directions for dunes in Population 1-3, as expected within a sand-limited system (Courrech du Pont et al., 2014).

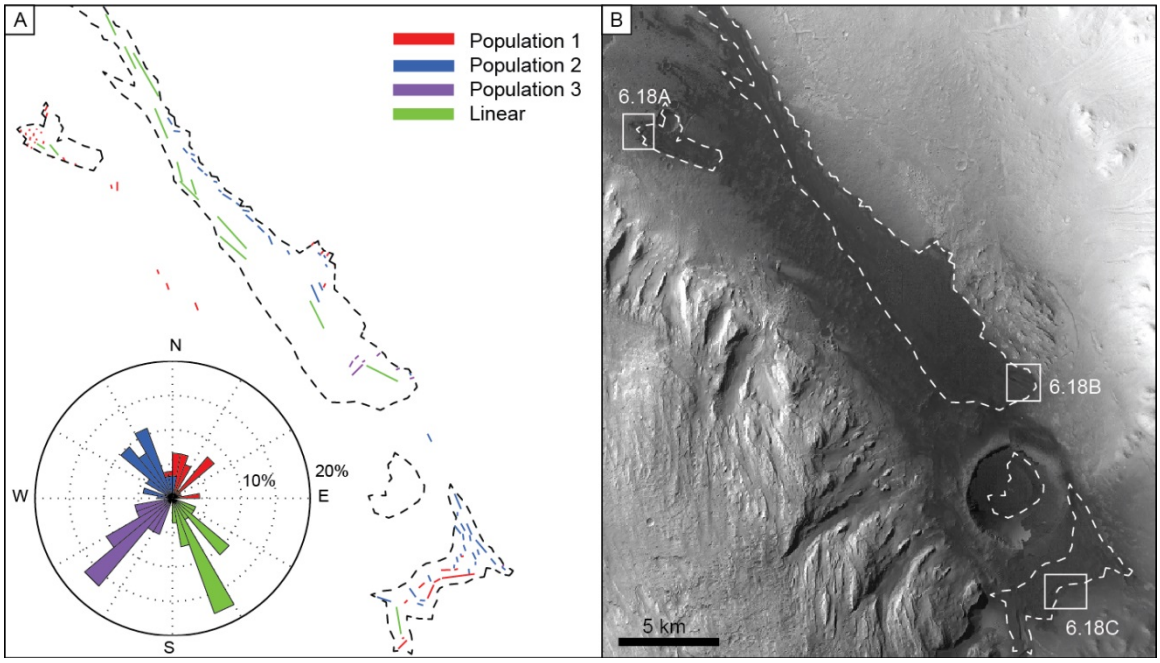

Figure 6.17: Northeastern Dune Field. (A) Bedform mapping in the Northeastern Dune Field. Three populations of slipface orientations were mapped in addition to the linear dune orientations. Rose diagram shows histogram of the measured orientations. Population 3 is shown in the southern hemisphere to limit overlap. (B) Northeastern Dune Field at the base of dissected Mount Sharp strata to the SW. Dashed line corresponds with dashed line in A and was used to estimate the volume of dune sand in this region. White boxes show the locations of panels in Figure 6.18. North-up oriented CTX image G23_027069_1748_XN_05S221W.

6.5.4.5 Southern Dunes

The southern floor of Gale crater hosts a swath of bedforms ~100 km long and 5 km wide (Fig. 6.19). Unlike the other fields, which form at the base of Mount Sharp, these dunes form far from the mound and instead are associated with steep rim topography. Morphologies in this region are again dominated by a continuum between barchan, crescentic, and linear dunes (Lee and Thomas, 1995). Barchans dunes seen across the field form tear-drop morphologies that elongate into linear dunes (Fig. 6.20D)

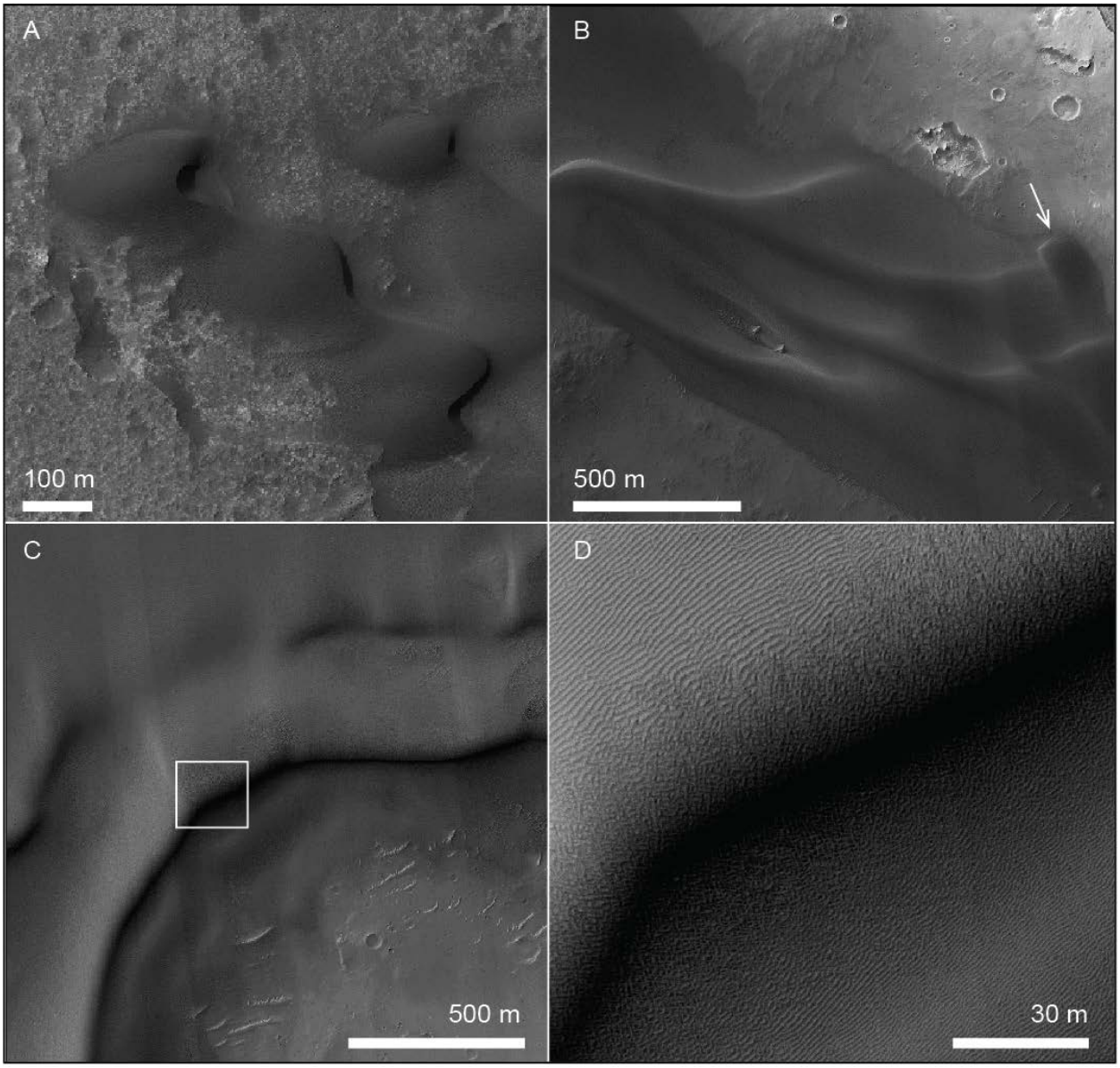

Figure 6.18: Dune morphologies in the Northeastern Dune Field. (A) Barchans becoming increasingly asymmetric and linking to form chains of defect arms elongating to the SE. Note the sharp brinklines defining the slipface Population 1. HiRISE image ESP_026291_1750. (B) NW-trending asymmetric linear dunes with steep north-facing slopes. Note the degraded teardrop barchan (arrow) and its two slipfaces. (C) Crescentic dune with steep SE-facing slope forming south of the 4.8 km diameter crater. White box shows the location of (D). (D) Ripples on crescentic dune surface are parallel to the crest on both the NW stoss and at the base of the steep lee face to the SE. Note the interference patterning near the brinkline. All images have been contrast stretched and are oriented north-up. HiRISE image ESP_026502_1750 covers (B), (C), and (D).

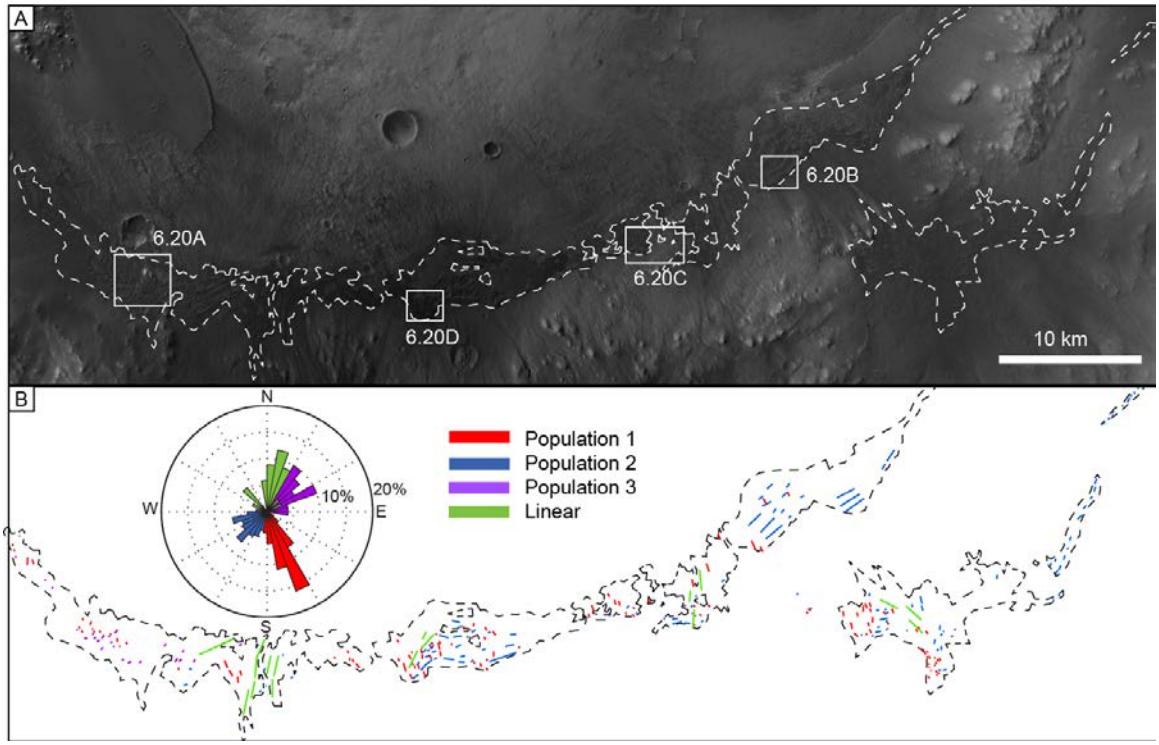

Figure 6.19: Southern Dunes. (A) Southern Dunes distributed across the floor of Gale crater over north-up oriented CTX mosaic. Dashed line corresponds with the dashed line in B and was used to estimate the volume of dune sand in this region. Dunes are spread along the base of the crater rim and absent close to the base of Mount Sharp. White boxes show the locations of panels in Figure 6.20. (B) Mapping of the Southern Dunes. Three populations of slipface orientation were mapped in addition to the linear dunes. Populations are shown in the rose diagram in both the north and south hemispheres to prevent overlap, and highlight the difference between north-facing Populations 1 and 2 in this region and south-facing Populations 1 and 2 in the other dune fields. Note the variation in linear dune trend from west to east that roughly follows normal to crater rim curvature.

or coalesce into crescentic dunes (Fig. 6.20B). Topography from raised ridges and small hills clearly disrupts bedform morphology in southern Gale crater (Figs. 20A, 20C). This region also appears sediment-starved. Bedrock plains can be seen in most interdune areas, and dunes grade into sand sheets to the north and laterally (Fig. 6.20C).

The orientations of resolvable brinklines and linear dunes were mapped across southern Gale crater (Fig. 6.19, Table 6.3). Three populations of brinkline orientations emerged, in addition to the linear dune trends. In the west, the sharpest and most abundant brinklines (Population 1) trend NW (339°) with lee faces oriented toward the NE (69°). In the east, however, the sharpest brinklines (Population 2) trend NE (49°) with lee faces oriented toward the NW (319°). The trend of the linear dunes varies from west to east as well. Trending on average N-S (05°), the linear dunes form perpendicular to the strike of the rim, swinging from a NE-SW trend in the west to a NW-SE trend in the east. The radial pattern in the orientations of both the linear and barchan dunes suggests that the formative winds for these southern dunes is associated with flow down rim topography and toward the crater interior (Hobbs et al., 2010).

A third population of brinklines, trending NE (55°) but with SE-facing (145°) lee faces, was observed only in the western end of the area (Fig. 6.19). Figure 6.20A shows where these Population 3 slipfaces interact with Population 1 slipfaces, capturing the transition from dominantly north winds in the Western Dune Field to south winds in the Southern Dunes region.

6.6 SURFACE OBSERVATIONS

The traverse of Curiosity from its landing site at Bradbury Landing to the base of Mount Sharp at Pahrump Hills allowed for field observations of landscapes that can otherwise only be viewed from orbit. Toward the goal of characterizing this interpreted aeolian landscape, terrain along the first 960 sols of the traverse was surveyed using Navcam mosaics to determine landscape morphologies typical of this area of Gale crater (Fig. 6.21). The observed landscapes can be grouped into four broad categories: rocky plains, undercut bedrock, capped mesas, and remnant hills (Fig. 6.22).

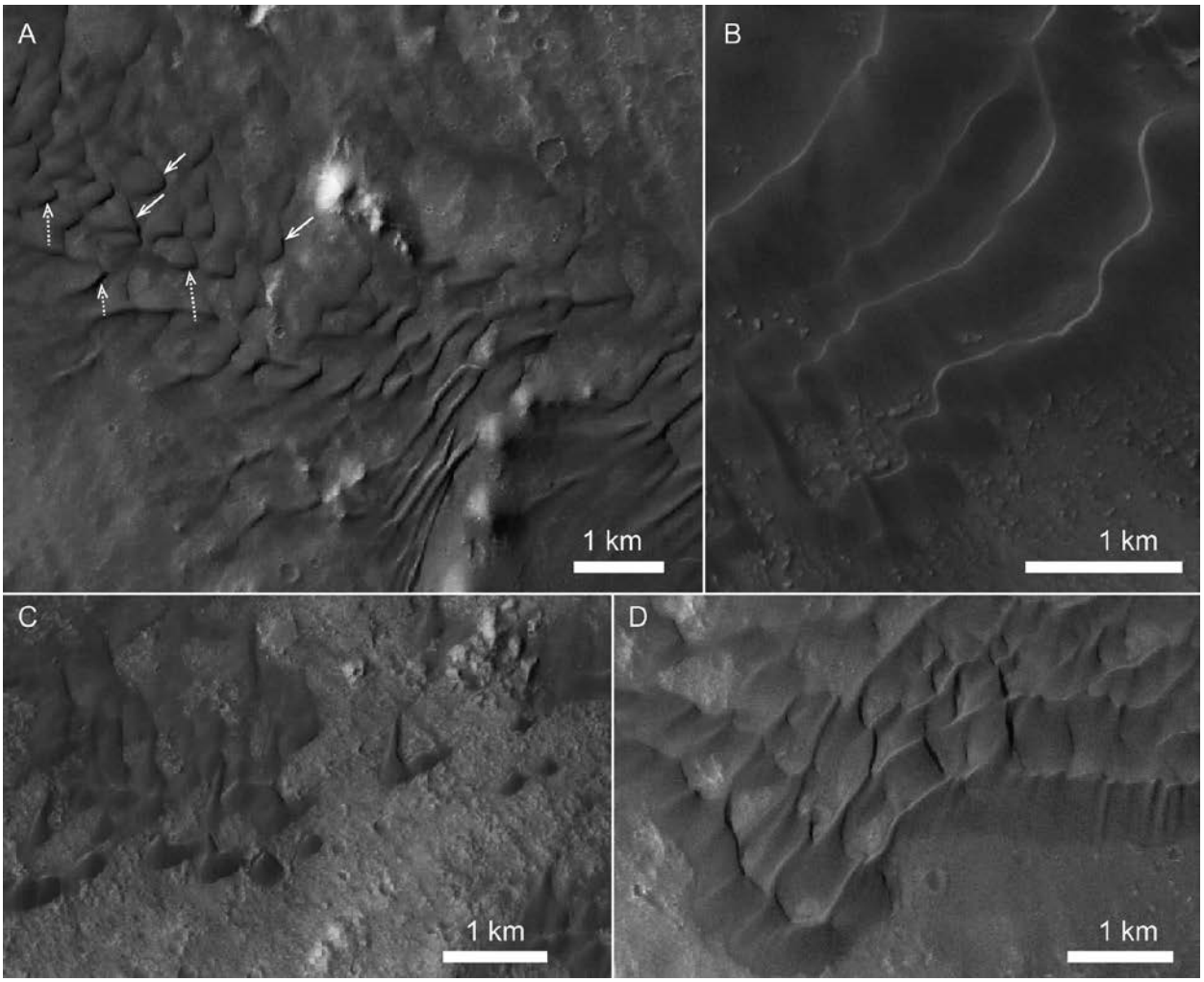

Figure 6.20: Dune morphologies in southern Gale crater. (A) Teardrop barchan dunes with slipfaces from Populations 1 (solid arrows) and 3 (dotted arrows) depicting the transition from dominantly north to southerly winds. Note divergence around hill topography and gradation into linear dunes streaming toward the crater center (NNE). CTX image P15_006855_1746_XN_05S222W. (B) Crescentic ridges with steep NW-facing lee slopes form along from the opposite end of this region from (A). Note that the orientation has swung around such that inferred wind direction is still normal to the crater rim. CTX image P01_001554_1754_XI_05S221W. (C) Asymmetric barchans elongating to the north and evidencing two populations of slipfaces (Populations 1 and 2). Note the bare interdune areas and gradation to sand sheets to the north. CTX image P01_001620_1749_XI_05S222W. (D) Sinuous crescentic ridge splitting into tear-drop dunes as defects elongate to the north. Note the two populations of slipfaces also observed in (C). CTX image P14_006644_1747_XI_05S222W. All images have been contrast stretched and are oriented north-up.

As of sol 960, Curiosity had traveled 8.3 km across the floor of Gale crater, moving generally up-section for a total elevation gain of ~70 m. The traverse aimed to capture the diversity of landforms and chemistry observed from orbit, targeting several named waypoints to characterize distinct units in the stratigraphy (Fig. 6.21). The four landscapes discussed in this section are not unique to any one terrain or stratigraphic unit (Anderson and Bell, 2010; Grotzinger et al., 2014), but rather are broadly representative of processes repeatedly seen shaping the crater interior. In addition, some of the features observed in these landscapes indicate a formative wind direction, thus adding to the body of wind directions inferred from orbital observations.

6.6.1 Rocky plains

The most common landscape observed along the traverse can be characterized as a flat plain with a varying amounts of scattered rock sitting atop a hard, dusty surface (Fig. 6.23A). Rocky plains are captured in nearly all scenes from the first 500 sols, after which they are less dominant, but still ubiquitously observed. The “Rugged” and “Hummocky Plains” terrain units, mapped in Grotzinger et al. (2014), are overwhelmingly dominated by this landscape. The distribution of rock across the surface appears pseudo-random with no clustering or preferential alignment between rocks. Unassociated with outcrop, these rocks come from no obvious near-field source and range in size from pebbles to decimeter-sized cobbles. Transport by wind of a ~3 cm clast was observed by the Viking 1 lander after a substantial storm (Arvidson et al., 1983), but many cobbles on these plains are too large to have been transported by winds. Rather, rocks on these plains are most similar to terrestrial desert pavements. Formed when fine material is deflated away from a surface faster than rock is weathered and eroded, desert pavements armor planar surfaces with tightly packed rock, slowing and ultimately halting

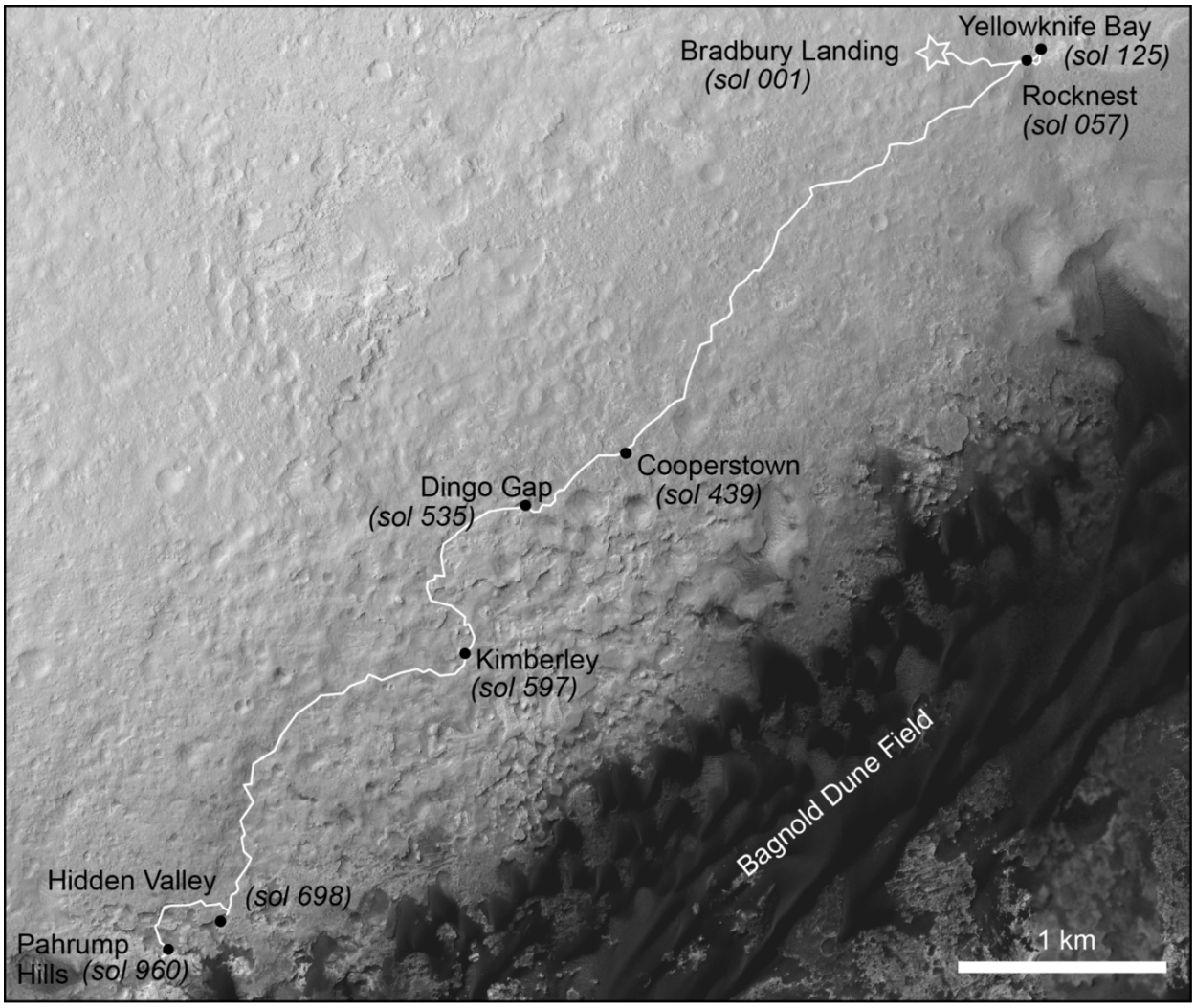

Figure 6.21: Curiosity rover traverse from sols 1-960. Waypoints discussed in Section 6.6, and approximate sol when they were first reached, are indicated by the black dots. This image also covers barchan and linear dunes in the main region of the Bagnold Dune Field. North is up.

aeolian deflation of the surface (Cooke, 1970). In some cases, desert pavement can even be aggrading, raising surface stones with kinetic sieving as trapped fines are vibrated to below the armored surface (McFadden et al., 1987), similar to the hypothesized TAR formation mechanism (Bridges et al., 2015). The Gale crater surface rock armor is typically less closely-packed than some interlocking pavements observed on Earth (e.g.,

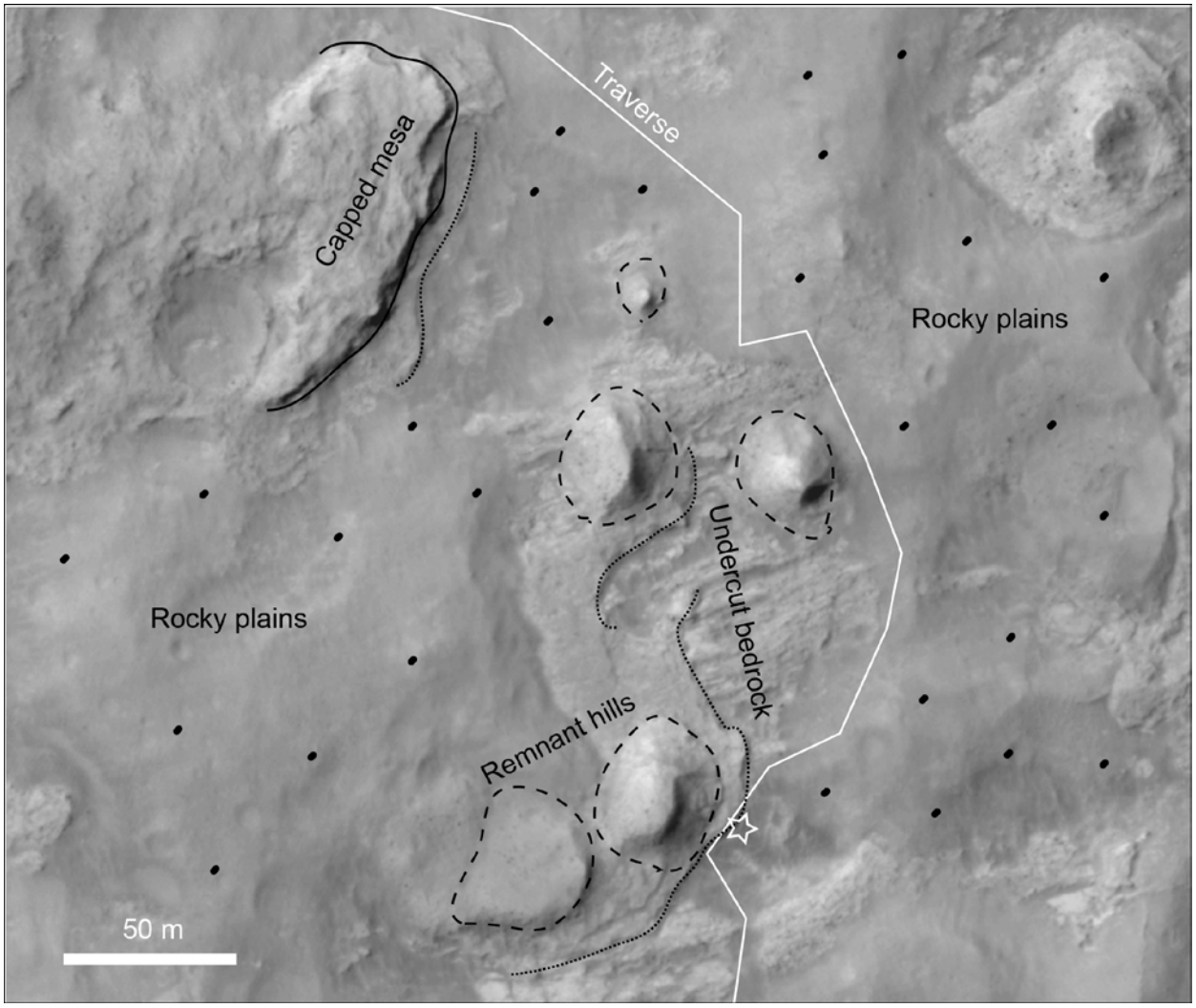

Figure 6.22: Orbital view of the four landscapes classified in Section 6.6. This view of the Kimberly waypoint along the MSL traverse shows all four stages of the erosional process. Capped mesas (solid line) once overlaid the Kimberly (star), but have retreated to the northwest, leaving behind remnant hills (dashed lines) and rocky plains (dotted area). At the eastern base of the remnant hills we see where plains have eroded down to a new bedrock level, already forming low scarps (dotted line) that will eventually become the capped mesas. White line shows the approximate rover traverse, and the star indicates the rover position when Mastcam mosaic in Figure 6.29 was taken. North-up oriented HiRISE image ESP_036128_1755.

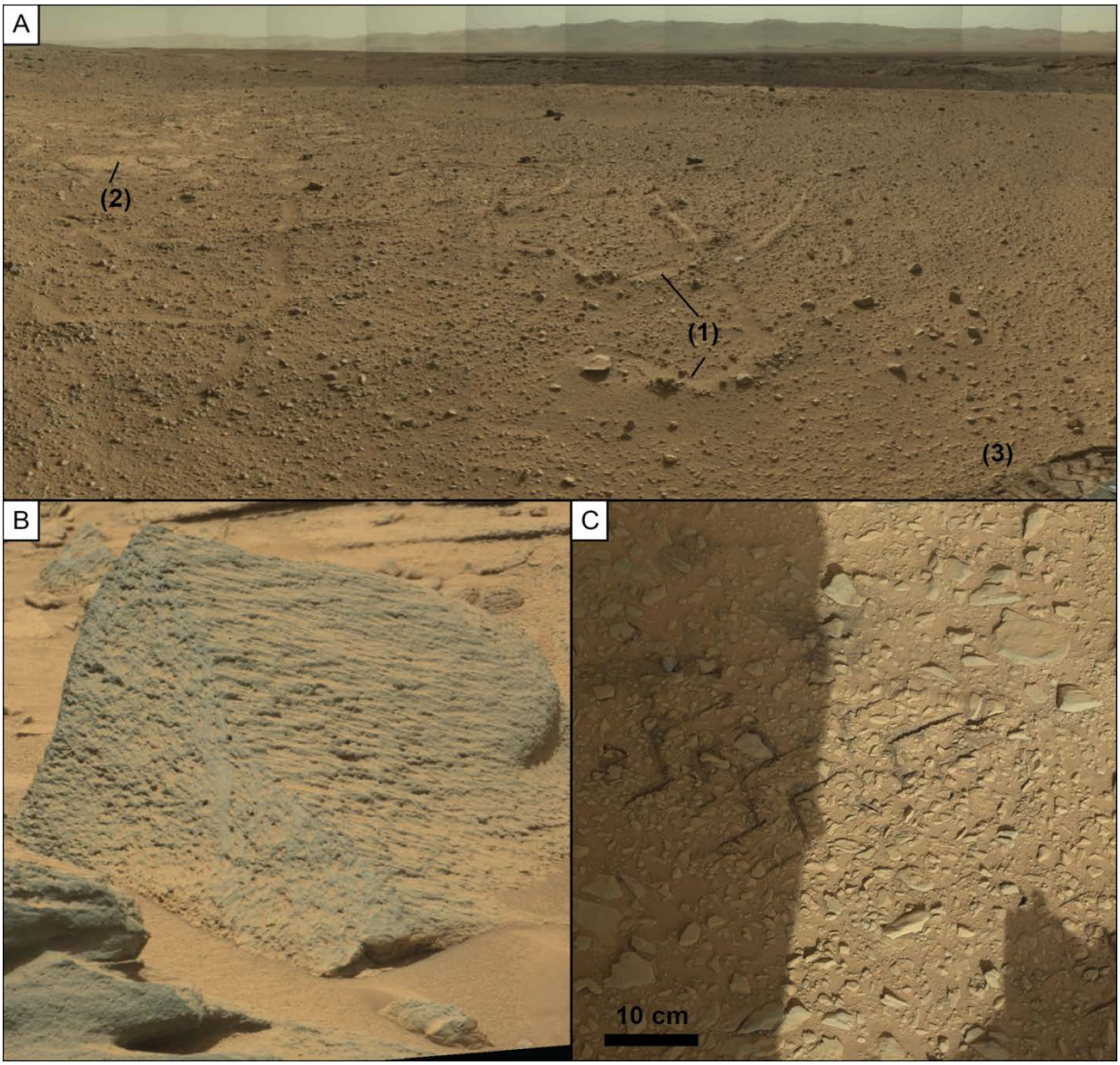

Figure 6.23: Rocky plains landscape. (A) Mastcam mosaic of flat cobbled plains taken on sol 541 (mcam02134). Plains show dust-filled fractures from underlying bedrock (1) and exposures of light toned bedrock (2). Foreground wheel track (3) is 30 cm wide (Mastcam mosaic starting at 0541ML0021340010203723E01_DRCX). (B) Ventifact observed on sol 694. Note the elongated pits and fluting on the right hand face as compared with the blunted (upwind) left face. Image is ~40 cm wide (Mastcam image 0694MR0029330020402220E01_DRCX). (C) Light toned dust mantling rocky cobble surface is disturbed by wheel tracks that cut into the surface and reveal dark-toned regolith (Mastcam mosaic from sol 456 starting at 0456ML0018370000201931E01_DRCX).

Death Valley, CA; Haff, 2001), but the spatial density of clasts on the surface (Fig. 6.23C) is sufficient to raise the aerodynamic surface roughness to preclude most deflation, making these surfaces stable.

Pebbles and cobbles littering the rocky plains commonly exhibit fluting, lineations and the distinctive polish characteristic of ventifacts formed from persistent aeolian abrasion (Fig. 6.23B), reflecting the long exposure of these stones on the surface (Laity and Bridges, 2009). Indicators of wind direction, measured in ventifacts along the first 100 sols of Curiosity's traverse, recorded a relatively wide NW-SW range of winds (Bridges et al., 2014). Comparison between ChemCam observations of the rock called Jake Matijevic, a well-defined ventifact near the Rocknest outcrop in Yellowknife Bay, and less abraded bedrock indicated that the high lithium rind seen on the bedrock outcrop is absent on highly ventifacted surfaces (Bridges et al., 2014). This argues that abrasion has removed the coating, or is resurfacing the rock faster than the rind can form, confirming the dominance of physical weathering over chemical. Heavily ventifacted rocks have also been observed in similar landscapes of rocky plains seen at the Pathfinder (Greeley et al., 1999), Viking 1 (Arvidson et al., 1983), and Mars Exploration Rover (MER) Spirit (Sullivan et al., 2008, fig. 50) landing sites.

In Gale crater, rocky plains landscapes are typically devoid of bedforms, consistent with the interpretation that these surfaces are highly deflated, and show a paucity of transport-available sand at the surface. Unlike the abundant ripples observed on rocky plains by Spirit (Sullivan et al., 2008, fig. 28), only occasional sand shadows were encountered along Curiosity's traverse across the rocky plains (Fig. 6.24A). Sand shadows are linear accumulations of sand that are deposited in the lee of obstacles even on sand-starved surfaces (Hesp, 1981), thus making them reliable indicators of the last significant wind direction. Measurement of the orientation of 69 sand shadows, from

Yellowknife Bay to Pahrump Hills, generated a mean orientation of 09º with standard deviation of 0.5º (Fig. 6.24B, Table 6.2), thereby indicating a narrowly constrained north formative wind. Ranging from 12 cm to 3.74 m long, these accumulations are similar to those observed at the Pathfinder landing site (Greeley et al., 1999, fig. 2). Despite an abundance of available obstacles, sand shadows and other bedforms were absent from the plains from sols 361-369, 429-439, and 634-644.

The Rocknest sand shadow, observed in Yellowknife Bay from sol 57 to 100, is the most studied sand shadow to date in conjunction with the first scooping activities by Curiosity (e.g., Blake et al., 2013). Also interpreted to have formed by northerly winds, this sand shadow exhibits a 2-3 mm thick armored surface formed by 1-2 mm rounded, dust-rimmed grains, which formed cohesive rafts during the excavations (Minitti et al., 2013). In contrast to the armored surface, the sand shadow interior consists of fine sediment largely below the resolution of MAHLI (~150 μm). This contrast between the coarse armored surface and the fine dusty interior suggests that the sand shadow may have originated as a coarse-grained feature that subsequently grew by the infiltration of dust and fine sand into the interior, similar to the dynamics of TARs described above.

6.6.2 Undercut bedrock

Bedrock outcrops are seen consistently every few hundred meters for the length of the traverse. Exposures are typically heavily fractured, with fractures forming local sediment traps filled with dust or sand (Fig. 6.25). Similarly fractured outcrops were observed near Home Plate by Spirit (Sullivan et al., 2008, fig. 43), and at the Burns formation by Opportunity (Grotzinger et al., 2005, fig. 4). Exposures of bedrock are commonly undercut, forming small scarps, and decimeter-scale relief shelters N-S trending sand shadows (Fig. 6.25). Float rocks can be seen on top of some exposed

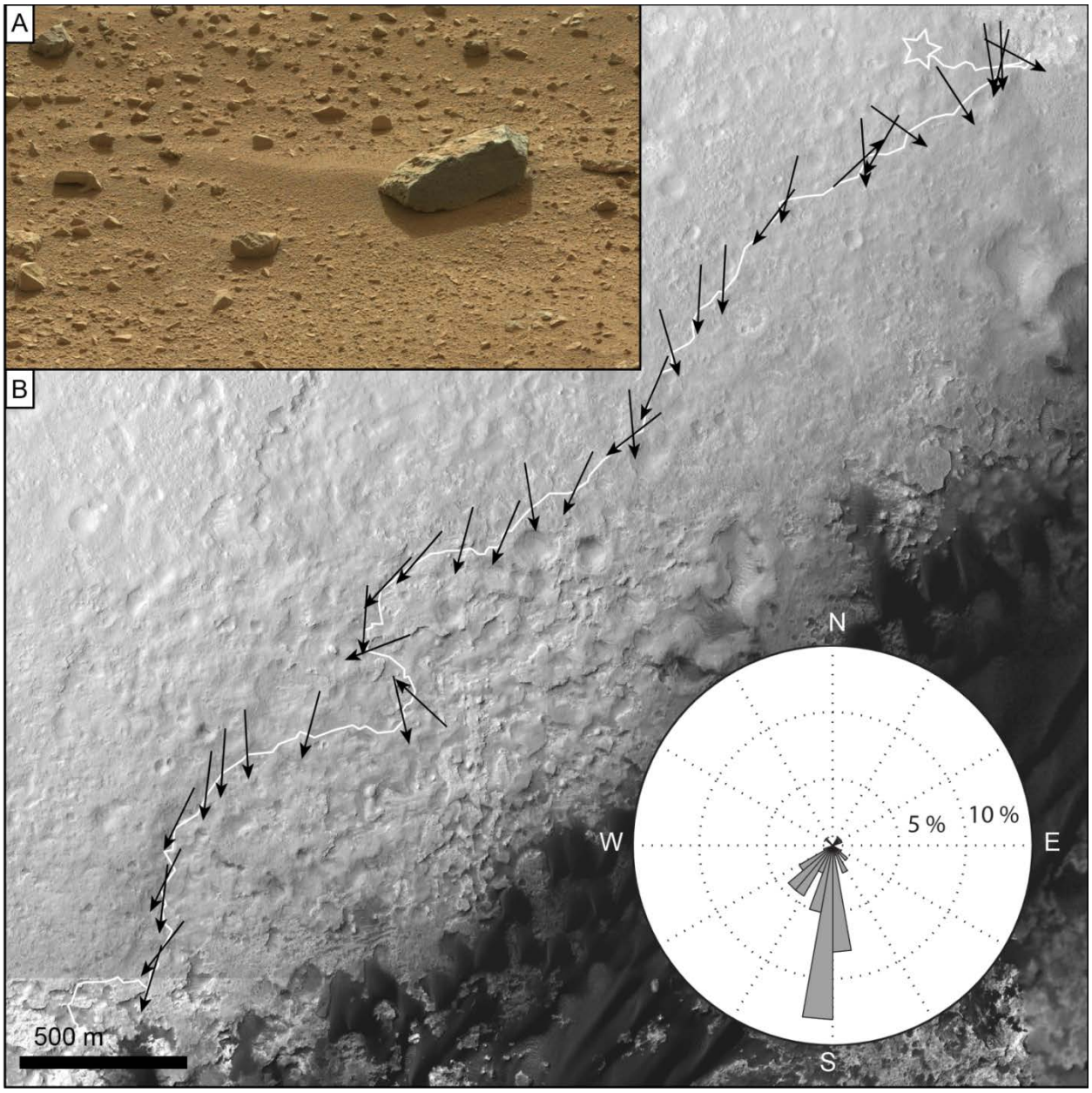

Figure 6.24: Sand shadow surface observations. (A) Sand shadow (50 cm long) accumulating behind a float rock obstacle in rocky plains (sol 333 Mastcam image 0333ML0013490070107979E01_DRCX). (B) HiRISE map of the Curiosity traverse with measured sand shadow orientation superimposed on location of observation. Where multiple sand shadows were observed in a single mosaic, the average orientation is shown. Rose diagram shows the orientation and inferred upwind azimuth of all 69 measured sand shadows.

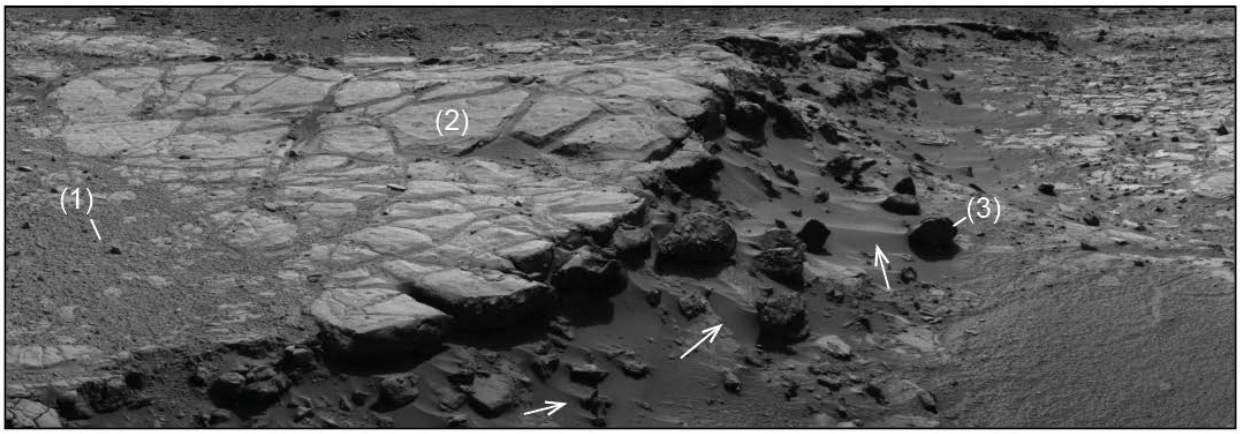

Figure 6.25: Undercut bedrock outcrop at Cooperstown (sol 440 Navcam mosaic centered on image NLB_436560260EDR_F0220000NCAM00259M). Float rock is visible atop bedrock exposure (1). Exposed surface is heavily fractured with sand and dust filling most fractures (2). Arrows indicate small sand shadows forming in the lee of scarp float boulders, including the 40 cm boulder indicate by (3).

bedrock, and in clusters at the base of small scarps, tending to decrease in size away from the outcrop. Outcropping bedrock is typically surrounded by rocky plains, and scalloping and polish of bedrock surfaces evidence long exposure to aeolian abrasion.

Close examination of exposed bedrock in Yellowknife Bay revealed streamlined nodules in the bedrock surface. Similar to concretions observed by Opportunity in the Burns formation (Grotzinger et al., 2005), these diagenetic features range from 1-3 mm in diameter. Nodules in the Sheepbed mudstone (Grotzinger et al., 2014) appear partially exhumed with one blunted edge and opposing tail of bedrock all aligned locally in the same direction (345º) (Fig. 6.26). These features are interpreted as caused by direct wind abrasion of bedrock from NW winds (Stack et al., 2014). A surface exposure age of 78 ± 30 Ma was measured on the Sheepbed mudstone at the Cumberland drill target (Farley et al., 2014). Cumberland is located ~1 m from an overlying scarp of Gillespie Lake unit, implying a relatively slow modern erosion rate of ~1 m of scarp retreat per 100 Ma.

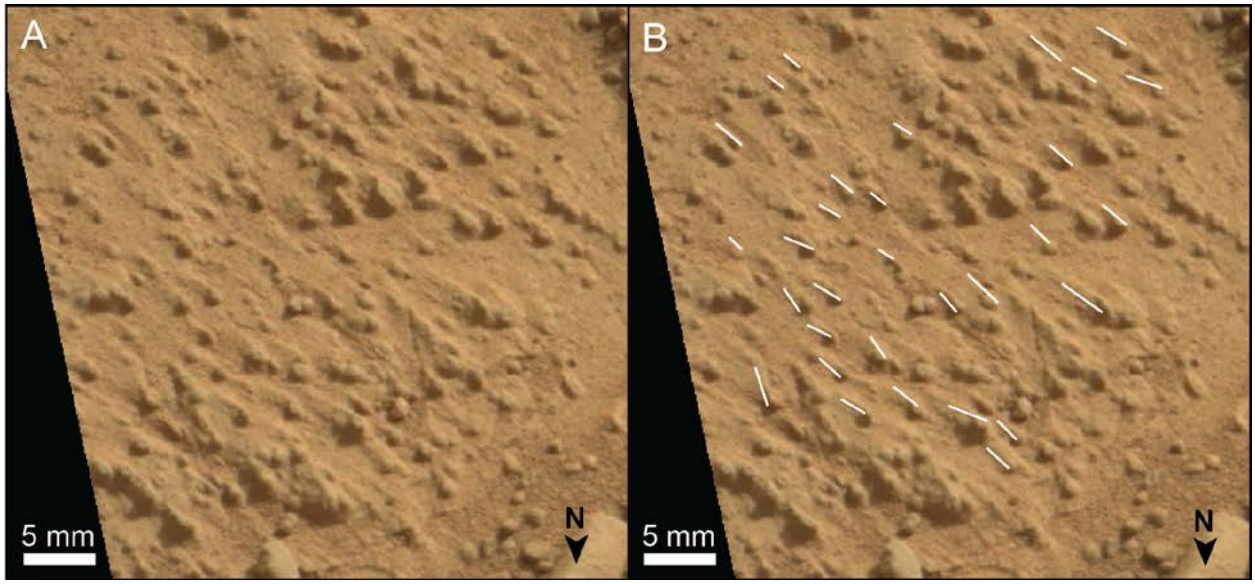

Figure 6.26: Streamlined nodules in the Sheepbed mudstone found at Yellowknife Bay. (A) In-place nodules being exhumed from bedrock (sol 298 Mastcam mosaic starting at 0298MR0012480590203737E01_DRCX). (B) Same image as A but with orientations of streamlines superimposed on leeward tails. Average orientation is 345º with inferred wind from the NE.

6.6.3 Capped mesas

Capped mesas become increasingly common along the traverse (Fig. 6.27). First observed on either side of Dingo Gap, mesas commonly form along the edges of the "Cratered Surface" terrain unit (Grotzinger et al., 2014), and on opposing sides of valleys (e.g., Hidden Valley, Dingo Gap). These flat-topped landforms are defined by 2-4 m high hills capped by scarps of retreating competent rock typically ~1 m thick. Below the scarps, decimeter- to meter-sized boulders, apparently sourced from the caprock, armor dusty slopes. Similar observations of eroded float rock are seen coming from capping layers in the Burns Formation along the Opportunity traverse (Grotzinger et al., 2005). In Gale crater, ventifacting was observed on float rock near the base of slopes, but fluting and polish textures could not be resolved nearer to the hilltops. Sand shadows were

commonly observed in association with basal slope boulders, and in some cases the topography sheltered fields of ripples (Fig. 6.27).

On sol 535 of its traverse, Curiosity crossed the TAR named Dingo Gap, spanning ~12 meters between two capped mesas. MAHLI images revealed the TAR to be topped with rounded 1-2 mm grains covering ~20% of the surface, similar to the Rocknest sand shadow but not as tightly packed (Fig. 6.28). These armoring grains are similarly coated in dust that fell away after contact with rover hardware. Imaging of the wheel tracks revealed the interior of the TAR to be dominated by the fine dust particles, with some rounded grains supported in a dust matrix. Surface armoring was also observed by Spirit

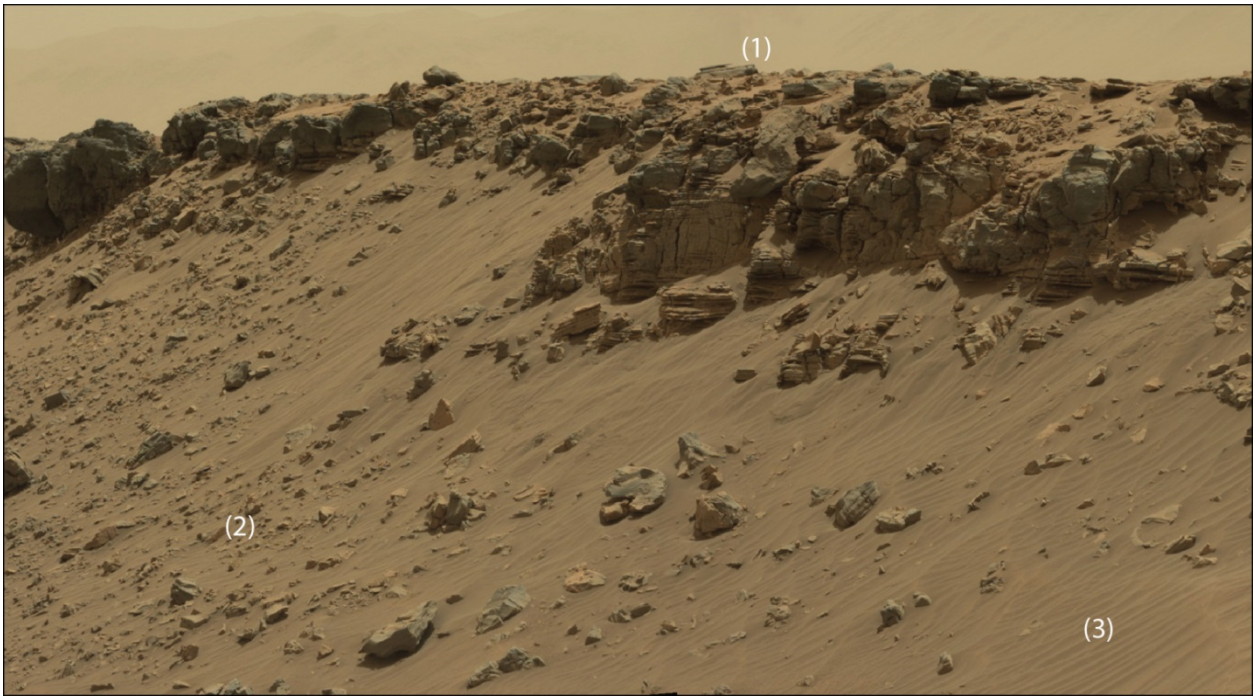

Figure 6.27: Retreating scarps cap the northwest wall of Hidden Valley, forming a flat-topped mesa (1). Boulders on the lower slopes (2) are partially covered by ripples (3) and appear to be sourced from the resistant caprock. Vertical relief in this image is ~ 4 m (sol 707 Masctam images 0707ML0030050030304604E01_DRCX and 0707ML0030050020304603E01_DRCX).

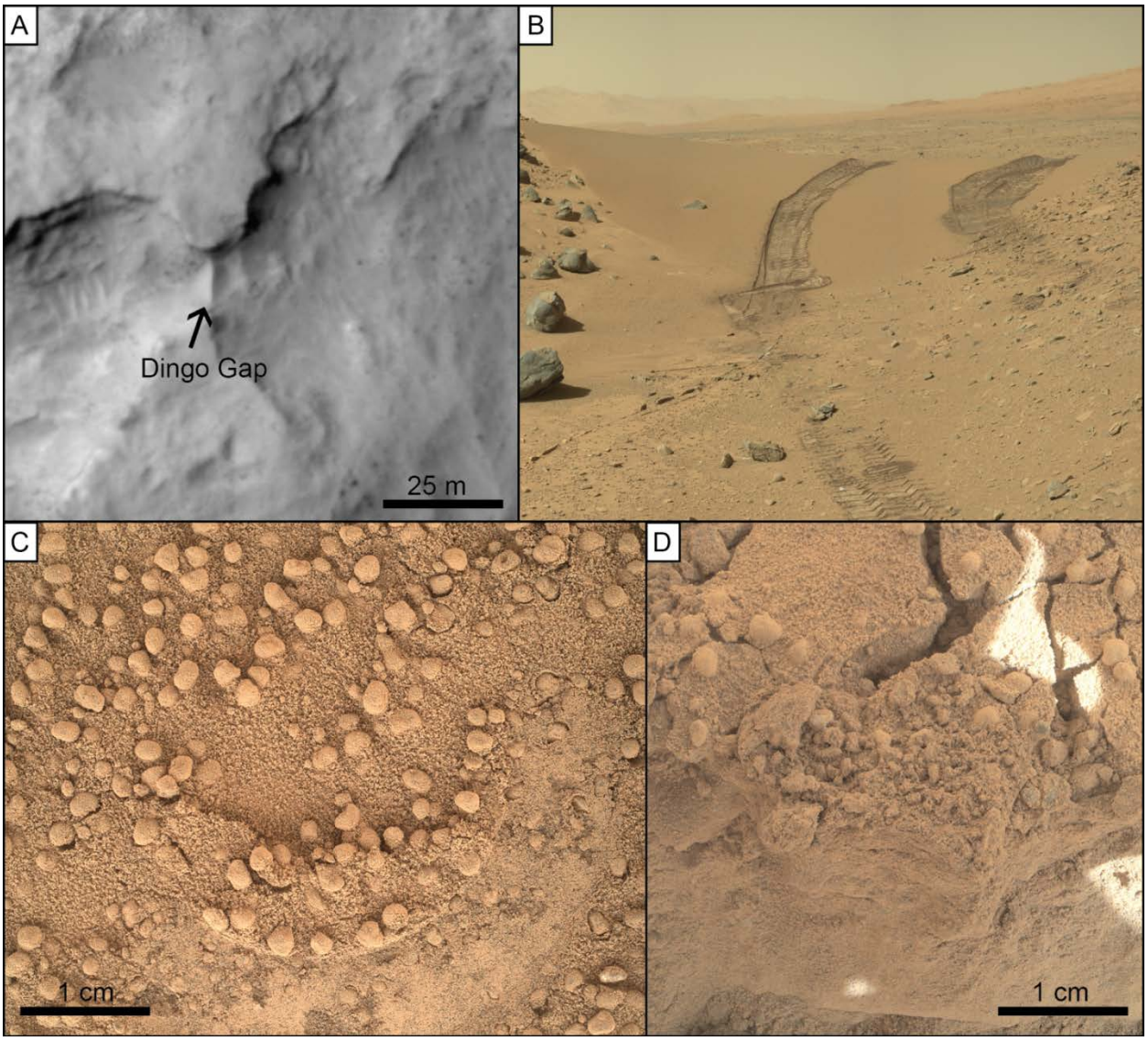

Figure 6.28: Dingo Gap TAR. (A) Valley-spanning TAR at Dingo Gap as observed from orbit (HiRISE image ESP_036128_1755). (B) East-facing Mastcam mosaic of Curiosity tracks across Dingo Gap TAR. Tracks are ~30 cm wide (sol 538, starting image 0538ML0021240000203532E01_DRCX). (C) MAHLI image of Dingo Gap surface. Rounded grains cover ~20% of the TAR surface in contrast to more tightly packed armoring seen on the Rocknest sand shadow. Note the thin coating of dust on all grains. Crescent impression on the surface is from Curiosity's Alpha Particle X-ray Spectrometer (APXS) on target Barker (sol 531, 0531MH0002990010201151C00). (D) MAHLI image wheel track wall target Dampier. Wall shows subsurface to be dominated by dust-sized fines, rafting at the dusty surface implies some cohesion of dust (sol 531, 0531MH0003470010201183C00).

on the El Dorado ripple field, but surface grains were only ~300 microns, and much more closely packed (Sullivan et al., 2008). Despite their differences, bedforms such as the Rocknest sand shadow, the Dingo Gap TAR, and the El Dorado ripples appear to represent a common class of Martian bedforms sharing coarse-grained armored surfaces and fine interiors. The well-rounded grain surfaces indicate that these sands are not freshly eroded from bedrock, but rather have been transported sufficiently to generate near-spherical rounding. As described above, these bedforms may also share a dynamic of surface stabilization with continued vertical growth by dust infiltration.

6.6.4 Remnant hills

Small hills, not capped by erosionally resistant rock layers, increase in frequency along the traverse in conjunction with the increasing frequency of the capped mesas. Characterized by rounded tops, slopes on remnant hills in Gale crater are typically shallower than slopes below capped mesas, but total relief is similar (1-3 m). These hills exhibit the same armoring of decimeter- to meter-scale boulders seen below capped mesas (Fig. 6.29). Float rock was measured in a ~50 m transect from the top of a hill just beyond Dingo Gap, down the slope, and across the plains until float rock size became uniform with the surrounding area (Fig. 6.30). Choosing the largest float rocks in the scene, rocks identified in the high resolution Mastcam mosaic were measured using stereo Navcam mosaic. Distance from the rover was used as an approximation for distance along the transect, and is differenced to be relative to the hilltop in Figure 6.30. Measured diameters decreased in size away from the hilltop, following roughly an exponential decay. Though resolution in this area was not high enough to resolve ventifact textures, ventifacts were observed at the base of remnant hills later in the traverse (e.g., at the Kimberley). No observations of larger hill-boulders were captured in

enough resolution to see fluting or pits. Small accumulations of sand in the form of ripples or sand shadows were again found against these hills, but remnant hill TARs have not yet been observed. Spirit observations of McMurdo capture rock-covered hillslopes with similar morphology (Greeley et al., 2008).

6.6.5 Landscape evolution by wind and gravity

The four landscapes observed along the traverse are proposed to represent a spectrum of progressive stages in a cycle of landscape evolution where aeolian erosion and gravity-driven mass wasting, coupled with physical weathering, compete to level the surface. These processes, operating over the last 3 Ga, are taken as necessary and sufficient for the removal of the ~ 6 x 10^4 km^3 of sediment from Gale crater needed for the exhumation of Mount Sharp.

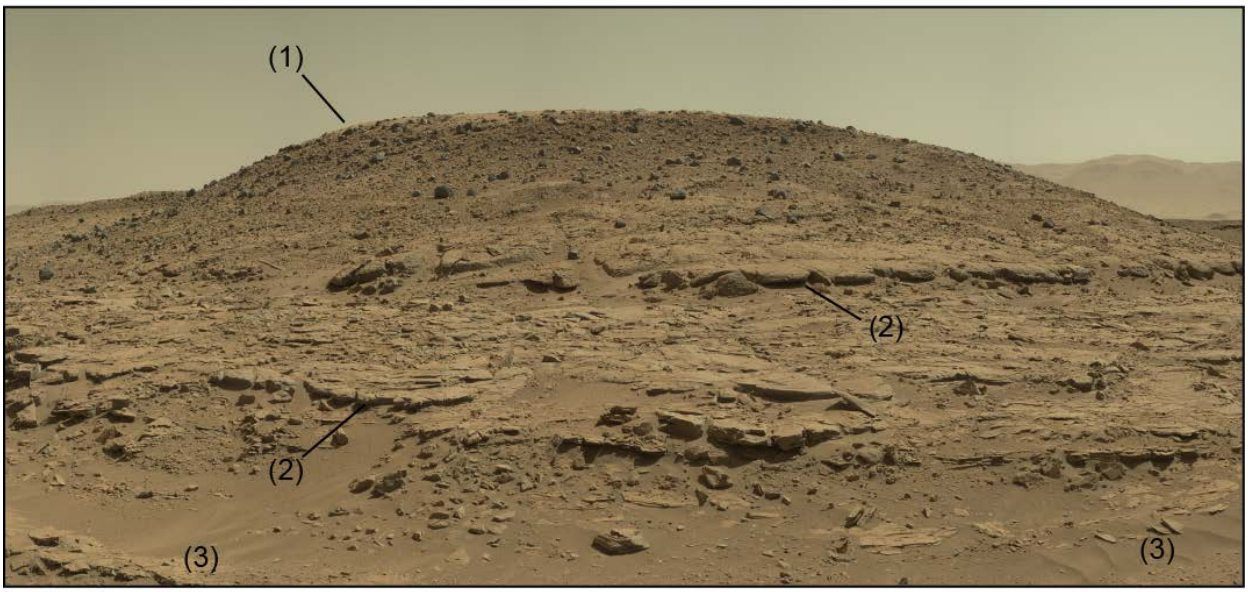

Figure 6.29: Remnant hill observed at the Kimberley. Boulders cover the rounded hillslopes (1), and outcrops of retreating bedrock scarps can be seen in the foreground (2). Relief in exposed bedrock shelters 10-20 cm sand shadows (3). East-facing image was taken at the location indicated in Figure 6.22 (sol 603Mastcam mosaic starting at image 0603ML0025440010301349E01_DRCX).

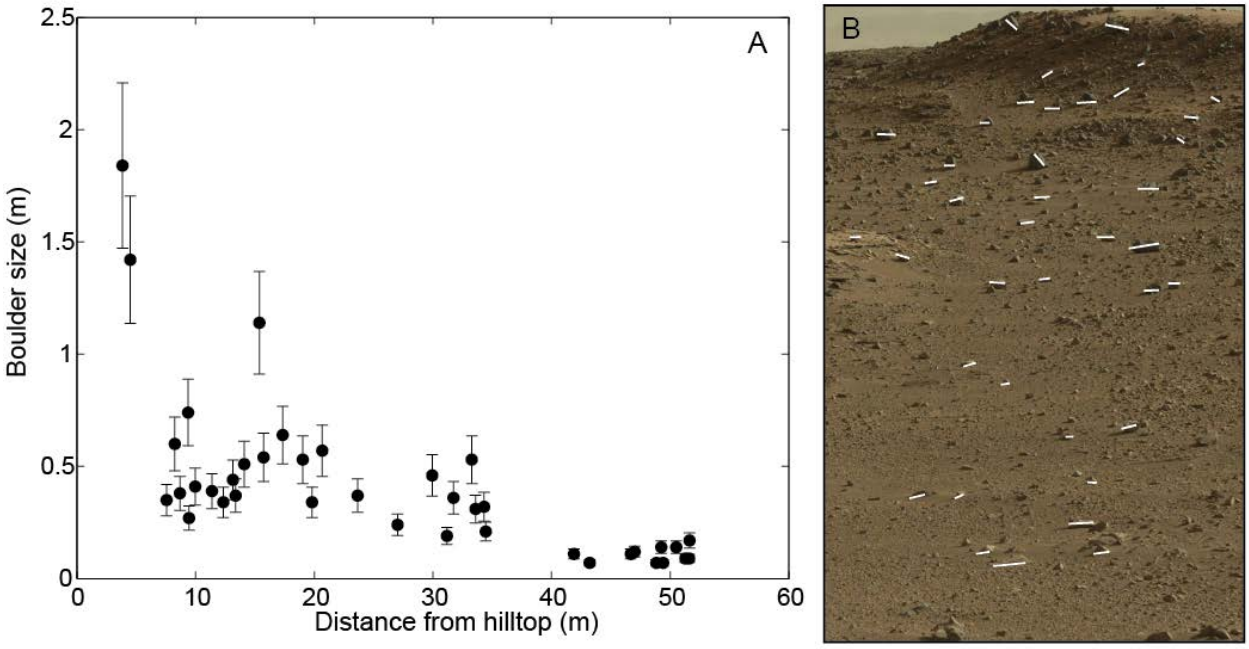

Figure 6.30: Float rock measurements on a remnant hill. (A) Graph shows decreasing rock size with distance from the hilltop shown in (B). Rover-relative distances were calculated and used as a proxy for distance along the transect. The size decrease is interpreted to reflect less first-cycle aeolian erosion on young hilltop rocks and more extensive erosion on older rock further from the degraded scarp. (B) Transect and measured float on a remnant hill just beyond Dingo Gap (sol 538 Mastcam image 0538ML0021250000203544E01_DRCX). White lines indicate the diameters measured on the largest boulders at various elevation levels in the scene.

Physical weathering by impact bombardment and thermal stressing appears to be the main cause of ubiquitous fractures observed along the Curiosity traverse and elsewhere on Mars (e.g., Sullivan et al., 2008; Grotzinger et al., 2005). Gale crater has been subjected to impact bombardment since its formation at ~3.6 Ga (Le Deit et al., 2013; Hartmann and Neukum, 2001). At the surface, small craters in Gale are seen ringed by blocks of fractured rock (Newsom et al., 2015, Fig. 6.8). Millennia of thermal cycling further weathers competent Martian rock as repeated expansion and contraction stresses and fractures the material (Viles et al., 2010). Mars temperature fluctuations occur on a

variety of scales, from diurnal to Milankovitch, around a cold mean annual equatorial temperatures of ~220 K (Schorghofer, 2008). Bedding planes and polygonal fractures provide additional zones of weakness along which bedrock can fracture.

Unlike on Earth, first-cycle aeolian erosion of bedrock is significant on Mars, and occurs because of long exposure of surfaces and the increased energy of grain impacts (Kok, 2010) even with infrequent significant wind events. Aeolian abrasion is evident in Gale crater from yardangs, ventifacts, fluting and polished surfaces of both bedrock and float, but first-cycle abrasion of rock and continued physical weathering must also account for the diminishing of clast size on the surface with distance from bedrock. In all the traversed landscapes, sand was absent except where it was trapped by local topography, and the volume of sand held in dune fields is a tiny fraction of the amount of sediment created during the exhumation of Mount Sharp. This relative paucity of loose sand on the surface of Gale crater indicates that potential sand transport from the surface greatly exceeds the production of sand on the surface ("availability-limited" system of Kocurek and Lancaster, 1999). Although rates of erosion have varied greatly in Gale crater, over geologic time wind transport has been sufficient to exhume nearly all of weathered material from the crater.

The progressive landscape evolution evident along the Curiosity traverse is idealized in Figure 6.31. Exposed fractured bedrock is subjected to aeolian abrasion and continued physical weathering. Fractures in the outcrop form nucleation points for increased weathering and erosion, funneling local flows that widen and deepen fractures by sand abrasion. Continued breakdown of bedrock and aeolian undercutting cause gravity failure of overhanging scarps. Weathering and abrasion then reduce the size of these fallen clasts. When no longer covered by resistant caprock, underlying less-resistant layers deflate at a much faster rate. Areas initially floored by resistant caprock deflate

down as caprock retreats to mesas. When the caprock is completely eroded, remnant hills with a residual cover of disjointed rocks remain. Hill topography is smoothed to flat, and the final surface resulting from this denudation is a desert pavement. On this armored surface, deflation is severely limited, but breaks in the pavement pattern provide holes where erosion is enhanced and the pavement can be eroded from both the surface and sides. Disruptions in the pavement can stem from impacts, fluvial dissection, or the natural uneven distribution of surface clasts. Over geologic time, first cycle erosion by abrasion can also break through the pavement, shrinking cobbles and exposing the surface below. Continued surface deflation by physical weathering and abrasion of surface clasts must ultimately lead to underlying bedrock exposure and a renewal of the cycle.

Despite the absence of fluvial or tectonic processes, the proposed landscape evolution model reflects the same patterns of erosion in classical terrestrial landscape evolution models (e.g., Davis, 1899; Gilbert, 1909). Both historical and the proposed aeolian model show the back-stepping that occurs in differentially resistant layers, and the progressive rounding of hillslopes to flat surfaces. The observation of King (1953) that all fluvially-sculpted landscapes share the same morphologies seems to hold true even when the sculpting fluid is air. The major difference is instead interpreted to be the time scale over which these landscapes form.

6.7 DISCUSSION AND CONCLUSIONS

6.7.1 Reconstruction of Gale crater wind regime over time

The range of aeolian features in Gale crater must have formed over orders of magnitude of time. Although their exact age is unknown, the oldest wind indicators are the exhumation of Mount Sharp, its streamlined morphology, and the position of the Gale

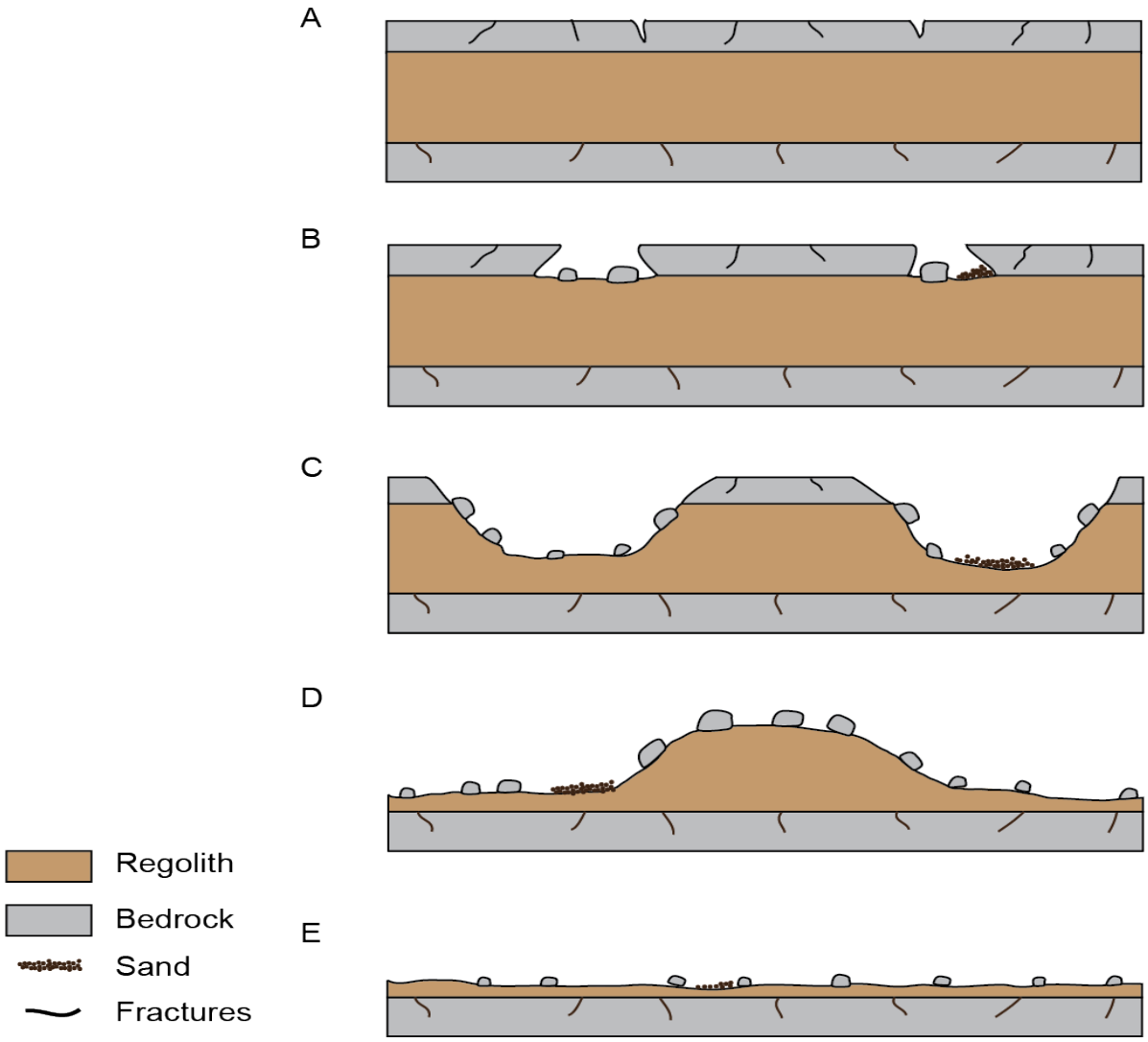

Figure 6.31: Landscape evolution model. (A) Bedrock is exposed at the surface and fractures form nucleation points for enhanced erosion. (B) Fractures in bedrock widen and cut downward through the competent layer, eventually undercutting the outcrop and pieces of outcrop spall off. Some sand shadows accumulate in the lee of local topography. (C) Underlying layers erode faster than bedrock, creating mesas capped by fractured bedrock. Float rock spalled off of the capping unit coats the hillslope. In general, rocks further from the hilltop are older, more heavily ventifacted, and smaller. Sand shadows and larger bedforms are sheltered behind meter-scale topography. (D) Eventually the capping unit is eroded away, leaving a remnant hill covered by ventifacted fragments of the capping unit. Float rock far from the hilltop has been subjected to more aeolian abrasion than more recently formed float near the hilltop, creating a decrease in rock size down the hill. Sand still accumulates in this meter-scale relief. (E) Hill regolith is winnowed away, leaving a heavily ventifacted desert pavement that slowly abrades and deflates until new fractured bedrock is exposed.

crater wind streak, all of which are consistent with northerly formative winds. These long-term wind indicators require first-cycle erosion of bedrock by the wind, as also directly reflected by the yardangs and ventifacts. Yardangs are overwhelmingly oriented N-S, consistent with northerly winds. At much finer spatial and temporal scales, streamlined nodules carved from bedrock at Yellowknife Bay also indicate a northerly wind. Ventifact measurements, some of which are on bedrock, are less consistent and the interpreted westerly winds are at odds with the other wind indicators. Bridges et al. (2014) suggested that the ventifacts may reflect rare high-speed winds, but given the consistency of the other wind indicators, the ventifacts more likely reflect flow affected by local topography or subsequent clast movement. With the exception of ventifacts, therefore, the long time-scale wind indicators overwhelmingly argue that winds from the north have persisted over the geologic-scale time spans over which Mount Sharp formed (Fig. 6.32).

Inferred wind directions from features forming over shorter time-scales reveal a regional north wind that is profoundly modified by crater-scale secondary flow. Crater rim and mound topography delineate the crater moat, and features in the moat are divided between northern and southern halves (Fig. 6.33). Primary wind from the north is argued by the: (1) deflationary pavements and absence of sand dunes at the sand-starved northern apex of Mount Sharp, (2) orientation of sand shadows, and (3) net southward transport of dunes in the Bagnold and Northeastern dune fields. In the northern half of the crater, secondary flow deflection around the topography of Mount Sharp is reflected by the: (1) channelization of dune fields along the flanks of Mount Sharp, (2) SW- facing slipfaces in the Bagnold Dune Field, and (3) SE-facing slipfaces in the Northeastern Dune Field. A second component of secondary flow is evident by: (1) crater-rim downward flow evident in all the northern half dune fields, and (2) mound downward

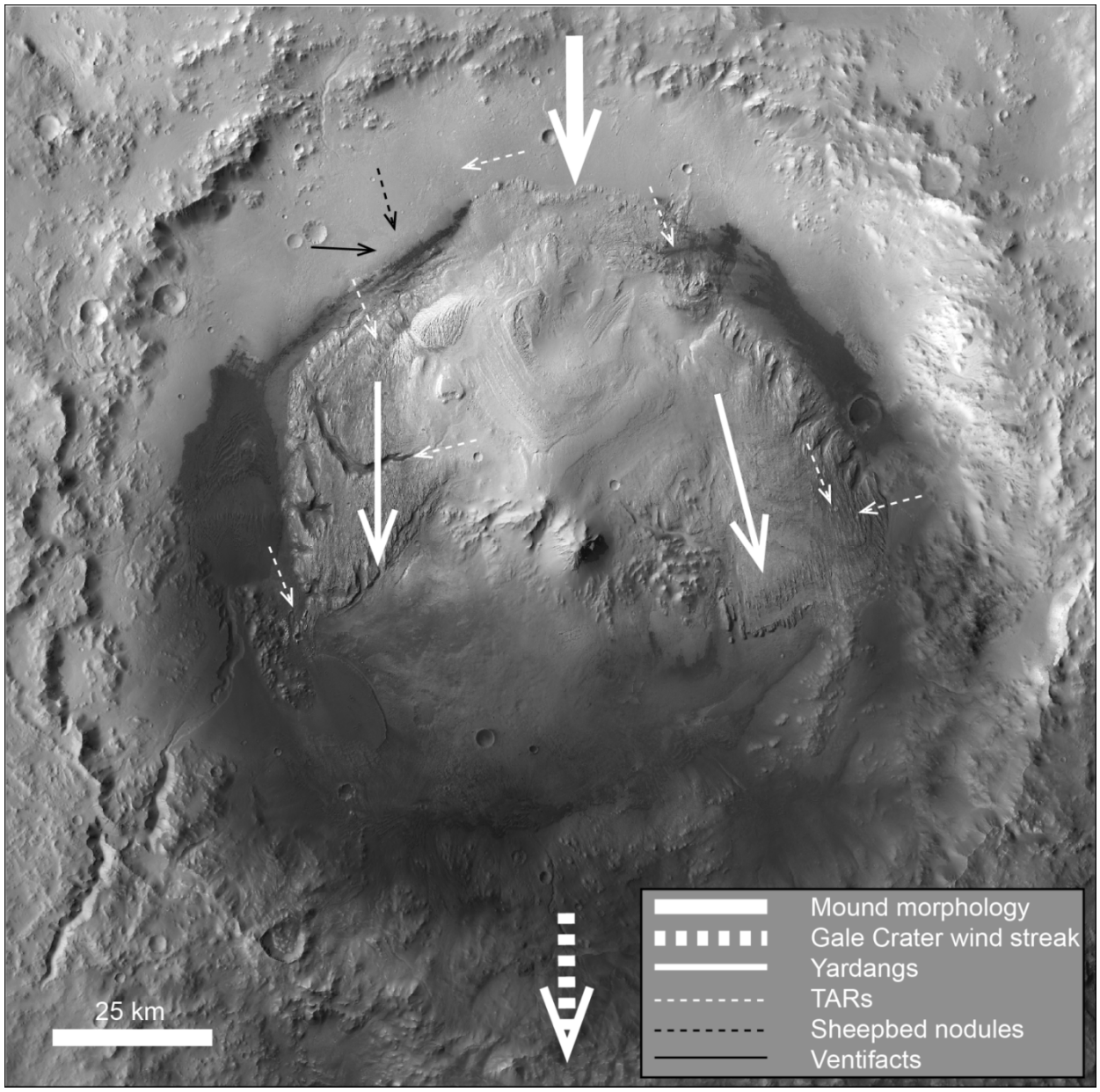

Figure 6.32: Inferred wind directions from aeolian features forming over long time-scales in Gale crater. Yardang orientation varies slightly (12º) from the east to west of Mount Sharp, and is interpreted to result from flow divergence around the 5 km high mound. TAR orientations are shown here in representation of the two dominant modes at locations where TARs are most dense. Both TARs and ventifacts cover a wide range of inferred winds and are thought to be poor indicators of regional circulation because of the influence of topography. The Gale crater wind streak extends south of this image (Fig. 6.3). North-up oriented HRSC background mosaic is also used in all following figures.

flow evident in the Western Dune Field. The interplay of the primary and secondary winds, plus the intrusion of southerly winds characteristic of the southern half of the crater moat, appear responsible for the flow convergence evident in the Western and Northeastern dune fields. In the southern half of the crater floor, small wind streaks on the crater rim and the dominant orientation of the Southern Dunes must arise from crater-rim downward flow. The convergence of northern and southern moat winds regimes is again evident in the northwestern area of the Southern Dunes. The TARs are not addressed here because their orientations appear strongly controlled by local topography, thus making them poor general wind indicators. It is nevertheless notable that TAR orientations, measured largely in the northern half of the crater, are dominated by two directions (71º and 337º) interpreted to result from the NW and NE winds evident from the other indicators.

Integrating all of the wind indicators argues for a crater wind regime with components of regional winds, topography-deflected secondary winds, and topography-created katabatic winds (Fig. 6.34). The relative impact of each component has evolved with exhumation of the mound and, potentially, global climate. Regional primary winds from the north must have dominated during the span of time over which Mount Sharp was exhumed, and emergence of Mount Sharp by excavation would have greatly altered the wind pattern through time. As the moat was formed, topography-deflected secondary flows included funneling of the wind along the mound flanks, and development of a wake in the southern lee of Mount Sharp. Downward flows on the crater-rim and mound are interpreted as topography-created katabatic winds, which have been emphasized in circulation models of Gale crater (Tyler and Barnes, 2013; Hobbs et al., 2010). Katabatic winds form from atmospheric density gradients caused by fluctuations in temperature, and can set up in opposition to large-scale regional flows (Rafkin et al., 2001). Such

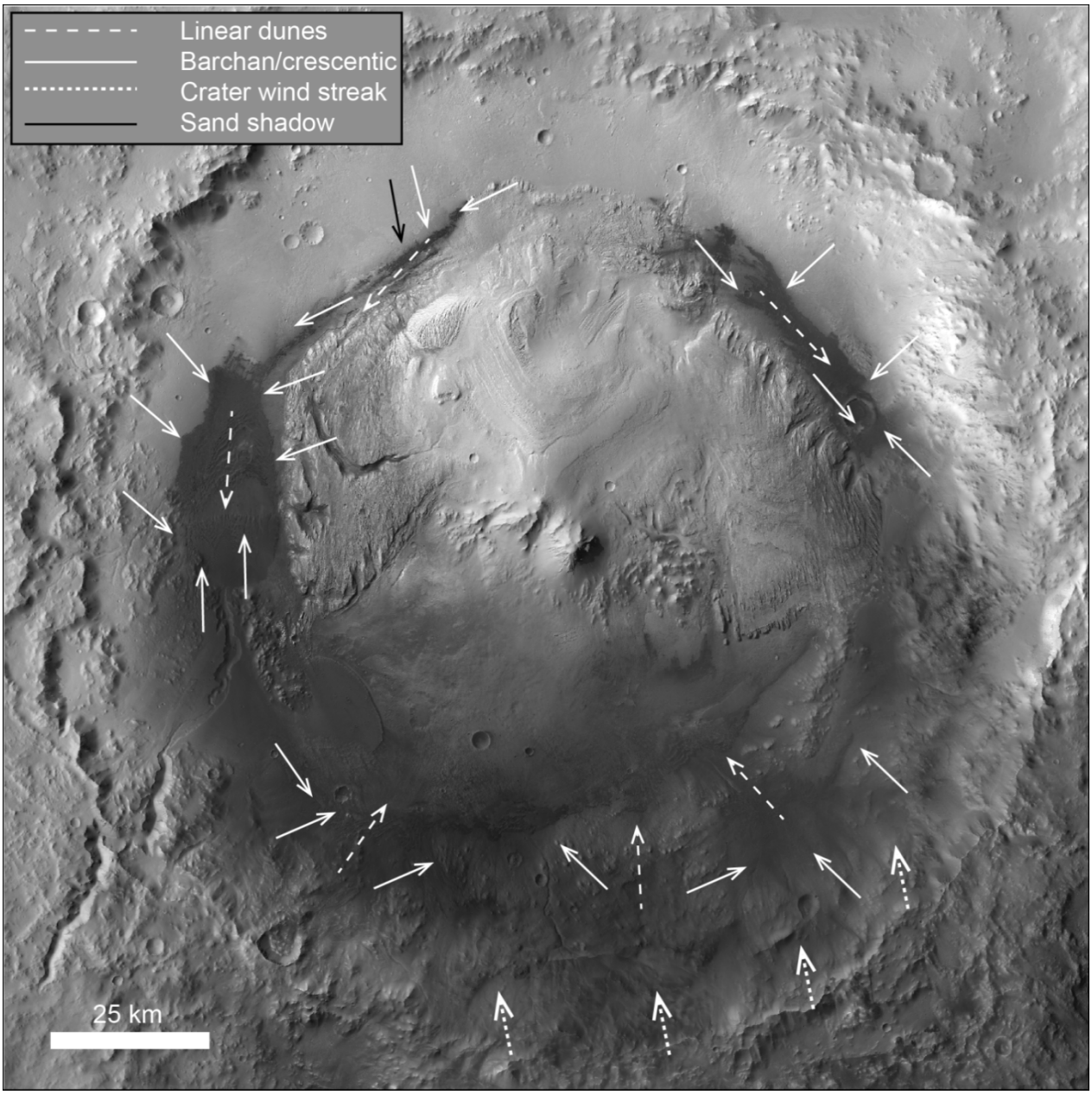

Figure 6.33: Inferred recent wind directions from aeolian features forming on short time-scales in Gale crater. Wind indicators are divided, with interpreted northerly winds dominating the northern half and southerly winds dominating the southern half. Note the relative association of wind direction and crater rim orientation in the south, and the apparent divergence of wind directions around Mount Sharp in the north.

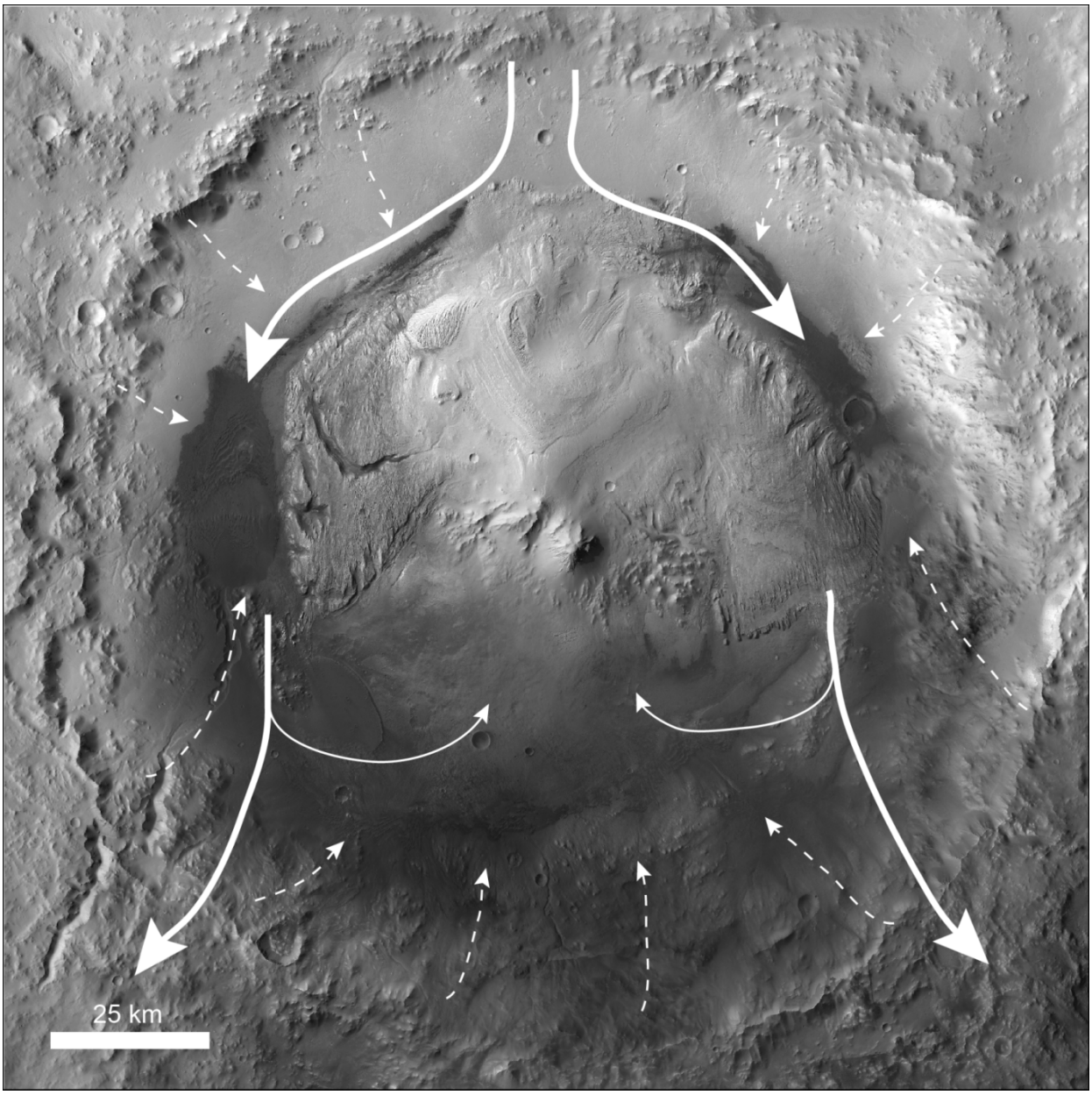

Figure 6.34: Circulation model for Gale crater interior. Regional northerly winds (solid lines) diverge as they encounter Mount Sharp, funneling between mound and rim to the east and west. Regional flows shed eddies and turbulent vortices in the wake of Mount Sharp. Katabatic slope-flow winds (dashed lines) flow inward down rim topography, dominating short time-scale morphologies. Eddies and katabatic flows oppose regional winds and account for convergence in the Western and Northeastern Dune Fields. Line thickness and arrow size are schematic representations of relative wind strength.

winds would flow radially into the crater moat from the top of the crater rim, as is evident from the recently-formed wind indicators, or from the mound, as is evident in the Western Dune Field (Fig. 6.33). Katabatic winds would reinforce regional winds in the north, and lee return flows behind Mount Sharp in the south. Current wind indicators argue for a modern dominance of crater-rim katabatic winds (Fig. 6.33), in contrast to the long-time wind indicators that argue for a dominance of regional northerly winds (Fig. 6.32).

The above analysis is based upon the interpretation of geomorphic features that span a range of spatial and temporal scales. Modeling of wind circulation in Gale crater is typically conducted for a particular set of conditions, rather than integrated over geologic spans of time. Hobbs et al. (2010) modeled circulation in Gale at ~4 km scale resolution under dust-storm atmospheric conditions. The model revealed a dominance of regional NNW winds and topography-driven deflection in agreement with the above results. During the two modeled Martian sols, both katabatic (downslope) and anabatic (upslope) winds occurred, but these were weak compared to the regional NNW winds. Tyler and Barnes (2013) modeled the mean diurnal cycle in Gale crater over 20 sols and at the same ~4 km resolution. Their model highlights the diurnal changes in wind regime, characterized by regional north winds deflected by topography in the daytime, with strong katabatic winds flowing down Mount Sharp and the crater rim at night. These models both agree with the conclusions of this study, but further indicate that variations in the crater wind regime are ongoing, rather than changing gradually with the exhumation of Mount Sharp. The suggested daily variations in wind regime are perhaps poorly represented in even the shortest time-scale aeolian features, and as such, our interpretation represents an integrated view of winds in Gale crater over geologic time.

6.7.2 Aeolian-dominated landscape evolution

At all scales of observation, from orbital images to surface views by Curiosity, the landscape in Gale crater is dominated by aeolian features. Evidence for subaqueous processes occurs only in the stratigraphic record and in relict or exhumed features, whereas no contemporary features were observed characteristic of landscapes eroded by water (e.g., dendritic drainage networks). This supports the representation of the landscape of Gale crater as one fashioned by physical weathering, gravity, and aeolian processes. Most of the landscape represents a sand-starved, erosional system, but the available sand is organized into aeolian bedforms comprising a relatively small volume of sediment. This observation is consistent with the interpretation that the inferred processes (i.e., physical weathering, downslope wasting, and aeolian abrasion and deflation) are sufficient for moat excavation and Mount Sharp exhumation from an initially filled crater.

The landscape patterns observed at the surface argue that denudation occurs in progressive stages from continuous bedrock-capped layers, to separated bedrock-capped mesas, to remnant hills capped by bedrock clasts, to desert pavements on rocky plains. Processes that drive the system include bedrock fracturing by impacts and thermal stress, aeolian abrasion that diminishes bedrock and widens fractures, and aeolian deflation that removes sediment. Preferential aeolian erosion of less resistant beds creates overhanging scarps that fail due to gravity. One implication of these processes is that first-cycle erosion of bedrock, directly evident by yardangs and ventifacts, is otherwise widely present on the Martian surface. A second implication is that desert pavements, generally considered as stable features on Earth, must undergo continued aeolian abrasion and deflation, and are ultimately removed on Mars. Given the documented extremely slow weathering rates on Mars and the apparent infrequency of high-energy wind events,

landscape evolution in Gale crater must be accredited to either the geologically long periods over which a surface is exposed, or much higher rates of surface denudation under a very different climatic regime at the time of initial excavation.

6.8 Acknowledgments

This material is partly based upon work supported by the National Aeronautics and Space Administration, under Contract No. 1450036 issued through the MSLPS Program, and the National Science Foundation Graduate Research Fellowship under Grant No. DGE-1110007. Authors thank the MSL team, Fred Calef for his work on orbital image mosaicking, and reviewers James Zimbelman and Simone Silvestro for their helpful feedback and suggestions.

Chapter 7: Conclusions

The topics covered in this dissertation span multiple planetary bodies and time scales of billions of years, but all address open questions surrounding the formation and preservation of patterns in aeolian systems. The dune-field patterns addressed in Chapter 2 can be parameterized by the density of interactions, and when presented in terms of a dimensionless interaction index, the relationship between interaction density and spacing collapses to a point that depends only on morphology. The lack of variability in interaction index over a range of spacings implies that patterns in aeolian dune fields coarsen but do not change over time. Furthermore, the pattern similarity between Earth, Mars, and Titan demonstrates that the dynamic steady-state pattern for dunes of a given size is independent of planetary-scale boundary conditions. Those boundary conditions that do affect that pattern are expressed in the dune morphology. Linear and crescentic morphologies collapse to two different interaction indices because of differing mechanisms by which interactions occur in each morphology, and the relative stability of linear morphologies over crescentic morphologies in variable winds. However, in both cases when interactions occur they are conserved, either propagating a replacement defect or propelling a Y-junction downstream. Regardless of the scale, dune fields rapidly reach an equilibrium pattern that can be characterized by a density of interactions, a dune morphology, and a mean spacing.

Dune interactions control the development and equilibrium of dune-field patterns in modern systems, and it is reasonable to expect that interactions influenced the development of ancient systems. Similarly, it was also expected that a stratigraphic signature of interactions must be preserved in the rock record. In Chapter 3, five examples of interaction-generated stratigraphy confirm the presence of interactions in

ancient systems, and demonstrate a workflow by which one type of interaction architecture can be identified in outcrop. Only in plan-view and low-angle oblique exposures can the curvature in the interaction bounding surface be established, but this highlights an ambiguity in bounding surfaces seen in cross-section. Now that interaction surfaces are known to occur in the rock record, methods for interpreting ancient aeolian strata must be updated to incorporate interaction surfaces.

Interactions express the autogenic processes that alter dune fields, but allogenic processes also affect aeolian systems. In Chapter 4, the case study of Jurassic Entrada Sandstone demonstrates the relative brevity in time represented by the identified stratigraphic units, as compared with the time scales necessary to achieve systems capable of depositing those units. Units were predominantly deposited by a well-developed dune field, but the record of the growth of those dune fields is largely absent. This example demonstrates how the preservation of aeolian systems is non-linear in time and significant events even including entire dune fields may not be preserved. Autogenic processes including dune interactions and cannibalization by trough scour determine the character of the associated aeolian strata, but what actually gets preserved from a passing dune field is controlled by allogenic forcings external to the dune field dynamics.

The interplay between autogenic and allogenic forces influences the morphologies of aeolian patterns on both Earth and Mars. In a radially symmetric system, such as a filled crater, allogenic changes in wind direction and magnitude will affect the landscape in the same way, but to varying degrees and at varying places. If the feedbacks between topographic deflection of winds and erosion of topography by winds can be said to be an autogenic feedback, then the debate regarding the formation mechanism of intra-crater layered mounds can be distilled to whether the mounds were formed by autogenic (i.e., erosion of existing deposits by topographically-channeled winds), or allogenic (i.e., in-

place deposition controlled by changes in climate) conditions. The physical and numerical models discussed in Chapter 5 demonstrated that aeolian erosion of existing deposits is a feasible mechanism by which the spectrum of intra-crater mound morphologies could have formed. In the experiments, sediment-laden turbulent flows deflected around and along topography, setting up gradients in shear stress and erosion potential, and eroded deposits in crater interiors preferentially along the rim to create a retreating mound morphology. Although allogenic processes would have controlled the filling of the crater and the direction and magnitude of the winds, the retreating mound morphologies arise from the autogenic feedback between topography and wind. Because both the craters and the spectrum of retreating mound morphologies are radially symmetric (for the most part), allogenic changes in wind direction or atmospheric density would not alter the continued erosion or spectrum of morphologies resulting from autogenic feedbacks between topography and turbulent fluid flow. The conclusions of Chapter 5 are reinforced by the observations and conclusions of the Gale crater case study in Chapter 6. From the crater-scale wind streak to the centimeter-scale streamlined nodules, the wind directions preserved in the features within Gale crater are consistent with unidirectional turbulent winds deflected by topographic obstacles. In addition, small-scale features with short formation time scales showed a superimposed katabatic wind signature that was subordinate to the formative northerly winds responsible for the majority of the mound erosion. Although the abundance of erosional features on Mount Sharp rules out a formation mechanism in which intra-crater layered mounds are purely depositional, the aeolian-erosional and aeolian-depositional formation mechanisms are not mutually exclusive. Significant erosion has clearly altered the morphology of Mount Sharp, and basal strata of Mount Sharp are suggested to have lacustrine origins (Grotzinger et al., 2015; Grotzinger et al., 2014). However, strata form the upper mound

may yet be revealed to have a dust-fall origin associated with Milankovitch cycles (Lewis and Aharonson, 2014). Whatever the original deposition mechanism, the record of winds stored in geomorphic features on and around Mount Sharp shows the mound has been extensively altered by aeolian erosion perpetrated by largely unidirectional northerly winds.

The projects discussed in this dissertation examine the patterns created and preserved by aeolian systems on Earth, Mars, and briefly Titan. Aeolian systems on other planetary bodies not discussed include straight-crested ripples on the comet Churyumov-Gerasimenko (67P), which form despite the comet's lack of an atmosphere (Thomas et al., 2015), crescentic and linear dunes forming near the limit of existing image resolution on Venus (Greeley and Arvidson, 1990), and patterned features on the northeastern edge of recently acquired images of Pluto that may be aeolian in origin (Diniega et al., 2017). The diversity of exotic conditions in which aeolian patterns form suggests that pattern formation is a fundamental fallout of sediment transport independent of boundary conditions. The limits of this idea are currently unknown, but continued study of these patterns, particularly as they form in exotic boundary conditions, could lead to improved understanding of these systems in general and improvements in predictive techniques on Earth.

Appendix A: Dune fields measured in Chapter 2

Contained within this Appendix are the names, locations, and measured spacings of dune fields plotted in Figures 2.2 and 2.3 (Table A.1). Notable references discussing the dune field or desert are also given. The measured dune field spacing ranges from 25 m in the Registan Desert to 4.2 km in the Taklimakan Desert. Destabilized sand forming dunes on a flat bed initially forms dunes with spacings of ~20 m (Elbelrhiti et al., 2005), thus the range of spacings presented in Table A.1 is comprehensive for the range of dune spacings on Earth.

Dune fields on Mars and Titan were also included in this study and were measured using High Resolution Imaging Science Experiment and Cassini Radar images, respectively (Table A.2).

Table A.1: Study locations on Earth and notable references

Location	Center coordinates of study area	Dune type	Spacing (m)	Reference
Registan Desert (small-scale)	29.07° N, 065.22° E	Crescentic	25	(Whitney, 2007)
Coastal Peru	11.63° S, 077.17° W	Crescentic	58	(Finkel, 1959)
Baja California	27.98° N, 114.15° W	Crescentic	68	(Inman et al., 1966)
Coastal Somalia	04.89° N, 047.94° E	Crescentic	141	(Fagotto, 1987)
White Sands Dune Field	32.81° N, 106.28° W	Crescentic	182	(McKee, 1966)
Mu Us Desert	38.36° N, 102.98° E	Crescentic	307	(Sun, 2000)
Western Sahara (small-scale)	18.19° N, 012.91° E	Crescentic	321	(Lancaster et al., 2002)
Kyzylkum Desert	44.07° N, 065.12° E	Crescentic	514	(Maman et al., 2011)
Grand Erg Oriental Desert	32.17° N, 009.23° E	Crescentic	1209	(Wilson, 1971)
Karakum Desert	39.17° N, 059.32° E	Crescentic	1345	(Maman et al., 2011)
Southwestern Chad	13.17° N, 016.21° E	Crescentic	1658	(Mauz and Felix-Henningsen, 2005)
Western Sahara (large-scale)	17.96° N, 010.83° W	Crescentic	1988	(Lancaster et al., 2002)
Thar Desert	27.25° N, 069.29° E	Crescentic	2072	(Kar, 1993)
Rub' al Khali Desert	054.24° E, 22.38° N	Crescentic	2800	(Goudie et al., 2000)
Registan Desert (large-scale)	30.80° N, 065.77° E	Crescentic	3558	(Whitney, 2007)
Taklimakan Desert	39.80° N, 087.68° E	Crescentic	4264	(Wang et al., 2002)
Rice Valley	33.95° N, 114.77° W	Linear	154	(Zimbelman et al., 1995)
Tanami Desert	20.21° S, 131.49° E	Linear	266	(Wasson et al., 1988)
Kalahari Desert	24.55° S, 019.17° E	Linear	566	(Bullard et al., 1995)
Simpson Desert	25.15° S, 135.03° E	Linear	675	(Folk, 1971)
Great Victoria Desert	27.39° S, 129.69° E	Linear	685	(Pell et al., 1999)
Southwestern Sahara	17.69° N, 014.91° W	Linear	1124	(Lancaster et al., 2002)
Gibson Desert	21.68° S, 122.97° E	Linear	1299	(Wasson et al., 1988)
Northwestern Sahara	21.21° N, 009.59° W	Linear	1759	(Lancaster et al., 2002)
Rub’ al Khali Desert	17.98° N, 048.40° E	Linear	2297	(Goudie et al., 2000)
Namib Sand Sea	24.25° S, 015.17° E	Linear	2410	(Lancaster, 1989)
Grand Erg Oriental	29.25° N, 004.75° E	Linear	4012	(Wilson, 1971)

Table A.2: Study locations on Mars and notable references

Location	Center coordinates of study area	Dune type	Spacing (m)	Reference
Chasma Boreal – Mars	84.76° N, 000.00° E	Crescentic	238	(Schatz et al., 2006)
Siton Undae – Mars	72.53° N, 054.30° W	Crescentic	255	(Bishop, 2007)
Lopez crater – Mars	14.54° S, 097.66° E	Crescentic	323	(Zimbelman and Johnson, 2016)
Fensal Sand Sea – Titan	10° N, 050° W	Linear	2700	(Radebaugh et al., 2008)
Fensal Sand Sea – Titan	06° S, 040° W	Linear	4660	(Radebaugh et al., 2010)

Appendix B: Determination of competence

Large-eddy simulation (LES) was used to model turbulent flow over crater geometries with 1:10 and 1:30 depth-to-diameter (h:D) ratios. For h:D = 1:10 and 1:30, we selected D = 15 km and D = 150 km diameter craters, respectively (Fig. B1) (Robbins and Hynek, 2012); thus, maximum vertical relief was 1.5 km and 5 km for h:D = 1:10 and 1:30, respectively. These two baseline geometries were then given interior fill at four representative stages along the erosional spectrum observed in wind tunnel experiments. The LES computational domain was decomposed with 128 nodes in each direction, corresponding to grid resolution of 234 m and 2.3 km for h:D = 1:10 and 1:30, respectively. We assume that the prevailing planetary boundary layer depth (Michaels and Rafkin, 2004; Petrosyan et al., 2011) exhibits a depth that is at least twice the maximum vertical crater relief (i.e., the crater can be treated – numerically – as a topographic feature of the roughness sublayer). LES was used to model flow over these eight idealized topographies and produced a non-dimensional basal shear stress distribution field for each modeled domain. These non-dimensional values are normalized by a maximum shear stress in the domain such that:

$$\tau_{LES} = \frac{\tau_b}{\tau_{max}} \tag{B.1}$$

For a given wind speed, the maximum shear velocity can be estimated using the Law of the Wall (Coles, 1956):

$$U = \frac{u_{*max}}{\kappa} \ln\left(\frac{z}{z_0}\right) \tag{B.2}$$

where U is the ambient wind speed, κ the Von Karman constant, u_* the shear velocity, z a reference height above the bed, and z_0 a roughness length scale (Table B1). By definition, shear stress and shear velocity can be related by:

$$\tau = \rho_a u_*^2 \tag{B.3}$$

where ρ_a the density of the atmosphere. Thus by solving equation (2) for u_{*max} and using the definition in equation (3), τ_b can be given in terms of known values. Equation (3) can then be used to determine a shear velocity distribution across the modeled crater domains for a given ambient wind speed:

$$u_* = \sqrt{\tau_{LES}\left(\frac{U\kappa}{\ln\left(\frac{z}{z_0}\right)}\right)^2} \tag{B.4}$$

To initiate saltation of a given grain, shear velocities on the grain must meet or exceed the critical shear velocity for the grain diameter. On both Earth and Mars, once saltation has been initiated, it can be maintained for shear velocity values below the fluid threshold critical shear velocity. This hysteresis gives rise to an impact threshold critical shear velocity curve described by the numerical approximation (Kok, 2010, equation 25):

$$u_{it} = c_1\left(\frac{700}{P}\right)^{\frac{1}{6}}\left(\frac{220}{T}\right)^{\frac{2}{5}}\exp\left(\left(\frac{c_2}{d}\right)^3 + c_3\sqrt{d} - c_4 d\right) \tag{B.5}$$

where P is atmospheric pressure, T is temperature, d is grain size, and $c_{1\text{-}4}$ are coefficients listed in Table B1.

Local slope also affects transport potential. A correction for slope is given in terms of shear stress (Garcia, 2008). Using the relationship between shear stress and shear velocity in (3), this can be converted to a correction for shear velocity:

$$u_{its} = u_{it} S_c \tag{B.6}$$

$$S_c = \left[\cos(\alpha) \left(\cos(\theta) \sqrt{1 - \left(\frac{\tan(\theta)}{\tan(\phi)} \right)^2} - \frac{\tan(\alpha)}{\tan(\phi)} \right) \right]^{\frac{1}{2}} \tag{B.7}$$

where α is the longitudinal slope, θ the crosswise slope, and φ the angle of repose. Note that α is negative for uphill transport. u_{its} describes the impact threshold critical shear velocity as a function of grain size and local slope.

After calculating local slope across the domains of all eight crater models, LES-derived shear velocity values can be considered the local critical shear velocity and compared with u_{its} to determine the largest mobile grain size, or competence. Figure 5.3 in Chapter 5 shows the calculated largest mobile grain size in the crater for grain diameters of 50 to 1000 μm. The electrostatic effects associated with dust transport are beyond the scope of this work, thus dust-sized particles ($d < 50$ μm) are ignored (Shao and Lu, 2000). We emphasize that the above calculations are based on time-averaged basal shear stress, but that the inherently unsteady nature of vortex shedding means surface stress will exhibit large time variability. In the present treatment these fluctuations are averaged out so that the results model the general behavior over geologic time.

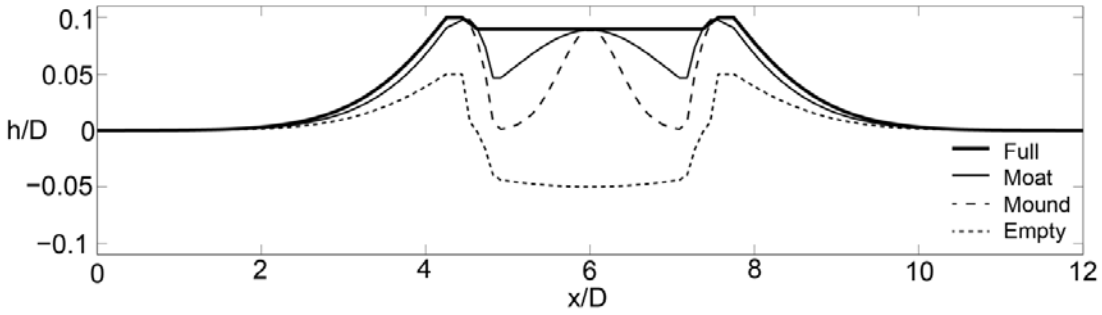

Figure B.1: Topographic profiles of four erosional stages modeled with large eddy simulation. 1:30 depth-to-diameter geometry. Axes are normalized by the crater diameter D.

Table B.1: Parameters used in calculation

	Value	**Units**	**Parameter**
g	3.71	m/s^2	Martian acceleration due to gravity
ρ_a	0.02	kg/m^3	Atmospheric density
ρ_p	3000	kg/m^3	Particle density, taken to be basaltic sediment
κ	0.407		Von Karman constant
z	1	m	Reference height above the bed
z_0	3×10^{-4}	m	Roughness length scale
U	1 to 100	m/s	Wind speed
T	200	K	Temperature
P	1000	Pa	Pressure
ϕ	30	°	Angle of repose
c_1	5.5×10^{-3}	m/s	Impact threshold critical shear velocity curve coefficient
c_2	49	μm	Impact threshold critical shear velocity curve coefficient
c_3	0.29	$\mu m^{-1/2}$	Impact threshold critical shear velocity curve coefficient
c_4	3.84×10^{-3}	μm^{-1}	Impact threshold critical shear velocity curve coefficient

References

Ahlbrandt, T.S. and Fryberger, S.G., 1981, Sedimentary features and significance of interdune deposits. SEPM Special Publication, 293-314.

Allen, J. R. L., 1963, The classification of cross-stratified units with notes on their origin. Sedimentology, v. 2, no. 2, p. 93-114.

Allen, J. R. L., 1970, A quantitative model of climbing ripples and their cross-laminated deposits. Sedimentology, v. 14, no. 1-2, p. 5-26.

Allen, P.A., Verlander, J.E., Burgess, P.M. and Audet, D.M., 2000, Jurassic giant erg deposits, flexure of the United States continental interior, and timing of the onset of Cordilleran shortening. Geology, 28, 159-162.

Anderson, R., and Bell, J., 2010, Geologic mapping and characterization of Gale Crater and implications for its potential as a Mars Science Laboratory landing site. The Mars Journal, v. 5, p. 76-128.

Armstrong, J. C., Titus, T. N., and Kieffer, H. H., 2005, Evidence for subsurface water ice in Korolev crater, Mars. Icarus, 173(2), 360-372.

Arvidson, R. E., Guinness, E. A., Moore, H. J., Tillman, J., and Wall, S. D., 1983, Three Mars Years: Viking Lander 1 Imaging Observations. Science 222, 463-468.

Arvidson, R., Guinness, E., and Lee, S., 1979. Differential Aeolian Redistribution Rates on Mars. Nature 278, 533-535.

Atwood-Stone, C., and McEwen, A., 2013, Avalanche slope angles in low-gravity environments from active Martian sand dunes. Geophys. Res. Lett. 40, doi:10.1002/grl.50586.

Baas, A. C. W., 2007, Complex systems in aeolian geomorphology. Geomorphology, v. 91, no. 3–4, p. 311-331.

Bagnold, R. A., 1941, The Physics of Blown Sand and Desert Dunes, London, Chapman and Hall.

Baitis, E., Kocurek, G., Smith, V., Mohrig, D., Ewing, R.C. and Peyret, A.P.B., 2014, Definition and origin of the dune-field pattern at White Sands, New Mexico. Aeolian Research, 15, 269-287.

Balme, M., Berman, D. C., Bourke, M. C., and Zimbelman, J. R., 2008, Transverse Aeolian Ridges (TARs) on Mars. Geomorphology 101, 703-720.

Benan, C.A.A. and Kocurek, G., 2000, Catastrophic flooding of an aeolian dune field: Jurassic Entrada and Todilto Formations, Ghost Ranch, New Mexico, USA. Sedimentology, 47, 1069-1080.

Bennett, K. A., and Bell, J. F., 2016, A global survey of martian central mounds: Central mounds as remnants of previously more extensive large-scale sedimentary deposits. Icarus, 264, 331-341.

Bibring, J. P., Langevin, Y., Mustard, J. F., Poulet, F., Arvidson, R., Gendrin, A., Gondet, B., Mangold, N., Pinet, P., and Forget, F., 2006, Global mineralogical and aqueous Mars history derived from OMEGA/Mars Express data. Science 312, 400-404.

Bishop, M. A., 2007, Point pattern analysis of north polar crescentic dunes, Mars: A geography of dune self-organization. Icarus, v. 191, no. 1, p. 151-157.

Bishop, S.R., Momiji, H., Carretero-Gonzalez, R. and Warren, A., 2002, Modelling desert dune fields based on discrete dynamics. Discrete Dynamics in Nature and Society, 7, 7-17.

Bjerrum, C.J. and Dorsey, R.J., 1995, Tectonic controls on deposition of Middle Jurassic strata in a retroarc foreland basin, Utah-Idaho trough, western interior, United States. Tectonics, 14, 962-978.

Blackwelder, E., 1934, Yardangs: Geological Society of America Bulletin, v. 45, no. 1, p. 159-166.

Blake, D. F. et al., 2013, Curiosity at Gale Crater, Mars: Characterization and Analysis of the Rocknest Sand Shadow. Science 341, 1239505. doi: 10.1126/science.1239505

Blakey, R.C., 1988, Basin tectonics and erg response. Sedimentary Geology, 56, 127-151.

Blakey, R.C., Peterson, F. and Kocurek, G., 1988, Synthesis of late Paleozoic and Mesozoic eolian deposits of the Western Interior of the United States. Sedimentary Geology 56 3-127.

Bouchette, F., Schuster, M., Ghienne, J. F., Denamiel, C., Roquin, C., Moussa, A., Marsaleix, P., and Duringer, P., 2010, Hydrodynamics in Holocene Lake Mega-Chad. Quaternary Res. 73, 226-236.

Bourke, M. C., 2010, Barchan dune asymmetry: Observations from Mars and Earth. Icarus 205, 183-197.

Breed, C. S., Fryberger, S. G., Andrews, S., McCauley, C., Lennartz, F., Gebel, D., and Horstman, K., 1979, Regional studies of sand seas using Landsat (ERTS) imagery: A study of global sand seas, v. 1052, p. 305-398.

Bridge, J., and Best, J., 1997, Preservation of planar laminae due to migration of low-relief bed waves over aggrading upper-stage plane beds: comparison of experimental data with theory. Sedimentology, v. 44, no. 2, p. 253-262.

Bridges, N. T. et al., 2014, The rock abrasion record at Gale Crater: Mars Science Laboratory results from Bradbury Landing to Rocknest. J. Geophys. Res. Planets 119, 1374-1389.

Bridges, N. T., Spagnuolo, M. G., de Silva, S. L., Zimbelman, J. R., and Neely, E. M., 2015, Formation of gravel-mantled megaripples on Earth and Mars: Insights from the Argentinean Puna and wind tunnel experiments. Aeolian Res. 17, 49-60.

Bristow, C., and Hill, N., 1998, Dune morphology and palaeowinds from aeolian sandstones in the Miocene Shuwaihat Formation, Abu Dhabi, United Arab Emirates. Quaternary Deserts and Climatic Change, p. 553-564.

Brookfield, M., 1977, The origin of bounding surfaces in ancient aeolian sandstones. Sedimentology, v. 24, no. 3, p. 303-332.

Brothers, S. C., Kocurek, G., Brothers, T. C., and Buynevich, I., 2017, Stratigraphic architecture resulting from dune interactions. White Sands Dune Field, New Mexico: Sedimentology, no. doi:10.1111/sed.12320.

Bullard, J. E., Thomas, D. S. G., Livingstone, I., and Wiggs, G. F. S., 1995, Analysis of linear sand dune morphological variability, southwestern Kalahari desert. Geomorphology, v. 11, no. 3, p. 189-203.

Busby-Spera, C.J., 1988, Speculative tectonic model for the early Mesozoic arc of the southwest Cordilleran United States. Geology, 16, 1121-1125.

Cabrol, N. A., and Grin, E. A., 2010, Lakes on Mars, Amsterdam, Elsevier, Book, Whole.

Cabrol, N. A., Grin, E. A., Newsom, H. E., Landheim, R., and McKay, C. P., 1999, Hydrogeologic evolution of Gale crater and its relevance to the exobiological exploration of Mars. Icarus, v. 139, no. 2, p. 235-245.

Carr-Crabaugh, M. and Kocurek, G., 1998, Continental Sequence Stratigraphy of a Wet Eolian System: A Key to Relative Sea-Level Change. Relative Role of Eustasy, Climage, and Tectonism in Continental Rocks 213-228.

Christensen, P. R., 1986, Regional dust deposits on Mars: Physical properties, age, and history. J. Geophys. Res. 91, 3533-3545.

Coles, D., 1956, The law of the wake in the turbulent boundary layer. Journal of Fluid Mechanics, 1, 191-226.

Conway, S. J., Hovius, N., Barnie, T., Besserer, J., Le Mouelic, S., Orosei, R., and Read, N. A., 2012, Climate-driven deposition of water ice and the formation of mounds in craters in Mars' north polar region. Icarus, 220(1), 174-193.

Cooke, R. U., 1970, Stone Pavements in Deserts. Annals of the Association of American Geographers 60, 560-577.

Cooper, W. S., 1958, Coastal Sand Dunes of Oregon and Washington, Geological Society of America.

Costard, F. M., and Kargel, J. S., 1995, Outwash Plains and Thermokarst on Mars. Icarus, v. 114, no. 1, p. 93-112.

Courrech du Pont, S. C., Narteau, C., and Gao, X., 2014, Two modes for dune orientation. Geology 42, 743-746.

Crabaugh, M. and Kocurek, G., 1993, Entrada Sandstone: an example of a wet aeolian system. Geological Society, London, Special Publications, 72, 103-126.

Craddock, R. A., and Howard, A. D., 2002, The case for rainfall on a warm, wet early Mars. Journal of Geophysical Research-Planets, 107(E11).

Davis, W. M., 1899, The geographic cycle. Geography J. 14, 481-504.

Day, M., and Kocurek, G., 2016, Observations of an aeolian landscape: From surface to orbit in Gale Crater. Icarus, DOI:10.1016/j.icarus.2015.09.042.

Day, M., Anderson, W., Kocurek, G., and Mohrig, D., 2016, Carving intracrater layered deposits with wind on Mars: Geophysical Research Letters, v. 43, no. 6, p. 2473-2479.

de Silva, S. L., Spagnuolo, M. G., Bridges, N. T., and Zimbelman, J. R., 2013, Gravel-mantled megaripples of the Argentinean Puna: A model for their origin and growth with implications for Mars. Geol. Soc. Am. Bull. 125, 1912-1929.

Dickinson, W.R. and Gehrels, G.E., 2009, U-Pb ages of detrital zircons in Jurassic eolian and associated sandstones of the Colorado Plateau: Evidence for transcontinental dispersal and intraregional recycling of sediment. GSA Bulletin, 121, 408-433.

Dickinson, W.R. and Gehrels, G.E., 2010, Insights into North American Paleogeography and Paleotectonics from U–Pb ages of detrital zircons in Mesozoic strata of the Colorado Plateau, USA. International Journal of Earth Sciences, 99, 1247-1265.

Diniega, S., Glasner, K. and Byrne, S., 2010, Long-time evolution of models of aeolian sand dune fields: Influence of dune formation and collision. Geomorphology, 121, 55-68.

Diniega, S., Kreslavsky, M., Radebaugh, J., Silverstro, S., Telfer, M., and Tirsch, D., 2017, Our evolving understanding of aeolian bedforms, based on observation of dunes on different worlds. Aeolian Research v. DOI: 10.1016/j.aeolia.2016.10.001.

Doré, A., Bonneton, P., Marieu, V., and Garlan, T., 2016, Numerical modeling of subaqueous sand dune morphodynamics. Journal of Geophysical Research: Earth Surface, v. 121, no. 3, p. 565-587.

Durán, O., Parteli, E. J., and Herrmann, H. J., 2010, A continuous model for sand dunes: Review, new developments and application to barchan dunes and barchan dune fields. Earth Surface Processes and Landforms, v. 35, no. 13, p. 1591-1600.

Eastwood, E. N, Nield, J., Baas, A., and Kocurek, G., 2011, Modelling controls on aeolian dune-field pattern evolution. Sedimentology, v. 58, no. 6, p. 1391-1406.

Eastwood, E. N., Kocurek, G., Mohrig, D., and Swanson, T., 2012, Methodology for reconstructing wind direction, wind speed and duration of wind events from aeolian cross-strata. J. Geophys. Res. 117, doi:10.1029/2012JF002368.

Edgett, K. S., and Malin, M. C., 2000, New views of Mars eolian activity, materials, and surface properties: Three vignettes from the Mars Global Surveyor Mars Orbiter Camera. J. Geophys. Res.. Planets, 105, 1623-1650.

Edgett, K. S. et al., 2012, Curiosity's Mars Hand Lens Imager (MAHLI) Investigation. Space Sci. Rev. 170, 259-317.

Elbelrhiti, H., 2012, Initiation and early development of barchan dunes: A case study of the Moroccan Atlantic Sahara desert. Geomorphology, 138, 181-188.

Elbelrhiti, H., Andreotti, B., and Claudin, P., 2008, Barchan dune corridors: field characterization and investigation of control parameters. Journal of Geophysical Research: Earth Surface, v. 113, no. F2.

Elbelrhiti H, Claudin P, and Andreotti B., 2005, Field evidence for surfacewave-induced instability of sand dunes. Nature 437: 720–723.

Endo, N., Taniguchi, K., and Katsuki, A., 2004, Observation of the whole process of interaction between barchans by flume experiments. Geophysical Research Letters, v. 31, no. 12.

Ewing, R. C., and Kocurek, G., 2010a, Aeolian dune interactions and dune-field pattern formation: White Sands Dune Field, New Mexico. Sedimentology, v. 57, no. 5, p. 1199-1219.

Ewing, R. C., and Kocurek, G., 2010b, Aeolian dune-field pattern boundary conditions. Geomorphology, v. 114, no. 3, p. 175-187.

Ewing, R. C., Kocurek, G., and Lake, L. W., 2006, Pattern analysis of dune-field parameters. Earth Surface Processes and Landforms, v. 31, no. 9, p. 1176-1191.

Ewing, R. C., McDonald, G. D., and Hayes, A. G., 2015, Multi-spatial analysis of aeolian dune-field patterns. Geomorphology, v. 240, p. 44-53.
Fagotto, F., 1987, Sand-dune Fixation in Somalia. Environmental Conservation, v. 14, no. 2, p. 157-163.
Farley, K. A. et al., 2014. In situ radiometric and exposure age dating of the Martian surface. Science 343, doi: 10.1126/science.1247166.
Fenton, L. K., Michaels, T. I., and Beyer, R. A., 2014. Inverse maximum gross bedform-normal transport 1: How to determine a dune-constructing wind regime using only imagery. Icarus 230, 5-14.
Finkel, H. J., 1959, The barchans of southern Peru. The journal of geology, v. 67, no. 6, p. 614-647.
Folk, R. L., 1971, Longitudinal dunes of the northwestern edge of the Simpson Desert, Northern Territory, Australia, 1. Geomorphology and grain size relationships Sedimentology, v. 16, no. 1-2, p. 5-54.
Fryberger, S.G., Al-Sari, A.M. and Clisham, T.J., 1983, Eolian dune, interdune, sand sheet, and siliciclastic sabkha sediments of an offshore prograding sand sea, Dhahran area, Saudi Arabia. AAPG Bulletin, 67, 280-312.
Gao, X., Narteau, C., and Rozier, O., 2015, Development and steady states of transverse dunes: A numerical analysis of dune pattern coarsening and giant dunes. Journal of Geophysical Research: Earth Surface, v. 120, no. 10, p. 2200-2219.
Garcia, M. H., 2008, Sediment transport and morphodynamics American Society of Civil Engineers Reston, VA.
Gay SP. 1999. Observations regarding the movement of barchan sand dunes in the Nazca to Tanaca area of southern Peru. Geomorphology 27: 279–293.
Geissler, P. E., 2014. The birth and death of transverse aeolian ridges on Mars. J. Geophys. Res.. Planets 119, 2583-2599.
Génois, M., Courrech du Pont, S., Hersen, P., and Grégoire, G., 2013, An agent-based model of dune interactions produces the emergence of patterns in deserts: When dunes move together. Geophysical Research Letters, v. 40, no. 15, p. 3909-3914.
Gilbert, G. K., 1909. The convexity of hillsloped. J. Geology 17, 344-350.
Gillies, J. A., Nickling, W. G., and Tilson, M., 2013. Frequency, magnitude, and characteristics of aeolian sediment transport: McMurdo Dry Valleys, Antarctica. J. Geophys. Res. Earth Surface 118, 461-479.
Glennie, K.W., 1970, Desert sedimentary environments. Elsevier Pub. Co, Amsterdam;New York;.
Golombek, M., Robinson, K., McEwen, A., Bridges, N., Ivanov, B., Tornabene, L., and Sullivan, R., 2010. Constraints on ripple migration at Meridiani Planum from Opportunity and HiRISE observations of fresh craters. J. Geophys. Res. Planets 115, doi:10.1029/2010JE003628.
Goudie, A. S., Colls, A., Stokes, S., Parker, A., White, K., and Al-Farraj, A., 2000, Latest Pleistocene and Holocene dune construction at the north-eastern edge of the Rub Al Khali, United Arab Emirates. Sedimentology, v. 47, no. 5, p. 1011-1021.

Grant, J. A., Wilson, S. A., Mangold, N., Calef, F., and Grotzinger, J. P., 2014. The timing of alluvial activity in Gale crater, Mars. Geophys. Res. Lett. 41, 1142-1149.

Greeley, R., and Arvidson, R. E., 1990, Aeolian processes on Venus. Earth Moon and Planets, v. 50-1, p. 127-157.

Greeley, R., and Iversen, J. D., 1987, Wind as a geological process: on Earth, Mars, Venus and Titan, CUP Archive.

Greeley, R. et al., 2008. Columbia Hills, Mars: Aeolian features seen from the ground and orbit. J. Geophys. Res. Planets 113, doi:10.1029/2007JE002971.

Greeley, R., Kraft, M., Sullivan, R., Wilson, G., Bridges, N., Herkenhoff, K., Kuzmin, R. O., Malin, M., and Ward, W., 1999. Aeolian features and processes at the Mars Pathfinder landing site. J. Geophys. Res. Planets 104, 8573-8584.

Greeley, R., Leach, R., White, B., Iversen, J., and Pollack, J., 1976, Mars - Wind friction speeds for particle movement. Geophysical Research Letters, v. 3, no. 8, p. 417-420.

Greeley, R., Skypeck, A., and Pollack, J. B., 1993, Martian Aeolian Features and Deposits - Comparisons with General-Circulation Model Results. Journal of Geophysical Research-Planets, v. 98, no. E2, p. 3183-3196.

Grotzinger, J. P., and Milliken, R. E., 2012. The sedimentary rock record of Mars: Distribution, origins, and global stratigraphy. Sed. Geol. of Mars, SEPM no. 102, p. 1-48.

Grotzinger, J. P. et al., 2005. Stratigraphy and sedimentology of a dry to wet eolian depositional system, Burns formation, Meridiani Planum, Mars. Earth and Planetary Sci. Lett. 240, 11-72.

Grotzinger, J. P. et al., 2014. A habitable fluvio-lacustrine environment at Yellowknife Bay, Gale Crater, Mars. Science 343, doi:10.1126/science.1242777.

Grotzinger, J. P., et al., 2015, Deposition, exhumation, and paleoclimate of an ancient lake deposit, Gale crater, Mars, Science, 350(6257), aac7575-U7569.

Haff, P. K., 2001. Desert Pavement: An Environmental Canary? Geology 109, 661-668.

Hansen, W.R. 1965. Geology of the Flaming Gorge area, Utah-Colorado-Wyoming, U.S. Govt. Print. Off, Washington DC.

Hartmann, W. K., and Neukum, G., 2001. Cratering chronology and the evolution of Mars. Space Sci. Rev. 96, 165-194.

Havholm, K. G., Blakey, R. C., Capps, M., Jones, L. S., King, D. D., and Kocurek, G., 1993, Aeolian genetic stratigraphy: an example from the Middle Jurassic Page Sandstone, Colorado Plateau. Sedimentology, v. 16, p. 87-107

Havholm, K.G. and Kocurek, G., 1994, Factors controlling aeolian sequence stratigraphy - Clues from super bounding surface-features in the Middle Jurassic Page sandstone. Sedimentology, 41, 913-934.

Hayward, R. K., Fenton, L. K., and Titus, T. N., 2014. Mars Global Digital Dune Database (MGD(3)): Global dune distribution and wind pattern observations. Icarus 230, 38-46.

Head, J. W., Hiesinger, H., Ivanov, M. A., Kreslavsky, M. A., Pratt, S., and Thomson, B. J., 1999, Possible Ancient Oceans on Mars: Evidence from Mars Orbiter Laser Altimeter Data. Science, v. 286, no. 5447, p. 2134-2137.

Hedin, S. A., 1903. Central Asia and Tibet Towards the Holy City of Lassa, Hurst and Blackett.

Hersen, P., and Douady, S., 2005, Collision of barchan dunes as a mechanism of size regulation. Geophysical Research Letters, v. 32, no. 21, p. L21403.

Hersen, P., Andersen, K. H., Elbelrhiti, H., Andreotti, B., Claudin, P., and Douady, S., 2004, Corridors of barchan dunes: Stability and size selection. Physical Review E, v. 69, no. 1.

Hesp, P. A., 1981. The formation of shadow dunes. J. of Sed. Res. 51, 101-111.

Hileman, M.E., 1973, Stratigraphy and paleoenvironmental analysis of the Upper Jurassic Preuss and Stump formations, western Wyoming and southeastern Idaho, University of Michigan, Ann Arbor, MI.

Hobbs, S. W., Paull, D. J., and Bourke, M. C., 2010. Aeolian processes and dune morphology in Gale Crater. Icarus 210, 102-115.

Howard, A., 1977. Effect of slope on the threshols motion and its application to orientation of wind ripples. Geol. Soc. Am. Bull. 88, 853-856.

Howard, A. D., 2007, Simulating the development of Martian highland landscapes through the interaction of impact cratering, fluvial erosion, and variable hydrologic forcing, Geomorphology, 91(3-4), 332-363.

Hugenholtz, C. H., and Barchyn, T. E., 2012, Real barchan dune collisions and ejections. Geophysical Research Letters, v. 39, no. 2.

Hummel, G. and Kocurek, G., 1984, Interdune areas of the back-island dune field, North Padre Island, Texas. Sedimentary Geology, 39, 1-26.

Hunter, R. E., 1977a, Basic types of stratification in small eolian dunes. Sedimentology, v. 24, no. 3, p. 361-387.

Hunter, R. E., 1977b, Terminology of cross-stratified sedimentary layers and climbing-ripple structures. Journal of Sedimentary Research, v. 47, no. 2, p. 697.

Hunter, R. E., and Rubin, D. M., 1983, Interpreting cyclic crossbedding, with an example from the Navajo Sandstone. Developments in sedimentology, v. 38, p. 429-454.

Imlay, R.W., 1952, Marine origin of Preuss sandstone of Idaho, Wyoming, and Utah. AAPG Bulletin, 36, 1735.

Inman, D. L., Ewing, G. C., and Corliss, J. B., 1966, Coastal Sand Dunes of Guerrero Negro Baja California Mexico. Geological Society of America Bulletin, v. 77, p. 787-&.

Jerram, D.A., Mountney, N.P., Howell, J.A., Long, D. and Stollhofen, H., 2000, Death of a sand sea: an active aeolian erg systematically buried by the Etendeka flood basalts of NW Namibia. Journal of the Geological Society, 157, 513-516.

Jimenez, J., 2004, Turbulent flows over rough walls, Annual review of fluid mechanics, 36(1), 173-196.

Kar, A., 1993, Aeolian processes and bedforms in the Thar Desert. Journal of Arid Environments, v. 25, no. 1, p. 83-96.

Katsuki A, Nishimori H, Endo N, Taniguchi K. 2005a. Collision dynamics of two barchans dunes simulated using a simple model. Journal of the Physical Society of Japan 74: 538–541.

Kerber, L., J. W. Head, J. B. Madeleine, F. Forget, and L. Wilson, 2011, The dispersal of pyroclasts from Apollinaris Patera, Mars: Implications for the origin of the Medusae Fossae Formation, Icarus, 216(1), 212-220.

Kerr, R. A., 2003, Eons of a Cold, Dry, Dusty Mars. Science, v. 301, no. 5636, p. 1037-1038.

King, L. C., 1953. Canons of landscape evolution. Geol. Soc. Amer. Bull. 64, 721-752.

Kite, E. S., Lewis, K. W., Lamb, M. P., Newman, C. E., and Richardson, M. I., 2013, Growth and form of the mound in Gale Crater, Mars: Slope wind enhanced erosion and transport. Geology 41, 543-546.

Kite, E. S., Sneed, J., Mayer, D. P., Lewis, K. W., Michaels, T. I., Hore, A., and Rafkin, S. C., 2016, Evolution of major sedimentary mounds on Mars: Buildup via anticompensational stacking modulated by climate change. Journal of Geophysical Research: Planets, v. 121, no. 11, p. 2282-2324.

Kocurek, G., 1981, Significance of interdune deposits and bounding surfaces in aeolian dune sands. Sedimentology, 28, 753-780.

Kocurek, G., 1983, Erg reconstruction: The entrada sandstone (Jurassic) of northern Utah and Colorado. Palaeogeography, Palaeoclimatology, Palaeoecology, v. 36, no. 1, p. 125-153.

Kocurek, G., 1988, First-order and super bounding surfaces in eolian sequences - Bounding surfaces revisited. Sedimentary Geology, 56, 193-206.

Kocurek, G., 1996, Desert aeolian systems, Oxford, Blackwell Science, Sedimentary Environments: Processes, Facies, and Stratigraphy.

Kocurek, G., 1999, The Aeolian Rock Record. Aeolian Environments, Sediments and Landforms, 239-259.

Kocurek, G. and Dott, R.H., 1981, Distinctions and uses of stratification types in the interpretation of eolian sand. Journal of Sedimentary Research, 51.

Kocurek, G. and Dott, R.H., 1983, Jurassic paleogeography and paleoclimate of the central and southern Rocky Mountains region. Rocky Mountain Section (SEPM).

Kocurek, G. and Ewing, R.C., 2005, Aeolian dune field self-organization – implications for the formation of simple versus complex dune-field patterns. Geomorphology, 72, 94-105.

Kocurek, G. and Ewing, R.C., 2017, Trickle-down and trickle-up boundary conditions in eolian dune-field pattern formation SEPM special publication: Autogenic dynamics and self-organization in sedimentary systems 106, 18-39.

Kocurek, G. and Havholm, K.G., 1993, Eolian sequence stratigraphy - a conceptual framework. In: Siliciclastic Sequence Stratigraphy. Recent Developments and Applications, M. 58, pp. 393-409.

Kocurek, G. and Hunter, R.E., 1986, Origin of polygonal fractures in sand, uppermost Navajo and Page sandstones, Page, Arizona. Journal of Sedimentary Research, 56, 895.

Kocurek, G. and Lancaster, N., 1999, Aeolian system sediment state: theory and Mojave Desert Kelso dune field example. Sedimentology, 46, 505-515.
Kocurek, G. and Nielson, J., 1986, Conditions favourable for the formation of warm-climate aeolian sand sheets. Sedimentology, 33, 795-816.
Kocurek, G., Ewing, R. C., and Mohrig, D., 2010, How do bedform patterns arise? New views on the role of bedform interactions within a set of boundary conditions. Earth Surface Processes and Landforms, v. 35, no. 1, p. 51-63.
Kocurek, G., Townsley, M., Yeh, E., Havholm, K. G., and Sweet, M. L., 1992, Dune and dune-field development on Padre Island, Texas, with implications for interdune deposition and water-table-controlled accumulation. Journal of Sedimentary Research, v. 62, no. 4, p. 622-635.
Kok, J. F., 2010. Analytical calculation of the minimum wind speed required to sustain wind-blown sand on Earth and Mars. Geophys. Res. Lett. 37, doi:10.1029/2010GL043646.
Laity, J. E., and Bridges, N. T., 2009. Ventifacts on Earth and Mars: Analytical, field, and laboratory studies supporting sand abrasion and windward feature development. Geomorphology 105, 202-217.
Lancaster, N., 1988, The development of large aeolian bedforms. Sedimentary Geology, v. 55, no. 1, p. 69-89.
Lancaster, N., 1989a. The Namib sand sea : dune forms, processes and sediments, A. A. Balkema, Rotterdam. Brookfield, Vermont.
Lancaster, N., 1989b. Star dunes. Progress in Physical Geography 13, 67-91.
Lancaster, N., 1996, Field studies of sand patch initiation processes on the northern margin of the Namib sand sea. Earth Surface Processes and Landforms, 21, 947-954.
Lancaster, N., Kocurek, G., Singhvi, A., Pandey, V., Deynoux, M., Ghienne, J.-F., and Lo, K., 2002, Late Pleistocene and Holocene dune activity and wind regimes in the western Sahara Desert of Mauritania. Geology, v. 30, no. 11, p. 991-994.
Le Deit, L. L., Hauber, E., Fueten, F., Pondrelli, M., Rossi, A. P., and Jaumann, R., 2013. Sequence of infilling events in Gale Crater, Mars: Results from morphology, stratigraphy, and mineralogy. J. Geophys. Res. Planets 118, 2439-2473.
Lee, P., and Thomas, P. C., 1995. Longitudinal dunes on Mars: Relation to current wind regimes. J. Geophys. Res. Planets 100, 5381-5395.
Lewis, K. W., and Aharonson, O., 2014, Occurrence and origin of rhythmic sedimentary rocks on Mars. Journal of Geophysical Research: Planets, v. 119, no. 6, p. 1432-1457.
Loope, D.B., 1984, Origin of extensive bedding planes in aeolian sandstones: a defence of Stokes' hypothesis. Sedimentology, 31, 123-125.
Lorenz, R. D., 2006, The sand seas of Titan: Cassini RADAR observations of longitudinal dunes: Science, v. 312, p. 724-727.
Malin, M. C., and Edgett, K. S., 2000. Sedimentary rocks of early Mars. Science 290, 1927-1937.

Malin, M. C., Edgett, K. S., Posiolova, L. V., McColley, S. M., and Dobrea, E. Z. N., 2006, Present-day impact cratering rate and contemporary gully activity on Mars. Science, v. 314, no. 5805, p. 1573-1577.

Maman, S., Blumberg, D. G., Tsoar, H., Mamedov, B., and Porat, N., 2011, The Central Asian ergs: A study by remote sensing and geographic information systems. Aeolian Research, v. 3, no. 3, p. 353-366.

Mandelbrot, B. B., 1967, How long is the coast of Britain: Science, v. 156, no. 3775, p. 636-638.

Mandt, K. E., L. d. S. Shanaka, J. R. Zimbelman, and D. A. Crown, 2008, Origin of the Medusae Fossae Formation, Mars: Insights from a synoptic approach, Journal of Geophysical Research - Planets, 113(E12), E12011.

Mauz, B., and Felix-Henningsen, P., 2005, Palaeosols in Saharan and Sahelian dunes of Chad. Archives of Holocene North African climate changes: The Holocene, v. 15, no. 3, p. 453-458.

McFadden, L. D., Wells, S. G., and Jercinovich, M. J., 1987. Influences of eolian and pedogenic processes on the origin and evolution of desert pavements. Geology 15, 504-508.

McKee, E. D., 1966, Structures of dunes at White Sands National Monument, New Mexico (and a comparison with structures of dunes from other selected areas) Sedimentology, v. 7, no. 1, p. 3-69.

Melosh, H. J., and B. A. Ivanov, 1999, Impact Crater Collapse, Annual Review of Earth and Planetary Sciences, 27(1), 385-415.

Michaels, T. I., and S. C. R. Rafkin, 2004, Large-eddy simulation of atmospheric convection on Mars, Q. J. R. Meteorol. Soc., 130(599), 1251-1274.

Milliken, R. E., R. C. Ewing, W. W. Fischer, and J. Hurowitz, 2014, Wind-blown sandstones cemented by sulfate and clay minerals in Gale Crater, Mars, Geophysical Research Letters, 41(4), 1149-1154.

Minitti, M. E. et al., 2013. MAHLI at the Rocknest sand shadow: Science and science-enabling activities. J. Geophys. Res. Planets 118, 2338-2360.

Mountney, N. P., 2006a, Eolian facies models, SEPM, Eolian Sediments and Processes doi:10.2110/pec.2106.2184.0019

Mountney, N. P., 2006b, Periodic accumulation and destruction of aeolian erg sequences in the Permian Cedar Mesa Sandstone, White Canyon, southern Utah, USA. Sedimentology, 53, 789-823.

Mountney, N.P., 2012, A stratigraphic model to account for complexity in aeolian dune and interdune successions. Sedimentology, 59, 964-989.

Mountney, N.P. and Jagger, A., 2004, Stratigraphic evolution of an aeolian erg margin system: the Permian Cedar Mesa Sandstone, SE Utah, USA. Sedimentology, 51, 713-743.

Mountney, N.P. and Thompson, D.B., 2002, Stratigraphic evolution and preservation of aeolian dune and damp/wet interdune strata: an example from the Triassic Helsby Sandstone Formation, Cheshire Basin, UK. Sedimentology, 49, 805-833.

Narteau, C., Zhang, D., Rozier, O., and Claudin, P., 2009, Setting the length and time scales of a cellular automaton dune model from the analysis of superimposed bed forms: Journal of Geophysical Research: Earth Surface, v. 114, no. F3.

Newsom, H. E. et al., 2015. Gale crater and impact processes - Curiosity's first 364 Sols on Mars. Icarus 249, 108-128.

Nield, J.M. and Wiggs, G.F.S., 2011, The application of terrestrial laser scanning to aeolian saltation cloud measurement and its response to changing surface moisture. Earth Surface Processes and Landforms, 36, 273-278.

Nielson, J., Kocurek, K., 1986. Climbing zibars of the Algodones. Sediment. Geol. 48, 1-15.

Palucis, M. C., Sumner, D. Y., Dietrich, W. E., Hayes, A. G., Williams, R. M. E., Gupta, S., Mangold, N., Newsom, H., Hardgrove, C., and Calef, F., 2014. The origin and evolution of the Peace Vallis fan system that drains to the Curiosity landing area, Gale Crater, Mars. J. Geophys. Res. Planets 119, 705-728.

Paola, C., and Borgman, L., 1991, Reconstructing random topography from preserved stratification. Sedimentology, v. 38, no. 4, p. 553-565.

Parteli, E. J. R., Durán, O., Tsoar, H., Schwämmle, V., Herrmann, H. J., and Stanley, H. E., 2009. Dune Formation under Bimodal Winds. Proceedings of the National Academy of Sciences 106, 22085-22089.

Parteli, E. J. R., Duran, O., Bourke, M. C., Tsoar, H., Poschel, T., and Herrmann, H., 2014. Origins of barchan dune asymmetry: Insights from numerical simulations. Aeolian Res. 12, 121-133.

Pedersen, A., Kocurek, G., Mohrig, D. and Smith, V., 2015, Dune deformation in a multi-directional wind regime: White Sands Dune Field, New Mexico. Earth Surface Processes and Landforms, 40, 925-941.

Pell, S. D., Chivas, A. R., and Williams, I. S., 1999, Great Victoria Desert: Development and sand provenance. Australian Journal of Earth Sciences, v. 46, no. 2, p. 289-299.

Pelletier, J. D., 2009, Controls on the height and spacing of eolian ripples and transverse dunes: A numerical modeling investigation. Geomorphology, v. 105, no. 3, p. 322-333.

Peterson, F., 1988, Pennsylvanian to Jurassic eolian transportation systems in the western United States. Sedimentary Geology, 56, 207-260.

Petrosyan, A., et al., 2011, The Martian Atmospheric Boundary Layer, Reviews of Geophysics, 49(3).

Ping, L., Narteau, C., Dong, Z.B., Zhang, Z.C. and Courrech du Pont, S., 2014, Emergence of oblique dunes in a landscape-scale experiment. Nature Geoscience, 7, 99-103.

Radebaugh, J., Soderblom, L., Allison, M., Janssen, M., Paillou, P., Callahan, P., Spencer, C., the Cassini Radar, T., Lorenz, R. D., Lunine, J. I., Wall, S. D., Boubin, G., Reffet, E., Kirk, R. L., Lopes, R. M., Stofan, E. R., and Cassini Radar, T., 2008, Dunes on Titan observed by Cassini Radar. Icarus, v. 194, no. 2, p. 690-703.

Radebaugh, J., Lorenz, R., Farr, T., Paillou, P., Savage, C., and Spencer, C., 2010, Linear dunes on Titan and earth: Initial remote sensing comparisons. Geomorphology, v. 121, no. 1, p. 122-132.

Rafkin, S. C. R., Haberle, R. M., and Michaels, T. I., 2001. The Mars regional atmospheric modeling system: Model description and selected simulations. Icarus 151, 228-256.

Robbins, S. J., and B. M. Hynek, 2012, A new global database of Mars impact craters >= 1 km: 2. Global crater properties and regional variations of the simple-to-complex transition diameter, Journal of Geophysical Research-Planets, 117.

Rubin, D. M., 1987, Cross-bedding, bedforms, and paleocurrents, Tulsa, Okla, SEPM (Society of Economic Paleontologists and Mineralogists), Society for Sedimentary Geology.

Rubin, D. M., 2012, A unifying model for planform straightness of ripples and dunes in air and water: Earth-Science Reviews, v. 113, no. 3–4, p. 176-185.

Rubin, D. M., and Carter, C. L., 2006, Bedforms and cross-bedding in animation, Sepm Society for Sedimentary, v. 2.

Rubin, D.M. and Hunter, R.E., 1982, Bedform climbing in theory and nature. Sedimentology, 29, 121-138.

Rubin, D. M., and Hunter, R. E., 1983, Reconstructing Bedform Assemblages from Compound Crossbedding, in Brookfield, M. E., and Ahlbrandt, T. S., eds., Developments in Sedimentology, Volume 38, Elsevier, p. 407-427.

Rubin, D. M., and Hunter, R. E., 1987a. Bedform Alignment in Directionally Varying Flows. Science 237, 276-278.

Rubin, D.M. and Hunter, R. E., 1987b, Field guide to sedimentary structures in the Navajo and Entrada sandstones in southern Utah and northern Arizona. Chapter in Field-trip guidebook, 100th annual meeting, The Geological Society of America, Phoenix, Arizona, October 26-29, 1987. Special Paper 5, 126-139.

Sadler, P. M., 1981, Sediment Accumulation Rates and the Completeness of Stratigraphic Sections. The Journal of Geology, v. 89, no. 5, p. 569-584.

Sagan, C., and Bagnold, R. A., 1975. Fluid transport on Earth and aeolian transport on Mars. Icarus 26, 209-218.

Sagan, C., Smith, B. A., Veverka, J., Fox, P., Dubisch, R., Lederberg, J., Levinthal, E., Quam, L., Tucker, R., and Pollack, J. B., 1972. Variable features on Mars: Preliminary Mariner 9 television results. Icarus 17, 346-372.

Schatz, V., Tsoar, H., Edgett, K. S., Parteli, E. J. R., and Herrmann, H. J., 2006, Evidence for indurated sand dunes in the Martian north polar region. Journal of Geophysical Research - Planets, v. 111, no. E4, p. E04006.

Scherer, C.M.S., 2002, Preservation of aeolian genetic units by lava flows in the Lower Cretaceous of the Paraná Basin, southern Brazil. Sedimentology, 49, 97-116.

Schon, S. C., J. W. Head, and C. I. Fassett, 2012, An overfilled lacustrine system and progradational delta in Jezero crater, Mars: Implications for Noachian climate, Planetary and Space Science, 67(1), 28-45.

Schorghofer, N., 2008. Temperature response of Mars to Milankovitch cycles. Geophys. Res. Lett. 35, doi:10.1029/2008GL034954.
Shao, Y., 2000, Physics and modelling of wind erosion, edited, Kluwer Academic, Boston; Dordrecht.
Shao, Y., and H. Lu, 2000, A simple expression for wind erosion threshold friction velocity. Journal of Geophysical Research, 105(D17), 22437-22443.
Shockey, K. M., and Zimbelman, J. R., 2013. Analysis of transverse aeolian ridge profiles derived from HiRISE images of Mars. Earth Surface Processes and Landforms 38, 179-182.
Silvestro, S., Vaz, D. A., Ewing, R. C., Rossi, A. P., Fenton, L. K., Michaels, T. I., Flahaut, J., and Geissler, P. E., 2013. Pervasive aeolian activity along rover Curiosity's traverse in Gale Crater, Mars. Geology 41, 483-486.
Simpson, E.L. and Loope, D.B., 1985, Amalgamated interdune deposits, White Sands, New Mexico. Journal of Sedimentary Research, 55, 361.
Sorby, H. C., 1869, On the structures produced by the currents present during the deposition of stratified rocks. The Geologist v. 2, p. 137-147.
Squyres, S. W., and Kasting, J. F., 1994, Early Mars: How Warm and How Wet?. Science, v. 265, no. 5173, p. 744-749.
Stack, K. M. et al., 2014. Diagenetic origin of nodules in the Sheepbed member, Yellowknife Bay formation, Gale crater, Mars. J. Geophys. Res. Planets 119, 1637-1664.
Sullivan, R. et al., 2005. Aeolian processes at the Mars Exploration Rover Meridiani Planum landing site. Nature 436, 58-61.
Sullivan, R. et al., 2008. Wind-driven particle mobility on mars: Insights from Mars Exploration Rover observations at "El Dorado" and surroundings at Gusev Crater. J. Geophys. Res. Planets 113, doi:10.1029/2008JE003101.
Sullivan, R., Bridges, N., Herkenhoff, K., Hamilton, V., and Rubin, D., 2014. Transverse aeolian ridges (TARs) as megaripples: Rover engounters at Meridiani Planum, Gusev, and Gale. Eighth International Conference on Mars, Abstract #1424.
Sun, J., 2000, Origin of Eolian Sand Mobilization during the Past 2300 Years in the Mu Us Desert, China. Quaternary Research, v. 53, no. 1, p. 78-88.
Swanson, T. E., 2015, Bedform interaction and preservation, dissertation, PhD. University of Texas at Austin.
Swanson, T., Mohrig, D., Kocurek, G., and Liang, M., 2016a, A Surface Model for Aeolian Dune Topography: Mathematical Geosciences, doi:10.1007/s11004-016-9654-x.
Swanson, T., Mohrig, D., Kocurek, G., and Lancaster, N., 2016b, Aeolian dune sediment flux variability over an annual cycle of wind: Sedimentology, v. 63, no. 6, p. 1753-1764.
Talbot, M.R., 1985, Major bounding surfaces in aeolian sandstones-a climatic model. Sedimentology, 32, 257-265.
Tanaka, K. L., 2000, Dust and Ice Deposition in the Martian Geologic Record. Icarus, 144(2), 254-266.

Tanaka, K. L., Skinner, J.A., Jr., Dohm, J.M., Irwin, R.P., III, Kolb, E.J., Fortezzo, C.M., Platz, T., Michael, G.G., and Hare, T.M., 2014, Geologic map of Mars.

Thomas, N., et al., 2015, The morphological diversity of comet 67P/Churyumov-Gerasimenko. Science, v. 347, no. 6220.

Thomson, B. J., Bridges, N. T., Milliken, R., Baldridge, A., Hook, S. J., Crowley, J. K., Marion, G. M., de Souza Filho, C. R., Brown, A. J., and Weitz, C. M., 2011. Constraints on the origin and evolution of the layered mound in Gale Crater, Mars using Mars Reconnaissance Orbiter data. Icarus 214, 413-432.

Tirsch, D., Jaumann, R., Pacifici, A., and Poulet, F., 2011. Dark aeolian sediments in Martian craters: Composition and sources. J. Geophys. Res. Planets 116, doi:10.1029/2009JE003562.

Tsoar, H., 1989. Linear dunes - forms and formation. Progress in Physical Geography 13, 507-528.

Tsoar, H., Blumberg, D. G., and Stoler, Y., 2004. Elongation and migration of sand dunes. Geomorphology 57, 293-302.

Turcotte, D., and Huang, J., 1995. Fractal distributions in geology, scale invariance, and deterministic chaos, Fractals in the earth sciences, Springer, p. 1-40.

Tyler, D., and Barnes, J. R., 2013. Mesoscale Modeling of the Circulation in the Gale Crater Region: An Investigation into the Complex Forcing of Convective Boundary Layer Depths. Mars 8, 58-77.

Van Wagoner, J.C., Mitchum, R.M., Campion, K.M., Rahmanian, V.D.K. and American Association of Petroleum, G. (1990) Siliciclastic sequence stratigraphy in well logs, cores and outcrops: concepts for high-resolution correlation of time and facies. American Association of Petroleum Geologists, Tulsa, Oklahoma.

Veverka, J., 1975. Variable features on Mars V: Evidence for crater streaks produced by wind erosion. Icarus 25, 595-601.

Viles, H., Ehlmann, B., Wilson, C. F., Cebula, T., Page, M., and Bourke, M., 2010. Simulating weathering of basalt on Mars and Earth by thermal cycling. Geophys. Res. Lett. 37, doi:10.1029/2010GL043522.

Vincelette, R.R. and Chittum, W.E., 1981, Exploration for oil accumulations in Entrada Sandstone, San Juan Basin, New Mexico. AAPG Bulletin, 65, 2546.

Waichel, B.L., Scherer, C.M.S. and Frank, H.T., 2008, Basaltic lava flows covering active aeolian dunes in the Paraná Basin in southern Brazil: Features and emplacement aspects. Journal of Volcanology and Geothermal Research, 171, 59-72.

Walker, R.G., 1963, Distinctive typed of ripple-drift cross-lamination Sedimentology, 2, 173-188.

Wang , Z. T., Wang, H. T., Niu, Q. H., Dong, Z. B., and Wang, T., 2011. Abrasion of yardangs. Physical Rev. E 84, doi: 10.1103/PhysRevE.84.031304.

Wang, X., Dong, Z., Zhang, J., and Chen, G., 2002, Geomorphology of sand dunes in the Northeast Taklimakan Desert. Geomorphology, v. 42, no. 3, p. 183-195.

Ward, A. W., 1979. Yardangs on Mars - Evidence of recent wind erosion. J. Geophys. Res. 84, 8147-8166.

Warner, N., Gupta, S., Lin, S. Y., Kim, J. R., Muller, J. P., and Morley, J., 2010. Late Noachian to Hesperian climate change on Mars: Evidence of episodic warming from transient crater lakes near Ares Vallis. J. Geophys. Res. Planets 115, doi:10.1029/2009JE003522.

Warren, J.K., 2016, Sabkhas, Saline Mudflats and Pans. In: Evaporites: A Geological Compendium, pp. 207-301. Springer International Publishing, Cham.

Wasson, R. J., Fitchett, K., Mackey, B., and Hyde, R., 1988, Large-scale patterns of dune type, spacing and orientation in the Australian continental dunefield. Australian Geographer, v. 19, no. 1, p. 89-104.

Werner, B. T., 1995, Eolian dunes: Computer simulations and attractor interpretation. Geology, v. 23, no. 12, p. 1107-1110.

Werner, B. T., 1999, Complexity in Natural Landform Patterns. Science, v. 284, no. 5411, p. 102-104.

Werner, B. T., 2003, Modeling landforms as self-organized, hierarchical dynamical systems. Prediction in geomorphology, p. 133-150.

Werner, B. T., and Kocurek, G., 1997, Bed-form dynamics: Does the tail wag the dog?. Geology, v. 25, no. 9, p. 771-774.

Werner, B. T., and Kocurek, G., 1999, Bedform spacing from defect dynamics. Geology, v. 27, no. 8, p. 727-730.

Whitney, J. W., 2007, Geology, water, and wind in the Lower Helmand Basin, Southern Afghanistan. STAR, v. 45, no. 7.

Williams, R. M. E. et al., 2013a. Martian Fluvial Conglomerates at Gale Crater. Science 340, 1068-1072.

Williams, R. M. E., et al., 2013b, Variability in martian sinuous ridge form: Case study of Aeolis Serpens in the Aeolis Dorsa, Mars, and insight from the Mirackina paleoriver, South Australia, Icarus, 225(1), 308-324.

Wilson, I. G., 1971, Journey across the Grand Erg Oriental. The Geographical Magazine, v. 43, no. 4, p. 264-270.

Wilson, S. A., Howard, A. D., Moore, J. M., and Grant, J. A., 2007, Geomorphic and stratigraphic analysis of Crater Terby and layered deposits north of Hellas basin, Mars, Journal of Geophysical Research-Planets, 112(E8).

Wilson, S. A., Zimbelman, J. R., 2004. Latitude-dependent nature and physical characteristics of transverse aeolian ridges on Mars. J. Geophys. Res. 109, doi:10.1029/2004JE002247.

Wordsworth, R. D., 2016, The Climate of Early Mars. Annual Review of Earth and Planetary Sciences, v. 44, no. 1, p. 381-408.

Worman, S. L., Murray, A. B., Littlewood, R., Andreotti, B., and Claudin, P., 2013, Modeling emergent large-scale structures of barchan dune fields. Geology, v. 41, no. 10, p. 1059-1062.

Wray, J. J., 2013. Gale crater: the Mars Science Laboratory/Curiosity Rover Landing Site. Int. J. of Astrobiology 12, 25-38.

Zhang, D. G., Narteau, C., Rozier, O., and Courrech du Pont, S., 2012. Morphology and dynamics of star dunes from numerical modelling. Nature Geoscience 5, 463-467.

Zimbelman, J. R., 2010. Transverse Aeolian Ridges on Mars: First results from HiRISE images. Geomorphology 121, 22-29.

Zimbelman, J. R., and Johnson, M. B., 2016, Surface slope effects for ripple orientation on sand dunes in López crater, Terra Tyrrhena region of Mars. Aeolian Research, no. DOI:10.1016/j.aeolia.2016.08.007.

Zimbelman, J. R., and Scheidt, S. P., 2014. Precision topography of a reversing sand dune at Bruneau Dunes, Idaho, as an analog for Transverse Aeolian Ridges on Mars. Icarus 230, 29-37.

Zimbelman, J. R., Williams, S. H., and Tchakerian, V. P., 1995, Sand transport paths in the Mojave Desert, southwestern United States, Desert aeolian processes, Springer, p. 101-129.